UNIVERSITY OF CALIFORNIA
RIVERSIDE

Solid-state Photochemical and Photomechanical Studies of Nanostructures and Microstructures of Anthracene Derivatives

A Dissertation submitted in partial satisfaction
of the requirements for the degree of

Doctor of Philosophy

in

Chemistry

by

Lingyan Zhu

December 2011

Dissertation Committee:
Dr. Christopher J. Bardeen, Chairperson
Dr. Gregory Beran
Dr. Jingsong Zhang

The Dissertation of Lingyan Zhu is approved:

Committee Chairperson

University of California, Riverside

Acknowledgement

Looking back on these last five years at UCR, I am full of thanks to all those who have supported me to make this dissertation possible.

First, I owe my deepest gratitude to my supervisor, Professor Christopher Bardeen. I feel very lucky to have been his student. He has taught me not only ways to do science, but has also been a pattern of an upright person. He is approachable all the time, and his profound knowledge in multiple fields has given me countless valuable advices. His passion for science always inspires me to press on and do my best. I also learned a lot from his work attitude: hard-working, ever-learning, cooperative, and honest.

I would also like to thank Professor Rabih Al-kaysi and Dr. Fook S. Tham. Rabih helped me to synthesize many novel molecules, and Fook has helped to solve all the crystal structures. This dissertation wouldn't be possible without their support.

Furthermore, I appreciate the mutually helpful atmosphere of UCR. I would like to thank Professor Greg Beran, Professor Jingsong Zhang, Professor Lenard Muller, Professor Pingyun Feng, Professor Yushan Yan, and many other professors' generous help and instructions.

Last but not least, it is really my pleasure to thank my group members: Dr Kerry Hanson, Dr. Tai Sang Anh, Dr. Yaobing Wang, Dr. Taehyung Kim, Dr. Astrid Muller; and many doctors-to-be: Robert Dillon, Jonathan Burdett, Kathryn Colby, Xiaoquan Zhou, Valerie Nichols… Thank you!

ABSTRACT OF THE DISSERTATION

Solid-state Photochemical and Photomechanical Studies of Nanostructures and Microstructures of Anthracene Derivatives

by

Lingyan Zhu

Doctor of Philosophy, Graduate Program in Chemistry
University of California, Riverside, December 2011
Dr. Christopher Bardeen, Chairperson

Photoactuators are devices made of photoreactive materials, which undergo shape changes to generate mechanical motions upon irradiation. Research on photoreactive materials has attracted much attention; this dissertation mainly focuses on photoreactive molecular crystals, which provide us great freedom to modify photoresponse through organic derivatization.

Various anthracene derivatives were synthesized and fabricated into nano- and micro-scale structures; multiple measurements, including Atomic Force Microscopy, solid-state Nuclear Magnetic Resonance, X-ray diffraction, etcetera, were applied with three goals: (1) maximize the photoresponse; (2) develop new modes of photoresponse; (3) enhance the reversibility of the photoresponse.

To maximize the photoresponse, we engineered the crystal structures and packing motifs of anthracene esters with diverse-sized substituents. The largest expansion of nanorods we obtained was 25% by length. We also tried to establish the relationship between the macroscopic photoresponse and the molecular-level structural changes, so

that the photoresponse of molecular crystals may be predicted based on their crystal structures. A detailed study of the photochemistry of 9-tertbutyl-anthracene-carboxylic-acid-ester (9TBAE) shows that the solid-state photoproduct is a metastable intermediate, which slowly converts into another stable equilibrium form. This is a general phenomenon among anthracene esters. Thus, the metastable structure is the key for predicting the macroscopic photoresponse. Further studies are required to obtain the crystal structure of this crucial intermediate.

Our proposal to develop new modes of photoresponse is through morphology control. Using the floating drop method, we managed to grow 9-anthracene carboxylic acid (9AC) into single-crystalline microribbons, which generate reversible photo-induced twisting motions under uniform irradiation. The interfacial strain between the unreacted monomer and the photodimer regions within the ribbon is the driving force for the twisting.

To enhance the reversibility of the photoresponse, we tried to use the steric effects to accelerate the dissociation of the photodimer. However, only one out of six derivatives of 9AC, 10-flouro-9-anthracenecarboxylic-acid, shows the reversible photoreactivity yet with much longer response time. Attempts to self-consistently rationalize observed trends in terms of excited state lifetimes or steric effects were only partly successful. Balancing factors like electronic relaxation, steric interactions, and crystal packing presents a challenge for engineering photoactive solid-state materials based on molecular crystals.

Table of Contents

List of Tables

List of Figures

Chapter 1 Introduction

1.1 Background and Motivation

Actuators, in general, are devices capable of converting external stimuli (magnetic field, electronic field, light, temperature, etc.) into action or mechanical motion. The development of actuators based on materials that respond to external stimuli has attracted a lot of interest. Their special properties can be applied in many potential applications, including artificial muscles, [1] micro-pumps, [2] molecular switching, [3] fluorescence sensing, [4] etc. Compared with other materials, photoresponsive materials are particularly appealing because of their unique advantages: 1) they are good media to transform photon energy directly into mechanical motions, without going through intermediate step such as transforming photon energy into electricity; 2) they can be remotely operated without physical contact, which enables easy fabrication of the devices since no wires or connections are necessary; 3) the motions of photoactuators can be manipulated precisely to different points or segments by spatially selective illumination; [5] 4) the wavelength of the light can be tuned for biological applications, and it's less likely to perturb delicate biological structures than most other stimuli. [6]

1.2 Photoreactive Polymer Gels and Films

There have been many types of photo responsive materials developed so far, such as polymer gels, films, liquid crystal elastomers, and molecular crystals. For photoresponsive polymer gels and films, their photoresponse usually come from

incorporated photoactive molecules or moieties. The photochromic reactions of the incorporated photochromophores are usually associated with certain changes in their physical and chemical properties. These changes would then bring forth the phase transition or shape deformation of the polymer matrix. Some typical photochromic reactions are shown in the table 1. [7]

Table 1. 1 Photochromic reactions

Type of reaction	Example
Isomerization	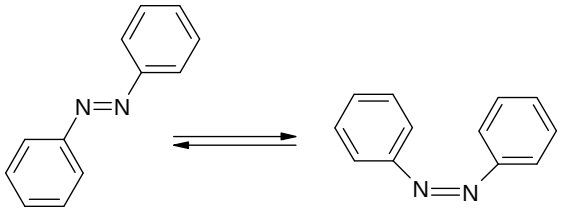
Zwitterion formation	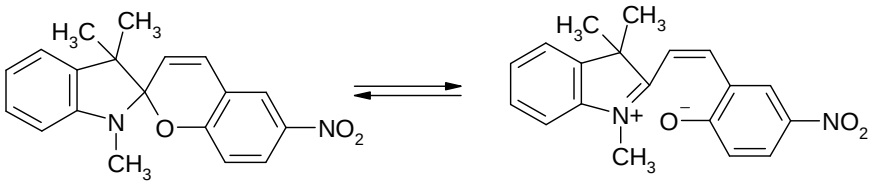
Ionic dissociation	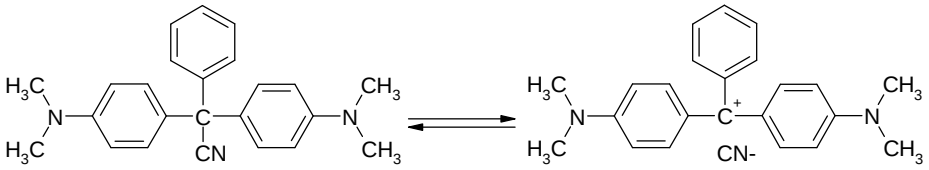
Ring formation and ring cleavage	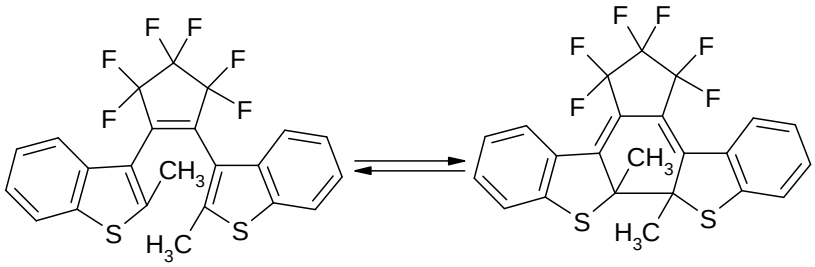

There have been several previous reports concerning photo responsive gels and films. For example, Irie and co-workers demonstrated that triphenylmethane leuco

derivatives of polyacrylamide gels exhibit a large reversible deformation. [8] Upon irradiation with UV light, the weight of the gel increased by as much as 13 times, and the swollen gel contracted in the dark and regained its initial weight. Athanassiou et al. prepared poly(ethylmethacrylate-co-methyl acrylate) film doped with 5.0 wt % spiropyran derivatives. Upon exposure to initial UV laser pulses, and following green light pulses, the film bent in the direction of the laser source (green). The maximum bending was observed after 40 pulses of green light, and continuing green pulses led to the recovery of the film after 160 pulses. [9]

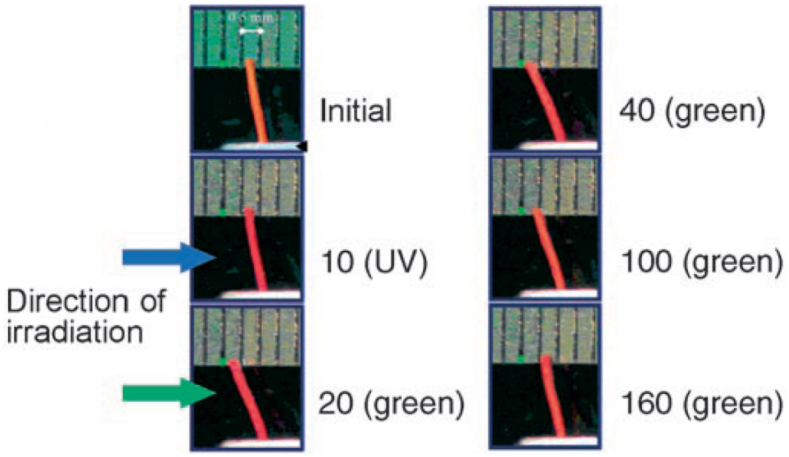

Figure 1. 1 Bending cycle of a spiropyran-doped polymer film**.** The photographs were taken after irradiation of the film with the number of laser pulses shown. [9]

However, polymer gels and films have several disadvantages: 1) the response time is relatively slow because their deformation comes from the photoresponse of the incorporated molecules, in other words, they response to the illumination indirectly. 2) Most of the polymer gels and films are amorphous, without microscopic or macroscopic order, and thus their deformations are isotropic. [10] They produce weaker mechanical force

compared with materials with anisotropic properties. 3) The incorporated photochromophores are the real force-generating source, but they are often distributed randomly in the polymers. In other words, the polymer carriers 'dilute' the photochromophores, which also leads to weaker mechanical force compared with materials with higher density of photoreactive molecules like molecular crystals.

1.3 Photoreactive Liquid crystalline elastomers (LCEs)

Liquid crystalline elastomers (LCEs) are another widely studied class of materials for photoactuators. Their special properties come from the combination of flexibility from polymer networks and ordered alignment from liquid crystals. LCEs are usually lightly cross-linked networks, which consist of several components: cross-linker (polymerization segment), liquid crystal unit or liquid crystal core, and polymer backbone (flexible side chains). Figure 1.2 demonstrates the anisotropic contraction and elongation of liquid crystal elastomers under external stimuli such as light, temperature, and electronic field. This is a general scheme to use LCEs as potential artificial muscles.[11]

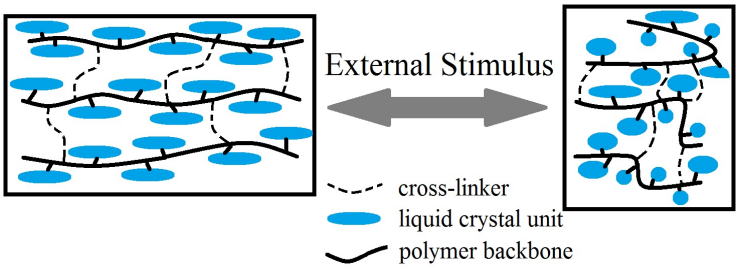

Figure 1. 2 Anisotropic contraction and elongation of liquid crystal elastomers

Similar to polymer gels and films, the photoresponsive behavior of LCEs is usually induced by the incorporated photoactive molecules, especially azobenzene

moieties and their variously substituted analogues. Azobenzene and its derivatives are special molecular cores that they can act both as photochromic and mesogenic units. The more stable *trans* form of the azobenzene moiety is rod-like and supports the liquid-crystalline phase; while the photoinduced *cis* form has a bent shape and is not compatible with the liquid-crystalline phase. The two forms can interconvert reversibly by photoinduced isomerization as shown in Table 1. In addition to the photochromism, the optical properties of azobenzene materials can be changed by illumination with polarized light, depending on the polarization of the pump light. [12]

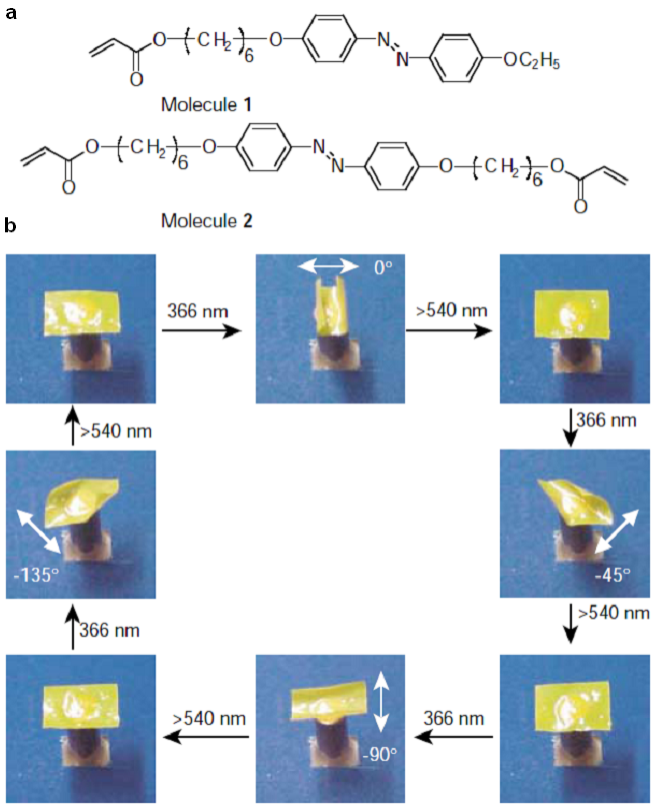

Figure 1. 3 Directed bending of a polymer film by light. **a)** Chemical structures of the liquid-crystal monomer (molecule 1) and crosslinker (molecule 2) used for preparation of the film. **b)** Photographic frames of the film bending in different directions in response to irradiation by linearly polarized light of

different angles of polarization (white arrows) at 365 nm, and being flattened by visible light longer than 540 nm. The film scale is 4.5 mm x 3 mm x 7 um; the response time of the film is about 10 s. [13]

The unique characteristics of LCEs make them very useful materials for soft actuators, such as artifical muscle. Light-driven actuation has been achieved in many systems; For example, Ikeda and co-workers prepared polymer films shown in Figure 1.3 with azobenzene moieties. The film bent toward the direction of 365-nm irradiation, with the bending occurring parallel to the direction of light polarization. When the bent film was exposed to visible light with a wavelength longer than 540 nm, it completely reverted to its initial flat state.

LCEs are promising materials for the construction of artificial muscles driven by the light; however, many considerations must be taken into account while applying them to biological systems. One concern is that artificial muscle needs to be able to contract and stretch, but so far reversibility is a weakness of LCEs. For example, the cycling of azobenzene and their derivatives contained LCEs degrade within about five cycles. Another concern is that artificial muscle must undergo the greatest shape change with the least amount of energy. Developing the pathways to translate a neurological signal into a conformational change in the artificial muscle is perhaps the greatest problem to be resolved. [14]

1.4 Photoreactive Molecular Crystals

The research in this dissertation has focused on a different class of photoactive materials, namely, molecular crystals. A molecular crystal is a crystal whose molecules

are held together by weak physical bonding such as van der waals forces, dipole-dipole bonds, or hydrogen bonding as opposed to chemical bonding like covalent bond, ionic bond. While polymer gels, films and LCEs are for potential applications of 'soft' actuators, molecular crystals can be considered as potential 'stiff' actuators. Compared with polymers, molecular crystals have several potential advantages: 1) their photo response can be much faster since every single molecule packing in the crystal is photoreactive; in other words, the photo response time is only limited to the photoreaction itself but not to the rearrangement of guest/host system. 2) They can generate stronger forces due to the high density of photochromic molecules (molecular crystals 100 wt % vs. polymers ~5-10 wt %). Furthermore, these molecules are highly ordered, which generates anisotropic deformations of the materials, and this also helps to generate more force; 3) Crystals have higher young's modulus than polymers in general. [15-23] The Young's modulus measures the resistance of a material to elastic (recoverable) deformation under load, and reflects the stiffness of a material. In the applications of mechanical work, materials with a higher Young's modulus, which deform less under a given load, are preferred.

Organic molecular crystals are of particular interest; [24] one of their unique properties is the possibility to tune the structures and properties of the material by adding different substituent groups. There are many researches carried out on photo reactions of organic molecular crystals since 1960s. [25] Reversible photomechanical changes were first observed in charge-transfer crystals[26] and later workers have exploited photoinduced charge transfer dynamics to drive rapid mechanical motions in microcrystals.[27-28] In

general, there are two types of the photoreactions of organic molecular crystals: intramolecular reactions and intermolecular reactions. For intramolecular events, there are cis-trans isomerization, cyclization, and ring formation/ring cleavage, etc (as illustrated in Table 1.1). Irie and coworkers utilized the ring formation/ring cleavage reaction of diarylethene derivatives and demonstrated the photomechanical work of the single crystal moving a 90-times-heavier gold microparticle for 80 cycles as shown in Figure 1.4. [29] Koshima and coworkers demonstrated the reversible bending of a narrow plate-like azobenzene derivative crystal using the cis-tans isomerization reaction[30]. These are considerable achievements considering that photo-induced reactions of macroscopic organic crystals typically shatter the crystal and do not lead to useful mechanical motions. [31-32]

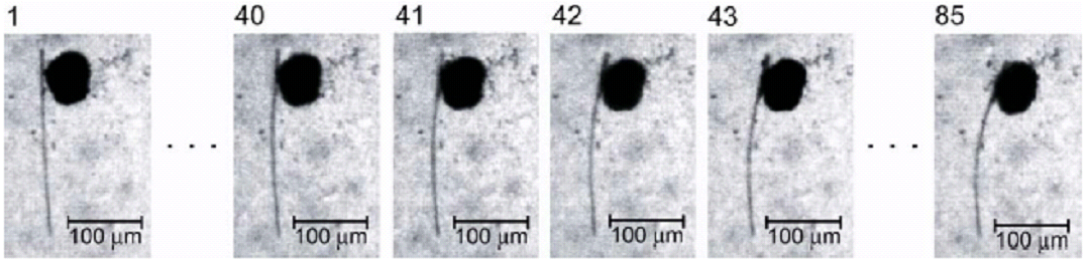

Figure 1. 4 High-speed camera images of the rod-like crystal bent and push the gold microparticle on irradition of ultraviolet (365 nm) light. The gold microparticle is 90 times heavier than the rod-like crystal (250 x 5 x 5 um).

However, these crystals fabricated were very limited in regard to their morphology and response; both of their crystals were on the micro-scale. Furthermore, the structure changes of intramolecular photoreactions are relatively small, usually on the order of 1 Å or less. [33] For intermolecular events, there are [2+2] photocycloaddiction,

[4+4] photocycloaddition, and photopolymerization. Since intermolecular photoreaction involves large-scale atomic motions in the crystal structures, they are more likely to produce larger shape deformations if the shattering of the crystals can be avoided. [34] The previous work of Dr. Rabih O. Al-Kaysi in Bardeen group successfully solved the problem of shattering by controlling the nanoscale morphology of organic molecular crystal and demonstrated irreversible (as illustrated in Figure 1.5) and reversible (as illustrated in Figure 1.6) shape changes in rod-shaped nanocrystals of anthracene derivatives. [33, 35] The work of Jacob Good in Bardeen group demonstrated the controllable bending of 9AC nanorods by selective illumination. [5]

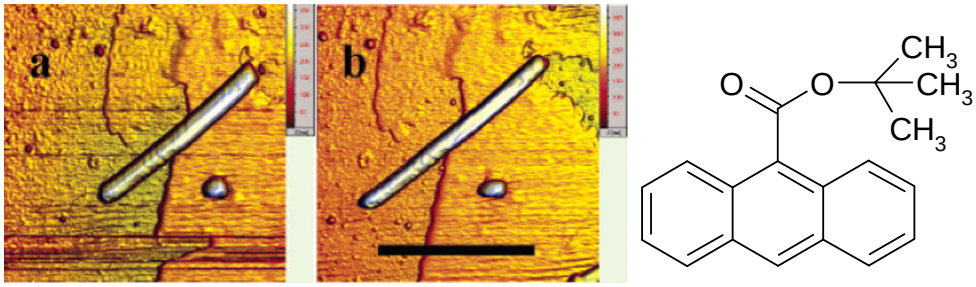

Figure 1. 5 (**a**) AFM image of a single 200 nm nanorod of 9-tertbutyl-anthracene ester (9TBAE) before illumination; (**b**) 9TBAE nanorod expanded by 15% in length after illumination with 365 nm. Scale bar is 6 um. Molecular structure of 9TBAE is shown on the above right.

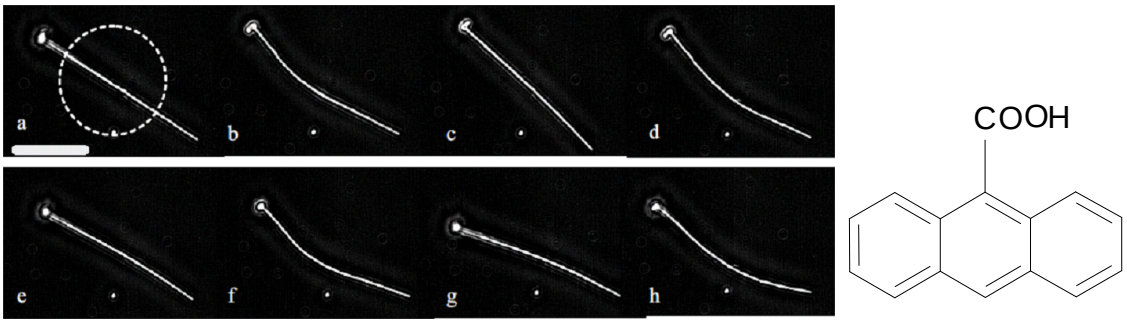

Figure 1. 6 The optical microscopy images of the reversible bending of a single 200 nm diameter nanorod of 9-anthracene carboxylic acid (9AC) (after UV illumination = panels **b, d, f, h**; after dark period = panels

a, c, e, g). The time required to revert back is around 2 min at room temperature. The dotted circle shows the illuminated region (35 um in diameter). Scale bar = 20.7 um. Molecular structure of 9AC is shown in the above right.

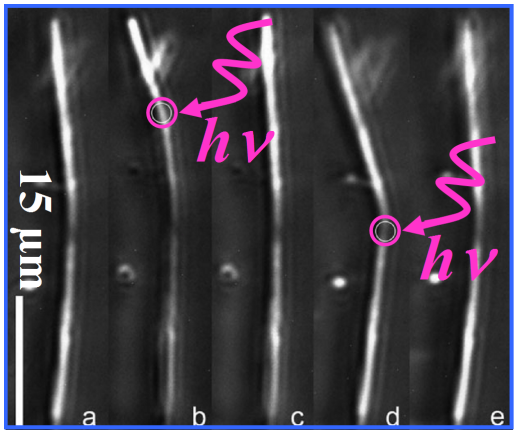

Figure 1. 7 The optical microscopy images of the reversible selective bending of a single 200 nm diameter nanorod of 9-anthracene carboxylic acid (9AC). The red circle is where 9AC nanorod was exposed to the selective illumination (UV 365nm). Scale bar = 15 um.

1.5 [4+4] Photocycloaddition Schemes

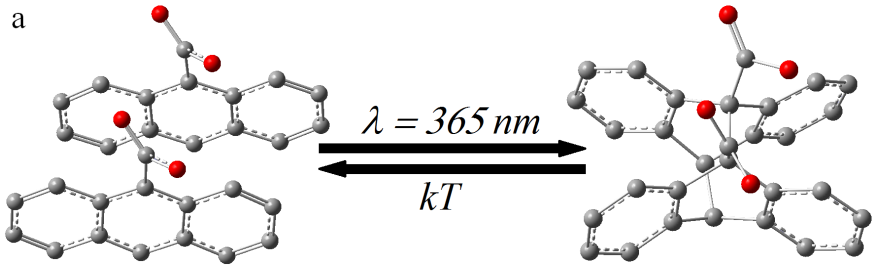

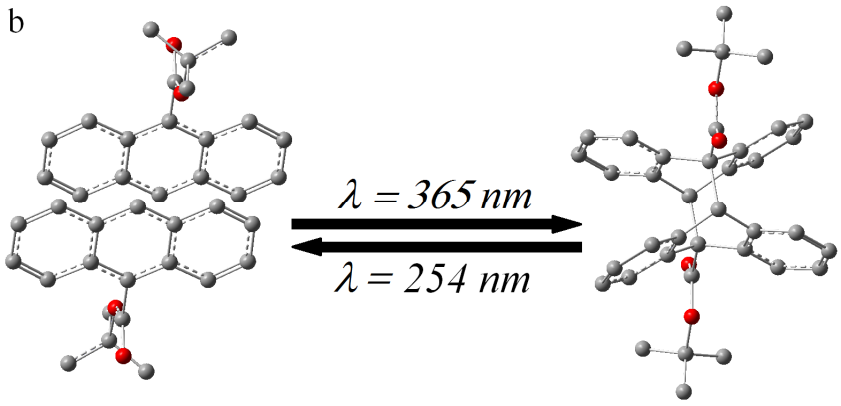

Figure 1. 8 [4+4] photocycloaddition schemes (**a**) head-to-head photoreaction of 9AC; (**b**) head-to-tail photoreaction of 9TBAE.

Several studies were carried out on the photoreaction of anthracene and their derivatives; with the exception of a few special cases, [36-37] the [4+4] cycloaddition occurs at the 9 and 10 positions of anthracene. The photodimers could be head-to-head and/or head-to-tail as shown in Figure 1.8. [38] In general, the head-to-tail photodimer is less stable due to the static effect of two adjacent substituent groups on 9th positons. This aspect of the head-to-tail photodimer can contribute to the reversible property of the material, for example, 9AC nanorods relax back to the original shape within 5min in room temperature after shape deformation from irradiation (Figure 1.6).

1.6 Conclusion

Dr. Al-Kaysi has done the pioneering work on harnessing [4+4] photocycloaddiction reaction to make photoreactive molecular crystal nanorods of anthracene derivatives. Yet there are still many questions waiting to be answered in order to utilize molecular crystals as potential photoactuators. For example, what is the mechanism of the photoresponse of these nanorods? Can we relate the macroscopic

expansion of the nanorods with the molecular level photoreaction? Can we predict the final photoresponse of the nanorods by comparing the crystal structures of anthracene derivatives and their photodimers? Can we amplify the photoresponse? Is there a possible maximum photoresponse of these nanorods? Is there any more complicated photoresponse other than expansion and bending? How can we utilize the photoresponse of these nanorods to do some mechanical work?

In this dissertation, families of 9-anthracene carboxylic acid ester derivatives and 9-anthracene carboxylic acid derivatives were synthesized and fabricated into various nano- and micro-structures. Multiple instruments and measurements were applied to study their solid-state photochemistry, photophysics and photomechanical motions, with three main goals: (I) maximize the photoresponse; (II) explore different forms of photomechanical motions; (III) strengthen and fasten the reversibility of the photomechanical motions. This dissertation is composed of three main projects, trying to accomplish these three goals.

The details of the instrumental measurements, experimental methods, and set-ups for calculations in this dissertation are presented in Chapter 2. The instrumental measurements include atomic force microscope (AFM), scanning electronic microscope (SEM), single crystal and powder X-ray diffraction (XRD), ^{13}C, ^{1}H solid-state and liquid Nuclear Magnetic Response (NMR), UV-vis absorption spectroscopy, steady-state and time-resolved fluorescence spectroscopy. The experimental methods include organic synthesis of anthracene derivative families, single crystal growth, and fabrication of nano-scale and micro-scale structures. The calculation part gives out the detail of our set-

ups to calculate the chemical shifts for 9TBAE with its dimers and to optimize the molecular structures of 9AC and its derivatives.

Concerning the maximization of the photoresponse, we have two hypotheses: a) the photomechanical properties of organic molecular crystals are closely related to their crystal structures and packing motifs. We may increase the photoresponse through adding different series of substituents; b) if we can identify the possible relationship between the macroscopic photomechanical motions and the changes of molecular crystal structures from the irradiation, we would be able to pre-select molecules with potential dramatic photoresponse based on their structures, and synthesize them for further research. To test our hypotheses, we studies the photochemistry of a family of 9-anthracenecarboxylic acid esters, mainly focusing on the photodimerization of 9TBAE **8** in Chapter 3. Among 13 derivatives with various lengthy or bulky substituents, the nanorods of 9-anthracenecarboxylic 1-methyl-cyclohexyl ester (9MCHAE) **12** undergo the largest photo-induced expansion: 25% in length (10% more than the published 15% expansion of 9TBAE nanorods); yet the expansion of nanorods varies from rod to rod, due to the crystallinity of each rod and the adhesion to the surface. A detailed study of the solid-state photochemistry of 9TBAE **8** shows that the photoproduct has more than one polymorph. The solid-state photoproduct is a metastable intermediate structure that slowly converts into the stable equilibrium structure. Thus we cannot predict the macroscopic photoresponse only based on the equilibrium crystal structures of the reactant and product. Further effort was made to obtain the crystal structure of the metastable solid-state photoproduct.

As to the modes of photoresponse, expansion and bending are so far most-known basic photoresponse; more complicated photo-induced shape changes would be more favored for the application of photoactuation. In Chapter 4 we demonstrate how to generate a new mode of photoresponse through a new morphology of 9-anthracene carboxylic acid (9AC). We found that 9AC microribbons within certain dimensions undergo reversible photo-induced twisting. Unlike the reversible bending of 9AC nanostructures, which has to be carried out under selective irradiation, the reversible twisting of the 9AC microstructures only needs uniform irradiation. Using combination of AFM and optical microscopy measurements, we found that the interfacial strain between the photodimer and unreacted monomer within the ribbon is the driving force for the twisting.

Regarding fastening the reversibility, in Chapter 5 we discuss the photochemistry of a family of 7 9AC derivatives; aimed to discover molecules with shorter recovery time than 9AC. 9AC nanorods usually recover their shape deformations and fluorescence within ~ 5 min at room temperature. The steric repulsion between the two head-to-head carboxylic acid groups of the 9AC photodimer causes the dimer to dissociate into the monomers. According to our preliminary calculations and literature study, the carboxylic acid group must be at the 9-position of anthracene for the molecular crystals to be solid-state photoreactive. Thus, one possible scheme to have faster reversibility is to add different substituent groups at the 10-position of anthracene to increase the steric repulsion. However, among the 6 derivatives of 9AC, only one molecule, 10-flouro-9-anthracenecarboxylic acid shows reversible photoreactivity; yet with much slower

response time. 9AC is still the best candidate concerning the reversibility. Attempts to self-consistently rationalize observed trends in terms of excited state lifetimes or steric effects were only partly successful. Balancing factors like electronic relaxation, steric interactions, and crystal packing presents a challenge for engineering photoactive solid-state materials based on molecular crystals.

Chapter 6 summerizes our unpublished work on crystalline polymer nanorods. Chapter 7 is the conclusion and suggestions for future research. In the Appendices, we have the crystal data, NMR spectra for the molecules synthesized in this dissertation. The details of AFM operation and trouble shooting are also included.

References

1. De Gennes, P. G. A semi-fast artificial muscle. *C. R. Acad. Sci. Series IIB* **1997**, 324, 343.
2. Naka, Y., Fuchiwaki, M., Tanaka, K. A micropump driven by a polypyrrole-based conducting polymer soft actuator, *Polym Int* **2010**, 59, 352.
3. Koumura, N., Geertsema, E. M., Meetsma, A., Feringa, B. L. Light-driven molecular rotor: unidirectional rotation controlled by a single stereogenic center, *J. Am. Chem. Soc.* **2000**, 122, 12005.
4. Gaylord, B. S., Wang, S., Heeger, A. J., Bazan, G. C. Water-soluble conjugated oligomers effect of chain length and aggregation on photoluminescence-quenching efficiencies *J. Am. Chem. Soc.* **2001**, 123, 6417.
5. Good, J., Burdett, J. J., Bardeen, C. J. Using two-photon excitation to control bending motions in molecular-crystal nanorods, *Small*, **2009**, 24, 2902.
6. (a)Rosario, R.; Gust, D.; Hayes, M.; Springer, J.; Garcia, A. A. Solvatochromic Study of the Microenvironment of Surface-Bound Spiropyrans *Langmuir* **2003**, 19, 8801. (b) Bunker, B. C.; Kim, B. I.; Houston, J. E.; Rosario, R.; Garcia, A. A.; Hayes, M.; Gust, D.; Picraux, S. T. Direct observation of photo switching in tethered spiropyrans using the interfacial force microscope. *Nano Lett*. **2003**, 3, 1723.
7. Irie, M. Photo-responsive shape memory effect, "Shape Memory Materials", Otsuka, K.; Wayman, C. W.; Cambridge, **1998**, pp 212-217
8. Irie, M. Photoresponsive polymers. Reversible bending of rod-shaped acrylamide gels in an electric field. *Macromolecules* **1986**, 19, 2890-2892.
9. Athanassiou, A.; Kalyva, M.; Lakiotaki, K.; Geprgopi. S.; Fotakis, C. All-optical reversible actuation of photochromic-polymer microsystems. *Adv. Mater*. **2005**, 17, 988-992.
10. Ikeda, T.; Mamiya, J.; Yu, Y. Photomechanics of liquid-crystalline elastomers and other polymers, *Angew. Chem. Int. Ed.* **2007**, 46, 506-528.
11. Naciri, J.; Srinivasan, A.; Jeon, H.; Nikolov, N.; Keller, P.; Ratna, B. R. Nematic Elastomer Fiber Actuator, *Macromolecules*, **2003**, 36, 8499-8505.
12. Galli, G.; Chiellini, E. Azobenzene containing polymers: what is yet viable with aged liquid crystals. *Liquid Crystals*, **2006**, 33, 1297-1301.
13. Yu, Y.; Nakano, M.; Ikeda, T. Directed bending of a polymer film by light, *Nature*, **2003,** 425, 145,
14. Woltman, S. J.; Jay, G. D.; Crawford, G. P. Liquid-crystal materials find a new order in biomedical applications, *Nature Materials*, **2007**, 6, 929-937.
15. Boldyreva, E. V.; Sinelnikov, A. A.; Chupakhin, A. P.; Lyakhov, N. Z.; Boldyrev, V. V., Deformation and mechanical destruction of [Co(NH3)5NO2]X2 crystals (X = chloride, bromide, nitrate) during photostimulated linkage isomerization. *Doklady Akad. Nauk USSR* **1984,** *277*, 893-896.
16. Lange, C. W.; Foldeaki, M.; Nevodchikov, V. I.; Cherkasov, V. K.; Abakumov, G. A.; Pierpont, C. G., Photomechanical properties of rhodium(I)-semiquinone complexes.

The structure, spectroscopy, and magnetism of (3,4-di-tert-butyl-1,2-semiquinonato)dicarbonylrhodium(I). *J. Am. Chem. Soc.* **1992,** *114*, 4220-4222.
17. Koshima, H.; Ojima, N.; Uchimoto, H., Mechanical motion of azobenzene crystals upon photoirradiation. *J. Am. Chem. Soc.* **2009,** *131*, 6890-6891.
18. Naumov, P.; Kowalik, J.; Solntsev, K. M.; Baldridge, A.; Moon, J.-S.; Kranz, C.; Tolbert, L. M., Topochemistry and photomechanical effects in crystals of green fluorescent protein-like chromophores: effects of hydrogen bonding and crystal packing. *J. Am. Chem. Soc.* **2010,** *132*, 5845-5857.
19. Kobatake, S.; Takami, S.; Muto, H.; Ishikawa, T.; Irie, M., Rapid and reversible shape changes of molecular crystals on photoirradiation. *Nature* **2007,** *446*, 778-781.
20. Flannigan, D. J.; Samartzis, P. C.; Yurtsever, A.; Zewail, A. H., Nanomechanical motions of cantilevers: direct imaging in real space and time with 4D electron microscopy. *Nano Lett.* **2009,** *9*, 875-881.
21. Colombier, I.; Spagnoli, S.; Corval, A.; Baldeck, P. L.; Giraud, M.; Leaustic, A.; Yu, P.; Irie, M., Diarylethene microcrystals make directional jumps upon ultraviolet irradiation. *J. Chem. Phys.* **2007,** *126*, 011101/1-011101/3.
22. Uchida, K.; Sukata, S.; Matsuzawa, Y.; Akazawa, M.; Jong, J. J. D. d.; Katsonis, N.; Kojima, Y.; Nakamura, S.; Areephong, J.; Meetsma, A.; Feringa, B. L., Photoresponsive rolling and bending of thin crystals of chiral diarylethenes. *Chem. Commun.* **2008**, 326-328.
23. Morimoto, M.; Irie, M., A diarylethene cocrystal that converts light into mechanical work. *J. Am. Chem. Soc.* **2010,** *132*, 14172-14178.
24. Khuong, T.-A. V.; Nunez, J. E.; Godinez, C. E.; Garcia-Garibay, M. A. Crystalline molecular machines: a quest toward solid-state dynamics and function. *Acc. Chem. Res.* **2006**, 39, 413-422.
25. Thomas, J. M. Organic reactions in the solid sate: accident and design, *Pure & Appl. Chem.*, **1979**, 51, 1065.
26. Lange, C. W.; Foldeaki, M.; Nevodchikov, V. I.; Cherkasov, V. K.; Abakumov, G. A.; Pierpont, C. G., Photomechanical properties of rhodium(I)-semiquinone complexes. The structure, spectroscopy, and magnetism of (3,4-di-tert-butyl-1,2-semiquinonato)dicarbonylrhodium(I). *J. Am. Chem. Soc.* **1992,** *114*, 4220-4222.
27. Flannigan, D. J.; Lobastov, V. A.; Zewail, A. H., Controlled nanoscale mechanical phenomena discovered with ultrafast electron microscopy. *Ang. Chem. Int. Ed.* **2007,** *46*, 9206-9210.
28. Flannigan, D. J.; Samartzis, P. C.; Yurtsever, A.; Zewail, A. H., Nanomechanical motions of cantilevers: direct imaging in real space and time with 4D electron microscopy. *Nano Lett.* **2009,** *9*, 875-881.
29. Kobatake, S.; Takami, S.; Muto, H.; Ishikawa, T.; Irie, M. Rapid and reversible shape changes of molecular crystals on photoirradiation, *Nature*, **2007**, 446, 778-781.
30. Koshima, H.; Ojima, N.; Uchimoto, H., Mechanical motion of azobenzene crystals upon photoirradiation. *J. Am. Chem. Soc.* **2009,** *131*, 6890-6891.
31. Enkelmann, V. Single-crystal-to-single-crystal transformations: the long wavelength tail irradiation technique. *Mol. Cryst. Liq. Cryst.* **1998**, 313, 15-23.

32. Kaupp, G. Photodimerization of anthracenes in the solid-state: new results from atomic force microscopy. *Angew. Chem., Int. Ed.* **1992**, 31, 595-598.
33. Al-Kaysi, R. O.; Bardeen, C.J. Reversible photoinduced shape changes of crystalline organic nanorods, *Adv. Mater*. **2007**, 19, 1276-1280.
34. Turowska-Tyrk, I. Structural transformation in organic crystals during photochemical reactions. *J. Phys. Org. Chem.* **2004**, 17, 837-847.
35. Al-Kaysi, R. O.; Muller, A. M.; Bardeen, C. J. Photochemically driven shape change of crystalline organic nanorods, *J. Am. Chem. Soc.* **2006**, 128, 15938-15938.
36. Fages, F.; Desvergne, J-P.; Frisch, I.; Bouas-Laurent, H. The first intermolecular 9, 10-1', 4' photodimerizaiton of the anthracene ring. *J. Chem. Soc., Chem. Commun.*, **1988**, 1413.
37. Becker, H. D.; Becker, H. C., Langer, V. Photochemical dimerization modes of 1-acetylanthracene and methyl 1-anthracenecarboxylate *J. Photochem. Photobiol. A,* **1996**, 97, 25-32.
38. Grimme, S.; Peyerimhoff, S. D.; Bouas-Laurent, H.; Desvergne, J-P.; Becker, H. D.; Sarge, S. M.; Dreeskamp, H. Calorimetric and quantum chemical studies of some photodimrs of anthracenes, *Phys. Chem. Chem. Phys*., **1999**, 1, 2457.

Chapter 2 Experimental details

2.1 Instruments

In this dissertation, Atomic Force Microscopy (AFM), Scanning Electronic Microscopy, and optical Microscopy were used to study the dimensions, morphology, and photomechanical responses of the nano- and micro-scale molecular crystal structures. The photoresponse of molecular crystals are directly related with their crystal structure and packing motifs; we used powder X-ray diffraction, single crystal X-ray diffraction, solid-state Nuclear Magnetic Resonance (ssNMR) to obtain the information of crystal orientations, crystal structures and conformations. Fluorescence lifetime measurements, UV-vis absorption spectra, and steady-state emission spectra were the means for us to probe the photophysics of each molecule crystal, and thus gain deeper understanding of the different photoresponse of each derivative.

In this section, we have the brief introduction of the set-up/parameters of each instrument we used, and also sample preparation for each instrument.

2.1.1 Atomic Force Microscopy (AFM)

To examine the topology of the nano- and micro-scale structures of anthracene derivatives, a Novascan AFM with the model of ESPM 3D mounted on top of an Olympus IX-70 inverted fluorescence microscope was used. The AFM was calibrated in x, y, and z directions before the measurements. The details of calibration, operation and trouble shooting are in the Appendix A1. In a typical experiment, an intermittent contact mode scan was performed with a scan rate of 1 Hz, scan resolution of 400 x 400, and

scan size of 73 x 73 μm. Illumination with 410 nm light from a Hg lamp were applied for the photo responses of the samples. Images (videos) of nanorods/microribbons before and after irradiation were taken by DCM300 digital camera.

(a) Organic molecular crystal nanorods sample preparation

For the nano-scale samples, it is preferred to have separated nanorods rather than bundles of nanorods. The reason is that while scanning for the bundles of nanorods, some of the nanorods would attach to the AFM tip, affect the signal, and result in a noisy image. There are two methods we use to prepare individual nanorods samples: (1) Silanize the coverslip surface to make it hydrophobic: ~5% (w/w) solution of octadecyltrichlorosilane in dichloromethane was prepared by adding 2 g of octadecyltrichlorosilane to 40ml dichloromethane, then several coverslips were immersed into this solution and sonicated for 5 min; after sonication, the surfaces of the coverslips were wiped by kimwipe to get rid of the extra silane solution. Make sure to wipe them really well until they are transparent and smooth in both sides. The silanized coverslips were kept in a clean Petri dish for further use; ideally they should be stored under vacuum or nitrogen. Prepare the sample on a silanized coverslip by adding a drop a diluted aqueous solution of nanorods to the silanized coverslip, blow nitrogen on it gently to help separate the nanorods and also air dry the water. (2) Coat every single nanorod with Sodium Dodecyl Sulphate (SDS) by pretreating the AAO template with SDS (shown in Figure 2.1). The commercially available concentrated sulfuric acid solution (95~98%) was diluted to pH ≈ 1, and a drop of this diluted sulfuric acid solution was then added to 3 mL 1% (w/w) SDS, which gave us an acidic SDS solution with pH ≈ 2. Several alumina templates (also

known as AAO template) were dipped into this acidic SDS solution for a couple times, and then were dried for ~18 hours in air. The nanorods were then grown in these pretreated AAO template with the regular procedure.

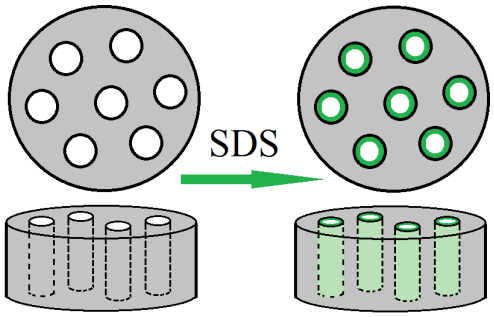

Figure 2. 1 Schematic of AAO template being coated with a layer of SDS on the inter walls of the template.

(b)Organic molecular crystal microribbons sample preparation

A concentrated solution of ribbons floating in H_2O was first placed on a glass slide and then slowly dried. The drying could be accomplished either by slow evaporation or by carefully using kimwipe to wick away the excess water underneath the floating ribbons.

2.1.2 X-Ray Diffraction Measurements

Single-crystal X-ray diffraction data were collected on a Bruker APEX2 platform CCD x-ray diffractometer system (Mo-radiation, λ = 0.71073 Å, 50KV/40mA power) at 296 K and 100 K. The frames were integrated using the Bruker SAINT software package and a narrow-frame integration algorithm. Absorption corrections were applied (absorption coefficient μ = 0.081 mm^{-1}; max/min transmission = 0.9839/0.9603) to the raw intensity data using the SADABS program. The Bruker SHELXTL software package

was used for phase determination and structure refinement.[1-4] Powder X-ray diffraction data were collected on a Bruker D8 Advance X-ray powder diffractometer (CuK radiation, λ = 1.5418 Å, 40KV/40mA power) at 296 K.

Note (1): while preparing the powder sample of photodimer of 9-anthracenecarboxylic acid esters, it's better to grind them in between two microscope slides instead of in the mortar. After grinding, the dimer powder could be a little 'waxy', hard to get them off from the mortar and pestle.

Note (2): The height of the sample will affect the 2θ value of the peaks. In Prof. Feng's lab, they have different sample holders for different powder samples. The most common one is a plastic piece with a microscope-slide-size slit as shown in Figure 2.2. For some microscope slides, their size is slightly bigger than the slit of the sample holder and couldn't be fit in. I tried to place the microscope slide directly on the sample stage without this sample holder, and turns out that all the diffraction peaks shift ~2 degrees. It would be helpful to test out the microscope slide before making the sample.

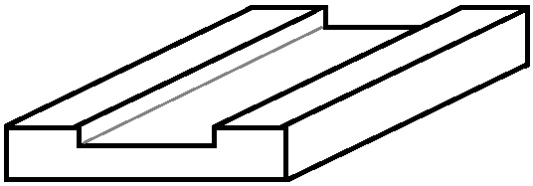

Figure 2. 2 Sample holder for Powder X-ray diffraction measurement, a thin layer of powder sample can be on a piece of microscope slide, and slide can be fit in this sample holder.

2.1.3 Scanning Electron Microscopy (SEM) Measurements

For SEM measurements, a drop of the nanorods/microribbons sample in distilled water was placed on a piece of microscope coverslip and stuck to a piece of conducting copper tape which was then fixed on a SEM stub. The water was gently evaporated under vacuum leaving behind dispersed bundles of nanorods. The SEM stub was placed in a Sputter coater (Cressington 108 Auto) and coated with Pt/Au for 40 seconds. The SEM stub was placed inside a Scanning Electron Microscope (XL30-FEG) and the data were collected.

Note: For the 9-anthracenecarboxylic acid ester nanorods samples, it is important to wash away all the H_3PO_4 from the nanorods after dissolving the template. Otherwise, the left over acid will not be dried out under vacuum. During the measurement, the electron beam will hit the wet part of the sample and destroy it.

2.1.4 ^{13}C Solid-State Nuclear Magnetic Response (ssNMR) Measurements

Cross-polarization (CP) magic-angle-spinning (MAS) solid-state NMR experiments were performed at 14.1T (^{1}H frequency 600 MHz) on a Bruker AVANCE spectrometer equipped with a double-resonance 2.5 mm MAS probe, spinning at a MAS rate of 27 kHz. 83 kHz 1H $\pi/2$ and decoupling pulses were used along with a 2 ms CP spin-lock. During CP the ^{13}C nutation rate was set to 40.5 kHz and the ^{1}H nutation rate ramped from 58 kHz – 77 kHz. For each spectrum, 4096 complex data points with a dwell of 12.5 μs (spectral width 40 kHz, total acquisition time 51.26 ms) were acquired with a recycle delay of 5 s for a total experiment time of 5 hours and 45 minutes.

2.1.5 ^{13}C, ^{1}H Nuclear Magnetic Response (NMR) Measurements

^{13}C, ^{1}H NMR spectra were acquired on a Varian Inova 400 two channel Z axis gradient spectrometer equipped with 5 mm probe, spinning at the rate of 20 kHz. For each spectrum, data points were acquired with a recycle dalay of 3 s with variations of total experiment time based on the concentrations of the samples. For most ^{1}H spectra, total experiment time is usually in the range of a few minutes (1~5 min); for ^{13}C spectra, total experiment time is usually in the range of couple hours (7~13 hours).

2.1.6 Optical Absorption and Emission Spectra Measurements

UV-vis absorption spectra were collected by Varian Cary 50 UV/Vis spectrophotometers from 200 nm to 500 nm at 296 K with background correction. Tetrahydrofuran (THF) was used as the solvent for the solution samples; and the solid samples were prepared by drop casting from the THF solution on microscope slides.

Steady-state fluorescence spectra were collected by Spex Fluorolog Tau-3 fluorescence spectrophotometer. The same samples for UV-vis absorption were used here. The solution samples were excited at 380 nm, and the spectra were collected from 390 nm to 700 nm at 296 K; the solid samples were excited at 410 nm, and the spectra were collected from 420 nm to 700 nm at 296 K.

2.1.7 Fluorescence Lifetime Measurements

Time-resolve fluorescence lifetime data were collected with a Hammastsu C4334 Streakscope. The crystal samples were kept under vacuum in a Janis ST100 cryostat.

Two sets of data were collected using different excitation sources: a 1 kHz Coherent Libra and a 40 kHz Spectra Physics Spitfire laser system. In both cases, the 800 nm output pulse was frequency doubled to 400 nm and residual 800 nm light was removed with dichroic mirrors and Schott glass BG39 filters. The per-pulse excitation fluences used were 50 nJ/cm^2 on the 1 kHz system and 0.2 nJ/cm2 on the 40 kHz system. All fluorescence was detected at a 54.7° polarization angle, relative to the excitation polarization.

2.1.8 Optical Microscope Measurements

To prepare aqueous samples of 9AC microribbons, a few drops of 50% H_3PO_4 were added to Milli·Q H_2O containing 9AC ribbons to prevent H_2O evaporation during the measurements. We use H_3PO_4 because our previous work on molecular crystal nanorods has shown that it is compatible with crystalline 9AC and does not change the hydrogen-bonding of the carboxylic acid groups within the crystal. The presence of H_2O and H_3PO_4 does not play any role in the observed twisting, since this motion also occurs in ribbons on dry surfaces. A drop of the acidic solution of 9AC ribbons was transferred to a microscope slide and then covered with a microscope coverslip. To measure the dynamic process of 9AC ribbons untwisting, 9AC ribbons were first irradiated by 440nm light (~20 mW/mm^2) for a few seconds and then imaged in transmission using a 40x 0.6 NA objective and visible light. Images were captured by a DCM300 digital camera to record the untwisting.

2.2 Experimental Methods

2.2.1 Organic Synthesis

In this dissertation, three families of anthracene derivatives were synthesized: 9-anthracene carboxylic acid ester derivatives, 9-anthracene carboxylic acid derivatives, and di-anthracene ester derivatives. Many of 9-anthracene carboxylic acid esters undergo an irreversible [4+4] photodimerization in the solid-state upon irradiation, and ideally can give a large expansion. This sections covers the experimental details to synthesize the above three families of anthracene derivatives.

(a) 9-anthracene carboxylic acid esters

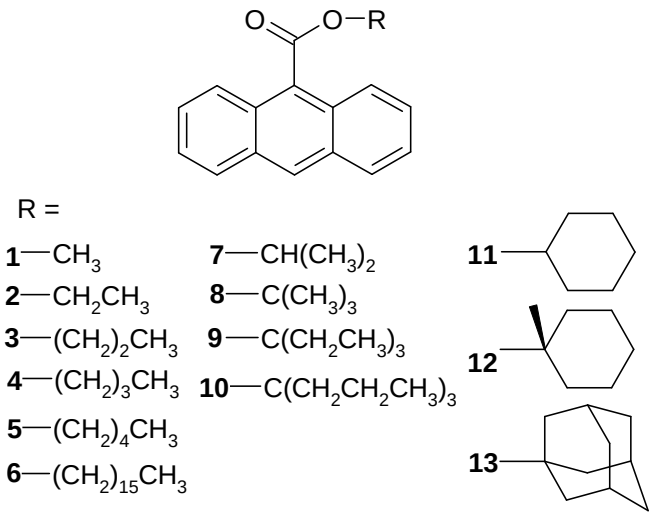

Figure 2. 3 9-anthracenecarboxylic acid ester derivatives.

The 9-anthracenecarboxylic acid esters (**1, 2, 7-13**) were synthesized by the method of Parish and Stock.[5] As an example, we describe the synthesis of 9-anthracenecarboxylic acid 1-methyl-cyclohexyl ester (**12**) in detail. 9-anthracenecarboxylic acid (TCI, 97% pure, 1.0 g, 4.5 mmoles) was suspended in dry

benzene (30 mL). Note: make sure the benzene is dry, and all the glassware being used is dry. Trifluoroacetic anhydride (Aldrich, 99% pure, 2.5 mL, 17.8 mmoles) was added via syringe to the stirring suspension of 9-anthracenecarboxylic acid in benzene; trifluoroacetic anhydride works as a dehydrating condensing agent. The mixture was allowed to stir until the carboxylic acid dissolved and the mixture became a clear yellow solution. 1-Methyl-cyclohexanol (TCI, 96% pure, 1.1=g, 9.6 mmoles) was dissolved in benzene (Aldrich, 99.9%, 1.5 ml) and dried by adding activated molecular sieves (4 Å). The alcohol/benzene solution was added to the carboxylic acid solution and stirred for 1 hour at room temperature. The progress of reaction was monitored using thin layer chromatography (silica, 50:50 CH_2Cl_2: Hexane). After the 9AC was consumed, the organic layer was first washed with 20mL of distilled water, and then with 15mL of a K_2CO_3 (w/w 20%) water solution to hydrolyze excess trifluoroacetic anhydride and remove the generated trifluoroacetic acid. The organic layer was then washed with enough distilled water to get rid of excess K_2CO_3 and dried with anhydrous $MgSO_4$. The organic solvents were removed under reduced pressure and the crude product recrystallized using a minimum amount of hot ethanol (20 mL). The product was obtained as yellow grey crystals 0.94g (65% yield). Melting point: uncorrected 124-125°C. 1H-NMR (400MHz, CDCl3): δ 1.58 (m, 8H), 1.90 (s, 3H), 2.38 (d, 2H), 7.49 (m, 4H), 8.00 (d, 2H), 8.12 (d, 2H), 8.47 (s, 1H). The other 9-anthracenecarboxylic acid esters were synthesized by the same method, but with different alcohols and reaction times (30min ~ 2hrs).

The 9-anthracenecarboxylic acid esters (**3-6**) were synthesized by adding the 9-anthracenecarboxylic acid to a solution of N, N-dimethylmethanamide / K_2CO_3 to produce the anthracene-9-carboxylate anion which is then reacted with excess of the corresponding n-alkyl bromide or iodide. The average product yield was around 55% after recrystallization from ethanol. For example, we describe the synthesis of 9-anthracenecarboxylic acid hexadecyl ester (**6**) in detail. 9-anthracenecarboxylic acid (1.0 g) was added to 8 mL of dry N, N-dimethylmethanamide. To the solution was then added 3.0 g of anhydrous potassium carbonate. The mixture was heated to 50 ºC; then 1.2 g of n-hexadecylbromide was added. The mixture was stirred at 50 ºC for 24 hours. 100 mL distilled water was added and the precipitated solid was extracted twice with 20 mL of ethyl acetate. The organic layer was dried using anhydrous magnesium sulfate, filtered and the solvent was removed under reduced pressure. The crude solid was dissolved in 20 mL of boiling ethanol, and 0.5 mL distilled water was added to induce crystallization. 1.7 g of pure plate-like yellowish orange crystals was collected after crystallization in freezer. Melting point: uncorrected 56.5-57 °C. 1H-NMR (400MHz, CDCl3): δ 0.86 (m, 3H), 1.43 (m, 26H), 1.85 (m, 2H), 4.59 (m, 2H), 7.50 (m, 4H), 8.01 (m, 4H), 8.51 (s, 1H).

(b) Di-anthracene esters

All the di-anthracene esters were synthesized with similar procedure using different dibromoalkanes. As an example, we describe the synthesis of 1, 6-dibromohexane-bis-anthracene ester in detail.

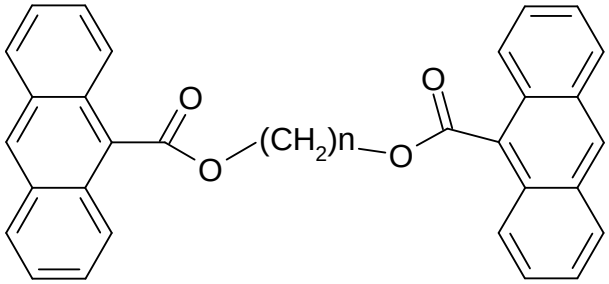

Figure 2. 4 Di-anthracene ester derivatives (n= 2, 3, 4, 6, and 12).

9-anthracenecarboxylic acid (TCI, 97% pure, 0.5512 g) was suspended in 4.0ml of dry N, N-DMF (dried by 4 Å molecular sieves); then 2.0100 g of anhydrous K_2CO_3 was added and the mixture was stirred at 80 ºC H_2O bath (covered with a layer of silicone oil). 0.40 equivalent of 1, 6-dibromohexane (0.2700 g, ~0.4 ml) was added to the mixture after being dried over 4 Å molecular sieves. The mixture was stirred at 80 ºC for 6 hours. The progress of the reaction was monitored using TLC (silica, ethyl acetate: hexane = 1:3). The mono-substituted compound appears right above the bi-substituted one. When all mono-substituted compound disappears from the TLC, the reaction was quenched by adding 10 mL of distilled H_2O. 10 mL ethyl acetate was added to extract the organic layer. Then the organic layer was washed twice with 10 mL distilled H_2O each time, and dried by anhydrous $MgSO_4$. After solvent removal under reduced pressure, the crude product was purified by recrystallization from hot acetonitrile.

Note: the crude product of 1, 12-dibromodudecane-bis-anthracene ester (D12) is ‘oil’, the key to get crystals of D12 is the concentration. Using hot acetonitrille, if it is saturated solution, it would turn into creamy suspension within a few minutes and fail to

recrystallize; one suggestion is to start with the concentration like 1.5mg D12 in 0.5 mL acetonitrille.

(c) Anthracenecarboxylic acids

9-anthracene carboxylic acid (9AC, 99%), N-Fluorobenzenesulfonimide (97%), Bromine (99.5%), n-Butyl lithium (2.5 M in hexane), 9,10-Dibromo-anthracene (98%), Iodomethane (99.5%), 9-Anthracenecarboxaldehyde (97%), Bromobenzene (99%), Anthrone (97%), Magnesium ribbon, Potassium tert-butoxide (95%), and Ferric Chloride (97%) were purchased from Sigma-Aldrich and used without further purification. Dry diethyl ether was distilled over sodium and stored over activated molecular sieves (4 Å). Dry tetrahydrofurane (analytical grade) was prepared by storing over activated molecular sieves (4 Å)

1. 10-fluoro-9-anthracenecarboxylic acid (2)

10F9AC was prepared following a modified literature procedure. [6] The reaction sequence **a → b** was followed.

a) *Synthesis of 9-Bromo-10-fluoro-anthracene* : In a 25 mL oven dried round bottom flask a solution of 9,10-Dibromoanthracene (1.01 g, 3.0 mmoles) in 15 mL dry disilled diethyl ether was stirred at 0 ^{o}C under argon gas before n-butyl lithium (1.3 mL, 1.1 eq.) was added via syringe. The mixture was stirred for 30 minutes at that temperature after which powder N-Fluorobenzenesulfonimide (1.03 g, 3.3 mmoles, 1.1 eq) [7] was gradually added. The reaction mixture was stirred overnight at 30 ^{o}C. The reaction was quenched by adding 0.5 mL of water, then the solvent was removed under reduced pressure. The brown residue was washed with D.I. water to dissolve the lithium salts

(ultrasonication was applied to break up the organic aggregates). The crude product was filtered via suction filtration and recrystallized twice from 14 mL 1-propanol: water (90%:10%). The product was further purified using silica gel column chromatography with Hexanes as the eluting solvent. The first eluted fraction was collected and the solvent removed under reduced pressure to leave behind fine yellow needles of 9-bromo-10-fluoro-anthracene crystals, 0.29 g.

b) *Synthesis of 10-fluoro-9-anthracenecarboxylic acid (**2**)*: In a 25 mL oven-dried round bottom flask a solution of 9-bromo-10-fluoro-anthracene (0.29 g, 1.0 mmoles) in 15 mL dry distilled diethyl ether was stirred at -15^{o}C for 10 minutes before adding n-butyl lithium (0.45 mL, 1.1 eq). After 20 minutes of stirring at -15^{o}C, dry CO_2 gas was bubbled for 15 minutes. The solvent was removed under reduced pressure, and the residue was dissolved in 50 mL 0.2% K_2CO_3 solution. The solution was filtered by gravity, and 4 mL concentrated HCl solution was added to the filtrate. **2** precipitated out as a yellow solid which was collected by suction filtration and washed with D.I. water. The crude product was recrystallized from 75%:25% ethanol:water to yield yellow needles of 10F9AC 0.09 g, mp 231-234 ^{o}C (Lit, mp 235-237 ^{o}C [6]). ^{1}H-NMR (d-DMSO) δ (ppm), 7.6-7.7 (multiplet, 4H), 8.05-8.15 (doublet, 2H), 8.25-8.30 (doublet, 2H), 13.8-14.2 (broad, 1H). Mass spec., M^{+} 239.0518

2. 10-chloro-9-anthracenecarboxylic acid (3)

3 was prepared following a literature procedure. [8] Briefly, a solution of 9-anthracene carboxylic acid (0.25 g, 1.0 mmoles) in 8 mL glacial acetic acid was stirred at 5^{o}C while a saturated solution of Chlorine gas in acetic acid (2 mL, 0.057g Chlorine/ mL

acetic acid, [9] 1.5 eq) was added dropwise over a period of 10 minutes under dim lighting conditions. The reaction mixture was stirred for two hours at 10° C under argon gas. Crude **3** was precipitated by adding the acetic acid solution to 100 ml of ice/water slush, followed by suction filtration. The residue was dissolved in 50 mL 2% K_2CO_3, followed by gravity filtration to remove insoluble byproducts. The filtrate was acidified with 4 mL concentrated HCl to reprecipitate **3** which was later suction filtered and washed with D.I. water. The crude product was recrystallized from 15 mL 85% ethanol and air dried to yield dark yellow needles, 0.16 g, mp 262.5-264.5 °C (Lit, mp 262-264 °C [10]). ^{1}H-NMR (d-DMSO) δ (ppm) 7.6-7.8 (multiplet, 4H), 8.0-8.1 (doublet, 2 H), 8.4-8.5 (doublet, 2H)

3. 10-bromo-9-anthracenecarboxylic acid (4)

4 was prepared following a modified literature procedure. [8, 11] A solution of 9-anthracene carboxylic acid (0.70 g, 3.0 mmoles) in 15 mL glacial acetic acid was cooled to 5°C before slowly adding a solution of bromine in acetic acid (0.18 mL Br_2 in 2 mL acetic acid, 1.2 eq) over a period of 10 minutes. The reaction mixture was allowed to warm to room temperature before stirring for 2 hours at 65°. Crude **4** was precipitated by adding the acetic acid solution to 100 ml of ice/water slush, followed by suction filtration. The residue on the filter was dissolved in 50 mL 5% K_2CO_3 , followed by gravity filtration to remove undissolved side products such as 9,10-dibromoanthracene. The filtrate was acidified with concentrated HCl to precipitate crude **4**, which was recystallized from 25 mL 1-Propanol to yield 0.39 g of yellow needles, mp 260-262 °C

(Lit, 263-266 ^{o}C [12]). ^{1}H-NMR (d-DMSO) δ (ppm) 7.6-7.8 (mutiplet, 4H), 8.0-8.1 (doublet, 2H), 8.4-8.5 (doublet, 2H)

4. 10-methyl-9-anthracenecarboxylic acid (5)

The reaction sequence **a → b** was followed

a) *Synthesis of 9-bromo-10-methyl-anthracene*: In a 50 mL oven-dried round bottom flask a solution of 9, 10-dibromo-anthracene (0.50 g, 1.5 mMole) in 10 mL dry distilled diethyl ether was stirred at 5^{o}C under a blanket of Argon gas. n-butyl lithium (0.70 mL, 1.2 eq) was added slowly and the mixture was stirred for 30 minutes before iodomethane (0.6 mL, 6.5 eq) was added to the mixture and the reaction was stirred at room temperature for another 30 minutes. The organic solvent and excess iodomethane were removed under reduced pressure. The residue was sonicated in 50 mL water to dissolve the lithium salts, followed by suction filtration to collect the undissolved solid. The crude product was recrystallized from 5 mL 95%:5% acetic acid:water to obtain yellow plates, 0.26 g, mp 171-172 ^{o}C [13]

b) *Synthesis of* **5**: In a 25 mL oven-dried round bottom flask, a solution of 9-bromo-10-methyl-anthracene (0.26 g, 0.95 mmoles) in 10 mL dry distilled diethyl ether was stirred at 0^{o}C for 10 minutes before adding n-butyl lithium (0.75 mL, 2 eq). After 20 minutes of stirring at 0^{o}C, dry CO_2 gas was bubbled for 15 minutes. The solvent was removed under reduced pressure, and the residue was dissolved in 50 mL 1% K_2CO_3 solution. The solution was then filtered by gravity, after which 4 mL concentrated HCl was added to the filtrate. **5** precipitated out as a yellow solid and was collected by suction

filtration and washed with deionized water. The crude product was recrystallized from 75% ethanol to give yellow-brown crystals, 0.09 g, mp 210 -211.5 ^{o}C (Lit, mp 221.5-222.5 ^{o}C [8]) ^{1}H-NMR (d-DMSO) δ (ppm) 3.0-3.1 (singlet, 3H), 7.5-7.7 (multiplet, 4H), 7.95-8.05 (doublet, 2H), 8.35-8.45 (doublet, 2H) Mass spec., M^{+} 235.0764

5. 10-phenyl-9-anthracenecarboxylic acid (6)

Synthesis of the compound follows the sequence **a→b→c**

a) *Synthesis of 9-phenyl-anthracene*: This compound was prepared following a modified literature procedure. [13] Anthrone (1 g, 5.2 mmoles) was added to a solution of phenylmagnesium bromide, which was prepared from bromobenzene (2.4 g, 15 mmoles) and excess Mg (0.55 g, 23 mmoles) in 20 mL dry distilled diethyl ether. The mixture was allowed to stir overnight at room temperature, then the solvent was removed under reduced pressure. The solid residue was hydrolyzed with 30 mL 20% aqueous NH_4Cl, and then extracted with 15 mL dichloromethane. The organic layer was dried using anhydrous $CuSO_4$ before decanting and removing the solvent under reduced pressure. The residue was heated to 95 ^{o}C at 100 mbar pressure for 3 hours to remove traces of biphenyl byproduct. The crude product was recrystallized from 1-propanol to obtain white fluorescent needles, 0.70 g, mp (151-152 ^{o}C [14]). NMR [13]

b) *Synthesis of 9-Bromo-10-phenyl-anthracene*: This compound was prepared following a modified literature procedure. [13] A solution of 9-phenyl-anthracene (0.4 g, 1.6 mmoles) in 15 mL glacial acetic was warmed to 65^{o}. The temperature was held at 65^{o}C while a solution of bromine in acetic acid (0.1 mL bromine in 2 mL acetic acid) was added drop wisely. The reaction mixture was stirred overnight at room temperature

before the solvent was removed under reduced pressure, leaving behind a yellow brown powder. Column chromatography (silica gel, 70:30 hexane: ethyl acetate) was used to purify the product. The first eluted fraction was collected and the solvent was removed under reduced pressure to give an orange yellow powder of 9-Bromo-10-phenyl-anthracene, 0.18 g, mp 147-148.5 ^{o}C [15]

c) *Synthesis of 10-phenyl-9-anthracenecarboxylic acid* **6**: This compound was synthesized following a method similar to that described for **5**. Starting with 0.12 g 9-Bromo-10-phenyl-anthracene we obtained fluorescent white needles, 0.07 g, m.p. 260-261 ^{o}C (sublimed) (Lit, 264 ^{o}C [16]) ^{1}H-NMR (d-DMSO) δ (ppm) 7.35-7.65 (multiplet, 11H), 8.0-8.1 (multiplet, 2H, peri-H)

6. 3-Anthracen-9-yl-acrylic acid (7)

Synthesis of the compound starts with preparing the acylal derivative of 9-anthracenecarboxaldehyde (**a**) followed by Perkin condensation (**b**).

a) *Synthesis of Acetic acid acetoxy-anthracen-9-yl-methyl ester*: This compound was synthesized following a modified procedure. [17] In a 50 mL round bottom flask a mixture of 9-anthracenecarboxaldehyde (1.0 g, 4.9 mmoles) and 9.0 mL acetic anhydride were stirred over an ice/water bath for 10 minutes. A catalytic amount of the Lewis acid $FeCl_3$ (75 mg) was added to the mixture. The reaction mixture immediately turned blood red, followed by the formation of a brown precipitate. The mixture was stirred at room temperature for 30 minutes and quenched with 10 mL of water. The product was extracted with 20 mL ethyl acetate and washed with deionized water (3x10 mL). The

organic layer was dried using anhydrous $MgSO_4$ and the solvent was removed under reduced pressure to obtain a crude light brown solid. The crude product was recrystallized from 8 mL ethyl acetate and titrated with warm hexanes (~ 30 mL) to yield fluorescent white crystals, 0.96 g, mp 198-201 ^oC (Lit, mp 197 ^oC [18]) NMR [19]

b) *Synthesis of 3-Anthracen-9-yl-acrylic acid*: This compound was synthesized following a modified procedure. [20] Powder potassium tert-butoxide (0.5 g, 1.8 mmoles) was slowly added to a solution of acetic acid acetoxy-anthracen-9-yl-methyl ester (0.4 g, 1.3 moles) in 15 mL dry THF. The mixture was stirred for 2 hours at room temperature under argon gas. The mixture was added to 50 mL HCl solution (4 M) and the product was extracted with 25 mL ethyl acetate. The organic layer was dried with anhydrous $MgSO_4$ and the solvent was removed under reduced pressure. The crude product was recrystallized from ethanol to obtain yellow needles, 0.21g, mp 243.5-245 ^oC (sublimed) (mp 244-245 ^oC [21]) ^{1}H-NMR (d-DMSO) δ (ppm) 6.25-6.35 (doublet, 1H), 7.5-7.6 (mutiplet, 4H), 8.1-8.2 (multiplet, 4H), 8.4-8.5 (doublet, 1H), 8.6-8.7 (singlet, 1H)[22]

2.2.2 Single Crystal Growth

The crystal structures of 9-anthracenecarboxylic acid esters, di-anthracene esters, and 10-substituted-9-anthracenecarboxylic acids give important information of their solid-state photochemistry. In order to solve their crystal structures, we used multiple methods to grow single crystals. The first three methods described below are different set-ups of slow evaporation. The fourth method is sublimation; the home-made set-up is shown in Figure 2.6. We also tried to sublime 9-anthracenecarboxylic acid derivatives

with traditional set-up of sublimation, but the obtained crystals were not large enough for single crystal X-ray diffraction. The fifth method described below is long-wavelength tail irradiation; single crystal of the photo product of 9TBAE was obtained through this method.

(1) 5 mg of the 9-anthracenecarboxylic acid ester was dissolved in 0.1 mL THF in a 2 mL glass vial, which was then placed in a larger glass vial with 1 mL methanol in the bottom as shown in Figure 2.5a. The larger glass vial is sealed and the THF diffuses into the methanol over the course of several days. After all the THF has partitioned into the methanol, single crystals of the anthracene esters were collected from the bottom of the 2 mL vial.

(2) **a**) ***Monoclinic*** 9-anthracenecarboxylic acid crystals: 5.7 mg of 9-anthracenecarboxylic acid was dissolved in 1.0 mL filtered Ethyl Acetate in an 8 mL tooled-neck vial, with gentle heating on the hot plate to help dissolve. The glass vial was sealed with polyethylene lid, and the sealing lid has a needle to go through it as shown in Figure 2.5b. After all the ethyl acetate has evaporated through the needle over the course of several days, single crystals of monoclinic 9-anthracenecarboxylic acid were collected from the bottom of the glass vial. **b**) ***Triclinic*** 9-anthracenecarboxylic acid crystals: 5.5 mg of 9-anthracenecarboxylic acid was dissolved in 2.0 mL filtered xylenes in an 8 mL tooled-neck vial, with gentle heating on the hot plate to help dissolve. The glass vial was sealed with polyethylene lid, and the lid has a needle to go through it. After all the xylenes have evaporated through the needle over the course of several days, single

crystals of triclinic 9-anthracenecarboxylic acid were collected form the bottom of the glass vial.

Note: The solvent is the key to get different polymorphs of 9-anthracenecarboxylic acid. So far xylenes is the only solvent I found that can grow triclinic anthrace-9-carboxylic acid single crystals. While using the slow evaporation method under room temperature, many solvents like ethanol, THF, etc. give the combination of both monoclinic and triclinic polymorphs.

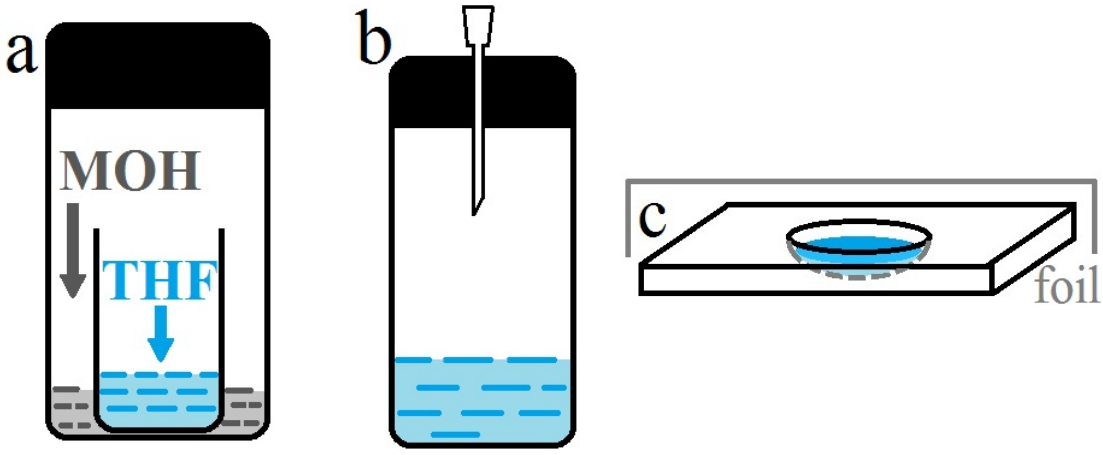

Figure 2. 5 Set-ups for slow solvent evaporation

(3) It is harder to grow nice single crystals of 9-anthracenecarboxylic acid derivatives because that the π- π interaction plus the hydrogen bonding makes a 'messy' system. After much trail-and-error, the set-up shown in the Figure 2.5c on the right grows single crystals of some 9-anthracenecarboxylic acid derivatives (Note, not all 9-anthracenecarboxylic acid derivative single crystals can be grown using this set-up): 1.0mg of 10-methyl-9-anthracenecarboxylic acid was dissolved in 0.1 mL DMSO in the well-plate, and covered by foil. The single crystal of 10-methyl-anthracene-9-carboxylic

acid was collected after several days. The advantage of well-plate is its smooth surface of the well.

(4)Sublimation: compared with set-up (3), this method/set-up is more promising for 9-anthracenecarboxylic acid derivatives. 2.5mg of 10F-9-anthracenecarboxylic acid was added to the central bottom of a glass vial. Three ~1 cm diameter glass cylinders were stacked over the powder of 10F-9-anthracenecarboxylic acid, with the powder in the center of the glass cylinders. The glass vial was sealed with a glass lid, covered with a beaker wrapped with aluminum foil, and heated by hot plate which was set to 200 ºC as shown in Figure 2.6.

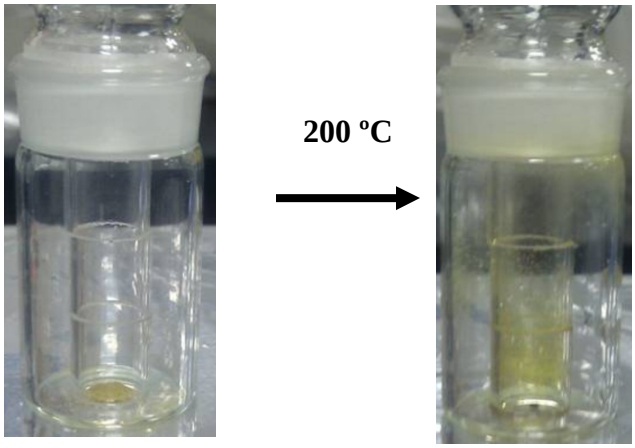

Figure 2. 6 Homemade Set-up for crystal sublimation for anthracenecarboxylic acids

Note: 190~200 ºC is the optimum temperature range for most compounds. After sublimation for about 15 hours, the bottom cylinder contains nice needle-shaped 10F-9-anthracenecarboxylic acid crystals. Single crystals were collected from the top most part of the bottom cylinder; the middle cylinder didn't contain any crystals; and the top cylinder contains volatile impurities which should be discarded.

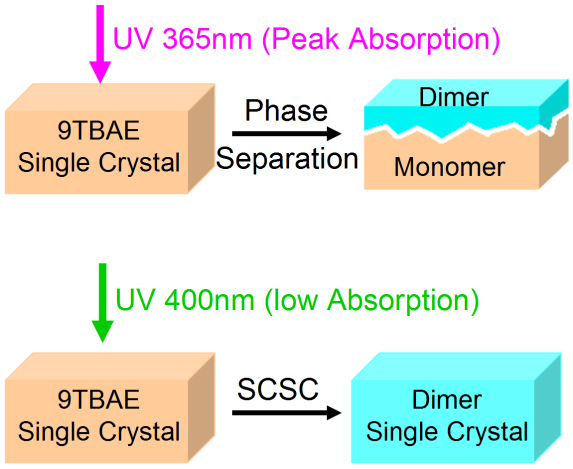

Figure 2. 7 Schematic for long wavelength tail irradiation

(5) Long wavelength tail irradiation: In order to photoreact a single crystal of 9TBAE, a monomer single crystal was mounted on to a glass fiber with epoxy resin, inserted into a hollow copper pin (glued with epoxy) and attached to a goniometer head. The goniometer head was placed on a three- dimensional translation stage to center the single crystal for uniform irradiation using a frequency-doubled Ti: Sapphire Laser at 400 nm. The laser power (µw) and exposure time (25 min) were controlled to convert monomer single crystal homogeneously into photodimer single crystal without breaking the crystal.

Most solid-state [4+4], [2+2] photodimerizations proceed heterogeneously, that is, at a certain (small) percentage of conversion from monomers to dimers, phase separation occurs which leads to the shattering of the crystals. This hampers further structural investigation. One possible way to get homogeneous photodimerization of crystals is to use long wavelength tail irradiation[23]. The mechanism behind is that if the irradiation is in the very tail of the absorption so that the absorption is low, the light intensity is

comparatively even throughout the crystal, and the transformation from monomer to dimers may take place homegenously. Instead of phase separation, the monomer and the dimer co-exist throughout the crystal. In other words, the states at intermediate conversions are substitutional mixed crystals where monomer and dimer molecules statistically occupy the same lattice sites. [23, 24] Yet examples of single-crystal-to-single-crystal photoreactions in the literature are rare. [25] For the anthracene derivatives we studied in this dissertation, it is impossible to get a 100% conversion without fragmentation; single crystal X-ray diffraction analysis revealed 20% conversion in our best sample. The published conversion percentage of 9-Methyl-Anthracene is 24%, [26] for comparison.

2.2.3 Molecular Crystal Nanorods Fabrication

Bulk molecular crystals usually fracture under irradiation due to phase separation. Making them into nano-scale structures is an effective way to avoid fracture and also generate photo-induced shape changes. This section describes how to fabricate molecular crystal nanorods.

All the nanorods were prepared using similar procedures [27] as shown in Figure 2.8. As an example, we describe the preparation of nanorods composed of molecule 9-anthracenecarboxylic acid 1-methyl-cyclohexyl ester **12** (the structure is shown in Figure 2.3). Approximately 5 mg of **12** was dissolved in 0.1 mL of dry spectroscopic grade tetrahydrofuran (THF). The solution was then deposited on top of anodized aluminum oxide (AAO) template (Whatman Anodisc-13, 200 nm pore diameter, with average

membrane thickness of 60 microns, and 13mm diameter). This AAO template, loaded with the molecule of interest, is then placed on top of a homemade Teflon support ring. The AAO/cover slip/Teflon holder were placed on a piece of Kimwipe (saturated with 2 mL of THF) on a piece of thick ground glass (Chemglass, 4 inch diameter, 0.25 inch thickness). The whole set up was covered by a 5 oz glass bell-jar. At room temperature, the solvent in the bell jar evaporates over the course of 8-24 hours. During this time, the solid **12** in the AAO dissolves in the solvent vapors and slowly recrystallizes in the AAO nanochannels to form single crystalline nanorods. After the solvent had evaporated, the AAO template surface was polished using 1500 grit sandpaper to remove excess **12** from both faces. Nanorods were released by dissolving the AAO template in 50% aqueous phosphoric acid, forming an aqueous suspension.

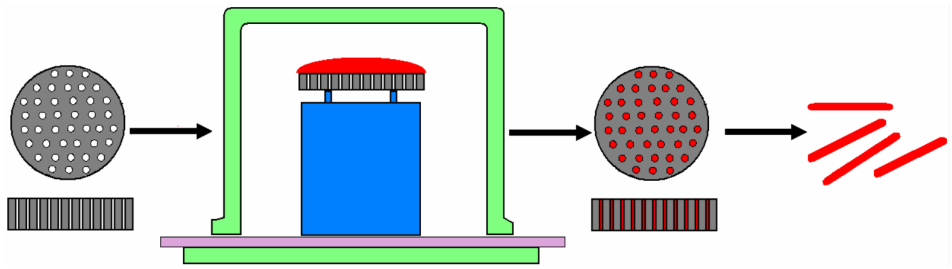

Figure 2. 8 Set-ups for nanorods fabrication: a) top and side looking of AAO template; b) The solution loaded AAO template was placed on the template holder, inside of a solvent vapor saturated bell-jar; c) AAO template was polished after solvent annealing; d) AAO template was dissolved and the nanorods were released from it.

Note: Compound 9-anthracenecarboxylic acid (1-admantyl) ester **13** (the structure is shown in Figure 2.3) has more than one polymorph. To grow the solid-state photoreactive polymorph for nanorods, the procedure is similar to the procedure

described above; the only change is to add a piece of cover slip in between the AAO template and the Teflon template holder. In other words, if we follow the procedure above, we would get solid-state **non**-photoreactive nanorods for **13**; however, if we alter the procedure by adding a piece of coverslip, we would get solid-state photoreactive nanorods for **13**.

2.2.4 Molecular Crystal Microribbons Growth

Compared with the nano-scale structures discussed in last section, micro-scale structures are inclined to fracture under irradiation; yet in this section we demonstrate how to control the right conditions to grow micro-scale structures of 9AC that undergo a new mode of photoresponse instead of shattering under uniform irradiation (Chapter 4).

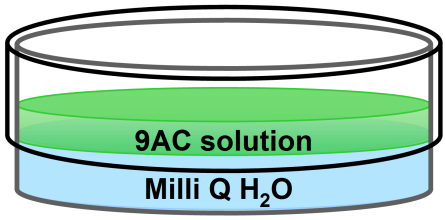

Figure 2. 9 Set-up for 9AC microribbons fabrication in petri dish: the crystallization of 9AC microribbons was carried out on smooth 'defect-free' Milli Q H2O.

The 9AC microribbons were prepared by floating drop method [28] on a smooth 'defect-free' Milli Q H_2O surface as shown in the Figure 2.9. 1.9 mg of 9AC (TCI, >97%) was dissolved in 1.0 ml filtered ethyl acetate (Sigma, 99.5+ %), and then this solution was slowly added to the surface of Milli·Q millipore purified H_2O in a Petri dish (VWR, 60x15mm). The solubility of ethyl acetate in water is 8.3 g in 100 mL; so when the ethyl

acetate solution was added to the Milli·Q water dropwise, it looked like boiling. The Petri dish was covered and left in the dark for 48 hrs. During this time, as the solvent evaporates, the 9AC slowly crystallized out as ribbons floating on the water surface. Note: The concentration of the 9AC solution is the key to grow the photo induced twisting microribbons. If it's more concentrated than 1.9 mg 9AC in 1.0 mL ethyl acetate, the microribbons would grow into bigger needles, and they shatter under irradiation; if it's less concentrated than 1.9 mg 9AC in 1.0 mL ethyl acetate, very few crystals would come out. Possible reasons: 9AC could be dissolved slightly in H_2O, when the concentration is too low, then 9AC would just be dissolved in the mixture of Milli Q H_2O and 1.0 mL ethyl acetate, and not easily crystallize out since H_2O is not as volatile as organic solvents.

2.3 Calculations

2.3.1 Chemical Shift Calculations

Ab initio calculations were performed at the density functional (DFT) level of theory using the B3LYfunctional [29-31] within the Gaussian 03 software package.[32] Molecules were optimized to their ground state geometries using the 6-31G(d,p) basis and NMR chemical shifts calculated with the 6-311++G(d,p) basis. Calculated ^{13}C chemical shifts were referenced to benzene at 128.0 ppm from TMS.

2.3.2 Gaussian *DFT-d* Calculation Setup

The Energies of 9-anthracenecarboxylic acid derivates monomer pairs and their photodimers were calculated at the density functional (DFT) level of theory using the

B97D functional within the Gaussian 09 software package. For the monomer pairs, the energies were calculated from the solved crystal structures; for their photodimers, the structures were first modified from optimized 9AC dimer, and then optimized to their ground state by semi-empirical, and finally optimized to their ground state geometries by B97D using the 6-31+G(d) basis set.

Building the molecular structures for calculation:

Monomer pairs: load the cif by Mercury, go to *Calculation/Packing and Slicing*, adjust *a*, *b* and *c* parameters to have only a pair of monomers showing on the screen, and save it in the format of *PDB (*.pdb, *ent).* Gaussview can open and recognize the *.pdb/ent file of crystal data.

Photodimers: load the 9AC monomer pair in *.pdb/ent file by Gaussview, make two new single bonds in between two 9^{th} carbons and two 10^{th} carbons by *modify bond*, and change the corresponding carbons in the middle rings of anthracenes from π bond into single bond by *modify bond*. Then go to *Calculation/Gaussian Calculation Setup*, set the *Job Type* to *Optimization*, *Method*: *Ground state/Semi-empirical* to optimize the newly built structure. For the other halogenated 9AC photodimers, change the H atom on the 10^{th} carbons of the *semi-empirical* optimized-then *DFT-d* optimized 9AC photodimers into halogen atoms, and optimize to the ground state by semi-empirical.

Note (1): while loading the *.pdb/ent files of monomer pairs, the Gaussview program would give a warning sign 'Invalid space group symbol on crystal data line (CRYST1…) Crystal data will be ignored'. Ignore the warning by clicking OK. The reason for this warning sign is that Gaussview 5.0.9 can't recognize the nonstandard

space group P 21/n in the CRYST1 line of the ent file. There are standard space group symbols, also known as ‘Hermann Mauguin space group symbols’. The difference between the standard and nonstandard space group symbols comes from different choices of orientations for the symmetry elements and crystallographic axes. The way to solve the problem of an unrecognized space group symbol is to transform the nonstandard space group P 21/n into the standard P 21/c. Mercury probably can do this. However, in our calculation setup it’s not necessary to do the transformation because we are not calculating molecules in the crystal environment, but a pair of molecules in the ‘gas phase’. In other words, the crystal data would be ignored in the calculation anyways.

Note (2): For halogenated photodimers, Gaussview gives an error while setting up the calculation for DFT-d, the way to solve is as the following:

Load the *.chk file after semi-empirical optimization from 9AC photodimers, go to Calculation/Gaussian Calculation Setup, set the Job Type to Optimization, Method to Ground state/Custom, Basis set to 6-31+G(d). Then click Edit button to customaries the DFT-d method, a window would pop up to ask to save the current input file, save it as *.gjf file, then edit the file by adding ‘b97d’ in between ‘opt’ and ‘6-31+G(d)’, the line would look like ‘# opt b97d/6-31+g(d) geom=connectivity’. The file is ready to be sent to Gaussian to calculate. The calculation would be ended right away, and on the row of *Run Progress*, it says ‘Link died!’ and gives a warning box as shown in the Figure 2.10.

Figure 2. 10 Warning information given by Gaussian 09W while starting the calculation.

The reason for this warning is that during the process of generating *.gjf file from the previously optimized *.chk file, some error happened to the labeling of the halogen atoms. It shows as blank in the *.gjf file as shown in the following (the information for hydrogen is shown in the correct format, but the bromine part is missing and this cause the problem):

H(PDBName=H7,ResName=UNK,ResNum=1)	*4.32309300*	*-2.65152800*	*-0.04340500*
H(PDBName=H8,ResName=UNK,ResNum=1)	*2.39552400*	*-2.09730400*	*1.40252500*
Br	*-0.13168404*	*2.21687257*	*-3.43086216*
Br	*-0.02882685*	*-0.40204025*	*-4.06523929*

The way to fix this is to type in (PDBName=Br1,ResName=UNK,ResNum=1) and (PDBName=Br2,ResName=UNK,ResNum=1), after two Br, with the same format as the Hydrogen an other atoms. Save the modified *.gjf file and submit it to Gaussian 09W for optimization.

References

1. *APEX 2*, 2009.5-1; Bruker AXS Inc.: Madison, WI, 2009.
2. *SAINT*, V7.60A; Bruker AXS Inc.: Madison, WI, 2009.
3. *SADABS*, 2008/1; Bruker AXS Inc.: Madison, WI, 2008.
4. *SHELXTL*, 2008/4; Bruker AXS Inc.: Madison, WI, 2008.
5. Parish, R. C.; Stock, L. M., A method for the esterification of sterically hindered carboxylic acids. *Tet. Lett.* **1964,** *5*, 1285-1288.
6. Stock, L. M.; Anderson, G. L., Chemistry of the bicyclo[2.2.2] octanes. X. Preparation of 9-fluoroanthracenes. *J. Org. Chem.* **1971,** *36* (8), 1140-1142.
7. Differding, E.; Ofner, H., N-fluorobenzenesulfonimide: a practical reagent for electrophilic fluorinations. *Synlett* **1991,** (3), 187-189.
8. Baker, F. W.; Parish, R. C.; Stock, L. M., Dissociation constants of bicyclo[2.2.2]oct-2-ene-1-carboxylic acids, dibenzobicyclo[2.2.2]octa-2,5-diene-1-carboxylic acids, and cubanecarboxylic acids. *J. Am. Chem. Soc.* **1967,** *89* (22), 5677-5685.
9. Davidson, A. W.; Chappell, W., The solubility of halides in anhydrous acetic acid. *J. Am. Chem. Soc.* **1938,** *60*, 2043-2046.
10. Mikhailov, B. M.; Bronovitskaya, V. P., Synthesis of polycyclic compounds. XVI. Preparation of meso-derivatives of anthracene with the aid of lithium-organic compounds. *Zh. Obshch. Khim.* **1952,** *22*, 157-162.
11. Gore, P. H.; Gupta, S. D.; Obaji, G. A., Anomalous reactions of cyanide with two hindered aromatic aldehydes. *J. Prakt. Chem.* **1984,** *326* (3), 381-384.
12. Latham, H. G., Jr.; May, E. L.; Mosettig, E., Studies in the anthracene series; derivatives of 1,2,3,4-tetrahydroanthracene. *J Am Chem Soc* **1948,** *70* (3), 1079-1081.
13. Zhang, X. M.; Bordwell, F. G.; Bares, J. E.; Cheng, J. P.; Petrie, B. C., Homolytic bond dissociation energies of the acidic carbon-hydrogen bonds in alpha -substituted and 10-substituted 9-methylanthracenes and their related radical anions. *J. Org. Chem.* **1993,** *58* (11), 3051-3059.
14. Hori, M.; Kataoka, T.; Shimizu, H.; Onogi, K., Dibenzothiepin derivatives and related compounds. II. A novel cyclization reaction of 6-chloro-11-phenyl-6,11-dihydrodibenzo[b,e]thiepins. *Chem. Pharm. Bull.* **1978,** *26* (7), 2170-2174.
15. Cava, M. P.; McGrady, J., Nonclassical condensed thiophenes. VI. Isothianaphthene 2,2-dioxides. *J. Org. Chem.* **1975,** *40* (1), 72-77.
16. Dufraisse, C.; Velluz, L., Dissociable organic oxides. 9-Phenylanthracene and its derivatives. *Compt. Rend.* **1936,** *203*, 327-329.
17. Kochhar, K. S.; Bal, B. S.; Deshpande, R. P.; Rajadhyaksha, S. N.; Pinnick, H. W., Protecting groups in organic synthesis. Part 8. Conversion of aldehydes into geminal diacetates. *J. Org. Chem.* **1983,** *48* (10), 1765-1767.
18. Khan, A. T.; Choudhury, L. H.; Ghosh, S., Silica-supported perchloric acid (HClO4-SiO2): A highly efficient and reusable catalyst for geminal diacylation of aldehydes under solvent-free conditions. *J. Mol. Catal. A Chem.* **2006,** *255* (1-2), 230-235.

19. Fry, A. J.; Rho, A. K.; Sherman, L. R.; Sherwin, C. S., Cobalt(II)-catalyzed reaction between polycyclic aromatic aldehydes and acetic anhydride. Formation of acylals, not 1,2-diketones. *J. Org. Chem.* **1991,** *56* (10), 3283-3286.
20. Chandrasekhar, S.; Karri, P., Revised mechanism and improved methodology for the Perkin condensation. Resuscitation of the mechanism involving benzal acetate and the improbability of the enolate of acetic anhydride. *Tetrahedron Lett.* **2006,** *47* (13), 2249-2251.
21. Arjunan, P.; Shymasundar, N.; Berlin, K. D.; Najjar, D.; Rockley, M. G., Syntheses of selected e-(2- or 9-anthryl)alkanoic acids and certain esters - carbon-13 spin-lattice relaxation time measurements of methyl 5-(2-anthryl)pentanoate and methyl 7-(2-anthryl)heptanoate. *J. Org. Chem.* **1981,** *46* (3), 626-629.
22. Reddy, M. J. R.; Srinivas, U.; Srinivas, K.; Reddy, V. V.; Rao, V. J., Photochemical E(trans)-Z(cis) isomerization in 9-anthraceneacrylic esters. *Bull. Chem. Soc. Jpn.* **2002,** *75* (11), 2487-2495.
23. Enkelmann, V.; Wegner, G. Crystal-to-crystal photodimrization, *Mol. Cryst. Liq. Cryst.* **1994**, 240, 121-126.
24. Novak, K.; Enkelmann, V.; Kohler, W.; Wegner, G.; Wagerer, K. B. Homogeneous photodimerization and thermal back reaction of a styrylpyrylium triflate, *Mol. Cryst. Liq. Cryst.* **1994**, 242, 1-8.
25. Ohba, S.; Ito, Y. Single-crystal-to-single-crystal photodimerization of 4-chlorocinnamoyl-O, O'-dimethyldopamine, *Acta Cryst.* **2003**, B59, 149-155.
26. Turowska-Tyrk, I.; Trzop, E. Monitoring structural transformatin in crystals. 6. The [4+4] photodimerization of 9-methyl-anthracene, *Acta Cryst.* **2003**, B59, 779-786.
27. Al-Kaysi, R. O.; Muller, A. M.; Bardeen, C. J., Photochemically driven shape changes of crystalline organic nanorods. *J. Am. Chem. Soc.* **2006,** *128*, 15938-15939.
28. Campione, M.; Ruggerone, R.; Tavazzi, S.; Moret, M., Growth and characterization of centimetre-sized single crystals of molecular organic materials. *J. Mater. Chem.* **2005,** *15*, 2437-2443.
29. Becke, A. D., Density-functional exchange-energy approximation with correct asymptotic behavior. *Phys. Rev. A* **1988,** *38*, 3098-3100.
30. Lee, C. T.; Yang, W. T.; Parr, R. G., Development of the Colle-Salvetti correlation energy formula into a functional of the electron density. *Phys. Rev. B* **1988,** *37*, 785-789.
31. Becke, A. D., Density-functional thermochemistry. 3. The role of exact exchange. *J. Chem. Phys.* **1993,** *98*, 5648-5652.
32. Frisch, M. J.; Trucks, G. W.; Schlegel, H. B.; Scuseria, G. E.; Robb, M. A.; Cheeseman, J. R.; Montgomery, J. J. A.; Vreven, T.; Kudin, K. N.; Burant, J. C.; Millam, J. M.; Iyengar, S. S.; Tomasi, J.; Barone, V.; Mennucci, B.; Cossi, M.; Scalmani, G.; Hasegawa, J.; Ishida, M.; Nakajima, T.; Honda, Y.; Kitao, O.; Nakai, H.; Klene, M.; Li, X.; Knox, J. E.; Hratchian, H. P.; Cross, J. B.; Bakken, V.; Adamo, C.; Jaramillo, J.; Gomperts, R.; Stratmann, R. E.; Yazyev, O.; Austin, A. J.; Cammi, R.; Pomelli, C.; Ochterski, J. W.; Ayala, P. Y.; Morokuma, K.; Voth, G. A.; Salvador, P.; Dannenberg, J. J.; Zakrzewski, V. G.; Dapprich, S.; Daniels, A. D.; Strain, M. C.; Farkas, O.; Malick, D. K.; Rabuck, A. D.; Raghavachari, K.; Foresman, J. B.; Ortiz, J. V.; Cui, Q.; Baboul, A.

G.; Clifford, S.; Cioslowski, J.; Stefanov, B. B.; Liu, G.; Liashenko, A.; Piskorz, P.; Komaromi, I.; Martin, R. L.; Fox, D. J.; Keith, T.; Al-Laham, M. A.; Peng, C. Y.; Nanayakkara, A.; Challacombe, M.; Gill, P. M. W.; Johnson, B.; Chen, W.; Wong, M. W.; Gonzalez, C.; Pople, J. A. *Gaussian 03, E.01*, Gaussian Inc.: Wallingford, CT, 2004.

Chapter 3 Photochemistry of 9-anthracenecarboxylic acid esters

3.1 Introduction

Organic solid-state photoreactions have long served as a testbed for theories about how spatial constraints influence chemical reactivity. [1-3] Reactions in the crystal provide an environment where the positions and orientations of both the reactant and product molecules can be determined to atomic precision using x-ray diffraction (XRD) analysis. But the study of photochemical reactions in organic crystals is hampered by the tendency of such crystals to shatter under illumination. This fragmentation is believe to result from the build-up of interfacial strain between reacted and unreacted regions of the crystal, and the resulting phase reconstruction leads to fracture and decomposition. [4] Attempts to circumvent this problem using irradiation in the long-wavelength tail of the reactant absorption[5-6], or using two-photon absorption[7], have been successful only in a few select cases. On the whole, observations of single crystal-to-crystal phototransformations of macroscopic organic molecular crystals remain relatively rare. But interest in such photoreactive systems is increasing because of their possible use as photomechanical transducers[8], providing an alternative type of material to complement well-known polymer based photomechanical materials. [9-14] Our group has taken a different approach, where we use nanostructured molecular crystals as a general way to avoid the fracture problem.[15-16] We have previously shown that crystalline nanorods composed of 9-anthracenecarboxylic acid tert-butyl ester (9TBAE) remain intact after undergoing an expansion of up to 15%. [17] Under identical irradiation conditions, macroscopic crystals of 9TBAE quickly fragment and disintegrate. We later showed that a reversible [4+4]

photodimerization reaction in 9-anthracenecarboxylic acid (9AC) crystalline nanorods could lead to reversible bending [18] and that using spatially localized two-photon excitation could induce controllable motion in these nanoscale structures. [19]

The use of nanostructured molecular crystals provides a general way to harness organic solid-state photochemical reactions to generate larger motions and perhaps do useful work on submicron lengthscales. But there are still several outstanding scientific questions in our work. First, how general is this phenomenon – can it be extended beyond the two molecules (9TBAE and 9AC) studied thus far? Second, what is the mechanism that underlies the observed photomechanical response? The role of molecular alignment within the nanorods, the nature of the crystal-to-crystal transformation, and the molecular-level conformational changes in conformation are all open questions raised by our previous work. In this Chapter, we attempt to address these questions in a systematic way. We first show that there exists a large family of anthracene ester derivatives, crystallizing in a variety of packing motifs, that can be formed into nanorods and that exhibit a significant photomechanical response. In order to better understand the molecular level origins of the photomechanical response, we study the 9TBAE system in detail. Using XRD and solid-state nuclear magnetic resonance (ssNMR), we find that the monomer nanorods consist of ordered single crystal domains, and that irradiation leads to a continuous transition to a second crystalline form. Surprisingly, XRD and ssNMR data show that the crystal formed immediately after photoreaction of the monomer solid is not the same as the crystal obtained by crystallization of the photodimer directly from solution. The photomechanical response

is actually determined by a crystalline intermediate that converts into the low-energy polymorph only after a period of months. For 9TBAE, the XRD and ssNMR data suggest that this intermediate structure involves a photodimer whose ester sidegroups have not yet rotated to their outward-facing equilibrium positions. The creation of metastable intermediate crystal structures via the solid-state photoreaction appears to be a general feature of the anthracene esters. An important conclusion is that the photomechanical response of this class of materials cannot be predicted based on equilibrium structures of the reactant and product molecular crystals, but instead arises from nonequilibrium crystal structures whose characterization is quite challenging.

3.2 Molecular Structures and Crystal Structures of 9-Anthracenecarboxylic Acid Esters

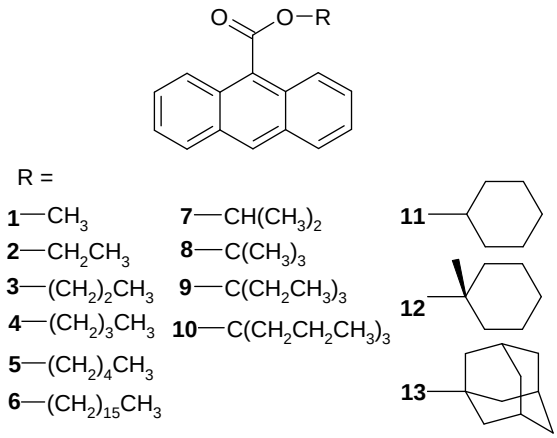

Figure 3. 1 Molecular structures of anthracene ester derivatives

Figure 3.1 shows the molecular structures of the compounds studied in this Chapter. We are interested in the anthracene esters because they comprise a family of

compounds whose molecular structure and crystal packing can be tuned by changing the ester group attached at the 9-anthracene position. They are highly soluble and, as shown below, amenable to nanorod growth. This family of compounds was previously studied in the context of solid-state triboluminescence [20], but here we are concerned with their solid-state photochemistry. The ester substituents can be divided into three broad classes: n-alkyl chains (**1**-**6**), branched alkyl chains (**7**-**10**), and cyclohexyl derivatives (**11**-**13**). Using single crystal XRD, we have determined the crystal structures for all the molecules in Figure 3.2. The photoreactive molecules crystallized into one of the two basic crystal classes summarized in Figure 2: herringbone pair (HBP) and layered pair (LP). The other molecules crystallized into structures where either neighboring anthracene rings were not cofacial, for example herringbone packing (**2**) or where the anthracene rings were two far away from each other to react (**10**, **13**) as shown in Figure 3.3.

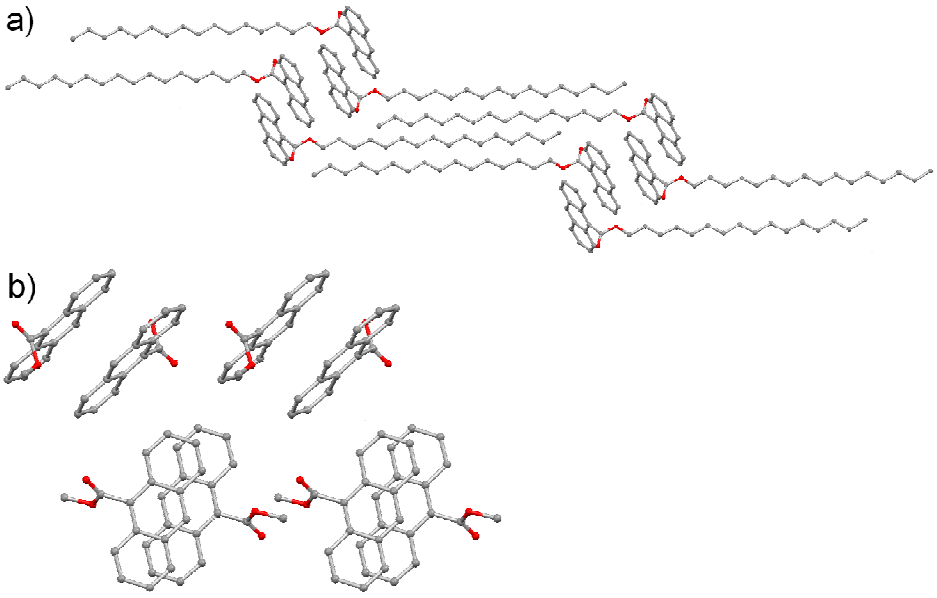

Figure 3. 2 Crystal packing motifs of the two classes of photoreactive anthracene esters: **a)** Layered Pair **(6); b)** Herringbone Pair **(1)**

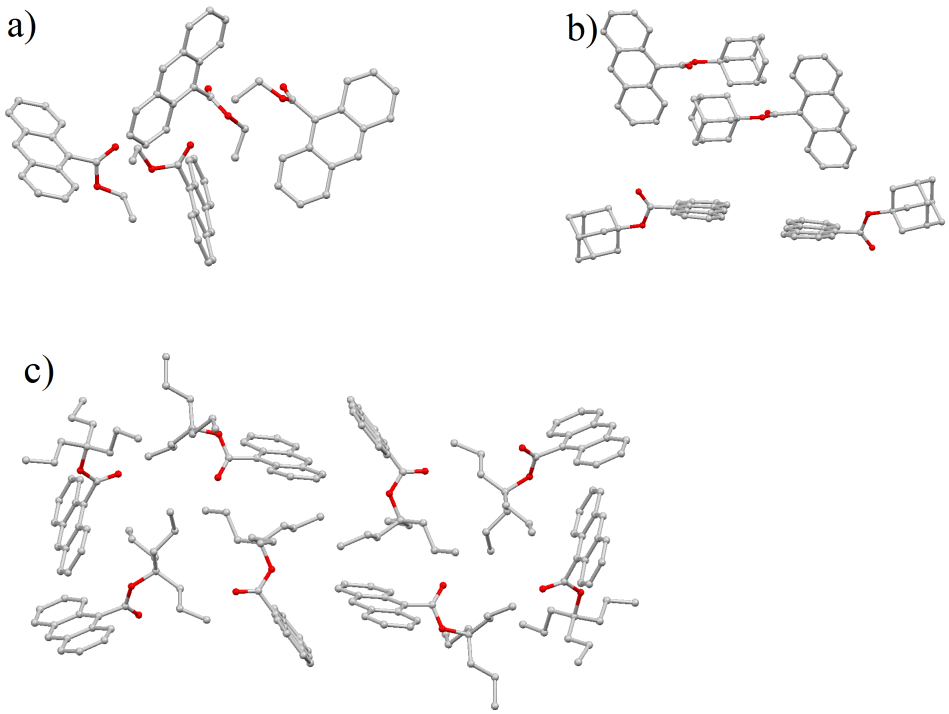

Figure 3. 3 Crystal packing motifs of the unphotoreactive anthracene esters: a) Herringbone (2); b) Offset Herringbone Pair (13); c) Distance Herringbone Pair (10).

Note that the distance limit for photodimerization is estimated to be 4.7 Å. [21] One sign that a solid would be reactive was a yellow color and yellow-green fluorescence, indicating excimer formation due to interacting anthracene π systems. In one case (**13**), the room temperature crystal was unreactive, but the growth of a different polymorph inside the AAO could be induced by modifying the nanorod growth conditions. For **13**, this entailed simply placing a microscope coverslip underneath the AAO template during the solvent annealing step. This polymorph was found to be photoreactive as illustrated in Figure 3.4, but its structure remains unknown since we were unable to grow bulk crystals.

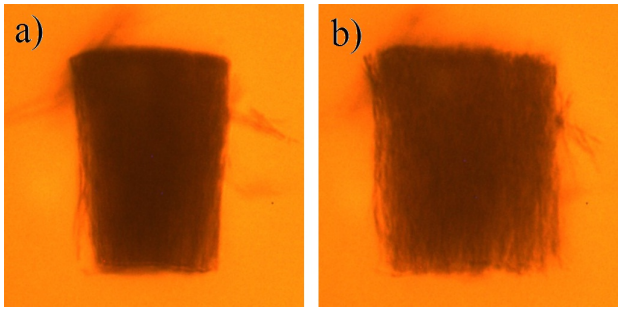

Figure 3. 4 Optical microscope images of a bundle of photoreactive nanorods **13** before and after UV irradiation, the nanorods are ~50 µm long, and 200 nm diameter. Part of the nanorods was not well-focused due to the limit of our objective.

A second point is that while molecules **4** and **5** were photoreactive in the solid, their very low melting points prevented observation of a mechanical response. The n-butyl and n-pentyl groups appear to lead to a high amount of packing disorder, making it difficult to grow single crystals and impossible to grow nanorods.

3.3 Characterization of Monomer Nanorods

3.3.1 Stability of Nanorods

All the photoreactive molecules (**1-3**, **6-12** and the photoreactive polymorph of **13**) could be formed into 200 nm diameter nanorods using our solvent annealing methods in AAO templates. SEM images of some representative examples are shown in Figure 3.5.

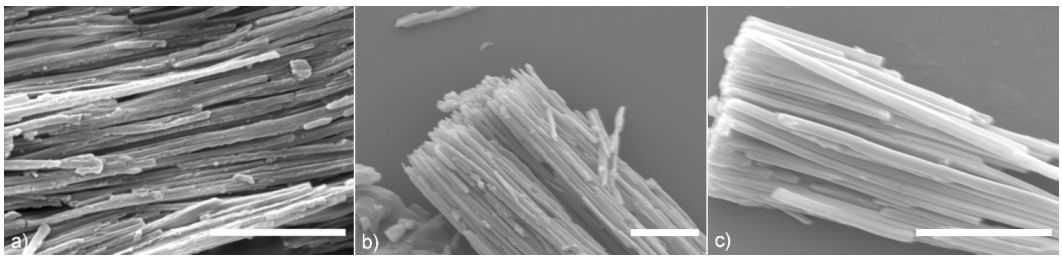

Figure 3. 5 SEM images of 200nm nanorods composed of different anthracene esters: **a**) **7**; **b**) **11**; **c**) **12**. (Scale bar is 5 µm)

In these samples, where the rods are clustered together, we noticed that over the course of several weeks, individual rods would sometimes merge with neighboring rods to form larger diameter crystals as shown in Figure 3.6. This indicates that the nanorods are not the equilibrium structure, and that the molecules retain some mobility and the ability to merge into larger crystals in the absence of the template constraints.

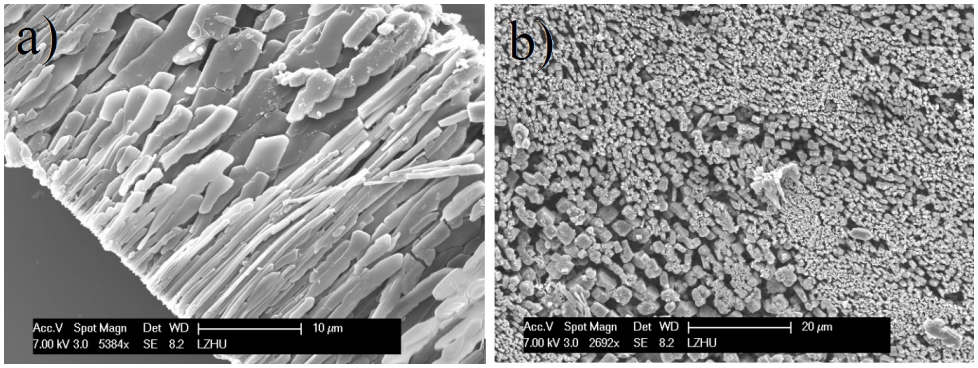

Figure 3. 6 a) side view of a bundle of nanorods **12** after sitting in water at room temperature for several months. It can be seen that part of it still shows as nanorods, but most of them have already merged into bigger chunks; **b**) top view of a bundle of old nanorods **12**, different diameters of rods can be seen, some of them are in the micrometer scale.

3.3.2 Photoresponse of Nanorods

When nanorods composed of photoreactive molecules were exposed to 365 nm light in a fluorescence microscope, they typically underwent movement and expanded in length. In bulk crystals, the coexistence of the two different crystalline phases during the course of the photodimerization reaction causes the crystal to build up internal stress and shatter.[4] Apparently, the nanorods' large surface-to-volume ratio allows them to accommodate the volume changes during photodimerization and remain intact. Bundles

tended to separate under the influence of the light as shown in Figure 3.7. The rods retained their shape and did not break.

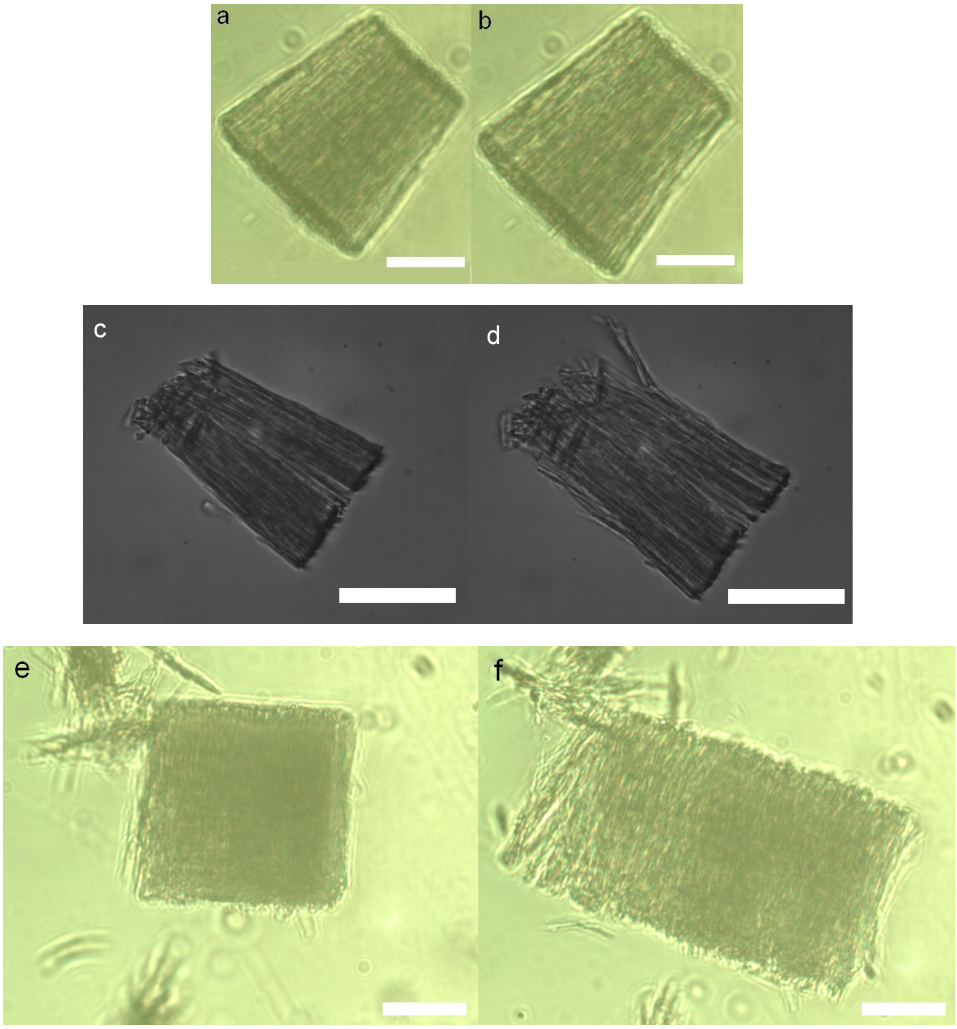

Figure 3. 7 Microscope images of nanorods: **a**) nanorods **6** before irradiation; **b**) nanorods **6** after irradiation; **c**) nanorods **7** before irradiation; **d**) nanorods **7** after irradiation; **e**) nanorods **12** before irradiation; **f**) nanorods **12** after irradiation, (Scale bar is 20 μm). Different ester nanorods have different photoresponse, for example, nanorods **12**, under irradiation, the bundle width can be doubled as shown above, but measurement of single rod **12** by AFM showed no obvious evidence that the single rod width changes that much. One possible reason for bundle width change of **12** may come from rods pushing each other during irradiation.

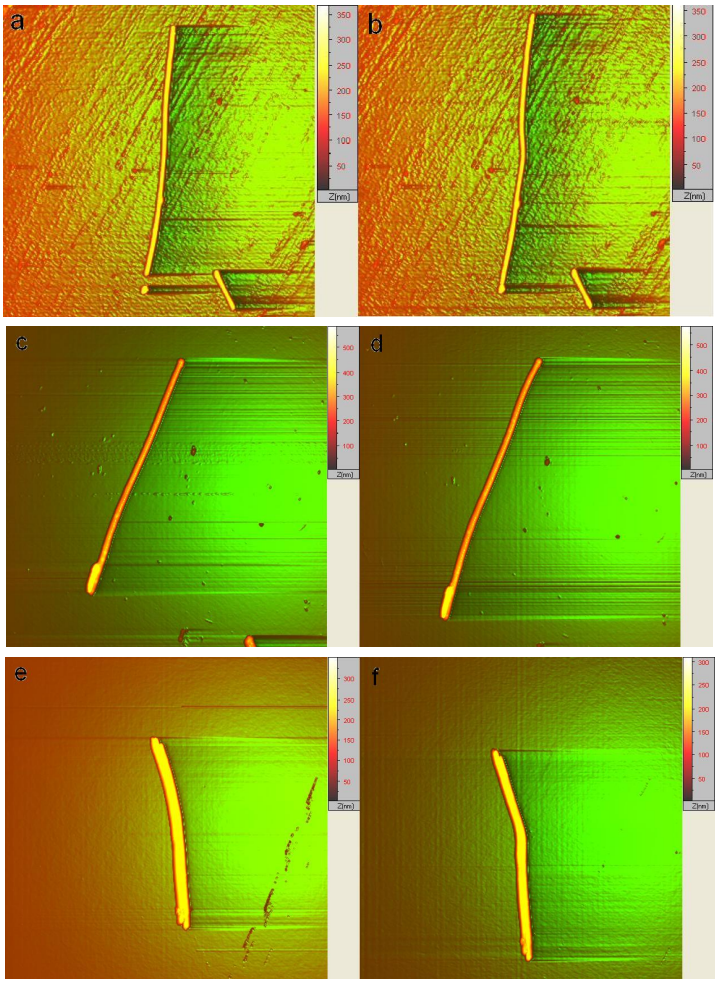

Figure 3. 8 (**a, b**) nanorod 8 expands by 11.5% after irradiation; (**c, d**) nanorod **8** expands by 10.5% after irradiation; (**e, f**) nanorod **8** expands by 9% after irradiation. The expansion of nanorods varies from rod to rod which may due to the crystalline of nanorods and the degree of surface adhesion.

We found that the amount of length change for a given molecular crystal nanorod varied within a sample. For example, for nanorods composed of **8**, expansions ranged from 7% to 15%. The variation is shown in Figure 3.8 for three different rods of **8**; and for nanorods composed of **12**, expansions ranged from 5% to 25%. This variability has also been observed in rods composed of 9AC that undergo reversible bending. [19] Variations in crystallinity or the degree of surface adhesion have been identified as

possible factors that contribute to the observed variability. Nevertheless, we can say that the 9-anthracenecarboxylic acid esters form a large family of compounds that can be solvent annealed into crystalline nanorods manifesting measurable photomechanical motions in response to near-UV irradiation. Table 3.1 summarizes the properties of the molecules studied in this paper. One surprising aspect of Table 1 is that the nanorod photomechanical response is not specific to a single crystal type.

Table 3. 1 Properties of anthracene esters

Anthracene Esters	Crystal Packing	Photoreactivity of Crystal	Nanorods Growth	Photomechanical Response
1	HBP	Shatter	Yes	Yes
2	HBP	No response	Not attempted	-
3	LP	Shatter	Yes	Yes
4	HBP	Melt	No	-
5	LP	Melt	No	-
6	LP	Shatter	Yes	Yes
7	HBP	Shatter	Yes	Yes
8	HBP	Shatter	Yes	Yes
9	HBP	Shatter	Yes	Yes
10	DP	No response	Not attempted	-
11	HBP	Shatter	Yes	Yes
12	LP	Shatter	Yes	Yes
13	OHBP	Shatter*	Yes	Yes

HB = herringbone, HBP = herringbone pair, LP = layered pair, DP = distant pair where anthracenes are too far apart to react, OHBP = offset herringbone pair where anthracenes are not aligned for reaction.

*photoreactivity and photomechanical response for 13 reported for polymorph with unknown crystal structure.

3.4 Photochemistry of 9TBAE 8

With the photomechanical response of the anthracene ester nanorods established as a general phenomenon, the next question concerns the physical basis of this response.

We have concentrated on the case of 9TBAE **8**, as a prototypical ester with a sizable photomechanical response. The photoreaction scheme of 9TBAE **8** is shown in Figure 3.9.

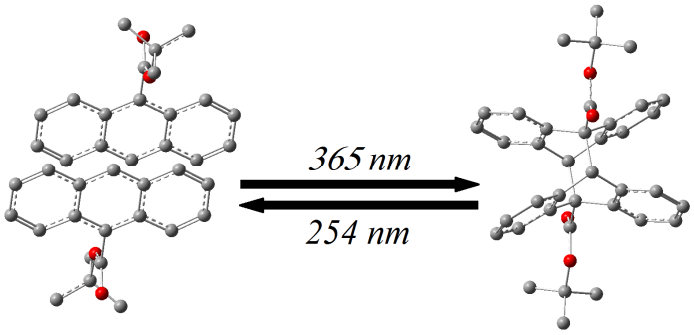

Figure 3. 9 Photoreaction scheme of 9TBAE **8**: under 365 nm UV irradiation, a pair of 9TBAE monomers go through [4+4] cycloaddition to form photodimer, under 254 nm irradiation, 9TBAE photodimer goes back to monomers.

The room temperature single crystal XRD structure reveals rotational disorder in the tert-butyl groups that disappears at 100 K as shown in Figure 3.10. The details of the XRD monomer crystal structure are summarized in Table 3.2. An earlier 9TBAE crystal structure [20] could not resolve this disorder and had larger standard deviations in the unit cell dimensions as well as a larger R1 value in comparison to our tert-butyl disordered model.

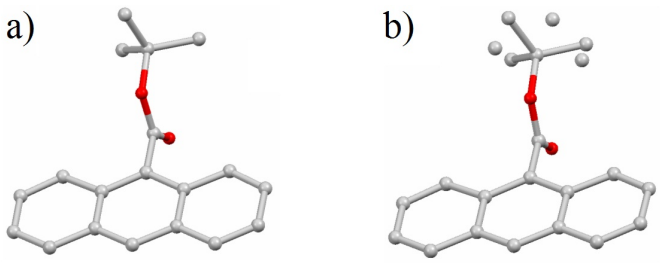

Figure 3. 10 Crystal structures of 9TBAE **8**, a) at 100 K with no disorder; b) at 296 K with tert-butyl group disorder, the grey balls signify carbon atoms from the tert-butyl group.

Table 3. 2 Crystal data and structure refinement for monomer, PRD and SGD

Empirical formula	$C_{19} H_{18} O_2$ (monomer)	$C_{19} H_{18} O_2$ (PRD)	$C_{38} H_{36} O_4$ (SGD)
Formula weight	278.33	278.33	556.67
Temperature	296(2) K	296(2) K	100(2)K
Wavelength	0.71073 Å	0.71073 Å	0.71073 Å
Crystal system	Monoclinic	Monoclinic	Triclinic
Space group	P2(1)/n (#14)	P2(1)/n (#14)	P-1
Unit cell dimensions	a = 9.1313(7) Å α= 90°	a = 9.1419(7) Å α= 90°	a = 9.1605(2) Å α= 67.1901(3)°
	b = 17.5205(14) Å β= 99.9029(14)°	b = 17.5398(14) Å β= 99.8192(13)°	b = 9.6923(2) Å β= 85.3952(4)°
	c = 9.7613(8) Å γ = 90°	c = 9.7526(8) Å γ = 90°	c = 10.2180(3) Å γ = 62.2311(3)°
Volume	1538.4(2) Å3	1540.9(2) Å3	734.34(3) Å3
Z	4	4	1
Density (calculated)	1.202 Mg/m^3	1.200 Mg/m^3	1.259 Mg/m^3
Absorption coefficient	0.077 mm^{-1}	0.077 mm^{-1}	0.080 mm^{-1}
F(000)	592	592	296
Crystal size	0.20 x 0.17 x 0.10 mm^3	0.47 x 0.39 x 0.18 mm^3	0.37 x 0.25 x 0.09 mm^3
Theta range	2.32 to 24.71°	2.32 to 29.57°	2.32 to 30.50°
Index ranges	-10<=h<=10, -20<=k<=20, -11<=l<=11	-12<=h<=12, -24<=k<=24, -13<=l<=13	-13<=h<=13, -13<=k<=13, -14<=l<=14
Reflections collected	23942	22802	17538
Independent reflections	2630 [R(int) = 0.0352]	4329[R(int) = 0.0192]	4448[R(int) = 0.0224]
Completeness to theta = 24.71°	100.00%	100.00%	99.70%
Absorption correction	Semi-empirical from equivalents	Semi-empirical from equivalents	Semi-empirical from equivalents
Max. and min. transmission	0.9925 and 0.9845	0.9864 and 0.9649	0.9926 and 0.9710
Refinement method	F^2	F^2	F^2
Data / restraints / parameters	2630 / 36 / 224	4329 / 230 / 260	4448 / 0 / 193
Goodness-of-fit on F2	1.038	1.021	1.056
Final R indices [I>2sigma(I)]	R1 = 0.0470, wR2 = 0.1144	R1 = 0.0391, wR2 = 0.1062	R1 = 0.0415, wR2 = 0.1110
R indices (all data)	R1 = 0.0688, wR2 = 0.1303	R1 = 0.0644, wR2 = 0.1254	R1 = 0.0467, wR2 = 0.1155
Largest diff. peak and hole	0.361 and -0.274 e.$Å^{-3}$	0.176 and -0.122 e.$Å^{-3}$	0.460 and -0.203 e.$Å^{-3}$

Both structures give the same overall picture of the herringbone-pair packing motif in the bulk and thus the first question concerns the form of the monomer crystal within the nanorods: is it the same as the bulk monomer crystal, and does it have a preferred orientation?

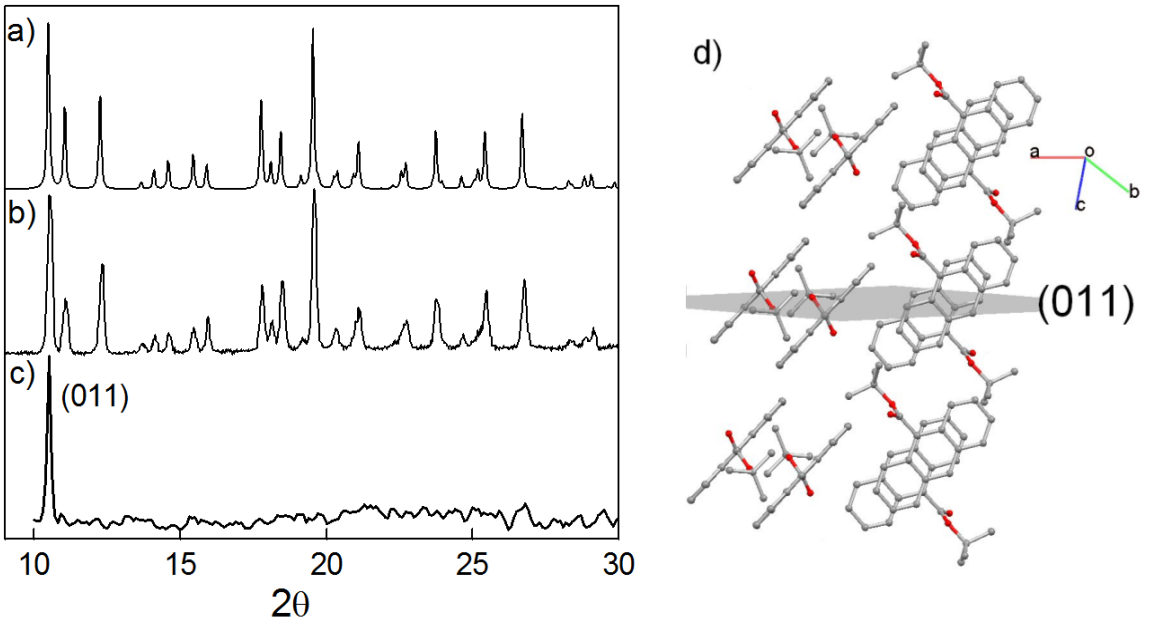

Figure 3. 11 Powder X-ray diffraction patterns of 9TBAE **8** monomers: **a)** pattern of 9TBAE monomer calculated based on the single crystal structure; **b)** experimental pattern of 9TBAE monomer bulk; **c)** orientated 9TBAE monomer nanorods; **d)** orientated 9TBAE monomer nanorods in AAO template. No peaks were observed below $2\theta=10^{o}$.

The powder XRD data in Figure 3.11 answer both questions in the affirmative. The powder XRD pattern calculated from the bulk single crystal (Figure 3.11a) structure matches up well with that obtained experimentally from the powdered sample (Figure 3.11b) – all predicted diffraction peaks are observed. If the nanorods are left in the amorphous AAO template, oriented vertically relative to the scanning x-ray beam, only a single diffraction peak appears, corresponding to the (011) plane as assigned from the

calculated XRD pattern (Figure 3.11c). This plane is shown in Figure 3.11d. The oriented, crystalline nature of individual nanorods prepared by the solvent annealing method has been previously established by TEM observations on individual rods. [22] The data in Figure 3.11 is consistent with previous powder XRD measurements on 9AC nanorods [23] and confirms that the preferential crystal orientation is a property of the entire sample and does not vary from rod to rod.

3.5 X-ray Diffraction Characterization of Photodimer Crystal Structures

3.5.1 Solution Grown Dimer (SGD)

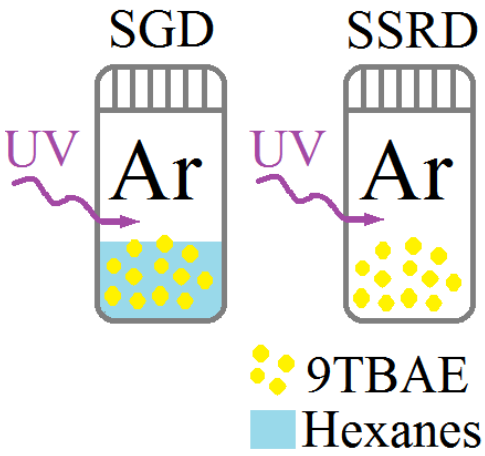

Figure 3. 12 Experimental set-ups for obtaining solid-state reacted dimer (SSRD) and solution grown dimer (SGD). For SGD, the photodimerization of 9TBAE was carried out in a sealed vial with Argon, with 9TBAE partially dissolved in n-hexanes; For SSRD, the photodimerization of 9TBAE was carried out in a sealed vial with Argon, with 9TBAE in the solid-state.

After exposure to UV light, the monomer photodimerizes and a new crystal structure is formed, which we will refer to as the solid-state reacted dimer (SSRD). In an earlier paper, we characterized the crystal structure of the dimer grown from a solution of

CH_2Cl_2, which resulted in solvent molecules being incorporated into the lattice. [17] After some trial-and-error, we found that slow evaporation of a monomer solution in n-hexane during UV irradiation could produce large photodimer crystals without solvent of crystallization molecules. This crystal structure, we will refer to as the solution grown dimer (SGD). The experimental set-ups for solid-state reacted dimer (SSRD) and solution grown dimer (SGD) is shown in the Figure 3.12. The crystal structure of SGD is shown in Figure 3.13a, and its characteristics are summarized in Table 3.2.

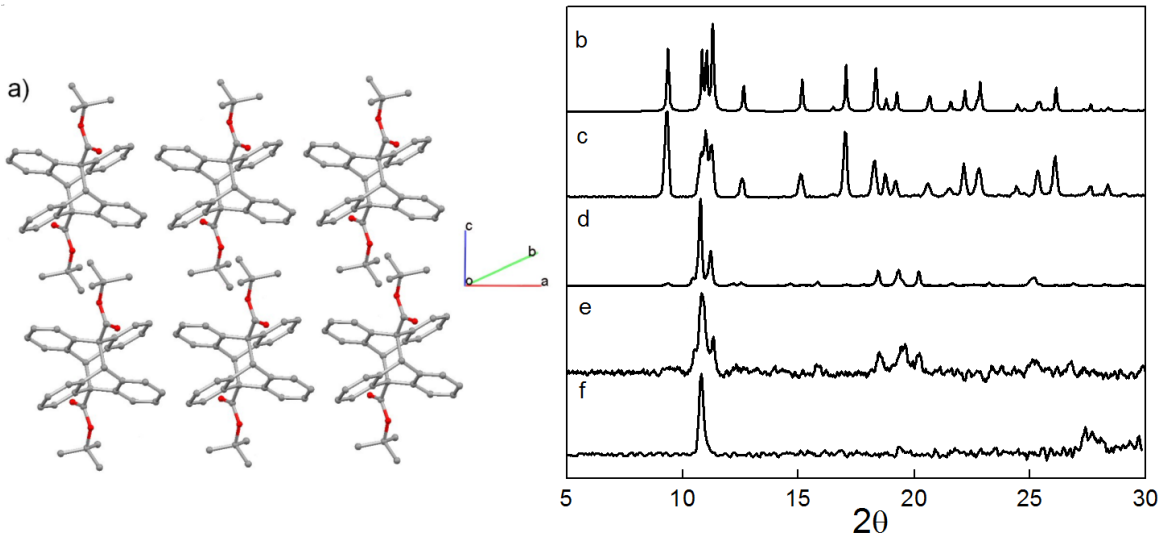

Figure 3. 13 a) Crystal structure of solution grown dimer (SGD) from hexane; Powder X-ray diffraction patterns: **b)** calculated pattern of SGD; **c)** experimental pattern of SGD; **d)** experimental pattern of dimer nanorods; **e)** experimental pattern of SSRD bulk; **f)** experimental pattern of dimer nanorods in AAO templat

In addition to the cyclohexyl bridge structure seen in all anthracene dimers, there are two other important changes in the SGD structure when compared to the monomer crystal in Figure 3.11d. First, the ester groups are now rotated ~180^o so that the tert-butyl group on one anthracene points outward, away from the neighboring anthracene. Second,

the anthracene dimers have rearranged themselves from the HBP structure into a layered crystal where the anthracene rings are parallel with each other. As can be seen from Table 3.2, the volume per anthracene of the SGD (367.17 Å^3) is significantly smaller than that of the monomer crystal (384.61 Å^3). At first glance, this result is surprising given our previous results that indicated a volume increase after irradiation.[17] But the powder XRD data make it clear that the crystal structure of the SGD is different from that of the SSRD crystal formed immediately after irradiation of the crystalline monomer. Figures 3.13b and 3.13c compare the calculated powder XRD pattern for the SGD to the experimental data for the powdered SGD. The good agreement between the two patterns shows that there is no systematic error in our powder XRD measurements. But when the SGD diffraction pattern is compared to that of the SSRD, obtained either from an irradiated powder (Figure 3.13d) or from the nanorods (Figure 3.13e), there are clear differences in peak positions and relative intensities. Figure 3.13f shows the powder XRD of the reacted nanorods in the AAO template, which exhibit only a single peak from the SSRD powder pattern, providing evidence that the preferential crystal orientation in the nanorod is still the property of the entire sample and doesn't vary from rod to rod after photoreaction.

3.5.2 Single-Crystal-to-Single-Crystal Transformation from Monomer to SSRD

The transformation from monomer to the SSRD appears to be a simple first-order kinetic process. We can monitor these kinetics using powder XRD peak areas. Figure 3.15 shows the transformation of the templated nanorods after exposure to 365 nm light.

The diffraction peak at 10.5^{o} disappears and a new peak grows in at 10.8^{o}. A series of powder XRD patterns showing the crystal-to-crystal transformation in this region is shown in Figures 3.14 a-f.

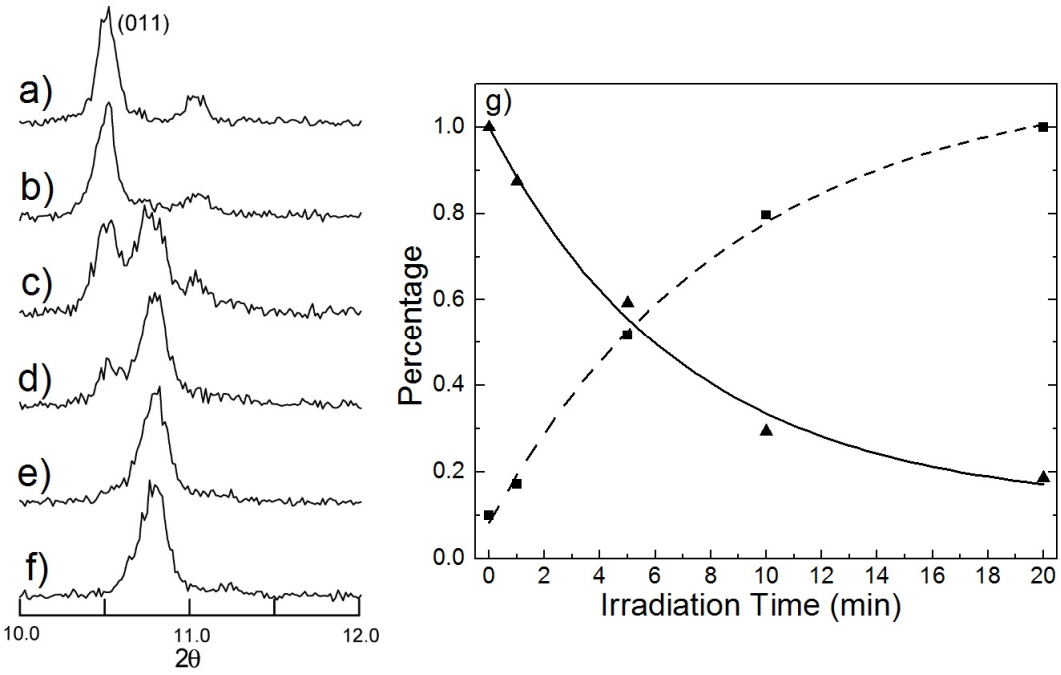

Figure 3. 14 Powder X-ray diffraction patterns of single-crystal-to-single-crystal transition from orientated 9TBAE monomer nanorods to dimer: **a)** (011) peak of 9TBAE monomer nanorods before irradiation; **b)** after 1 min irradiation; **c)** after 5 min irradiation; **d)** after 10 min irradiation; **e)** after 20 min irradiation; **f)** after 1 hour irradiation; **g)** exponential fit of the decay of the monomer peak (solid line) and the growth of the dimer peak (dashed line).

Analysis of the peak areas in Figures 3.14 a-f indicates that the reaction is a simple two-state process, since the exponential decay of the reactant peak is mirrored by the growth of the product peak, as shown in Figure 3.14g. The temporal evolution of the peaks in the ssNMR spectrum (Figure 3.15) can also be monitored during the course of the reaction. Again, no peaks other than the monomer and SSRD are observed during the

evolution of the spectrum. Thus both powder XRD and ssNMR data are consistent with formation of a single product during the reaction.

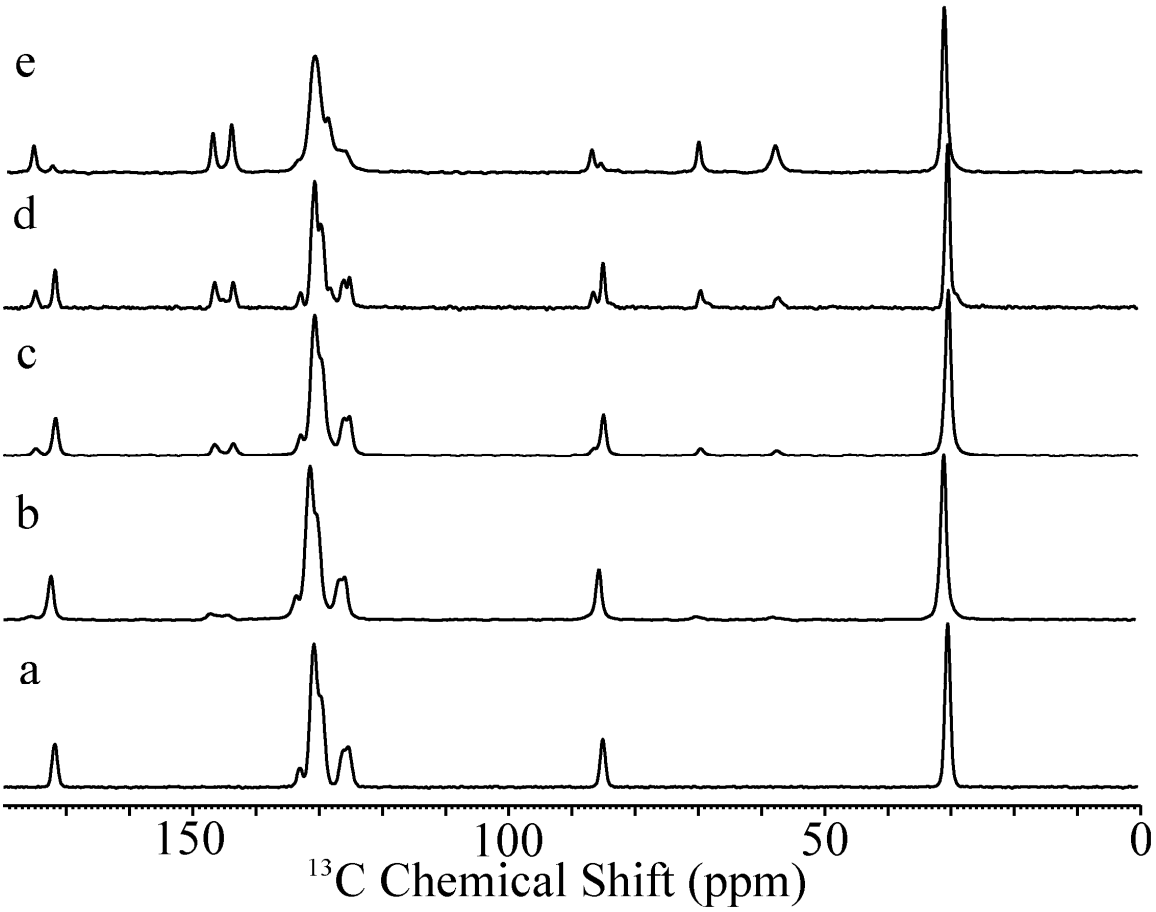

Figure 3. 15 Solid-state NMR spectra of the transition from 9TBAE monomer bulk to dimer bulk: **a**) 9TBAE monomer before irradiation; **b**) after 1 hr irradiation; **c**) after 3.5 hrs irradiation; **d**) after 5 hrs irradiation; e) after 24 hrs irradiation (SSRD).

3.5.3 SSRD is a Metastable Intermediate

On longer timescales, we have found that the SSRD crystal structure is metastable. Over the course of several months, powder XRD and SSNMR measurements indicate that the SSRD slowly converts into the SGD structure, which is stable on this timescale,

and also partially back to the monomer. The powder X-ray diffraction patterns in Figure 3.16 show the transformation of the SSRD powder XRD pattern into a mixture with both monomer and SGD crystal peaks. The red pattern shown in Figure 3.16b is the experimental powder pattern of an old SSRD (couple months old); compared with the black pattern of fresh SSRD in Figure 3.16b, the new peak features of old SSRD show peaks from both monomer and SGD.

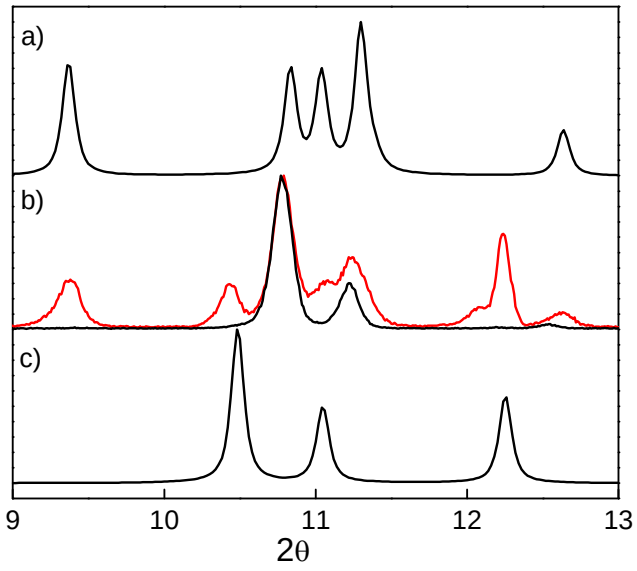

Figure 3. 16 Powder X-ray diffraction patterns: **a**) calculated pattern of SGD **8**; **b**) black-experimental pattern of fresh SSRD **8**, red-experimental pattern of old SSRD **8**; **c**) calculated pattern of monomer **8**. After several months, SSRD **8** slowly turn into monomer **8** (new peaks of SSRD **8** at 10.48°, 11.04° and 12.26° are features of monomer **8**) and SGD **8** (new peaks at 9.36°, 11.3° and 12.64° are features of SGD **8**).

We also measured the slow conversion of SSRD **8** into monomer **8** and SGD **8** by solid-state ^{13}CNMR (as shown in Figure 3.17). Survey with other esters show that the metastable intermediate SSRD is not limited to 9TBAE **8** only; the powder X-ray

diffraction patterns in Figure 3.18 illustrate that the SSRDs of **1** and **12** are different polymorphs from SGDs of **1** and **12**. Thus, it's a general phenomenon among the anthracene ester derivatives that the SSRD is metastable intermediate structures.

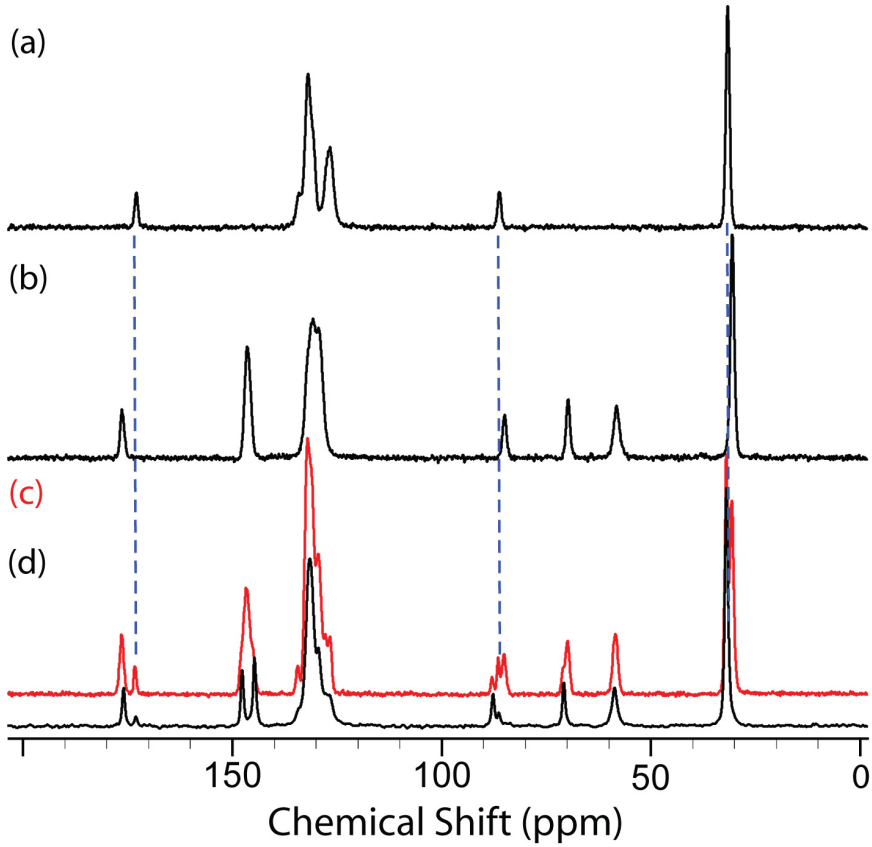

Figure 3. 17 ^{13}C solid-state NMR spectra for **a**) 9TBAE monomer **8**; **b**) SGD; **c**) 2 years old SSRD. **d**) SSRD immediately after irradiation. Note that in **c**) the peak around 145 ppm shows both SGD and SSRD peaks, and the region around 85 ppm shows peaks from all three species.

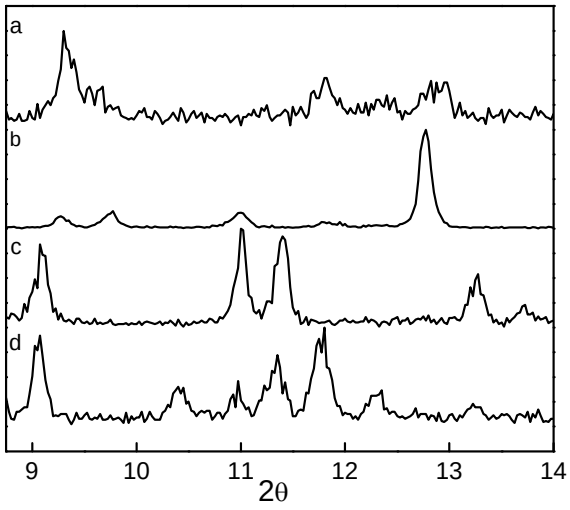

Figure 3. 18 Comparison of solid-state reacted dimer and solution grown dimer powder XRD patterns for limited angle range to show differences for other anthracene esters: **a**) solid-state reacted **1**; **b**) solution grown **1**; **c**) solid-state reacted **12**; **d**) solution grown **12**. For both compounds, as for **8**, the solid-state reacted dimer crystal is different from that obtained by crystallizing the dimer from solution.

3.5.4 Partially Reacted Dimer (PRD)

In an attempt to determine the structure of the SSRD, we used the long wavelength tail irradiation method to photoreact a millimeter-scale crystal without fragmenting it. Many workers have used single crystal XRD to follow the progress of solid-state photodimerization reactions, with trans-cinnamic acid derivatives comprising the most commonly studied system [24-28] in addition to other molecules. [29-32] After reacting a 9TBAE crystal under 400 nm illumination for 25min, ~20% of the crystal was converted into the dimer. The conversion was limited to about 20% due to crystal disintegration, so the reaction could not be followed to completion within a single macroscopic crystal, as seen previously for the solid-state [4+4] photodimerization of 9-

methylanthracene. [21-22] The structure was solved assuming a mixture of the known monomer crystal structure and the unknown dimer, and the crystal parameters are summarized in Table 3.2.

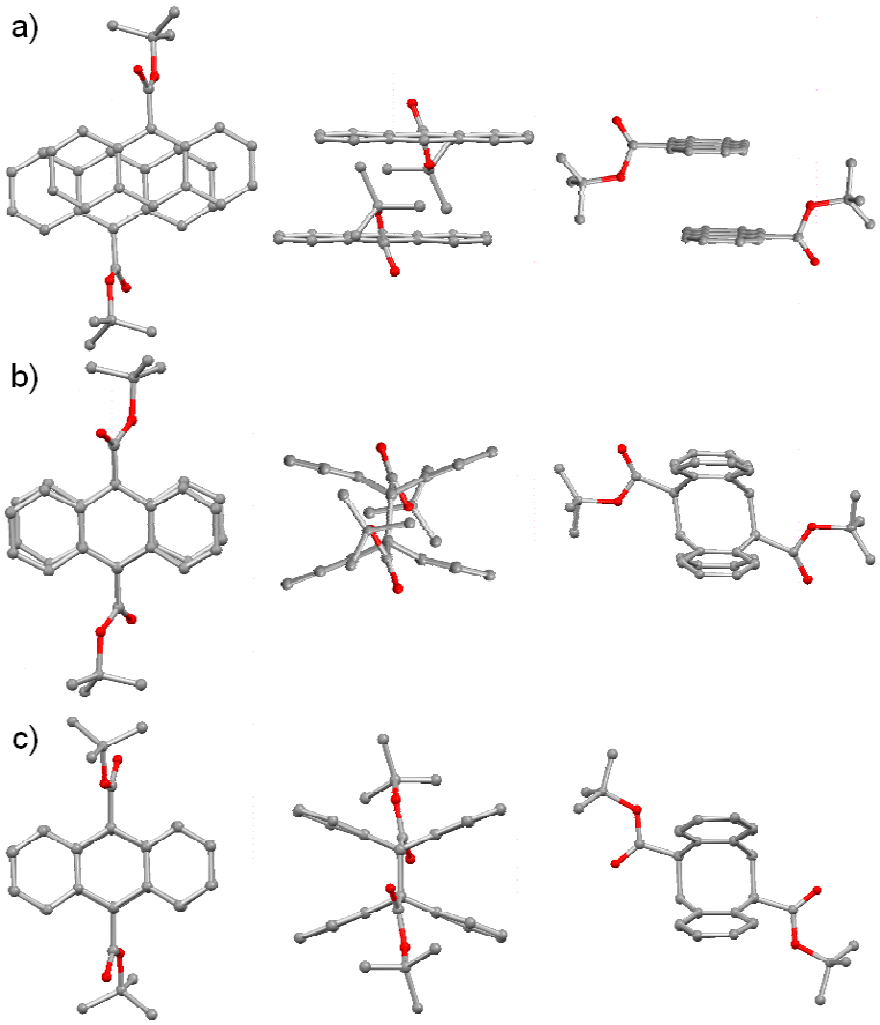

Figure 3. 19 Three different views of the reactive molecular pairs obtained from the crystal structures of **a**) monomeric **8**; **b**) the PRD; **c**) the SGD.

The resulting dimer structure, which we refer to as the partially reacted dimer (PRD) is shown in Figure 3.19, along with the monomer and SGD molecular structures for comparison. The main difference between the PRD and SGD molecular structures is

that the ester groups are inward-facing for the PRD but have rotated approximately 180^{o} to face outward in the SGD. The question is whether this inward-facing ester conformation is a hallmark of the metastable SSRD species that determines the photomechanical response of the nanorods.

3.6 NMR Chemical Shift Analysis of SSRD Molecular Conformation

3.6.1 Conformational Differences between SSRD and SGD

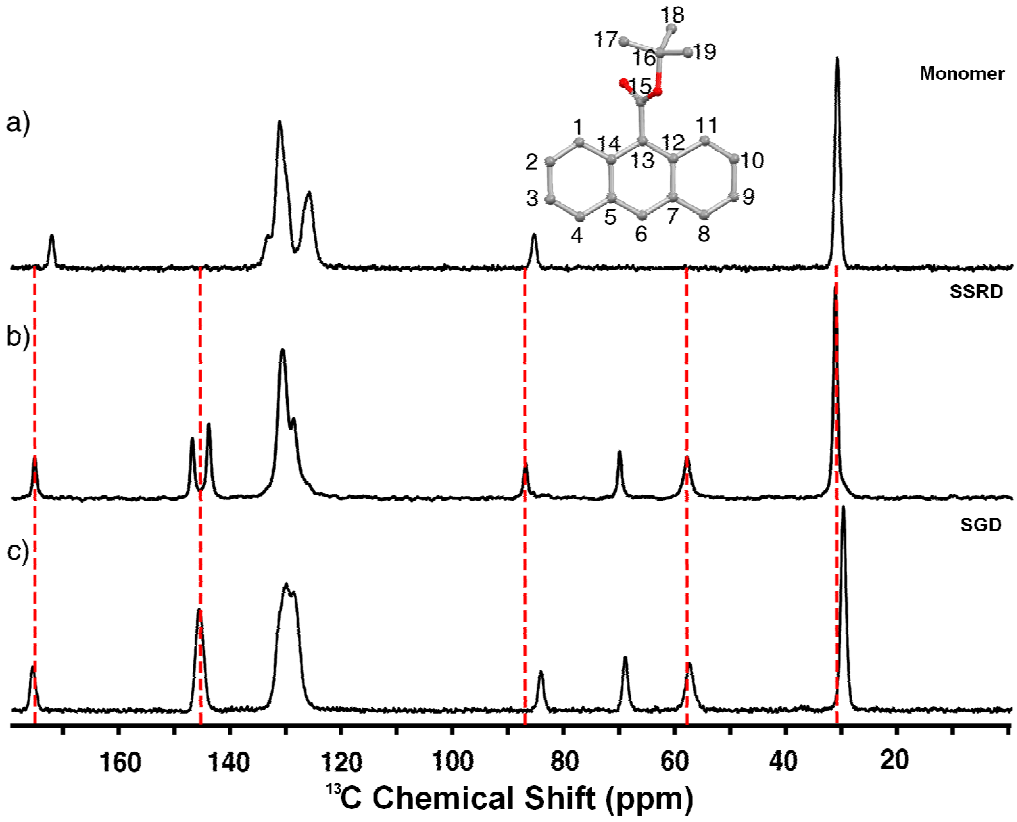

Figure 3. 20 inset) carbon numbering for 9TBAE monomer; **a**) the ^{13}C solid-state NMR spectra for the monomer 8; **b**) SSRD; **c**) SGD. The SSRD chemical shifts for C6 (58.6 ppm); C15 (175.8 ppm); C5, C7,C12 and C14 (144.5/147.5 ppm); C16 (87.6 ppm); and C18 (31.8 ppm) are marked with red dashed lines in order to facilitate evaluations of chemical shift changes between the three species as per the discussion in the text.

In orders to address the conformational structure of the dimer in the SSRD crystal, we turn to ssNMR. First, we compare the ^{13}C spectra of the different species. The inset in Figure 3.20 shows the carbon numbering of the carbons in **8**, while Figure 3.20a shows the ^{13}C spectrum of a monomer crystal powder of **8**. When this powder is irradiated, the spectrum smoothly transforms into that in Figure 3.20b. If, on the other hand, we irradiate the monomer in solution and grow the dimer crystal after reaction, this solid yields the SGD ^{13}C spectrum in Figure 3.20c. Obvious changes in both the SSRD and SGD spectra include the shift of four aromatic carbons (5, 7, 12 and 14) from 130 ppm to 145 ppm due to the creation of neighboring sp^3 carbons, the appearance of 2 new sp^3 (6, 13) carbon resonances at 58 ppm and 70 ppm, and the shift of the carbonyl carbon (15) from 172.7 ppm to ~176 ppm in the dimer. In addition, some clear differences between the spectra of the SSRD and SGD should be highlighted. First, there is a shift of the methyl carbons (17-19) from 31.5 ppm in the monomer and 31.8 ppm in the SSRD to 30.4 ppm in the SGD. Also, carbon 16 shifts from 87.6 ppm in the SSRD to 84.8 ppm in the SGD. Thus the environment of the tert-butyl group seems to be different between the SSRD and SGD. The most obvious difference between the two spectra is a symmetric pairing of the sp^2 carbon peaks (5, 7, 12, 14) at 145 ppm in the SSRD, whereas these peaks overlap each other and appear as a single broadened peak in the SGD. Detailed analysis of the ^{13}C chemical shifts supports the assignment of the SSRD to the inward-facing ester group species suggested by the PRD structure.

3.6.2 Is the Ester Group of SSRD Facing Inward or Outward?

ssNMR experiments have been used successfully to analyze both geometry changes and reaction dynamics, particularly in the trans-cinnamic acid [2+2] photodimerization [28, 33-36], but also for 9-methylanthracene. [37] In conjunction with *ab initio* calculations of the chemical shifts, these experiments can provide constraints on the molecular geometry. [38] Table 3.3 summarizes the experimental chemical shifts for the assigned carbons, along with the theoretically calculated values for the ester group rotated 0^o (inward facing, corresponding to the PRD structure) and 180^o (outward facing, corresponding to the SGD structure).

Table 3. 3 Experimental and Theoretical Chemical Shifts

	Experimental			**Theoretical**	
	Monomer	SGD	SSRD	0 degree	180 degree
C1	unassigned aromatic carbons	unassigned aromatic carbons	unassigned aromatic carbons	127.3	128.3
C2				125	124.7
C3				125.4	125.5
C4				127.8	126.7
C5		146.3	144.5	145.7	147.5
C6		58	58.6	57.1	55.6
C7		146.3	144.5	145.7	147.5
C8		unassigned aromatic carbons	unassigned aromatic carbons	127.8	126.7
C9				125.4	125.5
C10				125	124.7
C11				127.3	128.3
C12		146.3	147.5	150	149.5
C13		69.6	70.6	70.3	70.5
C14		146.3	147.5	150	149.5
C15	172.7	176.2	175.8	176.2	177.6
C16	86	84.8	87.6	84.1	83.8
C17	31.5	30.4	31.8	23.1	22.8
C18					
C19					

Table 3.3 Experimental chemical Shifts (ppm) for SSRD and SGD, and theoretical chemical shifts calculated for 0^o rotation (inward-facing) ester group, and 180^o rotation (outward-facing) ester group. The theoretical chemical shift of carbon C18 actually is the average chemical shift of carbons 17, 18, and 19, which are not resolved experimentally.

We found that the calculated shifts for the methyl carbons systematically underestimate the experimental values by 5 ppm or more, even for solution values. From calculations, it appears that rotation of the tert-butyl group, which we know is present from the XRD crystal structure, can increase the chemical shift values for these peaks by 3 ppm or more, which provides at least a partial explanation for the discrepancy. To simplify the analysis, we do not consider these peaks, centered around 30 ppm, when comparing the experimental and theoretical chemical shift values. We also have not tried to resolve individual shifts in the crowded aromatic region around 130 ppm. When we compare the chemical shifts calculated for the 0^o and 180^o structures to the experimental chemical shifts for the SSRD, we can calculate root-mean-square deviation (RMSD) values that reflect the sum of various ^{13}C chemical shifts that are better reproduced by the 0^o calculation than by the 180^o calculation. Using the values for the assigned carbons (except methyls) in Table 3.3, we obtain a RMSD for the SSRD/0^o chemical shift comparison of 1.9 ppm, as opposed to a RMSD for the SSRD/180^o chemical shifts of 2.6 ppm. This lower RMSD value indicates that the 0^o calculation provides a better fit for the SSRD data, although the two values are not sufficiently different to conclusively prove that the 0^o PRD structure provides a better fit to the SSRD.

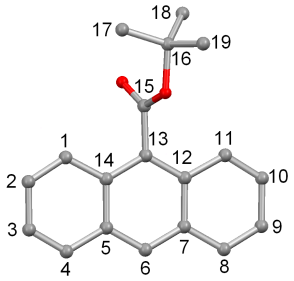

Figure 3. 21 Carbon numbering of 9TBAE monomer.

The pronounced symmetric pair at ~145 ppm in the SSRD deserves special mention. This chemical shift corresponds to the sp^2 carbons on both sides of the newly formed sp^3 carbons in the photodimer (carbons 5 and 7, and carbons 12 and 14 as shown in Figure 3.21). For any stationary structure where the esters are asymmetrically tilted (e.g. the SGD), these four carbons are inequivalent and each will have distinct but similar chemical shifts, appearing as a single broad peak in the ssNMR spectrum. If these four carbons see a symmetric environment, however, carbons 5 and 7 will be equivalent and carbons 12 and 14 will also be equivalent. The four individual peaks then collapse into a symmetric pair, with one peak due to carbons 5 and 7, and the other due to carbons 12 and 14. The question then becomes whether it is possible to distinguish between the outward-facing ester groups (180^o rotation from the monomer, similar to the ~160^o rotation in the SGD) and the inward-facing ester groups (0^o rotation, corresponding to the PRD) as shown in Figure 3.22.

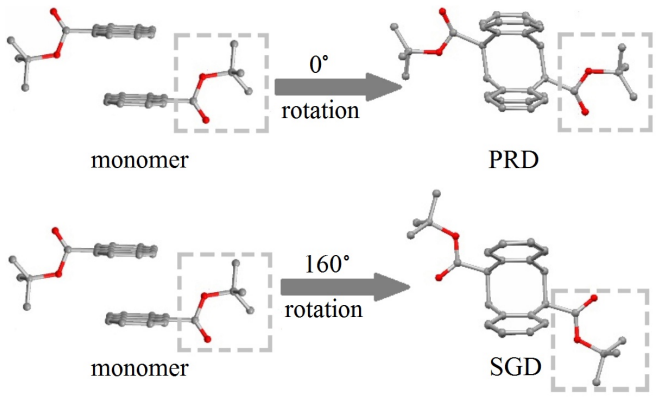

Figure 3. 22 The ester group of PRD facing inward, 0^o rotation to the monomer; the ester group of SGD facing outward, it takes about 160^o rotation from the monomer for the ester group to reach the SGD structure.

The advantage of using the relative shift to analyze the geometry is that any systematic error in the shift calculations will cancel out. From the theoretical values, we see that the difference between carbons 5, 7 and 12, 14 is predicted to be much larger for the 0^o ester (4.3 ppm) than for the 180^o ester (2.0 ppm), similar to what is observed for the SSRD (3.0 ppm) versus the SGD (<1.0 ppm). The smaller separation between the two resonances for the outward facing ester group is confirmed by comparison to the solution phase ^{13}C NMR spectrum of the SGD dimer, where the ester group is expected to be freely moving and facing outward. In solution, the separation between the two groups of peaks can be resolved at 1.1 ppm as shown in Figure 3.23. The large change in the 5, 7 and 12, 14 separation predicted for outward versus inward-facing ester groups is consistent with the experimentally observed difference between the SGD and the SSRD. Both the RMSD value and the value of the separation between the 5, 7 and 12, 14 peak pair are consistent with the inward-facing ester structure suggested by the PRD structure, and not with the outward-facing ester structure of the SGD. The last question is whether the symmetric environment experienced by these carbons is due to the ester perfectly oriented at 180^o, or whether it is due to dynamic averaging by ester rotation. Previous workers has shown how chemical reactions within a crystal lattice can generate strain and change the elastic properties of the crystal, which could in turn change dynamic properties like the ester rotation. [2, 39, 40] Since dynamic ester rotation would be most likely in the SSRD, we measured the spectrum of the SSRD at various temperatures and found that it does not change even after cooling to -30^o C. Thus there are no obvious signs of dynamic rotation of the ester group, although it is possible that the barrier is low enough

that the temperature decrease to -30^{o}C was not enough to affect the dynamics. We have also looked for changes in the dynamics by comparing the T_1 relaxation times of the various carbons in the monomer, SSRD and SGD spectra. All the carbon peaks exhibit at most a 10% change in the relaxation times as shown in the table 3.4.

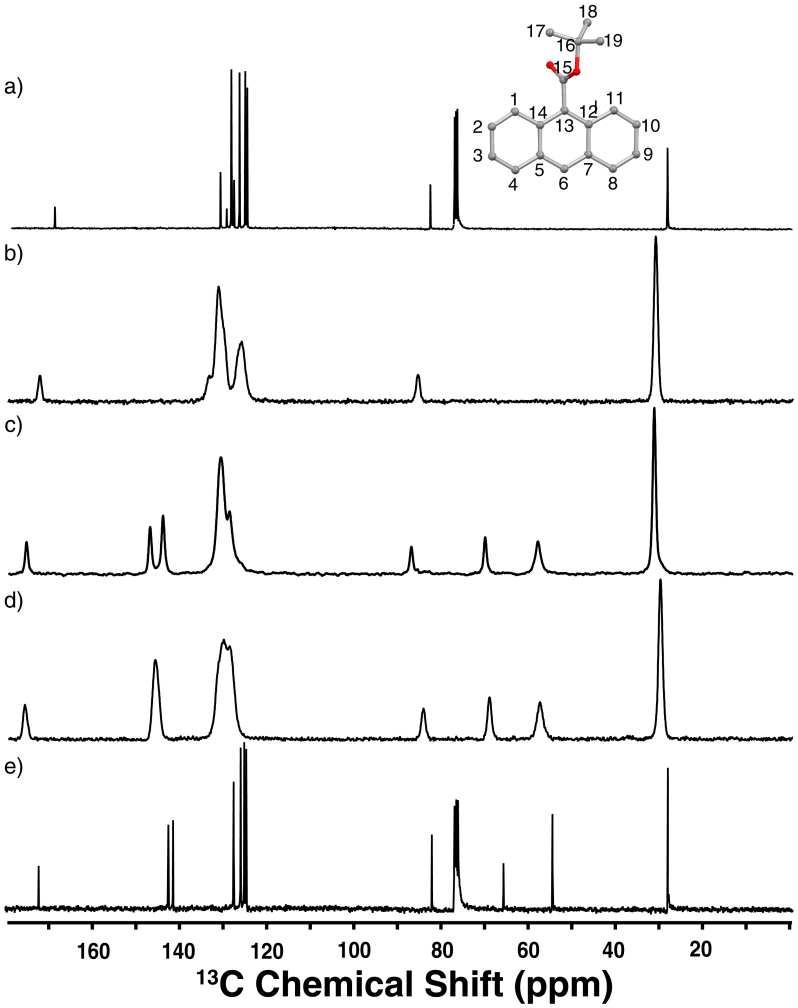

Figure 3. 23 inset) carbon numbering for 9TBAE monomer; **a)** the ^{13}C NMR spectra for 9TBAE monomer 8 in $CDCl_3$; **b)** 9TBAE monomer in solid-state; **c)** SSRD in solid-state; **d)** SGD in solid-state; **e)** the photodimer in $CDCl_3$.

Table 3. 4 Relaxation Time T1

	Monomer	20%SSRD	SGD
C5		0.979	0.88
C6		1.048	0.95
C7		0.979	0.88
C12		0.967	0.88
C13		0.959/0.98	0.88
C14		0.967	0.88
C15	0.979	0.934/1.086	0.87
C16	0.81	0.716/0.781	0.8
C17	0.707	0.648	0.76
C18			
C19			

Table 3.4 ssNMR relaxation times (T_1) for the carbons as labeled in Figure 3.21. The T_1 for carbon 18 is actually the average of carbons 17, 18 and 19. For the partially converted samples, T_1 for 15, the smaller T_1 is for the SSRD, and the larger T_1 is for the left over monomer.

3.6.3 Changes in Conformations and Packing Motifs

In order to illustrate the sequence of steps that occur after photoexcitation of **8** in the crystal, we now refer to the Figure 3.19. Figure 3.19 shows several views of the structures involved in the transformation, from the unreacted monomer pair (Figure 3.19a), to the PRD (Figure 3.19b), and finally to the fully converted equilibrium dimer structure of the SGD (Figure 3.19c). Upon irradiation, the two molecules that compose the dimer pair in Figure 3.19a must undergo two movements. First, the two anthracene rings must shift during the [4+4] dimerization reaction so that the new bonds can form. Second, the newly formed sp^3 carbons force the anthracene rings into a nonplanar "butterfly" conformation, as seen in Figure 3.19b. We hypothesize that both of these

processes are rapid (<< 1s) at room temperature and drive the formation of the SSRD immediately after the photoreaction. After the formation of the bicyclic ring between the anthracenes, the newly formed dimer molecules must execute two additional motions in order to eventually reach the low energy SGD conformation. First, the tert-butyl ester groups must rotate ~180^{o} from inward-facing with respect to the anthracene sandwich pair to an outward-facing position with the alkyl sidechains going diagonally up and away from the anthracene pair. Our *ab initio* calculations shown in Figure 3.24 have determined the barrier for this rotation is approximately 8 kcal/mole, suggesting that this motion would be slow at room temperature in the isolated molecule, and even slower in the dense crystal environment. Second, the dimer molecules must reassemble into the layered structure shown in Figure 3.13a. We hypothesize that both processes are very slow compared to the formation of the photodimer, which leaves the solid trapped in the metastable SSRD structure for a period of months.

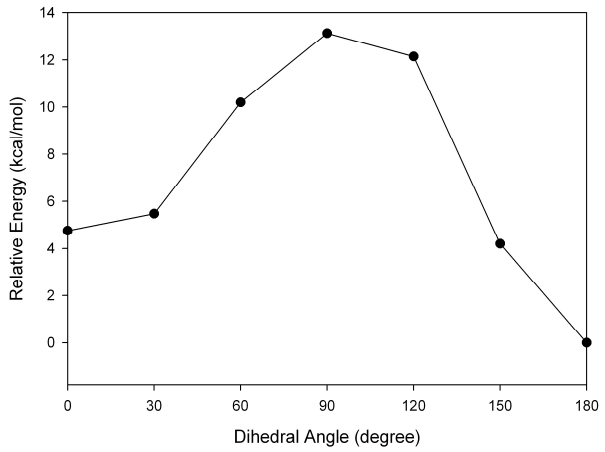

Figure 3. 24 Theoretical calculation of relative energy of dimerized **8** as a function of the ester dihedral angle. 0^{o} corresponds to the inward-facing ester, while 180^{o} corresponds to the outward-facing ester. All calculations were done in gas phase. The barrier height is ~8kcal/mol.

The micron-scale photomechanical response of the nanorods is determined by the change in going between the monomer and metastable SSRD crystal structures. To predict the overall response, we need to know both how the local molecular structure changes and how the intermolecular packing changes, i.e. how the unit cell changes in the SSRD. Unfortunately, the PRD crystal parameters in Table 3.2 are obtained by solving the crystal structure under the assumption that the crystal is a homogeneous mixture of the monomer and a disordered component whose structure is identical to the PRD. Thus the solution provides only a single set of unit cell parameters, which end up being close to those of the majority species, in this case the monomer. While this approach permits us to ascertain the molecular structure of the PRD, it does not provide a reliable way to predict the packing and thus the powder XRD pattern of the SSRD (Figure 3.25). Although there are qualitative similarities between the calculated and experimental patterns such similarities are not in general sufficient to infer crystalline structure. [41]

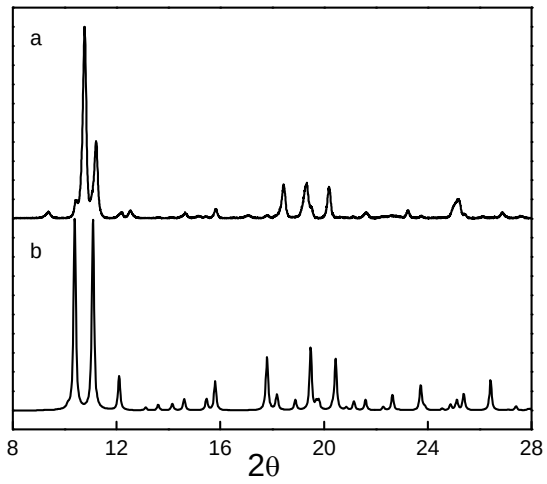

Figure 3. 25 a) experimental powder XRD pattern of SSRD; **b)** calculated powder XRD pattern of PRD

3.7 Attempt to Solve SSRD Structure by Powder X-ray Diffraction

To determine the packing motif of the PRD that generates the SSRD, we attempted to work backward from the SSRD powder diffraction pattern. Using the program DICVOL, we can index identifiable peaks in the pattern shown in Figure 3.13d to obtain the unit cell parameters a, b, c and angles α, β, γ. But while this approach works very well for the monomer crystal (it gives only one set of unit cell parameters and agrees well with the solved structure's unit cell), it failed for the SSRD, where we obtained a large number of solutions, often with quite different unit cell parameters, but with similarly poor Figures of merit. Like most indexing programs, DICVOL gives two Figures of merit, M (#lines) and F (#lines), for identifying the best solution. For synchrotron data, M (20) values of 50 or more and F (20) values of 100 or more are encouraging. Values of laboratory data will be generally lower, an M (20) of 20 or more might be considered reasonable and worthy of pursuit. Our input data is laboratory data; and our best fit is M(16) = 15.2 shown in the highlighted column in table 3.5, which is less than 20 and fitted lines/peaks is also less than 20. Furthermore, large numbers of solutions with poor Figures of merit is sign of poor input data. The input data-powder XRD pattern of SSRD-is already the best we can obtain, yet it's not qualified enough to decode unit cell parameters. Attempts to use these unit cell parameters as inputs for programs that optimize crystal structures for powder XRD analysis also failed to converge on structures with acceptable Figures of merit, at least when compared to previous literature results. We are currently pursuing a multi-pronged effort to understand

the structure of this intermediate crystal using computational methods subject to the constraints provided by our XRD and ssNMR measurements.

3.8 Conclusions

This Chapter extends our earlier study of the photophysics of photomechanically responsive molecular crystal nanostructures based on anthracene esters.[27] These molecules form a versatile family of compounds that can be formed into photoresponsive nanorods despite variations in molecular structure and crystal packing motifs. A detailed study of 9TBAE **8** provides significant insight into the molecular-level dynamics that give rise to the micron-scale response of the nanorods. The photomechanical response of the nanorods is determined by a metastable crystalline intermediate (SSRD) that slowly converts into the low energy solution grown dimer (SGD) crystal structure over the course of weeks. Thus the photomechanical response of the molecular crystal nanostructures arises from non-equilibrium crystal forms and cannot be predicted using only knowledge of the equilibrium reactant and product crystals. We have used a variety of experimental measurements to establish the structural characteristics of the SSRD, which appears to involve the photodimer in a higher energy conformation with the ester side groups pointing inward prior to rotating to the lower energy outward-facing position. The results in this paper indicate that a deeper understanding of solid-state reactivity is required to gain a predictive understanding of how solid-state photochemistry gives rise to micron-scale motions.

Crystal System	Monoclinic	Triclinic	Triclinic	Triclinic	Triclinic	Triclinic	Triclinic	Triclinic	Triclinic	Triclinic	Triclinic
a	9.6605	10.256	9.1262	8.9691	9.5671	8.6926	8.5482	6.0768	8.7939	8.5314	8.7647
b	7.8653	11.6666	10.0117	9.891	10.156	8.7526	9.2884	8.5093	9.2265	9.2222	9.204
c	16.7893	12.9454	10.032	9.9477	10.2763	10.3324	9.8318	9.7818	9.821	9.7915	9.7855
Alpha	90	68.253	105.111	98.452	89.144	109.302	82.38	76.327	100.511	83.331	100.49
Beta	101.27	77.122	112.411	109.54	62.747	98.532	75.685	86.135	93.93	75.924	94.17
Gamma	90	71.216	95.971	99.497	70.497	101.723	82.285	85.844	113.293	82.817	113.224
V	1251.09	1352.6	796.55	800.64	825.3	706.42	745.52	489.52	710.83	738.43	704.13
M	10	15.2	13.4	15.2	13.3	13.2	14.2	12.6	13.5	13.9	13
F	13.6	22.5	22.1	19.7	19.2	17.8	17	17.7	17.4	16.8	17.2
#peaks indexed	15	16	17	15	15	16	16	16	15	16	15

Table 3. 5 Unit cells calculated from powder XRD pattern of SSRD by Dicvol

Table 3.5 DICVOL generates more than one unit cells with competitive Figures of merit, and some of them have larger volume per dimer than the volume of a pair of monomer, while some have smaller volume per dimer than that of a pair of monomer.

References

1. Cohen, M. D., The photochemistry of organic solids. *Angew. Chem. Int. Ed.* **1975,** *14*, 386-393.
2. McBride, J. M.; Segmuller, B. E.; Hollingsworth, M. D.; Mills, D. E.; Weber, B. A., Mechanical stress and reactivity in organic solids. *Science* **1986,** *234*, 830-835.
3. MacGillivray, L. R.; Papaefstathiou, G. S.; Friscic, T.; Hamilton, T. D.; Bucar, D. K.; Chu, Q.; Varshney, D. B.; Georgiev, I. G., Supramolecular control of reactivity in the solid-state: from templates to ladderanes to metal-organic frameworks. *Acc. Chem. Res.* **2008,** *41*, 280-291.
4. Keating, A. E.; Garcia-Garibay, M. A., Photochemical solid-to-solid reactions. In *Organic and Inorganic Photochemistry*, Ramamurthy, V.; Schanze, K. S., Eds. Marcel Dekker: New York, 1998.
5. Kohler, W.; Novak, K.; Enkelmann, V., A holographic grating study on crystal-to-crystal photodimerization and thermal backreaction. *J. Chem. Phys.* **1994,** *101*, 10474-10480.
6. Enkelmann, V., Single-crystal-to-crystal transformations: the long wavelength tail irradiation technique. *Mol. Cryst. Liq. Cryst.* **1998,** *313*, 15-23.
7. Harada, J.; Nakajima, R.; Ogawa, K., X-ray diffraction analysis of photochromic reaction of fulgides: crystalline state reaction induced by two-photon excitation. *J. Am. Chem. Soc.* **2008,** *130*, 7085-7091.
8. Garci-Garibay, M. A., Molecular crystals on the move: from single-crystal-to-single-crystal photoreactions to molecular machinery. *Ang. Chem. Int. Ed.* **2007,** *46*, 8945-8947.
9. Finkelmann, H.; Nishikawa, E.; Pereira, G. G.; Warner, M., A new opto-mechanical effect in solids. *Phys. Rev. Lett.* **2001,** *87*, 015501/1-015501/4.
10. Yu, Y.; Nakano, M.; Ikeda, T., Directed bending of a polymer film by light. *Nature* **2003,** *425*, 145.
11. Camacho-Lopez, M.; H. Finkelmann, H.; Shelley, P. P.-M., Fast liquid-crystal elastomer swims into the dark. *Nat. Mater.* **2004,** *3*, 307-310.
12. Ikeda, T.; Mamiya, J.; Yu, Y., Photomechanics of liquid-crystalline elastomers and other polymers. *46* **2007**, 506-528.
13. White, T. J.; Tabiryan, N. V.; Serak, S. V.; Hrozhyk, U. A.; Tondiglia, V. P.; Koerner, H.; Vaia, R. A.; Bunning, T. J., A high frequency photodriven polymer oscillator. *Soft. Mater.* **2008,** *4*, 1796-1798.
14. Oosten, C. L. v.; Bastiaansen, C. W. M.; Broer, D. J., Printed artificial cilia from liquid-crystal network actuators modularly driven by light. *Nat. Mater.* **2009,** *8*, 677-682.
15. Takahashi, S.; Miura, H.; Kasai, H.; Okada, S.; Oikawa, H.; Nakanishi, H., Single-crystal-to-single-crystal transformation of diolefin derivatives in nanocrystals. *J. Am. Chem. Soc.* **2002,** *124*, 10944-10945.
16. Bucar, D. K.; MacGillivray, L. R., Preparation and reactivity of nanocrystalline cocrystals formed via sonocrystallization. *J. Am. Chem. Soc.* **2007,** *129*, 32-33.
17. Al-Kaysi, R. O.; Muller, A. M.; Bardeen, C. J., Photochemically driven shape changes of crystalline organic nanorods. *J. Am. Chem. Soc.* **2006,** *128*, 15938-15939.

18. Al-Kaysi, R. O.; Bardeen, C. J., Reversible photoinduced shape changes of crystalline organic nanorods. *Adv. Mater.* **2007,** *19*, 1276-1280.
19. Good, J. T.; Burdett, J. J.; Bardeen, C. J., Using two-photon excitation to control bending motions in molecular-crystal nanorods. *Small* **2009,** *5*, 2902-2909.
20. Sweeting, L. M.; Rheingold, A. L.; Gingerich, J. M.; A. W. Rutter; Spence, R. A.; Cox, C. D.; Kim, T. J., Crystal structure and triboluminescence 2. 9-anthracene carboxylic acid and its esters. *Chem. Mater.* **1997,** *9*, 1103-1115.
21. Ramamurthy, V.; Venkatesan, K., Photochemical reactions of organic crystals. *Chem. Rev.* **1987,** *87*, 433-481.
22. Al-Kaysi, R. O.; Bardeen, C. J., General method for the synthesis of crystalline organic nanorods using porous alumina templates. *Chem. Commun.* **2006**, 1224-1226.
23. Al-Kaysi, R. O.; Dillon, R. J.; Zhu, L.; Bardeen, C. J., Template assisted synthesis of silica-coated molecular crystal nanorods: from hydrophobic to hydrophilic nanorods. *J. Colloid. Interfac. Sci.* **2008,** *327*, 102-107.
24. Enkelmann, V.; Wegner, G.; Novak, K.; Wagener, K. B., Single-crystal-to-crystal photodimerization of cinnamic acid. *J. Am. Chem. Soc.* **1993,** *115*, 10390-10391.
25. Novak, K.; Enkelmann, V.; Wegner, G.; Wagener, K. B., Crystalligraphic study of a single crystal to single crystal photodimerization and its thermal reverse reaction. *Ang. Chem. Int. Ed.* **1993,** *32*, 1614-1616.
26. Fernandes, M. A.; Levendis, D. C., Photodimerization of the a-polymorph of ortho-ethoxy-trans-cinnamic acid in the solid-state. I. Monitoring the reaction at 293 K. *Acta Cryst. B* **2004,** *60*, 315-324.
27. Davaasambuu, J.; Busse, G.; Techert, S., Aspects of the photodimerization mechanism of 2,4-dichlorocinnamic acid studied by kinetic photocrystallography. *J. Phys. Chem. A* **2006,** *110*, 3261-3265.
28. Khan, M.; Brunklaus, G.; Enkelmann, V.; Spiess, H. W., Transient states in the [2+2] photodimerization of cinnamic acid: correlation of solid-state NMR and x-ray analysis. *J. Am. Chem. Soc.* **2008,** *130*, 1741-1748.
29. Honda, K.; Nakanishi, F.; Feeder, N., Kinetic and mechanistic study on single-crystal-to-single-crystal photodimerization of 2-benzyl-5benxylidenecyclopentanone utilizing x-ray diffraction. *J. Am. Chem. Soc.* **1999,** *121*, 8246-8250.
30. Natarajan, A.; Tsai, C. K.; Khan, S. I.; McCarren, P.; Houk, K. N.; Garcia-Garibay, M. A., The photoarrangement of a-Santonin is a single-crystal-to-single-crystal reaction: a long kept secret in solid-state organic chemistry revealed. *J. Am. Chem. Soc.* **2007,** *129*, 9846-9847.
31. Turowska-Tyrk, I.; Trzop, E., Monitoring structural transformations in crystals. 6. The [4 + 4] photodimerization of 9-methyl-anthracene. *Acta Crystal. B* **2003,** *59*, 779-786.
32. Turowska-Tyrk, I., Structural transformations in organic crystals during photochemical reactions. *J. Phys. Org. Chem.* **2004,** *17*, 837-847.
33. Harris, K. D. M.; Thomas, J. M., Probing polymorphism and reactivity in the organic solid-state using 13C NMR spectroscopy: studies of p-formyl-trans-cinnamic acid. *J. Solid. State. Chem.* **1991,** *93*, 197-205.

34. Bertmer, M.; Nieuwendaal, R. C.; Barnes, A. B.; Hayes, S. E., Solid-state photodimerization kinetics of a-trans-cinnamic acid to a-truxillic acid studied via solid-state NMR. *J. Phys. Chem. B* **2006,** *110*, 6270-6273.
35. Fonseca, I.; Hayes, S. E.; Bertmer, M., Size effects of aromatic substitution in the ortho position on the photodimerization kinetics of a-trans cinnamic acid derivatives. A solid-state NMR study. *Phys. Chem. Chem. Phys.* **2009,** *11*, 10211-10218.
36. Nieuwendaal, R. C.; Bertmer, M.; Hayes, S. E., An unexpected phase transition during the [2+2] photocycloaddition reaction of cinnamic acid to truxillic acid: changes in polymorphism monitored by solid-state NMR. *J. Phys. Chem. B* **2008,** *112*, 12920-12926.
37. Takegoshi, K.; Nakamura, S.; Terao, T., Solid-state photodimerization of 9-methylanthracene as studied by solid-state 13C NMR. *Solid-state Nucl. Magn. Reson.* **1998,** *11*, 189-196.
38. Fonseca, I.; Hayes, S. E.; Blumich, B.; Bertmer, M., Temperature stability and photodimerization kinetics of b-cinnamic acid and comparison to its a-polymorph as studied by solid-state NMR spectroscopy techniques and DFT calculations. *Phys. Chem. Chem. Phys.* **2008,** *10*, 5898-5907.
39. Peachey, N. M.; Eckhardt, C. J., Energetics of organic solid-state reactions: lattice dynamics and chemical pressure in the 2,5-distyrlpryazine photoreaction. *J. Phys. Chem.* **1993,** *97*, 10849-10856.
40. Luty, T.; Eckhardt, C. J., General theoretical concepts for solid-state reactions: quantitative formulations of the reaction cavity, steric compression, and reaction-induced stress using an elestaic multipole representation of chemical pressure. *J. Am. Chem. Soc.* **1995,** *117*, 2441-2452.
41. Bernstein, J., *Polymorphism in molecular crystals*. Oxford U. Press: Oxford, 2002.

Chapter 4 Reversible photoinduced twisting of molecular crystal microribbons

4.1 Introduction

The transformation of photon energy into mechanical work is interesting from both fundamental and practical standpoints. Photons provide a versatile and easily controllable energy source for various types of nanoscale machines.[1] However, photochemical reactions carried out in macroscopic molecular crystals often lead to phase separation between reacted and unreacted regions that shatter the crystal.[2] For example, Figure 4.1 shows the photo-induced fracture of the bulk molecular crystal 9TBAE, the molecular crystal studied in Chapter 3. Nevertheless, for smaller crystals with large surface-to-volume ratios, the build-up of interfacial stress between reacted and unreacted domains can be alleviated at a nearby surface, rather than by generating a fracture.[3-4] All the photoresponsive crystalline nanorods of anthracene ester derivatives in Chapter 3 are good representatives. Hence, the robustness of ultrasmall crystals permits a much wider variety of photochemical systems to be used in photomechanical structures. Our group's general strategy for making photoresponsive organic molecular crystals is to fabricate them into micro- and nano-structures.[5-8]

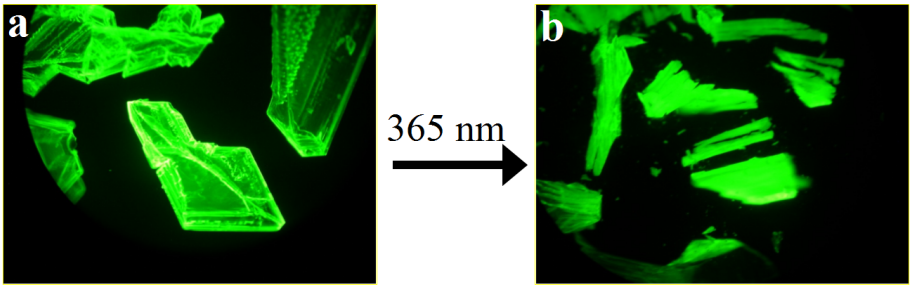

Figure 4. 1 Optical microscope images of **a**) sing crystal of 9-tertbutyl-anthracene ester (9TBAE), ~ 0.5 mm; **b**) same crystal after shatters into pieces after a few seconds irradiation of 365 nm UV light.

In Chapter 3, we studied the irreversible photoresponsive "head-to-tail" packing molecular systems; in this Chapter, we will turn to the reversible photoresponsive "head-to-head" packing molecular systems. Reversibility is an essential property for molecular crystals to be possibly used as photoactuators. The [4+4] photodimerization reaction of crystalline 9-anthracene carboxylic acid is known to be reversible due to the steric repulsion from the atypical "head-to-head" packing [9], as shown in Scheme 4.1.

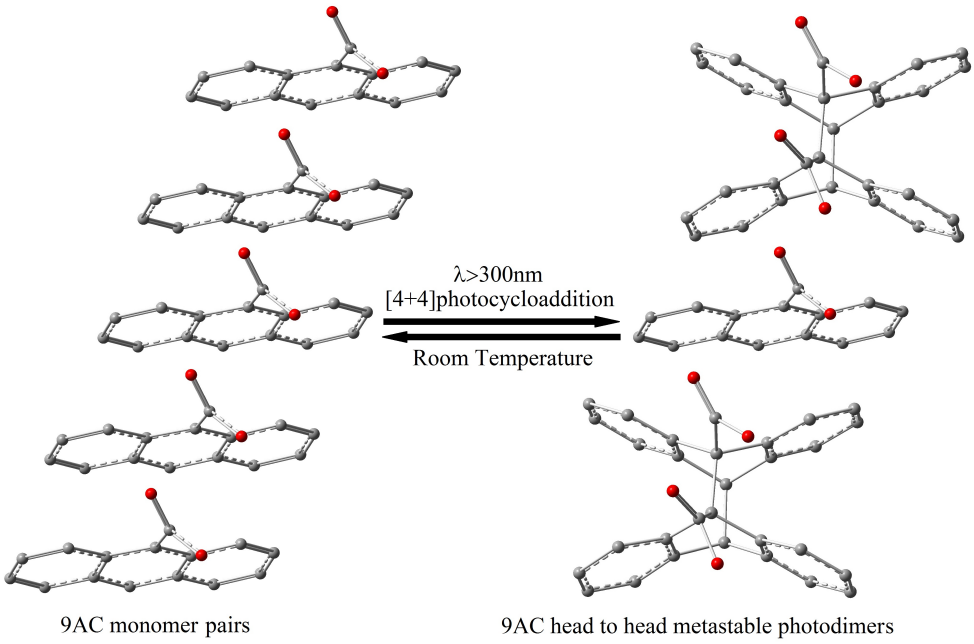

Scheme 4. 1 [4+4] photodimerization and dissociation reaction scheme of 9AC along a single crystal stack.

Note that in Scheme 4.1, some 9AC molecules are "left out" of the photodimerization reaction due to statistical considerations. This mix of reacted and unreacted molecules is unique to crystals containing one-dimensional stacks and is vital for interpreting the experimental results in this Chapter. We have previously demonstrated that crystalline nanorods composed of 9AC could undergo reversible

bending driven by strain generated between photoreacted and unreacted regions of the rod as shown in Figure 4.2. [8] This phenomenon does not rely on generating a gradient of reacted molecules along the direction of the bend, as in many polymer actuators,[10-11] and allowed us to demonstrate controlled, reversible bending in 9AC molecular crystal nanorods with diameters as small as 35 nm.[8]

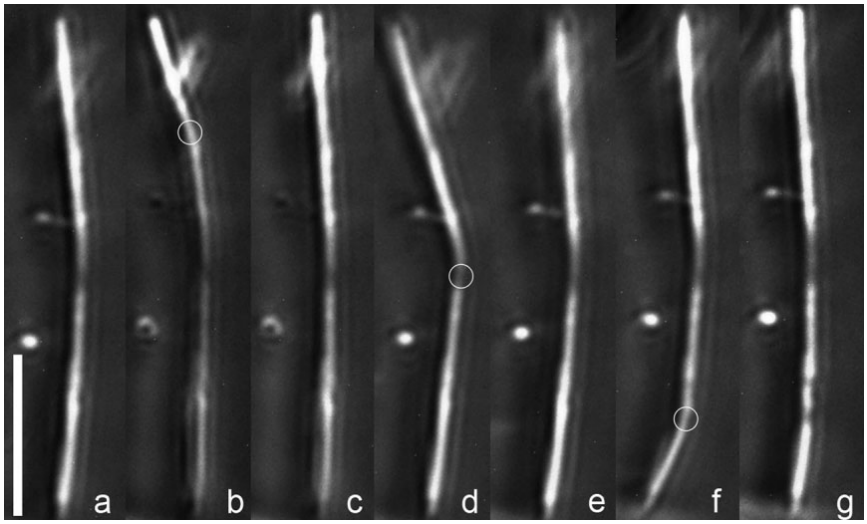

Figure 4. 2 Single 9AC rod 200nm in diameter exposed to 800 nm light (focused into a 1.5-nm spot) in phosphoric acid solution with surfactant. The rod in (**a**) is irradiated for 2 s in a spot near the top (white circle indicates location and diameter of laser spot), resulting in a bend near the top of the rod in (**b**). After 2 min in darkness it relaxes to its former configuration (**c**). This cycle is then continued with irradiation in one spot (**d, f**), where the bend is indicated by the white circle, followed by relaxation (**e, g**). Scale bar is 15 mm.

The previously studied nanorod bending required the selective illumination of a single point or segment of the rod. We became interested in whether other types of photoactivated motions could be induced, especially under conditions of spatially uniform irradiation. In this Chapter, we describe a different morphology of 9AC crystals,

namely microribbons, that undergoes reversible twisting under uniform illumination. The twist period is controlled by the amount of light exposure and saturates at a value that depends on the cross-section of the ribbon. The twist relaxes over the course of minutes (as illustrated in Figure 4.3), consistent with the dissociation of the dimer 9AC back into its monomeric form.[5, 8]

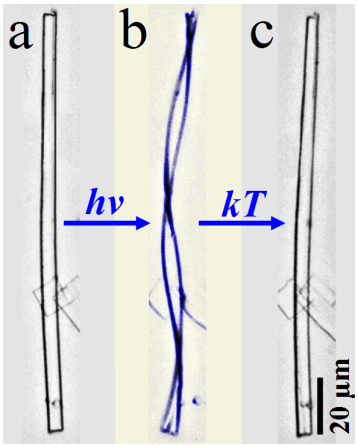

Figure 4. 3 Optical microscope images of **a**) 9AC crystalline microribbon; **b**) the microribbon twisted upon irradiation of 440 nm visible light; **c**) the twist relaxes after a few minutes (~9 min). The scale bar is 20 µm.

Using a combination of atomic force and optical microscopy, the twist period has been measured as a function of ribbon cross-section. We find that the mechanism of the twisting is consistent with stress induced by the presence of two incommensurate chemical species. In the 9AC system, these two species are most likely the photoreacted dimers and the unreacted monomers left over due to the statistical nature of the dimerization reaction. The reversible generation of a photoinduced twist in crystalline microribbons represents a new class of motions accessible through solid-state photochemistry, and also provides a new way to induce large deformations without

asymmetric or structured illumination conditions. The ability to induce repeated twisting in such small objects may make them useful for powering small-scale machines.

4.2 Characterizations of 9AC Microribbons

4.2.1 Scanning Electronic Microscope (SEM) Images

9AC crystals can grow in a variety of shapes and sizes, but the most commonly observed morphologies are ribbons and needles. After some experimentation, we found that the growth of microribbons could be maximized by making use of very flat growth surfaces, and our yields of microribbons was highest when the slow evaporation method was used with the solvent ethyl acetate. In general, all growth methods produced a distribution of microribbon lengths and cross-sections. The rectangular cross-section of the microribbons can be seen in the SEM images in Figure 4.4, as well as the distribution of lengths (*l*), widths (*w*) and thicknesses (*h*).

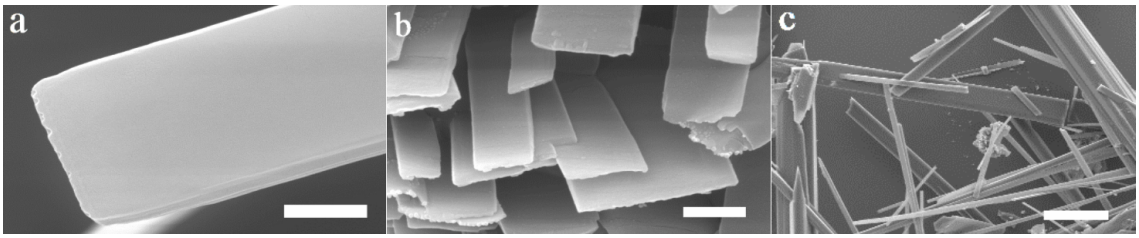

Figure 4. 4 SEM images of 9AC ribbons of different sizes, **a**) scale bar is 2µm; **b**) scale bar is 1µm; **c**) scale bar is 25µm.

4.2.2 Crystal Orientations of the Ribbons

The crystalline nature of the microribbons was confirmed by powder XRD measurements. 9AC crystallizes in columns of π-stacked anthracene moieties, where

each column is connected to a neighboring column through intermolecular hydrogen bonds between opposing carboxylic acid groups in Figure 4.5.

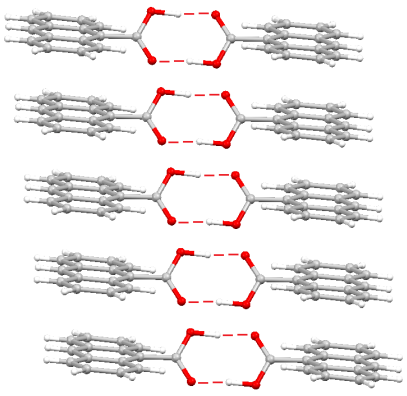

Figure 4. 5 Crystal structure of π-stacked 9AC, two neighboring stacks were connected through the hydrogen bonding shown by the red dotted line.

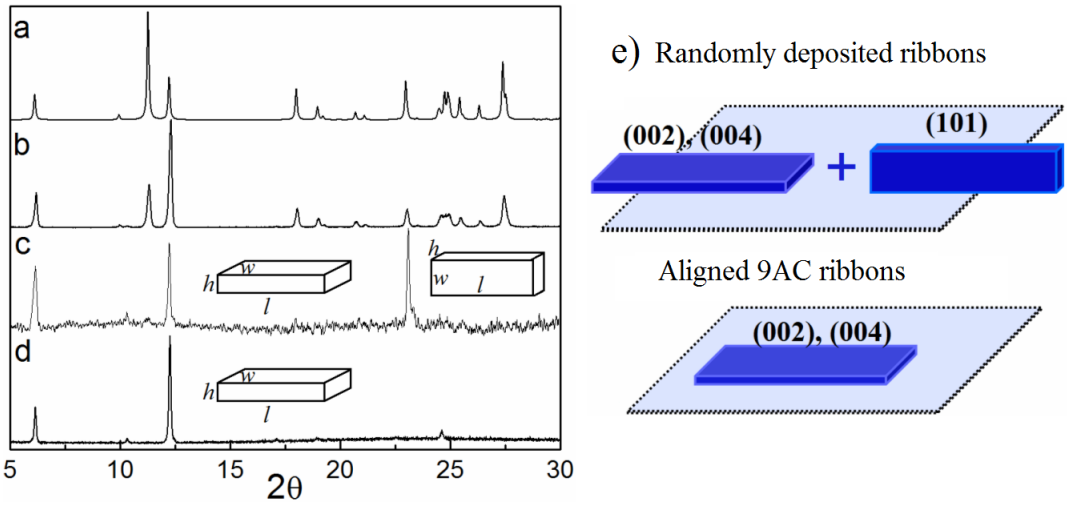

Figure 4. 6 X-ray powder diffraction patterns for 9AC **a**): Calculated pattern of monoclinic 9AC; **b**) experimental pattern of powdered 9AC crystals; **c**) pattern of ribbons randomly deposited on the surface as shown in the inset cartoon, with the three peaks corresponding to parallel planes (002) and (004), and the almost perpendicular (101) plane; **d**) pattern of ribbons lying flat on the surface as shown in the inset cartoon, with the two peaks corresponding to parallel planes (002) and (004) being most prominent; **e**) cartoon of randomly deposited ribbons from **c**) and aligned ribbons from d).

In Figure 4.6a, we show the calculated powder XRD pattern obtained from the monoclinic single crystal structure. Figure 4.6b shows the experimental powder XRD of the powdered microribbons. The peak positions and overall shape of this pattern agree well with the calculated pattern in Figure 4.6a, but there are some discrepancies in the peak intensities. These discrepancies are most likely due to residual orientation in the powdered sample arising from the tendency of 9AC crystals to form rods or ribbons that lie flat on the substrate, as discussed below. Figure 4.6c shows the powder XRD pattern for intact microribbons that have been dried and randomly deposited onto a flat substrate (as illustrated in Figure 4.6c and 4.6e). When the powder XRD pattern of this sample is measured, three major peaks are seen, corresponding to the 002 Miller plane at $2\theta=6.13^{o}$, the 004 plane at $2\theta =12.21^{o}$ and the 101 Miller plane at $2\theta=23.09^{o}$. The first two planes are parallel and extend between stacks of 9AC molecules, as shown in Figure 4.6a, while the 101 Miller plane makes an angle of 81.57^{o} with respect to the 002 plane as seen in Figure 4.6b.

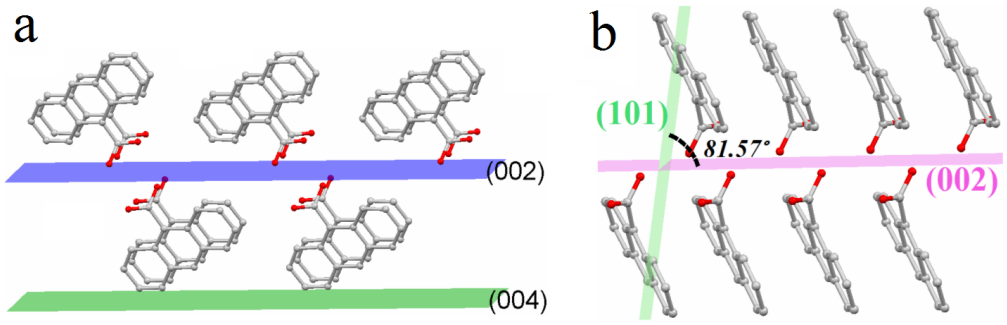

Figure 4. 7 Crystal packing of 9AC molecules a) with two parallel planes (002), (004); b) with two almost perpendicular planes (101) and (002).

In contrast, when the sample is carefully dried on the substrate, inspection using optical microscopy reveals that the majority of these ribbons lie flat on the surface, with their short axis pointing up (as illustrated in Figure 4.6d and 4.6e). We then obtain the powder XRD pattern in Figure 4.6d, which is dominated by the 002 and 004 peaks. The much smaller peak at $2\theta=24.62^{o}$ corresponds to the 008 Miller plane, also parallel to the 002 and 004 planes. In addition to these two dominant peaks, another very small peak at $2\theta=10.34^{o}$ is also observed in Figure 4.6c, corresponding to a small triclinic component within the largely monoclinic ribbons.[12] If we assume that the pattern in Figure 4.6c arises from a combination of ribbons lying on edge and lying flat, while that in Figure 4.6d arises from only ribbons that lie flat, then we can determine the absolute orientation of the crystal within the ribbon. The crystal orientation consistent with the data in Figures 4.6c and 4.6d has the 002 plane is perpendicular to *h* and the 101 plane perpendicular to *w*, as shown in Figure 4.8. It should be noted that the *c*-axis of the unit cell is aligned almost parallel to the height (*h*) of the ribbon, while the *ab* plane is parallel to the plane defined by the width (*w*) and length (*l*) of the ribbon. The stacks of 9AC monomers extend across the width of the ribbon.

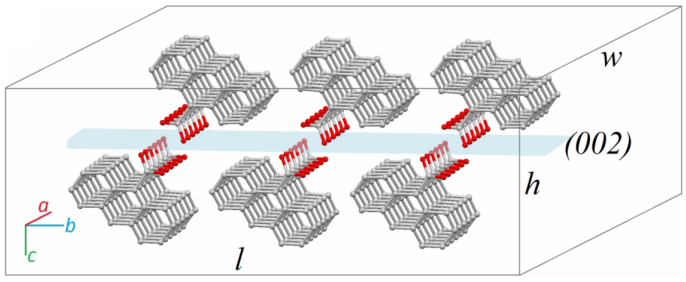

Figure 4. 8 Side view of the 9AC crystal packing within the microribbon, looking along the long axis. Note that for ribbons *h*<*w*.

Another thing worth mentioning is that (002) and (004) miller planes are not only the preferred crystal orientations for the microribbons, but also for 9AC bulk needles. The powder X-ray diffraction pattern of 9AC bulk needle crystals lying down on the substrate in Figure 4.9b shows the same two peaks, corresponding to (002), (004) miller planes.

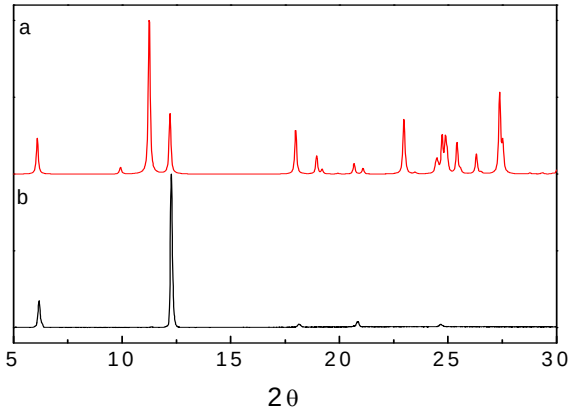

Figure 4. 9 Powder X-ray diffraction patterns: **a**) calculated pattern of monoclinic 9AC; **b**) experimental pattern of 9AC bulk needles laying down on the surface, with the two peaks corresponding to parallel planes (002) and (004) being most prominent. Thus both bulk needles and microribbons have the same crystal orientation.

4.3 Photoresponse of 9AC Microribbons

4.3.1 Reversible Twisting of 9AC Ribbons

We initially expected the microribbons to bend under localized photoexcitation but to retain their overall shape under uniform photoexcitation, similar to what was observed previously in 9AC nanorods. Instead, under uniform lamp irradiation, we observed a dramatic twisting behavior, as illustrated in Figure 4.10. Under either 410 nm

or 440 nm irradiation, a straight ribbon would rapidly twist over its entire length, while the intense green-yellow fluorescence disappeared, indicating that a photochemical reaction was consuming the 9AC molecules. No twisting or fluorescence decrease was observed for irradiation at wavelengths greater than 600 nm, ruling out a heating effect or phonon-mediated mechanism. The twisting could be observed in 25-80% of the ribbons, depending on the sample. The ribbons twisted more easily when suspended in an aqueous solution than on a dry surface. The reason for this may lie in increased surface adhesion in the dry samples.

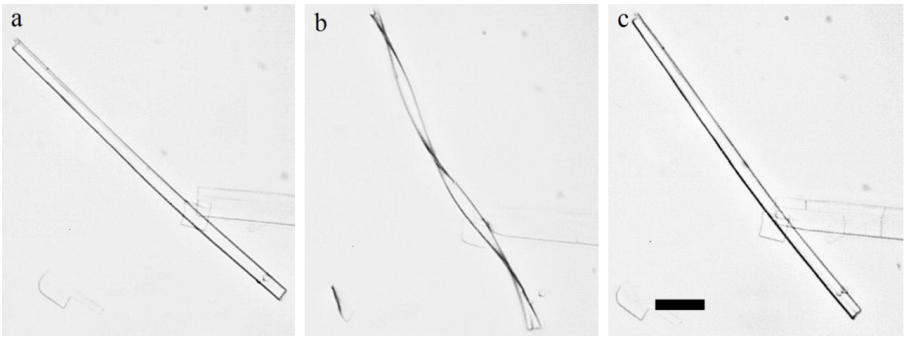

Figure 4. 10 Optical microscopy images of a 9AC ribbon's reversible twisting behavior: **a**) before irradiation; **b**) immediately after irradiation; **c**) 9AC belt recovered after 9 min in the dark; the scale bar is 20μm. Note that the 9AC ribbon on the bottom right of the frame has a larger width and fractures when exposed to the UV light.

4.3.2 Size-dependent Twisting Periods

Larger crystals would often break into segments during this process as shown in Figure 4.11, but ribbons with widths on the order of 20 μm or less were remarkably robust. In general, the twist period (L_{twist} = the distance required for the ribbon to undergo a full 2π rotation) was larger for larger ribbons (Figure 4.12).

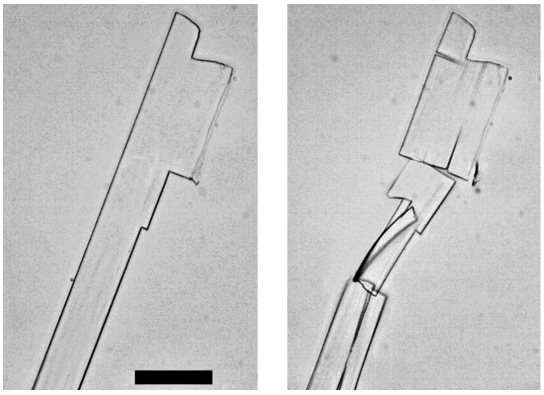

Figure 4. 11 Optical microscopy images of 9AC ribbon's fracture, a) before irradiation; b) the ribbon shatters after irradiation due to the phase seperation. The scale bar is 40 µm.

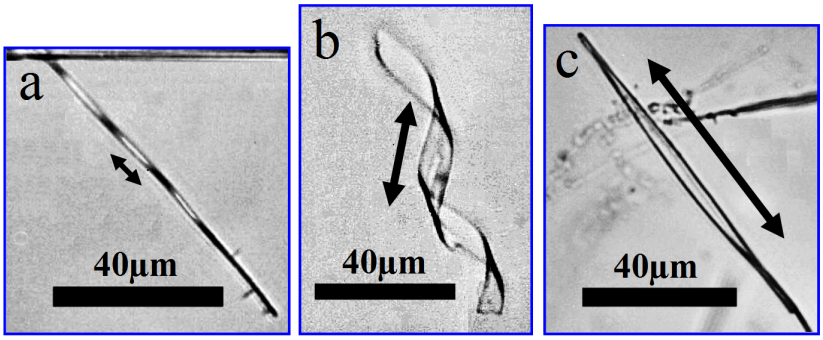

Figure 4. 12 Optical microscopy images of twisted 9AC ribbons with different twisted periods (L_{twist}), Arrows next to the ribbons signify the length of half twisting period (1/2 L_{twist}), the scale bars are 40 µm.

4.3.3 Special Features of Twisting

After the UV light was turned off, the twisted ribbon continued to twist for 2-4 minutes. Eventually, the twisting would stop and then reverse, the ribbon untwisting until it returned to its previous straight shape over the course of 5-15 minutes. This straightening process was 2-4 times slower than the rate of fluorescence recovery and nanorod unbending observed previously in 9AC nanorods.[5, 8] During the relaxation, the twist period changes continuously, as shown in the sequence of images in Figure 4.13.

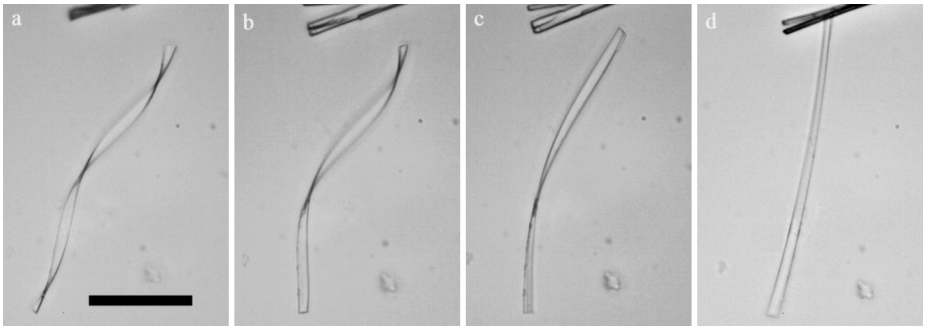

Figure 4. 13 Optical microscopy images of the slow detwisting of 9AC ribbons after the irradiation is turned off. Time interval between images: **a**) immediately after exposure; **b**) 3 min later, **c**) is 4.5 min later; d) 11.5 min later. The scale bar is 50µm.

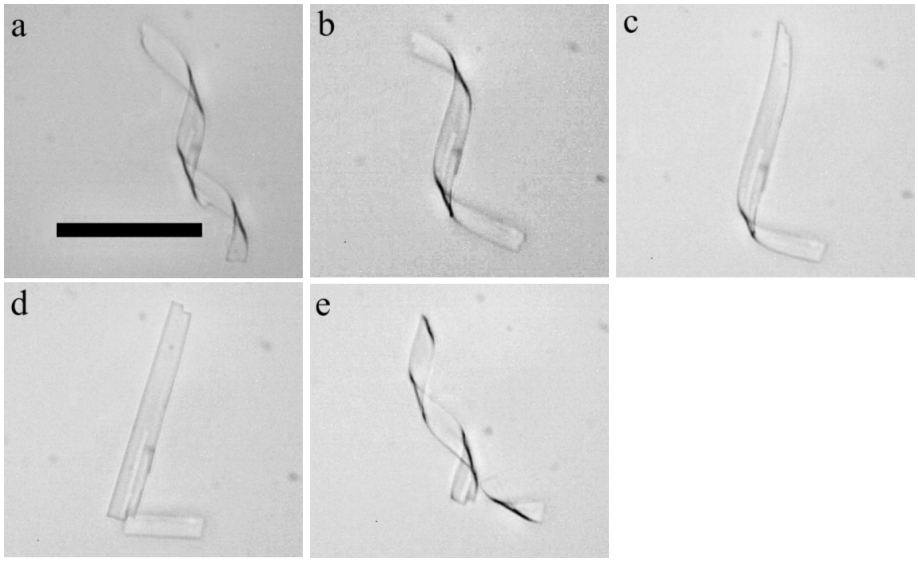

Figure 4. 14 9AC crystal ribbon twists under 440 nm (~20 mW/cm^2) irradiation, relaxes in room light; **a**) immediately after first exposure; **b**) after 2.5 minutes; **c**) after 4 minutes; **d**) after 13 minutes; **e**) immediately after second exposure. Notice that after the second exposure, the 9AC ribbon twists in a different direction compared with first exposure. The scale bar is 50 µm.

After the ribbon had returned to its original shape, the process could be repeated multiple times until the ribbon either broke or photobleached. The direction of each sequential twist for a given ribbon was random after each irradiation period (as illustrated in Figure 4.14). For some ribbons, we observed that prolonged (minutes) light exposure

leads to untwisting instead of a stable twisted structure. The origin of this behavior is discussed below.

4.4 Possible Twisting Mechanisms

4.4.1 Measurements of Twisting Parameters

Quasi-periodic twisting in crystals, as seen in Figures 4.10 and 4.13, can arise from several distinct mechanisms. In order to investigate the mechanism of twisting and the variability in twist period, we used AFM (Atomic Force Microscopy) to measure the cross-sectional profile of ribbons that exhibited twisting. Although we were unable to measure the cross section of a twisted ribbon, we do not expect it to be significantly different from that of the untwisted ribbon, since prior measurements on photoreacted nanorods of 9AC showed less than a 3% change in length and diameter as illustrated in Figure 4.15.[5]

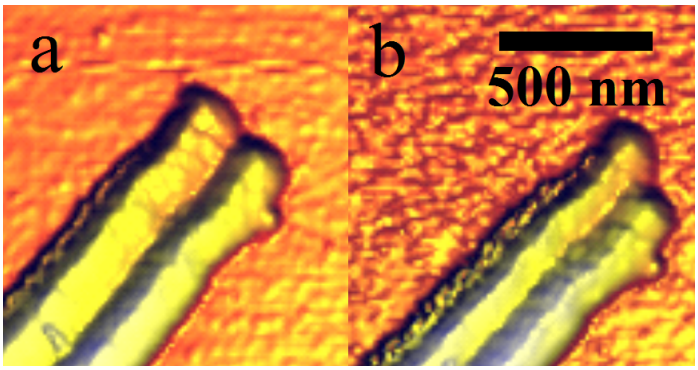

Figure 4. 15 AFM (Atomic Force Microscopy) images of 9AC nanorods **a**) before and **b**) after irradiation, the scale bar is 500 nm. The photoreacted nanorods only showed about 2% change in length and diameter.

In general, the cross section of a ribbon is not a perfect rectangle with well-defined *h* and *w* values. We chose to parameterize the cross section in two ways. First,

we simply integrate over the entire AFM profile to obtain a single quantity, the cross-sectional area *S*, that contains no information about the detailed shape. Second, to take into account the detailed shape of the ribbons, we extracted values for the height *h* and width *w* by defining the profile height at the center of the profile to be *h* and then taking the full width at *h*/2 to be *w*. An example of this measurement is given in Figure 4.16, along with an illustration of how *h*, *w*, and L_{twist} were determined. Note that we were limited in the size range we could examine: larger ribbons tend to fracture under illumination (Figure 4.11), while smaller ones had twist periods that were difficult to resolve using our optical microscopy set-up. Table 4.1 shows all the data extracted from 13 flat ribbons after they relaxed from twisting. Additional details for the ribbons examined by AFM are given in the Appendix.

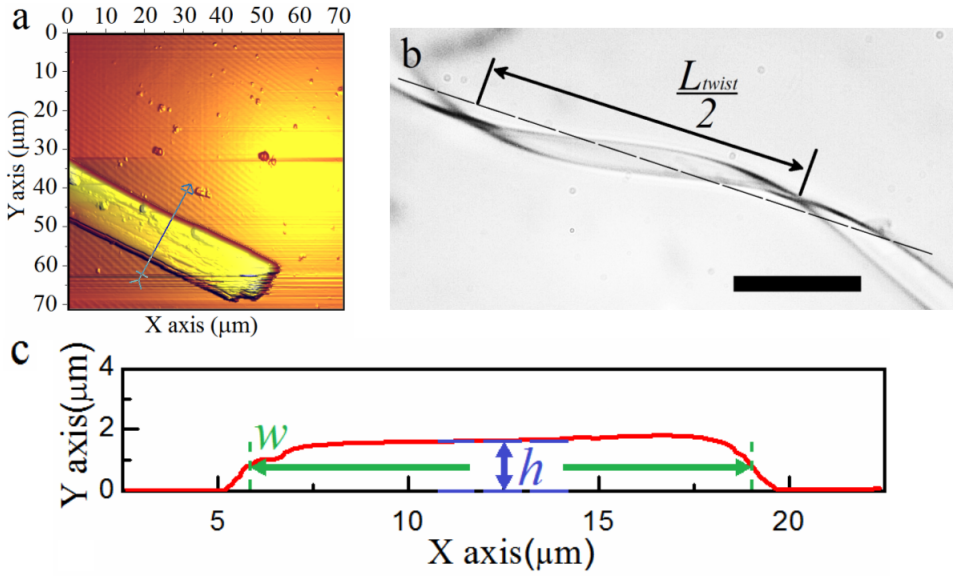

Figure 4. 16 a) AFM (Atomic Force Microscopy) images of 9AC crystalline ribbon; **b**) Optical mcroscopy image of a twisted ribbon, the scale bar is 20 μm; **c**) Scheme to extract height (*h*) and width (*w*) of the ribbon from the AFM profile curve: *h* was extracted from the center profile height; *w* was the full width at half height. The ribbons shown in **a**) and **b**) are different.

Table 4. 1 Profiles of 13 different ribbons

Ribbon #	*h* (μm)	*w* (μm)	*S* (μm^2)	$\sqrt{\frac{J(h,w)}{hw}}$	L_{twist} (μm)
1	0.38	2.72	1.08	0.42	39.4
2	1.29	4.09	5.08	1.33	187.18
3	0.82	3.37	2.47	0.87	33.5
4	1.33	2.62	3.39	1.27	147.78
5	1.42	9.84	13.31	1.56	148.46
6	1.93	4.57	8.74	1.91	177.34
7	0.62	1.67	0.97	0.62	23.64
8	0.51	3.94	2.00	0.56	86.7
9	0.86	2.75	2.4	0.89	27.58
10	1.14	8.76	9.86	1.26	167.48
11	1.11	4.53	5.16	1.18	88.66
12	1.77	7.73	14.59	1.89	153.7
13	1.64	13.01	21.45	1.82	179.32

Table 4.1 Profiles of 13 different ribbons: ***S, h***, ***w, and*** L_{twist} were extracted according to the scheme presented in last paragraph.

4.4.2 Eshelby's Theory

Measurements of *S*, *h*, *w*, and L_{twist} allow us to examine the mechanism of the twisting. Static twisted organic molecular crystals are relatively rare [13-14], and most instances have been interpreted in terms of a theory by Eshelby that explained the twist in terms of a propagating screw dislocation at the center of a crystal rod as illustrated in Figure 4.17.[15-16] Frank showed that if this screw dislocation is larger than a few lattice spacings, a void or pipe must form at the center of the crystal, parallel to the direction of twist propagation along *l*, with a giant Burgers vector associated with it.[17] Both types of screw-dislocation theories are valid for a single-component system and predict that the twist period L_{twist} should depend linearly on the cross-sectional area *S*,

$$L_{twist} = 2\pi k \frac{S}{b} \qquad (1)$$

where k is a constant on the order of unity and b is the magnitude of the Burgers vector associated with the screw dislocation defect.

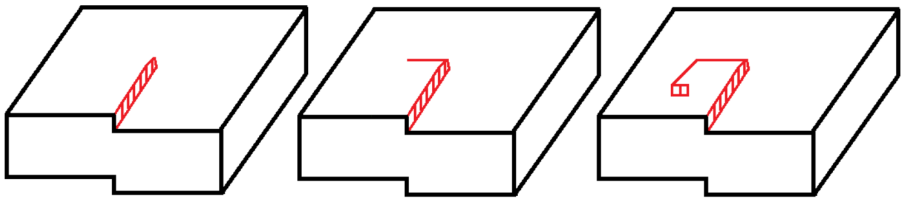

Figure 4. 17 An illustration cartoon showing the propagating screw dislocation at the center of a piece of crystal, which has successfully interpreted the phenomenon of twisted organic molecular crystals formed in the process of crystallization, by Eshelby's theory.

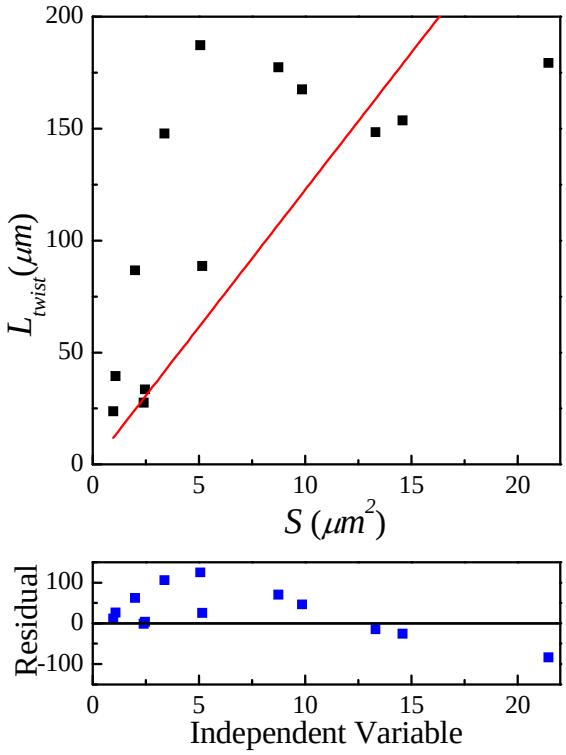

Figure 4. 18 Linear fit of twist period L_{twist} vs. cross-section area (S=hw) according to Eshelby theory as given by Equation (1). The R^2 value is 0.76, slope is 12.

Figure 4.18 shows a fit to our data using Equation (1), yielding a straight line with a slope of 12 and a relatively poor R^2 value of 0.76. It is clear from the residuals in Figure 4.18 that the fit systematically underestimates the amount of twist for smaller cross-section ribbons in particular. If we set k=1, we can extract a value for b=0.51 μm. This large value of b places our microribbons in the Frank regime, but our optical microscopy images provide no evidence for the formation of a void during the crystal twisting process. Given the value of b obtained experimentally, we can estimate the diameter D of the pipe using the following equation [18-19]:

$$D = \frac{Gb^2}{4\pi^2\gamma} \qquad (2)$$

where G is the shear modulus and γ is the surface energy. Typical values for organic molecular crystals are G = 5 GPa [20-21] and γ =0.2 J/m^2 [22-23], leading to a value of D>150 μm for b = 0.51 μm. This value of D is greater than the width of our microribbons. Even given the uncertainties in our estimate of D, any formation of a micron-scale hollow pipe within our ribbons should be easily observable by optical microscopy. The poor quality of the linear fit, coupled with the lack of the void formation necessary to explain the giant b value, suggest that the simple screw dislocation mechanism is not operative in our twisted ribbons.

4.4.3 The Interfacial Strain or 'Heterometry' Model

A second mechanism to explain crystal twisting involves strain energy that builds up due to the interaction between two different chemical species in a single crsytal. This

type of mechanism has been invoked to explain twisting in polymer spherulites [24-26] and is sometimes referred to as "heterometry".[27] The interaction can occur between the host molecule and a chemically distinct impurity, as seen in some minerals [28-29], or between reacted and unreacted forms of the same molecule.[30] We now consider whether chemically reasonable interaction energies can cause the observed twisting of our 9AC microribbons. For a rectangular cross-section ribbon of width *w* and height *h*, the energy density per unit volume *W* required to generate a twist $\left(\frac{\partial\theta}{\partial x}\right)$ (in radians per unit length) is given by [25]

$$W(h,w) = \frac{G \cdot J(h,w)\left(\frac{\partial\theta}{\partial x}\right)^2}{hw} \tag{3}$$

where *G* is the shear modulus and *J(h,w)* is the torsional constant of the ribbon. The function *J(h,w)* is rigorously given by an infinite sum.[25, 31] We found that only the first two terms of the sum had to be retained for an accurate calculation of *J(h,w)* given the range of experimental *h* and *w* values:

$$J(h,w) \cong h^3 w\left[\frac{1}{3} - \frac{64}{\pi^5}\frac{h}{w}\tanh\left[\frac{\pi w}{2h}\right]\right] \tag{4}$$

If we rearrange Equation (3), solve for $\left(\frac{\partial\theta}{\partial x}\right)$, and then integrate over a single period of twist (i.e. $\theta=2\pi$) we obtain an expression for the period L_{twist} as a function of *h* and *w*:

$$L_{twist} = 2\pi\sqrt{\frac{G}{W}}\sqrt{\frac{J(h,w)}{hw}} \tag{5}$$

Both G and W are unknown for the 9AC crystal. If we assume that W attains a maximum value after irradiation and then remains constant, and is the same for all the ribbons (see discussion below), then Equation (5) predicts that a plot of L_{twist} versus $\sqrt{\frac{J(h,w)}{hw}}$ should be linear, as shown in Figure 4.19. The R^2 value for a linear fit to this data is 0.93, significantly better than that obtained using Equation (1). The more uniform scatter of the data points above and below the fit line also results in better residuals and more confidence in this fitting model. The slope and R^2 values are robust with respect to the method used to extract h and w values from the AFM data. With a different scheme to extract h and w, we get almost the same slope (96 vs. 98) and R^2 values (0.93 vs. 0.93). Figure 4.20b shows our second scheme to extract h and w: to take the surface feature into consideration, we extracted values for h by taking average the height values of all the points in between the first inflection point, to the point on the other side of the cross-section with the same height as the first inflection point, and then taking the full width at $h/2$ to be w. The slope of the fit line in Figure 4.19 is 96, which from Equation (5) should equal $2\pi\sqrt{\frac{G}{W}}$. Assuming a typical value of G=5 GPa, and the concentration of 9AC in the crystal as 6.3 M, we obtain W=3.4 kJ/mol at the maximum photoconversion. This calculated energy density W falls within the range expected for noncovalent interactions between different molecules, indicating that this analysis leads to chemically reasonable values. Note that if the calculated value for W had been fallen outside this range, we would have to consider other types of energy contributions in addition to intermolecular interactions.

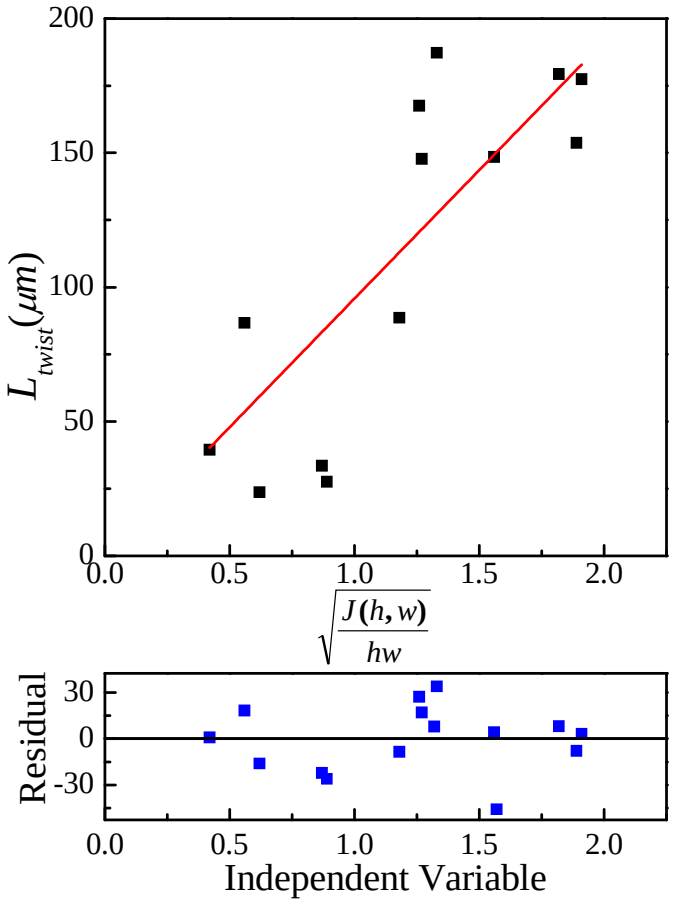

Figure 4. 19 Linear fit of twist period L_{twist} vs. $\sqrt{\frac{J(h,w)}{hw}}$ as given by Equation (5). The R^2 value is 0.93, slope is 96.

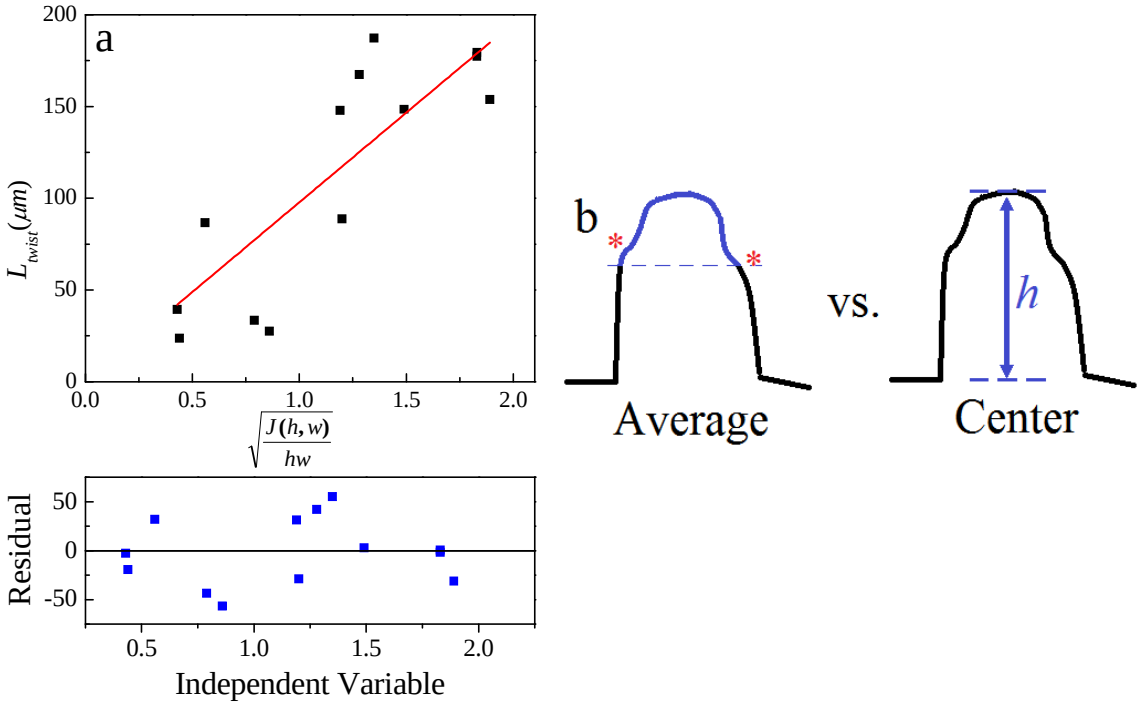

Figure 4. 20 In Figure 4.19, we take *h* to be the height at the center of the image and *w* to be the width at *h*/2. An alternative approach is to find the lowest inflection point on the cross-section, and take average the height values of all the points from this point to the point on the other side of the cross-section with the same height to be *h* and the full width at *h*/2 to be *w*. This procedure is shown in b). When we take this approach to tabulate *h* and *w* values, we can again plot L_{twist} vs. $\sqrt{\frac{J(h,w)}{hw}}$ as given by Equation (5). The R^2 value of this fit is 0.93, with a slope = 98, as compared to the slope = 96 from Figure 4.19.

In previous studies of heterometry-induced twisting, the two different chemical species were supplied by the environment. In our case, second chemical species must be reversibly generated *in situ* by the photochemical reaction. The most logical candidates for the two interacting species are the monomeric and dimeric forms of 9AC. When a dimerization reaction occurs within a stack of monomers, statistical considerations make

it impossible to react 100% of the 9AC molecules, even under continuous illumination. Theoretically, at least 13% of the monomers will be left out of the reaction [32-33], although recent studies indicate that this fraction is closer to 25% for 9AC.[34] This fraction of unreacted 9AC monomers comprises the second species needed to generate strain and drive the twisting without the need for tailored illumination conditions as illustrated in Figure 4.21.

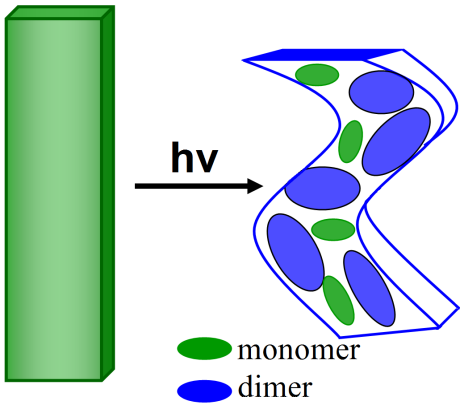

Figure 4. 21 The interfacial strain energy from two different chemical species-photodimers and unreacted monomers-drives the twisting of the crystalline ribbons.

In addition to the better fit to the data in Figure 4.19, there is further evidence for this mechanism. One factor that suggests that the twisting results from dynamic monomer and dimer domain formation is the random twist direction after each irradiation period (Figure 4.14). If the twisting relied on the presence of static structural or chemical defects, then they would be expected to initiate the same twist direction each time, contrary to what is observed. An additional piece of evidence in favor of this mechanism is that the linear slope in Figure 4.19 shows that *W*, the energy density, is the same for all ribbons after prolonged light exposure. If the energy is proportional to the concentration

of the unreacted monomers, then this constant *W* implies a constant fraction of "left-over" monomeric 9AC molecules, as predicted theoretically. If we assume that the interaction energy *W* results from the interaction of 25% of the total monomers (i.e. the minimum number left unreacted), then the actual interaction energy is approximately 13 kJ per mole of unreacted monomer. We may speculate that the strain energy *W* arises from the disruption of the intra-stack hydrogen bond network due to the presence of monomer regions that are not aligned with neighboring dimer stacks. It is important to point out that the photoinduced heterometry mechanism relies on the statistical nature of the 9AC photoreaction that prevents 100% conversion of the monomer into dimers, making the twisting an intrinsic property of the 9AC microribbons.

If we assume that the unreacted monomers are randomly distributed throughout the dimer crystal, they would have to migrate in order to form phase segregated regions that would give rise to the interfacial strain energy. The photodimerization of 9AC is associated with a disorder increase in the lattice[34], which could facilitate such migration. Molecular migration would also explain both the continued twisting that is observed after the light is turned off, and the fact that the shape recovery is slower than the measured time for fluorescence recovery or nanorod unbending in 9AC. However, molecular migration over long distances is difficult in the absence of cooperative effects and would be energetically costly.[35] A second explanation for the delayed response is that localized regions of monomers and dimers are formed during the photoreaction by exciton trapping at defect sites or stress points.[36-37] In this scenario, the time-lag between the light exposure and the completion of the physical motion would be a mechanical effect

resulting from slow lattice relaxation rather than molecular migration. The relative importance of molecular translation as opposed to larger scale mechanical effects in the crystal for determining the overall time response of the twisting remains to be determined.

4.4.4 Comparison with Previous Work of Nanorods

Lastly, we contrast the ribbon twisting described in this Chapter with the nanorod bending observed in our previous work. Previously, we have observed reversible bending for 9AC nanorods using spatially localized one-photon[5] and two-photon excitation.[8] We attributed the bending to local strain created at the interface between reacted and unreacted crystal regions along the nanorods as shown in Figure 4.22.

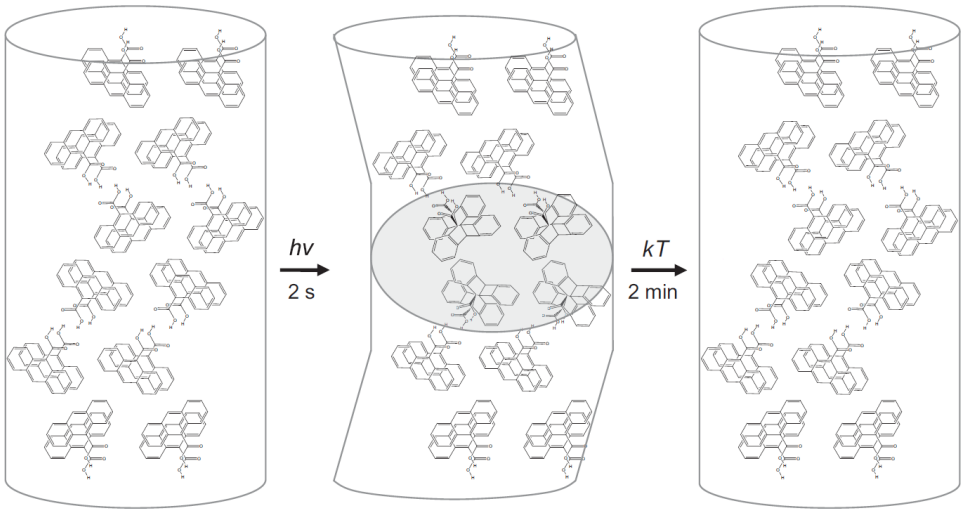

Figure 4. 22 Schematic illustrating 9AC nanorod's expansion. The darkened oval indicates the region consists of photodimer from irradiation, and local strain created at the interface between photodimer and unreacted monomer caused the nanorod to bend. [8]

When the rods were uniformly illuminated, no interfaces were created and no bending was observed, only a slight expansion (Figure 4.15).[5] At first glance, the twisting seen here appears to be different from the bending observed earlier. But Eshelby realized that a bend can be thought of as a partial twist.[15] Indeed, illumination of a short segment of a ribbon gives rise to a partial twist that looks like a bend. Direct comparison of the two morphologies is complicated by their different crystal orientations (the long axis of the rods corresponds to the crystal *c*-axis, which is perpendicular to the long axis of the ribbons as shown in Figure 4.23) and different aspect ratios (*h* and *w* are approximately equal for the cylindrical nanorods as opposed to *w*/*h*>2 for the microribbons). Nevertheless, it is likely that the same physical process underlies both types of motion.

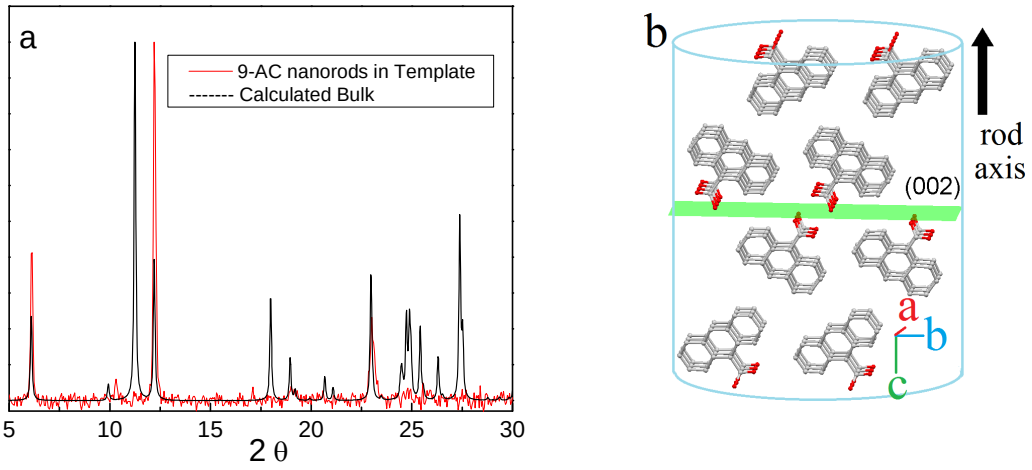

Figure 4. 23 a) Powder X-ray diffraction patterns: (**black**) calculated pattern of monoclinic 9AC; (**red**) experimental pattern of 9AC nanorods aligned within the AAO template, with the two peaks corresponding to parallel planes (002) and (004) being most prominent; **b**) crystal orientations of 9AC molecules within the nanorods, with the rod axis parallel to the c-axis of the unit cell. This is perpendicular to the long axis *l* of the microribbons.

4.5 Conclusions

The data in this Chapter demonstrate a new mode of reversible photomechanical deformation in molecular crystals. Microribbons consisting of oriented 9AC crystals undergo reversible twisting motions without the need for specialized irradiation conditions, like focused light or controlled polarization. The time-dependent relaxation of the twist period and its dependence on the cross-sectional dimensions of the ribbon are both consistent with a mechanism based on internal strain generated by the coexistence of regions composed of dimeric and monomeric 9AC. The twisting motion is specific to a single crystal morphology and size range: if the cross-sectional area of a ribbon is too large, it will fracture rather than twist. Since the twisting is an intrinsic crystal property, it should be manifested by much smaller structures that share the same ribbon morphology. It should also be insensitive to the illumination conditions as long as photons can reach the crystal and induce the [4+4] photocyclization reaction. This work provides a further illustration of the surprising versatility of molecular crystals as photoresponsive systems, and suggests that control of molecular crystal shape and size may prove to be a fruitful way to design systems with improved photomechanical properties.

References

1. Ballardini, R.; Balzani, V.; Credi, A.; Gandolfi, M. T.; Venturi, M., Artificial molecular-level machines: which energy to make them work? *Acc. Chem. Res.* **2001,** *34*, 445-455.
2. Keating, A. E.; Garcia-Garibay, M. A., Photochemical solid-to-solid reactions. In *Organic and Inorganic Photochemistry*, Ramamurthy, V.; Schanze, K. S., Eds. Marcel Dekker: New York, 1998.
3. Bucar, D. K.; MacGillivray, L. R., Preparation and reactivity of nanocrystalline cocrystals formed via sonocrystallization. *J. Am. Chem. Soc.* **2007,** *129*, 32-33.
4. Takahashi, S.; Miura, H.; Kasai, H.; Okada, S.; Oikawa, H.; Nakanishi, H., Single-crystal-to-single-crystal transformation of diolefin derivatives in nanocrystals. *J. Am. Chem. Soc.* **2002,** *124*, 10944-10945.
5. Al-Kaysi, R. O.; Bardeen, C. J., Reversible photoinduced shape changes of crystalline organic nanorods. *Adv. Mater.* **2007,** *19*, 1276-1280.
6. Al-Kaysi, R. O.; Dillon, R. J.; Zhu, L.; Bardeen, C. J., Template assisted synthesis of silica-coated molecular crystal nanorods: from hydrophobic to hydrophilic nanorods. *J. Colloid. Interfac. Sci.* **2008,** *327*, 102-107.
7. Al-Kaysi, R. O.; Muller, A. M.; Bardeen, C. J., Photochemically driven shape changes of crystalline organic nanorods. *J. Am. Chem. Soc.* **2006,** *128*, 15938-15939.
8. Good, J. T.; Burdett, J. J.; Bardeen, C. J., Using two-photon excitation to control bending motions in molecular-crystal nanorods. *Small* **2009,** *5*, 2902-2909.
9. Ito, Y.; Fujita, H., Formation of an unstable photodimer from 9-anthracene carboxylic acid in the solid-state. *J. Org. Chem.* **1996,** *61*, 5677-5680.
10. Dunn, M. L., Photomechanics of mono- and polydomain liquid crystal elastomer films. *J. Appl. Phys.* **2007,** *102*, 013506/1-013506/7.
11. Warner, M.; Mahadevan, L., Photoinduced deformations of beams, plates and films. *Phys. Rev. Lett.* **2004,** *92*, 134302/1-134302/4.
12. Heller, E.; Schmidt, G. M. J., Topochemistry. Part XXXIII. The solid-state photochemistry of some anthracene derivatives. *Isr. J. Chem.* **1971,** *9*, 449-462.
13. McClellan, A. L., On twisted organic crystals. *J. Chem. Phys.* **1960,** *32*, 1271-1272.
14. Kawabata, K.; Kumagai, T.; Mizutani, M.; Sambongi, T., Twist morphology of organic crystal (BPE-DMB)IBr_2. *J. Phys. I France* **1996,** *6*, 1575-1580.
15. Eshelby, J. D., Screw dislocations in thin rods. *J. Appl. Phys.* **1953,** *24*, 176-179.
16. Schultz, J. M.; Kinloch, D. R., Transverse screw dislocations: a source of twist in crystalline polymer ribbons. *Polymer* **1969,** *10*, 271-278.
17. Frank, F. C., Capillary equilibria of dislocated crystals. *Acta Cryst.* **1951,** *4*, 497-501.
18. Si, W.; Dudley, M.; Glass, R.; Tsvetkov, V.; Carter, C., Holloe-core screw dislocations in 6H-SiC single crystals: a test of Frank's theory. *J. Elect. Materl* **1997,** *26*, 128-133.
19. Jacobs, B. W.; Crimp, M. A.; McElroy, K.; Ayres, V. M., Nanopipes in Gallium Nitride nanowires and rods. *Nano Lett.* **2008,** *8*, 4353-4358.

20. Capaldi, F. M.; Boyce, M. C.; Rutledge, G. C., The mechanical properties of crystalline cyclopentyl polyhedral oligomeric silsesquioxane. *J. Chem. Phys.* **2006,** *124*, 214709/1-214709/4.
21. Roberts, R. J.; Rowe, R. C.; York, P., The relationship between Young's modulus of elasticity of organic solids and their molecular structure. *Powder Tech.* **1991,** *65*, 139-146.
22. Engkvist, O.; Price, S. L.; Stone, A. J., Developments in computational studies of crystallization and morphology applied to urea. *Phys. Chem. Chem. Phys.* **2000,** *2*, 3017-3027.
23. Nabok, D.; Puschnig, P.; Ambrosch-Draxl, C., Cohesive and surface energies of pi-conjugated organic molecular crystals: a first-principles study. *Phys. Rev. B* **2008,** *77*, 245316/1-245316/4.
24. Calvert, P. D.; Uhlmann, D. R., Surface stresses and crystal twisting in hippuric acid and in polymers. *J. Polym. Sci.* **1973,** *11*, 457-465.
25. Schultz, J. M., Self-induced field model for crystal twisting in spherulites. *Polymer* **2003,** *44*, 433-441.
26. Lotz, B.; Cheng, S. Z. D., A critical assessment of unbalanced surface stresses as the mechanical origin of twisting and scrolling of polymer crystals. *Polymer* **2005,** *46*, 577-610.
27. Shtukenberg, A.; Punin, Y., *Optically Anomalous Crystals*. Springer: Dordrecht, Netherlands, 2007.
28. Wang, Y.; Merino, E., Origin of fibrosity and banding in agates from flood basalts. *Am. J. Science* **1995,** *295*, 49-77.
29. Comer, J.; Ortoleva, P., Coexistence of twisted and untwisted crystals: an impurity/structural order model with implications for agate patterns. *Am. Mineralogist* **2007,** *92*, 1952-1957.
30. Shtukenberg, A. G.; Freudenthal, J.; Kahr, B., Reversible twisting during helical hippuric acid crystal growth. *J. Am. Chem. Soc.* **2010,** *132*, 9341-9349.
31. Barber, J. R., *Elasticity*. KIuwer: Dordrecht, Netherlands, 2002.
32. Cohen, E. R.; Reiss, H., Kinetics of reactant isolation. I. One-dimensional problems. *J. Chem. Phys.* **1963,** *38*, 680-691.
33. Even, J.; Bertault, M., Monte-Carlo simulations of chemical reactions in molecular crystals. *J. Chem. Phys.* **1999,** *110*, 1087-1096.
34. More, R.; Busse, G.; Hallmann, J.; Paulmann, C.; Scholz, M.; Techert, S., Photodimerization of crystalline 9-anthracene carboxylic acid: a nontopotactic autocatalytic transformation. *J. Phys. Chem. C* **2010,** *114*, 4142-4148.
35. Atwood, J. L.; Barbour, L. J.; Jerga, A.; Schottel, B. L., Guest transport in a nonporous organic solid via dynamic van der Waals cooperativity. *Science* **2002,** *298*, 1000-1002.
36. Schipper, P. E.; Walmsley, S. H., On the role of exciton trapping at extended defects in the photodimerization of anthracene. *Proc. Royal. Soc. London A* **1976,** *348*, 203-219.
37. Suzuki, M.; Iida, T.; Nasu, K., Relaxation of exciton and photoinduced dimerization in crystalline C60. *Phys. Rev. B* **2000,** *61*, 2188-2198.

Chapter 5 Crystal Structures and Photophysical Properties of 9-anthracene carboxylic acid derivatives for photomechanical applications

5.1 Introduction

As we mentioned in last Chapter, for a material to have potential as an actuator, the photochemical reaction should be reversible, either by ambient thermal fluctuations or by exposure to a different wavelength of light. The molecule 9-anthracene carboxylic acid (9AC), which crystallizes in an unusual head-to-head conformation driven by hydrogen bonding, forms a metastable photodimer that spontaneously dissociates back into its constituent monomers. [1] Using this molecule, we have demonstrated in our previous work the controlled bending of crystalline nanorods [2-4] and in the last Chapter the twisting of microribbons [5], where both types of motion spontaneously reverse over the course of minutes. Although this type of reversibility is robust and can be used for multiple cycles of light-induced shape changes, we became interested in whether we could develop systems with improved photomechanical responses. In particular, we wanted to decrease the recovery time of the actuator by accelerating the dissociation of the photodimer. We hypothesized that one way to accomplish this would be to modify the chemical substituents at the 9 or 10 position of the anthracene ring, thereby increasing the steric repulsion between the two halves of the photodimer.

In this Chapter, we report the synthesis and characterization of a series of 9AC derivatives in both solution and in the solid-state. The seven compounds that are the subject of this paper are shown in Scheme 5.1.

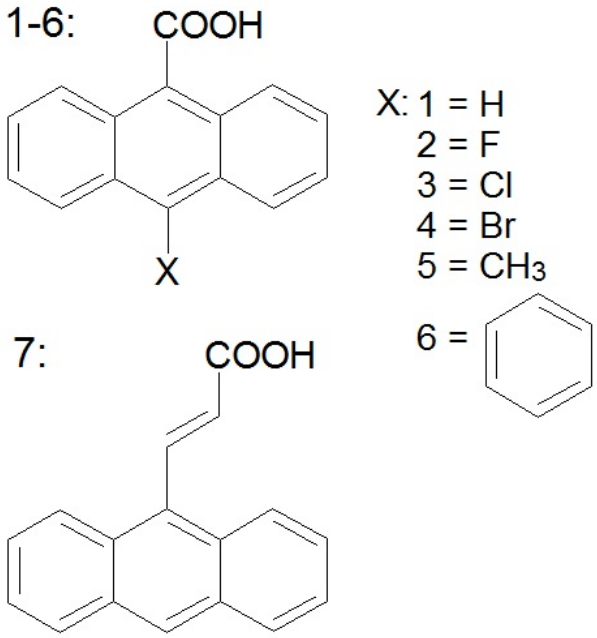

Scheme 5. 1 9-anthracene carboxylic acid derivatives **1-7**

Compounds **1-6** represent an attempt to explore how substitution at the 10-position opposite the COOH group influences both crystal packing and chemical reactivity. Compound **7** is an attempt to modify the COOH attachment at the 9-position. In all cases, we find that the hydrogen-bonding of the COOH groups plays an important role in determining the crystal packing, but that the crystal structures still vary quite a bit once the 10-position substituent becomes more complicated than a single atom. For the single atom series **1**-**4**, we find that only H and F substituents at the 10-position result in photochemically reactive solids, while larger atoms or molecular substituents appear to prevent the dimerization reaction altogether. If we leave the 10-position alone and modify the 9-position (compound **7**), photoreactivity is retained but reversibility is lost. Thus although it is possible to tune the solid-state reactivity of 9AC somewhat through

chemical substitution, unsubstituted 9AC still appears to be the best photomechanical material in terms of reactivity, ease of growth, and reversibility.

5.2 Crystal Structures of 1-7

5.2.1 Crystal Data and Structure Refinements for 1-7

The synthesis of molecules **1-7** followed standard literature procedures for analogous anthracene derivatives, and the details are provided in Chapter 2. After the molecules had been synthesized and purified, we had to grow crystals suitable for structure determination by XRD. For some molecules (**1**, **5**) this could be accomplished using standard solution-based crystal growth techniques. For the other derivatives (**2-4, 6, 7**), however, solution growth yielded dendritic crystals or crystals with high concentrations of defects. For these molecules, we used a modified sublimation procedure to obtain crystals large enough for single crystal XRD measurements. In all cases, we succeeded in obtaining good quality single crystal structures consistent with our expectations of the 9AC motif. The single crystal XRD parameters and crystal structure data for all 7 crystal structures determined in this work are summarized in Table 5.1. For 9AC **1**, only the triclinic form is included in Table 5.1. We used the monoclinic form from the CCDC database.

Table 5. 1 Crystal data and structure refinement for 1 triclinic

Empirical formula	C_{15} H_{10} O_2 (**1** triclinic)
Formula weight	222.23
Temperature	296(2) K
Wavelength	0.71073 Å
Crystal system	Triclinic
Space group	P-1
Unit cell dimensions	a = 3.8896(19) Å α= 101.784(7)°
	b = 9.384(5) Å β= 95.457(7)°
	c = 14.852(7) Å γ = 90.220(7)°
Volume	528.1(4) $Å^3$
Z	2
Density (calculated)	1.398 Mg/m^3
Absorption coefficient	0.092 mm^{-1}
F(000)	232
Crystal size	0.50 x 0.15 x 0.03 mm^3
Theta range for data collection	2.22 to 25.02°.
Index ranges	-4<=h<=4, -11<=k<=11, -16<=l<=17
Reflections collected	4510
Independent reflections	1849 [R(int) = 0.0404]
Completeness to theta = 29.13°	98.7 %
Absorption correction	Semi-empirical from equivalents
Max. and min. transmission	0.9974 and 0.9557
Refinement method	Full-matrix least-squares on F2
Data / restraints / parameters	1849 / 0 / 157
Goodness-of-fit on F2	1.095
Final R indices [I>2sigma(I)]	R1 = 0.0882, wR2 = 0.2265
R indices (all data)	R1 = 0.1109, wR2 = 0.2399
Largest diff. peak and hole	0.347 and -0.256 $e.Å^{-3}$

Table 5. 2 Crystal data and structure refinement for 2-4

Empirical formula	C_{15} H_9 $Br_{0.05}$ $F_{0.95}$ O_2 (**2**)	C_{15} H_9 Cl O_2 (**3**)	C_{15} H_9 Br O_2 (**4**)
Formula weight	243.27	256.67	301.13
Temperature	100(2) K	100(2) K	100(2) K
Wavelength	0.71073 Å	0.71073 Å	0.71073 Å
Crystal system	Monoclinic	Monoclinic	Monoclinic
Space group	P2(1)/c (#14)	P2(1)	P2(1)/c (#14)
Unit cell dimensions	a = 9.2885(14) Å α= 90°	a = 3.8116(7) Å α= 90°	a = 9.2037(6) Å α= 90°
	b = 3.7650(6) Å β= 97.517(3)°	b = 31.453(6) Å β= 90.463(3)°	b = 3.8638(3) Å β= 96.7531(10)°
	c = 30.373(5) Å γ = 90°	c = 9.2257(18) Å γ= 90°	c = 31.580(2) Å γ = 90°
Volume	1053.1(3) $Å^3$	1106.0(4) $Å^3$	1115.22(14) $Å^3$
Z	4	4	4
Density (calculated)	1.534 Mg/m^3	1.541 Mg/m^3	1.794 Mg/m^3
Absorption coefficient	0.301 mm^{-1}	0.333 mm^{-1}	3.674 mm^{-1}
F(000)	501	528	600
Crystal size	0.55 x 0.08 x 0.02 mm^3	0.54 x 0.17 x 0.03 mm^3	0.51 x 0.20 x 0.03 mm^3
θ range for data collection	2.21 to 29.13°.	2.21 to 28.70°.	2.23 to 29.57°.
Index ranges	-12<=h<=12, -5<=k<=5, -41<=l<=41	-5<=h<=5, -42<=k<=42, -12<=l<=12	-12<=h<=12, -5<=k<=5, -43<=l<=43
Reflections collected	21009	22556	22753
Independent reflections	2827 [R(int) = 0.0716]	5699 [R(int) = 0.0579]	3135 [R(int) = 0.0390]
Completeness to θ = 29.13°	99.9 %	99.9 %	99.9 %
Absorption correction	Semi-empirical from equivalents	Semi-empirical from equivalents	Semi-empirical from equivalents
Max. and min. transmission	0.9934 and 0.8518	0.9891 and 0.8416	0.9138 and 0.2579
Refinement method	Full-matrix least-squares on F^2	Full-matrix least-squares on F^2	Full-matrix least-squares on F^2
Data / restraints / parameters	2827 / 0 / 170	5699 / 1 / 331	3135 / 0 / 167
Goodness-of-fit on F2	1.083	1.042	1.351
Final R indices [I>2sigma(I)]	R1 = 0.0703, wR2 = 0.1910	R1 = 0.0503, wR2 = 0.1268	R1 = 0.0543, wR2 = 0.1153
R indices (all data)	R1 = 0.0920, wR2 = 0.2078	R1 = 0.0561, wR2 = 0.1313	R1 = 0.0584, wR2 = 0.1166
Largest diff. peak and hole	0.617 and -0.346 $e.Å^{-3}$	0.460 and -0.470 $e.Å^{-3}$	1.008 and -3.260 $e.Å^{-3}$

Table 5. 3 Crystal data and structure refinement for 5-7

Empirical formula	C16 H12 O2 (**5**)	C21 H14 O2 (**6**)	C17 H12 O2 (**7**)
Formula weight	236.26	298.32	248.27
Temperature	296(2) K	100(2) K	296(2) K
Wavelength	0.71073 Å	0.71073 Å	0.71073 Å
Crystal system	Monoclinic	Orthorhombic	Monoclinic
Space group	P2(1)/c (#14)	Pbca (#61)	P2(1)/c (#14)
Unit cell dimensions	a = 8.5743(3) Å α= 90°	a = 7.1691(5) Å α= 90°	a = 3.8919(4) Å α= 90°
	b = 8.2539(3) Å β= 94.9243(5)°	b = 13.5819(10) Å β= 90°	b = 16.5883(15) Å β= 93.7657(14)°
	c = 16.4805(6) Å γ = 90°	c = 30.767(2) Å γ = 90°	c = 19.0073(17) Å γ = 90°
Volume	1162.04(7) $Å^3$	2995.8(4) $Å^3$	1224.5(2) $Å^3$
Z	4	8	4
Density (calculated)	1.350 Mg/m^3	1.323 Mg/m^3	1.347 Mg/m^3
Absorption coefficient	0.088 mm^{-1}	0.084 mm^{-1}	0.088 mm^{-1}
F(000)	496	1248	520
Crystal size	0.44 x 0.42 x 0.18 mm3	0.58 x 0.07 x 0.04 mm3	0.54 x 0.07 x 0.05 mm3
θ range for data collection	2.38 to 29.13°.	2.65 to 25.67°.	1.63 to 28.70°.
Index ranges	-11<=h<=11, -11<=k<=11, -22<=l<=22	-8<=h<=8, -16<=k<=16, -37<=l<=36	-5<=h<=5, -22<=k<=22, -25<=l<=25
Reflections collected	16250	46262	16995
Independent reflections	3129 [R(int) = 0.0152]	2848 [R(int) = 0.0844]	3162 [R(int) = 0.0353]
Completeness to θ = 29.13°	100.0 %	100.0 %	100.0 %
Absorption correction	Semi-empirical from equivalents	Semi-empirical from equivalents	Semi-empirical from equivalents
Max. and min. transmission	0.9842 and 0.9623	0.9966 and 0.9527	0.9955 and 0.9542
Refinement method	Full-matrix least-squares on F_2	Full-matrix least-squares on F_2	Full-matrix least-squares on F_2
Data / restraints / parameters	3129 / 0 / 167	2848 / 0 / 210	3162 / 0 / 175
Goodness-of-fit on F_2	1.057	1.106	1.003
Final R indices [I>2sigma(I)]	R1 = 0.0467, wR2 = 0.1405	R1 = 0.0518, wR2 = 0.1243	R1 = 0.0418, wR2 = 0.0988
R indices (all data)	R1 = 0.0532, wR2 = 0.1497	R1 = 0.0731, wR2 = 0.1383	R1 = 0.0787, wR2 = 0.1201
Largest diff. peak and hole	0.317 and -0.228 $e.Å^{-3}$	0.268 and -0.268 $e.Å^{-3}$	0.221 and -0.231 $e.Å^{-3}$

5.2.2 Solid-state Photoreactivity of Anthracenecarboxylic Acids

We began our investigation of anthracene carboxylic acid derivatives by exploring the effect of COOH substitution at different points on the anthracene ring. We obtained crystals of anthracene derivatives with the carboxylic acid group located at the 1 and 2 positions, but neither of these crystals showed any reactivity when exposed to 365 nm radiation. The crystal structure of 1-anthracene carboxylic acid shows that the anthracene rings arrange themselves into an offset herringbone pair motif as shown in Figure 5.1. [6-7] The anthracenes form interleaved planar two-dimensional hydrogen bond networks, where the reactive anthracene rings are offset from each other. For a given pair of parallel anthracene rings, the central carbons are more than 6 Å apart, too far to permit the [4+4] photocyclization to occur.

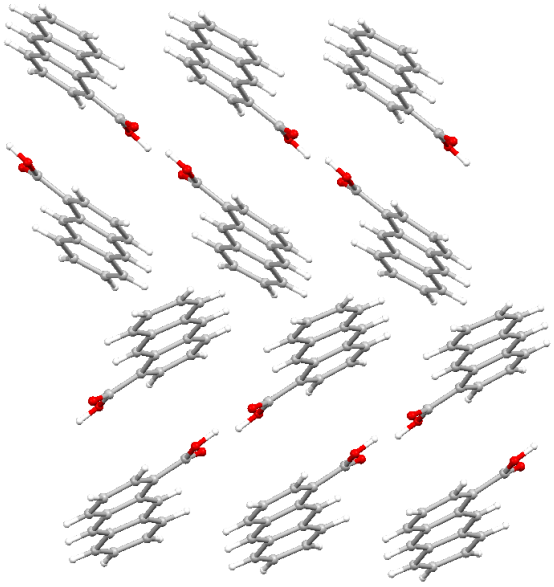

Figure 5. 1 Crystal structures and packing of 1-anthracene carboxylic acid (1AC), adjacent 1AC pairs are offset and the hydrogen bonding keeps them from shifting closer to react.

Using molecular mechanics simulations, we found that when the COOH group is placed at any point other than the 9-position on the anthracene ring, there is less steric interaction from the surrounding hydrogens and the COOH group can become almost coplanar with the anthracene ring. This permits the type of planar networks seen in the 1-anthracene carboxylic acid crystal. We were unable to grow crystals of 2-anthracene carboxylic acid suitable for x-ray structure determination. Given the empirical fact that only the 9-substituted member of this family appears to be photoreactive, we decided to investigate its derivatives in more detail.

5.2.3 Structural Comparisons between Monoclinic and Triclinic 9AC (1)

In contrast to the molecules described above, interactions with hydrogens at the 1 and 8 positions force the COOH group to rotate ~55° out of plane in 9AC (**1**). This rotation prevents formation of the planar two-dimensional crystal networks seen in 1-anthracene carboxylic acid. 9AC can crystallize in two polymorphs: monoclinic [8-9] and triclinic. [10] Figure 5.2a and 5.2b show the powder X-ray diffraction patterns of triclinic form and the monoclinic form of 9AC (**1**). Using powder XRD, we found that many solution-grown crystals contain both forms in varying amounts. The powder pattern in Figure 5.2c is from the bulk crystals of 9AC (**1**) grown from THF in room temperature; and Figure 5.2d shows the powder pattern of the bulk crystals of 9AC (1) grown from annealing in ethanol at 73 ºC. Both of them are mixtures of both polymorphs. Our earlier powder XRD measurements of nanorods grown from THF also contain peaks due to both monoclinic and triclinic forms.[3]

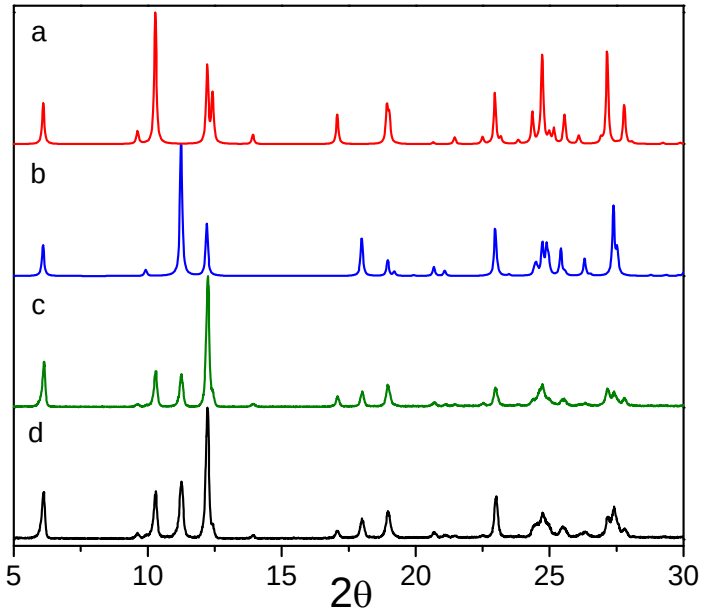

Figure 5. 2 Powder X-ray diffraction patterns of 9AC (**1**): **a**) triclinic polymorph; **b**) monoclinic polymorph; **c**) bulk crystals grown from THF in room temperature, contains peaks from both monoclinic and triclinic polymorphs; **d**) bulk crystals grown from annealing in ethanol at 73 ºC, also contains peaks from both monoclinic and triclinic polymorphs.

After some trial-and-error, we found that pure triclinic crystals could be grown using xylenes, while pure monoclinic crystals could be grown from ethyl acetate. The detailed structure of the monoclinic polymorph can be found in the Cambridge Database and is illustrated in Figures 5.3a and 5.3b. The crystal structure of the triclinic form is presented in this paper for the first time and is shown in Figures 5.3c and 5.3d. In both crystals, the 9AC molecules stack on top of each other, as shown in Figure 5.3b and 5.3d. The rotated COOH groups can participate in hydrogen bonding with molecules in neighboring stacks, resulting in hydrogen bonded stack pairs rather than the offset

herringbone pairs formed by anthracenes with coplanar COOH groups. It is these stacked 9AC molecules that provide the correct orientation and distance for the [4+4] photodimerization to take place.

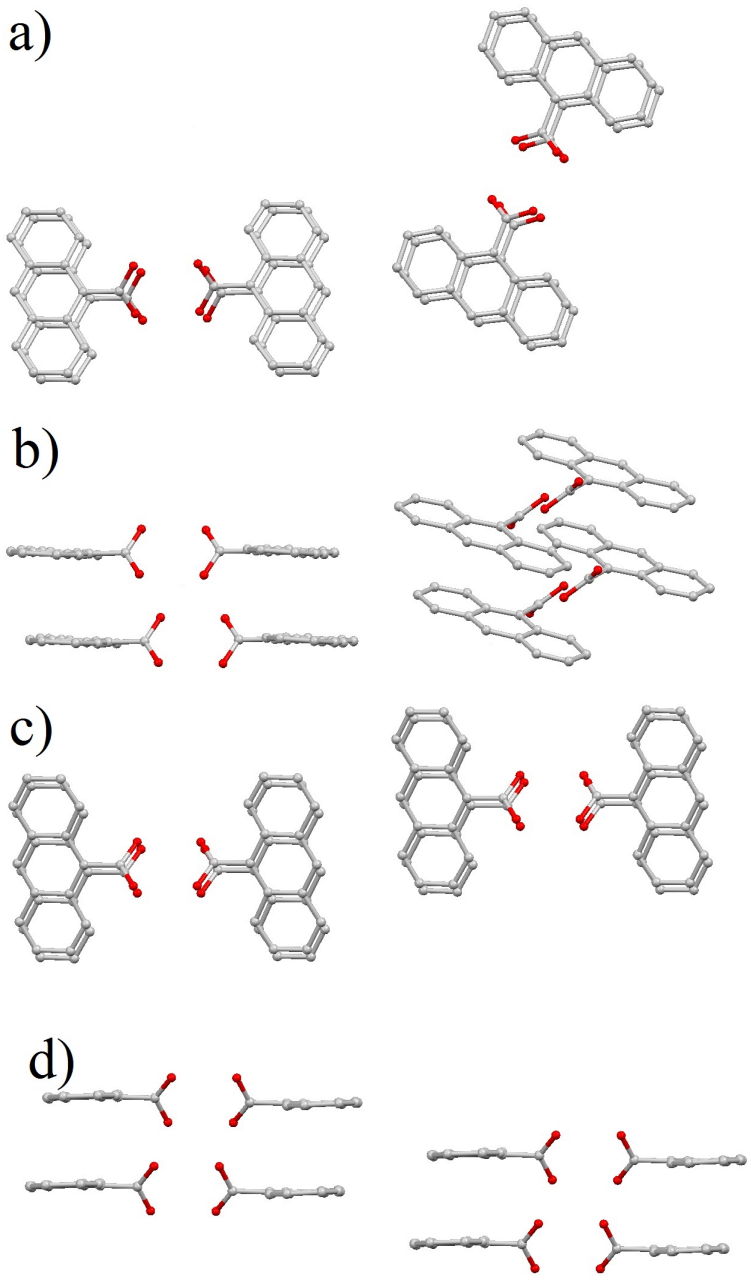

Figure 5. 3 Crystal structures and packing of **a**) top view of monoclinic **1** (9-anthracenecarboxylic acid); **b**) side view of monoclinic **1**; **c**) top view of triclinic **1**; **d**) side view of triclinic **1**.

Despite the similarities, there are two significant differences between the two polymorphs, which are highlighted in Figure 5.3. In the monoclinic form, neighboring pair stacks are rotated by 62.7° when viewed from the top (Figure 5.3a), and these stacks also form a 23.2° angle when the stack axes are compared (Figure 5.3b). In contrast, neighboring pair stacks in the triclinic form are completely parallel to each other, both when viewed from the top and when viewed from the side, as shown in Figure 5.3c and 5.3d. It is doubtful that these differences in packing change the photochemistry of individual anthracene pairs, since the distances between adjacent anthracenes, which participate in the [4+4] photodimerization, are the same in both crystal polymorphs at 3.9 Å. The presence of two different polymorphs may help explain the variability seen in the photoresponse of nanorods of **1** grown in THF[4], where both polymorphs are possible.

5.2.4 Crystal Packing Motifs of 2-7

Since placing the COOH group at the 9-position is vital for making a reactive crystal, we reasoned that modifying the reactivity of the crystal would require substitution at other positions around the anthracene ring. Changing the chemical group at the 10-position exactly opposite the COOH is a synthetically tractable approach that provides an opportunity to modify the steric properties of the molecule without dramatically changing its electronic properties. One of our hopes was that by placing a bulkier group at the 10-position, we could further destabilize the photodimer and decrease its dissociation time. When the hydrogen at the 10-position is replaced with a halogen atom (F, Cl, Br), the distance between the anthracenes changes by less than 3.5%

relative to **1**. The major change in the crystal packing involves the relative tilt angles of neighboring stacks, as shown in Figures 5.4 and 5.5. Whereas in triclinic **1** the H-bonded pair stacks line up parallel to each other, in **2-4** the packing is more similar to monoclinic **1**, with the pair stacks are tilted vertically with respect to each other (Figures 5.4a-c). This is true whether or not the top view shows the anthracene stacks rotated from each other.

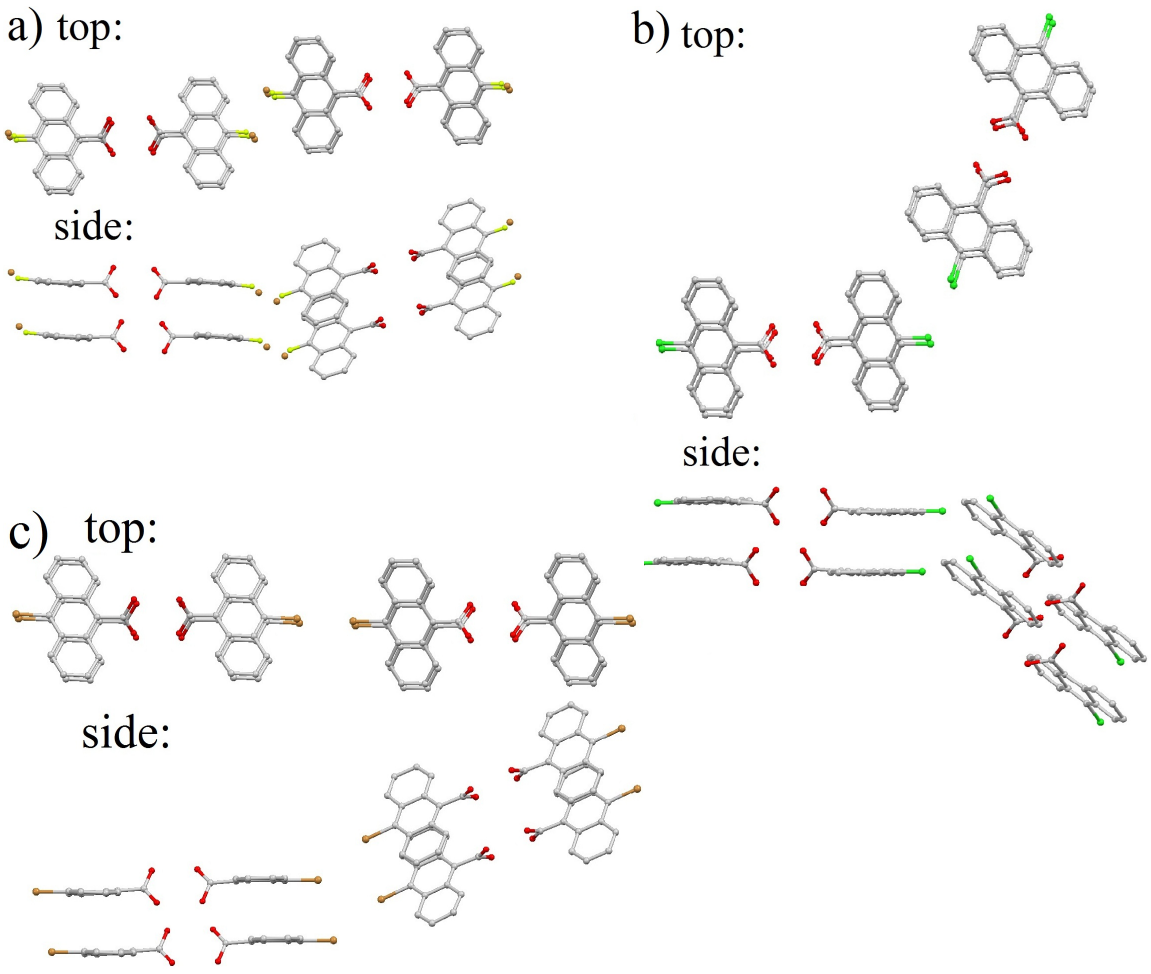

Figure 5. 4 Top and side views of crystal structures of anthracene carboxylic acid derivatives: **a**) 10-fluoro-9-anthracenecarboxylic acid **2** (with 5% disorder of 10-bromo-9-anthracenecarboxylic acid **4**); **b**) 10-chloro-9-anthracenecarboxylic acid **3**; **c**) 10-bromo-9-anthracenecarboxylic acid **4**.

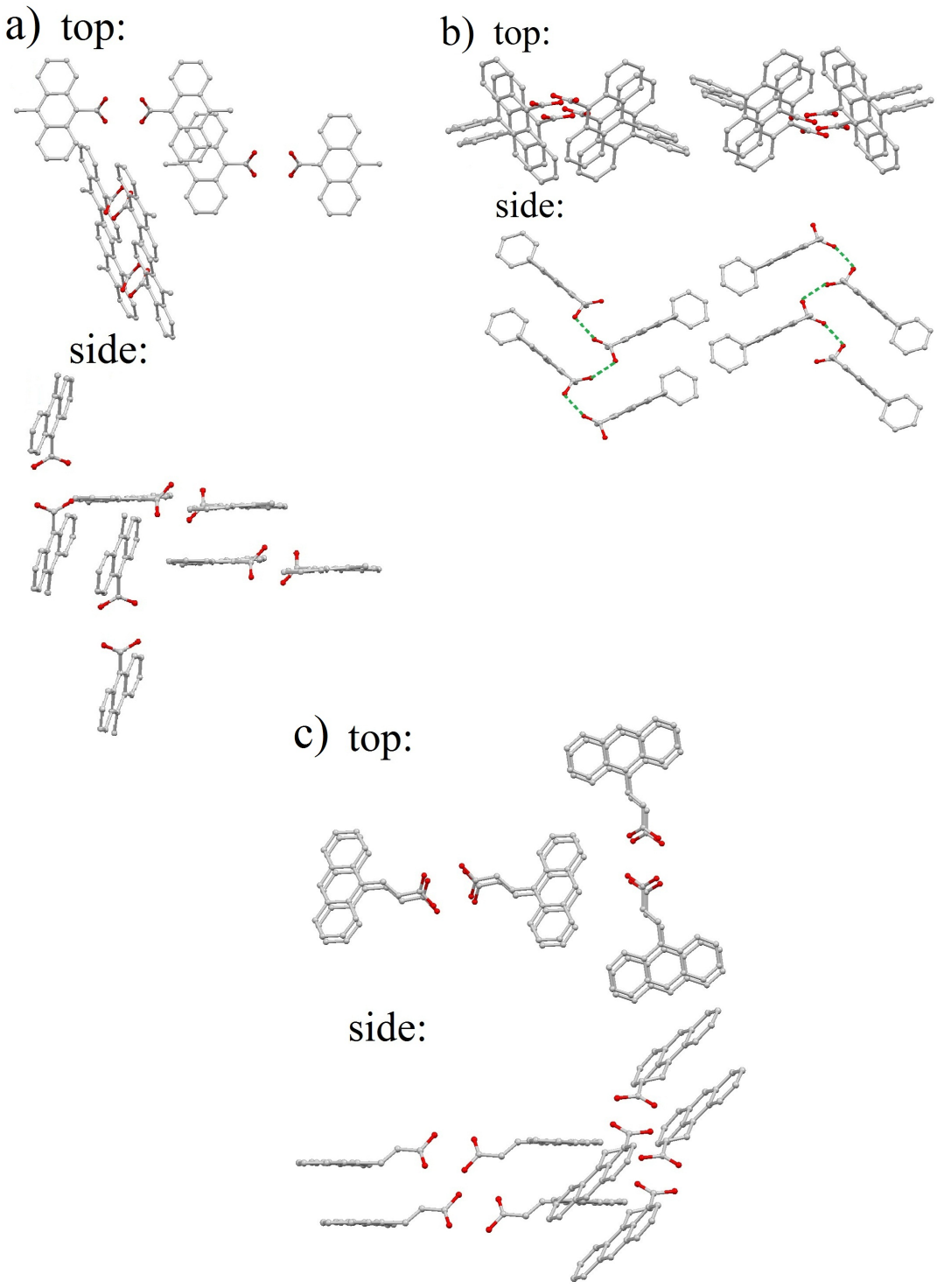

Figure 5. 5 a) 10-methyl-9-anthracenecarboxylic acid **5**; **b**) 10-phenyl-9-anthracenecarboxylic acid **6** (the green dotted line in the side view signify hydrogen bond chain); **c**)3-Anthracen-9-yl-acrylic acid **7**.

It is only when we put larger substituents at the 10-position (methyl = **5** or phenyl = **6**) that we see a disruption of the 9AC stacking motif. In **5**, the methyl group substituents lead to a reversal of the head-to-head stacking and instead we find the more common head-to-tail pair-wise arrangement, as shown in Figure 5.5a. The parallel anthracene rings are offset from each other and spaced farther apart (4.84 Å versus 3.90 Å in 9AC between two 9-position carbons in the pair). This arrangement of neighboring anthracenes is not conducive for the [4+4] photodimerization reaction, which is generally limited to pairs with a center-to-center distance of 4.7 Å or less. [11] In **6**, the anthracenes adopt the head-to-head pairwise arrangement shown in Figure 5.5b. But now the hydrogen-bonding arrangement is completely different, with a single COOH group interacting with two different molecules as illustrated by the green dotted line in Figure 3b, spreading the anthracene rings too far apart to photodimerize. In crystals of **5** and **6**, shifting of the molecules to spatial positions more amenable for reaction is presumably prevented by the hydrogen bonds that lock the anthracenes in place. In addition to modifying the 10-position, we also made one molecule with a vinylene group separating the COOH from the main anthracene ring (molecule **7**) in order to examine whether this separation could modify the standard H-bonding network seen in all the 9AC derivatives. This molecule exhibits the familiar stacking motif seen in compounds **1**-**4** as seen in Figure 5.5c. It should be emphasized that, in analogy with **1**, it is possible that other polymorphs of **2**-**7** exist. We were unable to detect them, however, and the structures in Figure 5.4 are consistent with the photophysics described below.

5.3 Photophysics of 1-7

5.3.1 Steady-state Absorption and Fluorescence Spectra of 1-7

Clearly, different substituents on 9AC can affect the crystal packing. The next question is how the photophysical properties, including photoreactivity, are affected. The photophysics in the solid-state will be affected by both intermolecular interactions and by intramolecular relaxation. Figure 5.6 shows the steady-state absorption and fluorescence spectra for compounds **1-7** in THF solution.

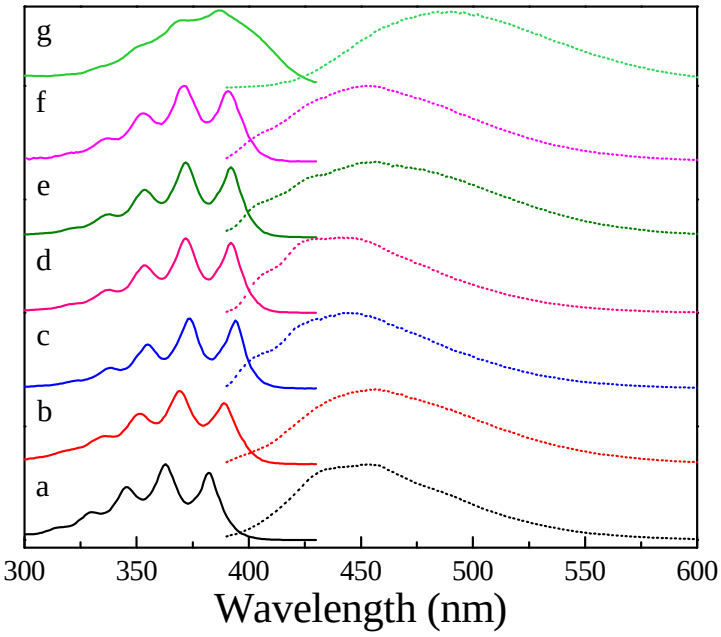

Figure 5. 6 Absorption and emission spectroscopy of 9-anthracene carboxylic acid (9AC) and its derivatives in THF solutions: **a**) 9-anthracenecarboxylic acid **1**; **b**) 10-fluoro-9-anthracenecarboxylic acid **2**; **c**) 10-chloro-9-anthracenecarboxylic acid **3**; **d**) 10-bromo-9-anthracenecarboxylic acid **4**; **e**) 10-methyl-9-anthracenecarboxylic acid **5**; **f**) 10-phenyl-9-anthracenecarboxylic acid **6**; **g**) 3-Anthracen-9-yl-acrylic acid **7**. The solid line plots are the absorption spectra, and the dotted line plots are the fluorescence spectra.

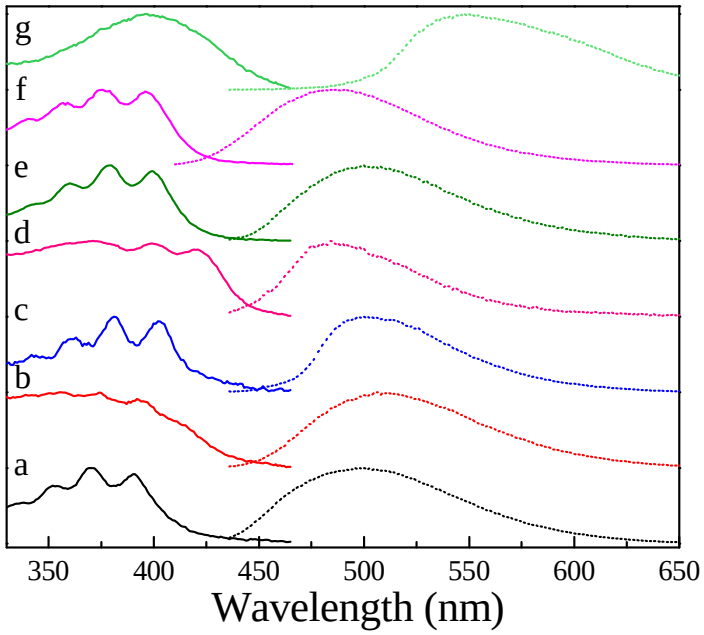

Figure 5. 7 Absorption and emission spectroscopy of 9-anthracene carboxylic acid (9AC) and its derivatives in solid-state: **a**) 9-anthracenecarboxylic acid **1**; **b**) 10-fluoro-9-anthracenecarboxylic acid **2**; **c**) 10-chloro-9-anthracenecarboxylic acid **3**; **d**) 10-bromo-9-anthracenecarboxylic acid **4**; **e**) 10-methyl-9-anthracenecarboxylic acid **5**; **f**) 10-phenyl-9-anthracenecarboxylic acid **6**; **g**) 3-Anthracen-9-yl-acrylic acid **7**. The solid line plots are the absorption spectra, and the dotted line plots are the fluorescence spectra.

The spectra for compounds **1**-**6** are all quite similar, with the characteristic anthracene vibronic progression in the absorption spectrum and the broadened, shifted fluorescence that arises from charge-transfer interactions with the carbonyl group in the excited state. [12] The only significant difference between the spectra is the redshift of both the absorption and fluorescence spectra as more electron-rich substituents are placed at the 10-position. For **7**, this conjugation effect is very pronounced, and there is additional broadening in the absorption spectrum and a much larger Stokes shift, by almost 50 nm,

than in the other compounds. When these molecules are examined as polycrystalline films on a glass surface, there is considerably more variation in their spectral properties, as shown in Figure 5.7. In all cases, the absorption spectrum shifts by only 10-20 nm, as expected from the solid-state solvatochromic effect. [13] The fluorescence undergoes a much larger shift of 50 nm or more. This large Stokes shift of the fluorescence is indicative of excimer formation, as is often seen in π-stacked anthracene crystals. The loss of structure in the absorption spectra of **2** and **4** is most likely due to scattering effects in the films. The steady-state spectra in both dilute liquid solution and in the solid films suggest that the overall electronic structures are similar for molecules **1**-**6**, and that gross changes in electronic structure (resulting from formation of H- or J-aggregates, for example) do not occur when the molecules crystallize. The presence of excimer emission is expected in these π -stacked systems and is probably an indication of the electronic interactions in the excited state that facilitate the [4+4] dimerization reaction. [14-16]

5.3.2 Solid-state Photoreactivity of 1, 2 and 7

Despite the presence of excimer emission in all crystals, only two besides **1** were found to be photoreactive. In both its triclinic and monoclinic forms, compound **1** reacts rapidly when exposed to light in the range 365-440 nm from a microscope mercury lamp. This photoreaction results in the loss of its bright green-yellow fluorescence and the appearance of a much less intense, blue fluorescence which we have attributed to unreacted monomers. [9, 17] This change in emission is accompanied by the fracture and jumping of individual crystals when viewed under a microscope. After several minutes,

the green-yellow fluorescence recovers and the process can be repeated. Crystallites composed of **2** showed similar photobleaching behavior as **1**, and this was usually accompanied by a deformation of the crystal. This bleaching and deformation was reversible in **2**, as shown in Figure 5.8 for a microneedle grown by sublimation. The bend and recovery sequence is similar to what has been observed in **1**, but the recovery time is roughly an order of magnitude longer. One qualitative observation is that crystals of **2** appear to be more plastic than crystals of **1** and less prone to shatter under irradiation.

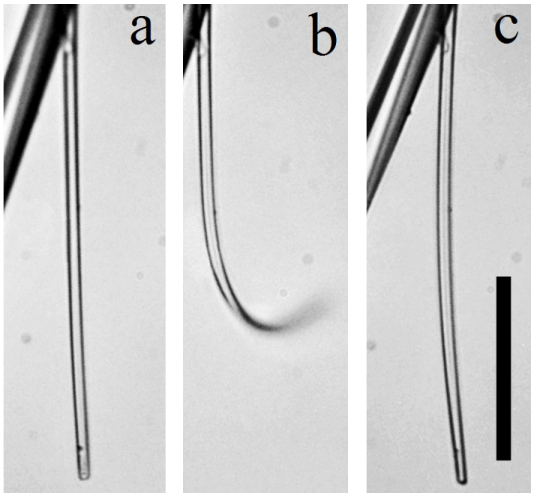

Figure 5. 8 Optical microscopy images of a microneedle crystal composed of 10-fluoro-9-anthracenecarboxylic acid **2**: **a**) before irradiation; **b**) after a few seconds of 440 nm irradiation; **c**) recovery after 30 min. The scale bar is 50 µm.

This was also true for crystals composed of **7**, the only other photoreactive molecule in our series. Even very large crystals of **7** could smoothly bend and deform under irradiation, and the photobleaching seemed to occur in two stages, perhaps indicating that both [2+2] and [4+4] dimerizations were occurring between pairs of vinylene groups and pairs of anthracene rings, respectively. Unfortunately, this reaction

was not reversible at room temperature on any timescale, making this molecule of less interest as a potential photoactuator. For the other molecules (**3**-**6**), no change in emission or physical shape was observed under even prolonged (> 10 minutes) irradiation.

5.3.3 Fluorescence Lifetime Measurements of 1-7 in Solid-state

While the lack of reactivity in **5** and **6** can be easily rationalized on the basis of the large distances between the anthracene rings, the reason that **3** and **4** do not photodimerize is less clear. We were concerned that the presence of the heavy atoms Cl and Br might lead to competing nonradiative decay processes, like intersystem crossing, so we measured the excited state lifetimes of all the solids at room temperature using fluorescence decays. We concentrated on the solid-state fluorescence lifetimes, since it is clear from Figures 5.6 and 5.7 that the emissive excimer in the solids is a new electronic state, distinct from the monomer singlet state that determines the emission properties in solution. The results of these measurements are given in Table 5.2, along with other relevant parameters for this family of compounds. All the molecules studied had lifetimes in the nanosecond range, indicating that dimerization does not occur on ultrafast (sub-nanosecond) timescales. The lifetime of **1** was 35±4 ns for both the triclinic and monoclinic polymorphs to within the experimental error. The measured dimerization quantum yield of monoclinic **1** in the solid-state is 7±1% [9], suggesting that the rate of dimerization is on the order of several hundred nanoseconds. This relatively slow reaction rate suggests that the [4+4] dimer formation is a minor channel for excited state relaxation, competing with many other channels. If the photochemical reaction rate is

similar for **1**-**4**, as seems likely given their similar crystal structures, then fewer competing channels should lead to both a longer fluorescence lifetime and a larger photoreaction yield. In this limit, a longer fluorescence lifetime should result in more efficient photoproduct formation. But the lifetime of the unreactive **3 (**15±2 ns) is longer than that of the reactive **2** (9.3±1 ns), while that of **4** (2.5±0.3 ns) is shorter, so there is no clear trend in excited state lifetime with halogen substitution. Molecules **5** and **6** had biexponential fluorescence decays that were the most rapid of all the 10-substituted compounds, despite their lack of heavy atoms or photoreactivity. It appears that fast intersystem crossing or internal conversion in the Cl and Br-substituted anthracenes does not provide a straightforward explanation for their lack of photoreactivity.

Table 5. 4 Fluorescence lifetimes of solid anthracene carboxylic acid derivatives

9AC derivatives	Lifetime (ns)	Crystal photoreactivity	Reversibility	Anthracene separation[(a)]	Stack angle[(b)]
1 monoclinic	35 ± 4	Yes	Yes	3.90 Å	23.2º
1 triclinic	35 ± 4	Yes	Yes	3.89 Å	0º
2	9.3 ± 0.9	Yes	Yes	3.77 Å	48.3º
3	15 ± 2	No	-	3.81 Å	44.6º
4	2.5 ± 0.3	No	-	3.86 Å	52.5º
5	t_1 = 1.6 ± 0.2 A_1 = 0.49 t_2 = 8.0 ± 0.8 A_2 = 0.51	No	-	4.84 Å	75.6º
6	t_1 = 1.3 ± 0.1 A_1 = 0.47 t_2 = 3.1 ± 0.3 A_2 = 0.53	No	-	7.17 Å	67.6º
7	not measured	Yes	No	3.89 Å	52.5º

(a) The separation distance was measured between the two 9-position carbons for two paired anthracene carboxylic acid molecules within a single stack.

(b) The stack angle was the angle between two anthracene planes within two different stacks which are not hydrogen bonded to each other, and which tilt in different directions.

5.3.4 Steric Effects for 1-7

Since the fluorescence lifetime measurements do not provide a clear explanation for the reactivity trends in the halogen-substituted 9AC series, we now consider steric effects. Compounds **1**-**4** provide a rare example of a situation where halogen substitution does not change the overall crystal packing, which is locked in place by the hydrogen-bond interactions. The reactive compounds' H- and F- atoms have atomic radii of 25 and 75 pm respectively, while the Cl and Br atoms have radii of 100 and 114 pm, respectively. The larger Cl and Br substituents may simply be too large to permit the dimers to form due to steric repulsion. Attempts to calculate the energy differences of the monomer pair versus the covalent dimer were unsuccessful due to their ill-defined geometries in the crystal environment, but steric effects are known to be important in solution phase photodimerization reactions of anthracene derivatives. [16, 18] But if larger atoms at the 10-position destabilize the dimer, we still are at a loss to explain why **2** has a much longer dissociation and recovery time than **1**. We expected the F-F repulsion to destabilize the dimer and result in a faster "reset" time but observed the opposite effect. One possible explanation is that the highly electronegative F atom interacts with other atoms of π-electron clouds within the crystal in new ways after photodimerization that act to stabilize the overall dimer structure. A detailed study of the crystal interactions before and after dimerization is beyond the scope of this paper. For now, we simply emphasize that steric considerations, like the fluorescence lifetime data described in the preceding paragraph, can explain some but not all of the trends observed experimentally.

5.4 Conclusions

The goal of this Chapter is to explore how chemical modification of the 9AC basic unit affects crystal packing and photoreactivity. One goal was to find materials with improved photomechanical properties, for example faster recovery times. We found that substitution at the 10-position often led to a complete loss of photoreactivity due to changes in either the crystal packing (**5** and **6**) or steric repulsion (**3** and **4**). Of the remaining candidates, crystals of **7** showed good photoreactivity and a lack of fracture, but no recovery after irradiation. Compound **2**, where the H has been replaced by an F atom, was the closest to 9AC in terms of its photomechanical behavior, but with a much longer recovery time. Attempts to self-consistently rationalize observed trends in terms of excited state lifetimes or steric effects were only partially successful. The present paper illustrates how competing effects complicate the search for an improved photomechanical material based on the 9AC framework. Although our search did result in the discovery of a new reversible photomechanical crystal (**2**), its properties are not obviously superior to that of **1**. While organic chemistry provides unlimited opportunities for chemical modification of the active chromophore, balancing various factors like electronic relaxation, steric interactions, and crystal packing remains a challenge for engineering materials based on molecular crystals. One possible strategy to overcome these competing effects is to use cocrystals to engineer better control over assembly in the solid-state.[19-20]

References

1. Ito, Y.; Fujita, H., Formation of an unstable photodimer from 9-anthracene carboxylic acid in the solid-state. *J. Org. Chem.* **1996,** *61*, 5677-5680.
2. Al-Kaysi, R. O.; Bardeen, C. J., Reversible photoinduced shape changes of crystalline organic nanorods. *Adv. Mater.* **2007,** *19*, 1276-1280.
3. Al-Kaysi, R. O.; Dillon, R. J.; Zhu, L.; Bardeen, C. J., Template assisted synthesis of silica-coated molecular crystal nanorods: from hydrophobic to hydrophilic nanorods. *J. Colloid. Interfac. Sci.* **2008,** *327*, 102-107.
4. Good, J. T.; Burdett, J. J.; Bardeen, C. J., Using two-photon excitation to control bending motions in molecular-crystal nanorods. *Small* **2009,** *5*, 2902-2909.
5. Zhu, L.; Al-Kaysi, R. O.; Bardeen, C. J., Reversible photoinduced twisting of molecular crystal microribbons. *J. Am. Chem. Soc.* **2011,** *accepted for publication*.
6. Fitzgerald, L. J.; Gerkin, R. E., Anthracene-1-carboxylic acid. *Acta Cryst. Sec. C* **1997,** *53*, 1080-1082.
7. Fitzgerald, L. J.; Gerkin, R. E., Anthracene-1,8-dicarboxylic acid. *Acta Cryst. Sec. C* **1996,** *52*, 1838-1841.
8. Fitzgerald, L. J.; Gerkin, R. E., 9-anthracenecarboxylic acid. *Acta Cryst. Sec. C* **1997,** *53*, 71-73.
9. More, R.; Busse, G.; Hallmann, J.; Paulmann, C.; Scholz, M.; Techert, S., Photodimerization of crystalline 9-anthracene carboxylic acid: a nontopotactic autocatalytic transformation. *J. Phys. Chem. C* **2010,** *114*, 4142-4148.
10. Heller, E.; Schmidt, G. M. J., Topochemistry. Part XXXIII. The solid-state photochemistry of some anthracene derivatives. *Isr. J. Chem.* **1971,** *9*, 449-462.
11. Ramamurthy, V.; Venkatesan, K., Photochemical reactions of organic crystals. *Chem. Rev.* **1987,** *87*, 433-481.
12. Dey, J.; III, J. L. H.; Warner, I. M.; Chandra, A. K., Fluorescence spectral study of 9-acridecarboxylic acid and its methyl ester. Understanding the unusual fluorescence behavior of 9-anthroic acid. *J. Phys. Chem. A* **1997,** *101*, 2271-2278.
13. Baldo, M. A.; Soos, Z. G.; Forrest, S. R., Local order in amorphous organic molecular thin films. *Chem. Phys. Lett.* **2001,** *347*, 297-303.
14. Stevens, B., Photoassociation in aromatic systems. *Adv. Photochem.* **1971,** *8*, 161-226.
15. Charlton, J. L.; Dabestani, R.; Saltiel, J., Role of triplet-triplet annihilation in anthracene dimerization. *J. Am. Chem. Soc.* **1983,** *105*, 3473-3476.
16. Bouas-Laurent, H.; Castellan, A.; Desvergne, J.-P.; Lapouyade, R., Photodimerization of anthracenes in fluid solutions: (part2) mechanistic aspects of the photocycloaddition and of the photochemical and thermal cleavage. *Chem. Soc. Rev.* **2001,** *30*, 248-263.
17. MacFarlane, R. M.; Philpott, M. R., Excimer and photochemically induced fluorescence of 9-cyanoanthracene crystals. *Chem. Phys. Lett.* **1976,** *41*, 33-36.
18. Castellan, A., Effect of substituents and solvents on the photodimerization quantum yield of anthracene derivatives. *Compt. Rend. Ser. C* **1975,** *281*, 221-224.

19. MacGillivray, L. R.; Papaefstathiou, G. S.; Friscic, T.; Hamilton, T. D.; Bucar, D. K.; Chu, Q.; Varshney, D. B.; Georgiev, I. G., Supramolecular control of reactivity in the solid-state: from templates to ladderanes to metal-organic frameworks. *Acc. Chem. Res.* **2008,** *41*, 280-291.
20. Kapadia, P. P.; Ditzler, L. R.; Baltrusaitis, J.; Swenson, D. C.; Tivanski, A. V.; Pigge, C. F., Semiconducting organic assemblies prepared from tetraphenylethylene tetracarboxylic acid and bis(pyridine)s vis charge-assisted hydrogen bonding. *J. Am. Chem. Soc.* **2011,** *133*, 8490-8493.

Chapter 6 Polymerizable dianthracene derivatives

In this Chapter, we include some of the work not published. They are presented here as data, but not as a complete story.

6.1 Crystalline Polymer Nanorods

The previous work in our group has developed a method to grow the molecular crystal nanorods of a dianthracene polymer precursor (9AC-ME) by alumina templates. [1] Subsequent exposure to ultraviolet light caused the monomer nanorods to undergo a [4+4] photocycloaddition reaction, forming highly crystalline polymer nanorods. The polymer nanorods are flexible, resistant to breakage, and insoluble in organic solvents and strong acid/base solutions.

We were curious if we could apply this method to other polymer precursors to make various crystalline polymer nanorods, and then dope them to polymer films for higher young's modulus and other improved properties. Thus, a series of derivatives analogous to the dianthracene molecule 9-anthracene carboxylic acid-methyl-ester (D1) were synthesized. Their molecular structures are shown in Figure 6.1. For the simplicity, in this Chapter they are named as D2, D3…according the carbon numbers of the center alkyl chain.

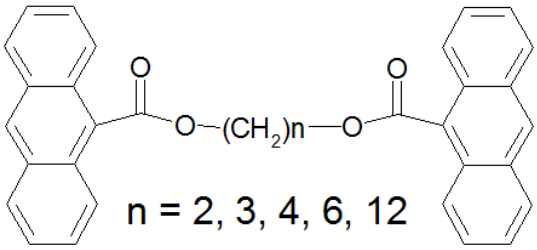

Figure 6. 1 Molecular structures of dianthracene polymer precursors.

6.2 Polymorphism for Polymer Precursors

In room temperature, D1 has more than one polymorphs (as shown in Figure 6.2b), and they are not photopolymerizable in solid-state; but the polymorph from high temperature annealing is photopolymerizable in solid-state as shown in Figure 6.2a. Our results indicate that this is a general phenomena for these dianthracene derivatives to have multiple polymorphs.

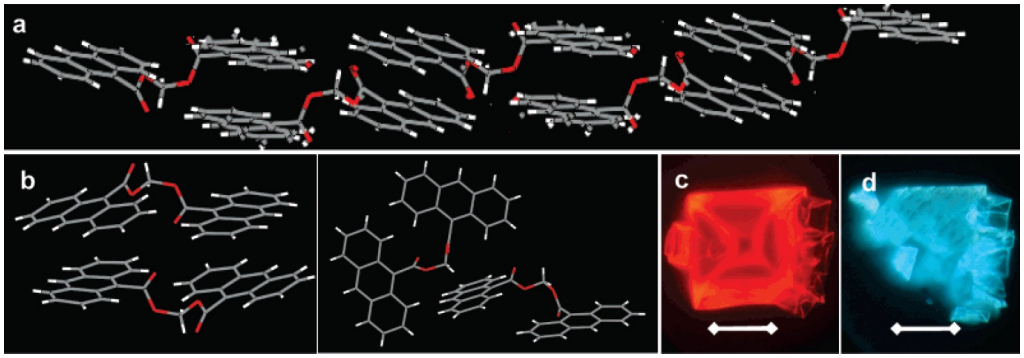

Figure 6.2 a) Crystal structure of D1 monomer crystals solvent annealed from THF at 68 ºC. The anthracene units of adjacent molecules stack in a parallel conformation, with the dianthracenes forming an alternating chain. **b**) Two different crystal structure renderings of D1 monomer crystals grown from THF at room temperature. The anthracene units are not parallel and there is no alternation in the dianthracene stacks. **c**) A single crystal of D1 monomer grown from THF at 68 ºC before illumination with 365 nm light. The microscope color filter only transmits red light, so the crystal appears red. **d**) After a brief illumination with 365 nm light, the polymer of D1 forms and the crystal shatters and turns fluorescent blue due to the residual unreacted anthracene units. Scale bar = 45 µm. [1]

6.2.1 Polymorphs of D2

D2 has different polymorphs at room temperature and high temperature. We solved the structure of the high temperature polymorph, which is shown is Figure 6.3. The distance between each pair of two anthracene molecules is 7.6 Å, indicates that this polymorph of D2 is not photoreactive in solid-state. [2] At room temperature, D2 tends to grow into polycrystalline crystals instead of single crystal, the structure remains unknown. Figure 6.4 shows powder patterns of polymorphs from high temperature (68 ºC) and room temperature.

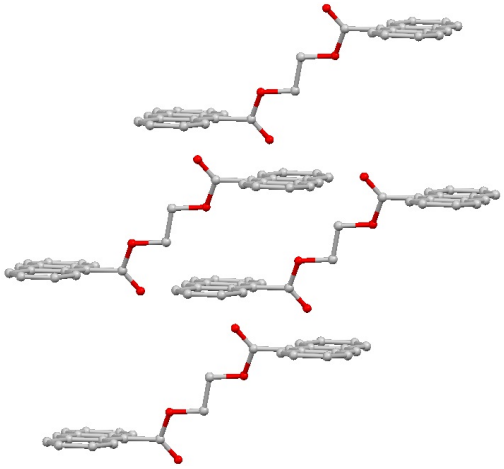

Figure 6.3 Crystal structure of D2 solvent annealed from high temperature. The distance of each anthracene pair is 7.612 Å, which indicates that this polymorph of D2 is not photoreactive in solid-state.

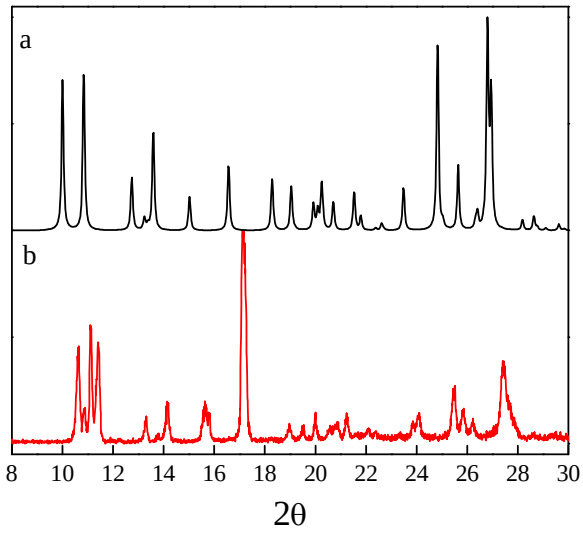

Figure 6. 4 Powder X-ray diffraction patterns of **a**) calculated powder pattern of D2 single crystal, which was grown from solvent annealing at high temperature; **b**) experimental powder pattern of D2 crystals, which was grown from slow solvent evaporation at room temperature.

6.2.2 Polymorphs of D3

D3 has two polymorphs in the same batch of the single crystals we grew and both of their crystal structures were solved, as shown in Figure 6.5. Both polymorphs are photo-polymerizable in solid-state. The polymorph **1** shown in Figure 6.3a tends to grow into needle shaped crystals; while the polymorph **2** shown in Figure 6.3b grows into plate shaped crystals.

To differentiate these two polymorphs, we varied concentration, temperature and set-up to find the proper condition to grow crystals with one polymorph only. We found that D3 prefers to grow in the form of polymorph **2**, regardless the changes of concentration or temperature (as illustrated in Figure 6.6). Figure 6.4a and 6.4b show the

calculated powder X-ray diffraction pattern of D3 in polymorph **1** and polymorph **2**; Figure 6.4c shows the experimental powder diffraction pattern of D3 crystal grown by slow solvent evaporation from concentrated THF solution at room temperature; the pattern agrees well with the pattern of polymorph **2**. Figure 6.4d shows the experimental powder pattern of D3 crystals, obtained through slow solvent evaporation from diluted THF solution at room temperature; it was also in the form of polymorph **2**. This indicates that concentration has little effect on the formation of different polymorphs. Figure 6.4e shows the powder pattern of D3 crystals from solvent annealing in THF at 68 ºC; D3 was still in the form of polymorph **2**; this indicates that temperature has few effect to the formation of different polymorphs.

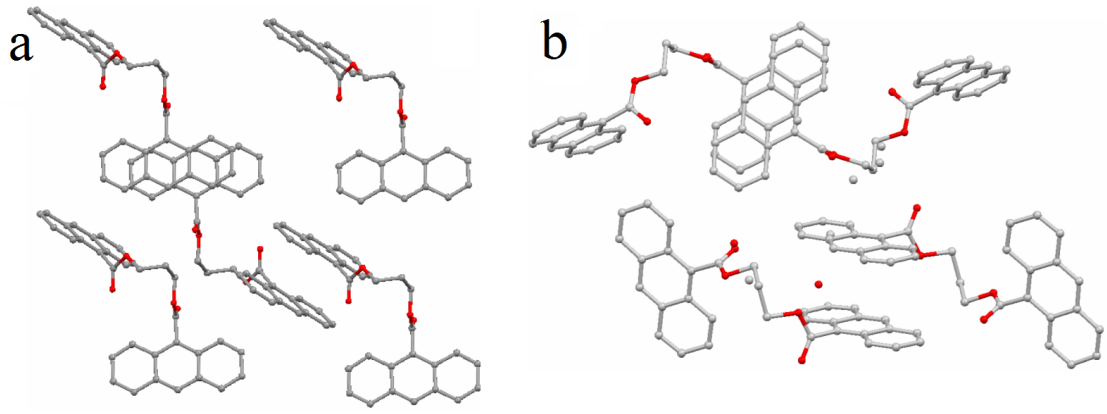

Figure 6. 5 Crystal structures and packing for D3; a) polymorph **1,** grows in 'needle' shapes; b) polymorph **2**, grows in 'plate' shape. Both polymorphs are reactive in solid-state.

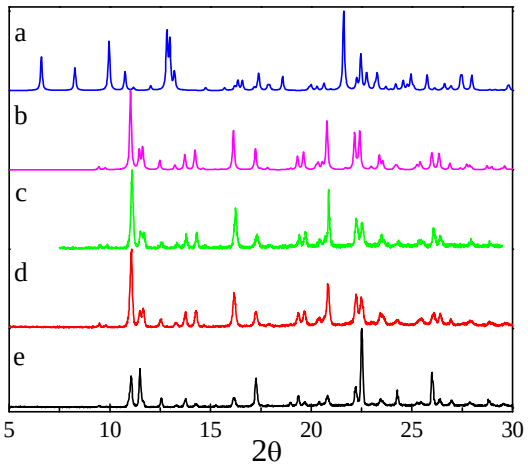

Figure 6.6 X-ray diffraction patterns of D3: **a**) calculated powder pattern of D3 in polymorph **1**; **b**) calculated powder pattern of D3 in polymorph **2**; **c**) experimental powder pattern of D3 crystals, which was recrystallized through slow solvent evaporation from concentrated THF solution at room temperature; **d**) experimental powder pattern of D3 crystals, which was recrystallized through slow solvent evaporation from diluted THF solution at room temperature; **e**) experimental powder pattern of D3 crystals, which was recrystallized from solvent annealing in THF at 68 ºC.

Since both concentration and temperature didn't contribute to polymorph control, we tried to modify set-up to grow polymorph **1** only crystals. After trial-and-errors, we found that there are two ways to grow polymorph **1** only in the form of polymorph **1**: a) use AAO template to grow D3 nanorods (Figure 6.7d); b) add a surface to the set-up of slow evaporation or solvent annealing, the surface can be a piece of cover slip or foil (Figure 6.7c). The experimental powder pattern of D3 nanorods shown in Figure 6.7c matches the calculated powder pattern of polymorph **1** shown in Figure 6.7b; The experimental powder pattern of D3 bulk crystals in Figure 6.7d also indicates that D3 is is in the form of polymorph **1**. The difference in between the set-ups for polymorph **2**

(Figure 6.6e) and polymorph **1** (Figure 6.7d) is a piece of foil, which provides a surface for D3 to recrystallize upon.

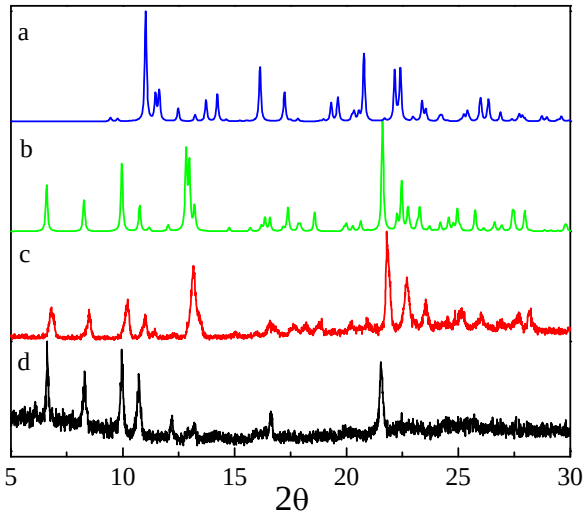

Figure 6.7 X-ray diffraction patterns of D3: **a**) calculated powder pattern of D3 in polymorph **2**; b) calculated powder pattern of D3 in polymorph **1**; **c**) experimental powder pattern of D3 bulk crystals grown from solvent annealing in THF on a piece of foil at 68 ºC; **d**) experimental powder pattern of D3 nanorods grown solvent annealing in THF at 68 ºC using AAO template.

Since the crystals in Figure 6.7 were both grown at 68 ºC, to test if the extra 'surface' is the only confinement for polymorph **1** growth, we repeated the above two methods at room temperature in different solvents. Our results in Figure 6.8 show that temperature has no effect on polymorph **1** growth. The experimental powder pattern of D3 bulk crystals grown from solvent annealing in DCM on top of AAO template at room temperature is in the form of polymorph **1** as shown in Figure 6.8b. Here the AAO template also serves as an extra surface; Figure 6.8 shows the experimental powder pattern of D3 nanorods grown in DCM at room temperature, which is also in the form of

polymorph **1**. The same measurements have been done with a different solvent-THF-and we got the same result that both the bulk crystal on top of AAO and nanorods are in the form of polymorph **1**. Thus for the polymorph control of D3, both concentration and temperature have little effect. Adding an extra 'surface' is the trick to grow polymorph **1** only for both bulk and nanorods; without the extra surface, D3 would just grow in the form of polymorph **2**.

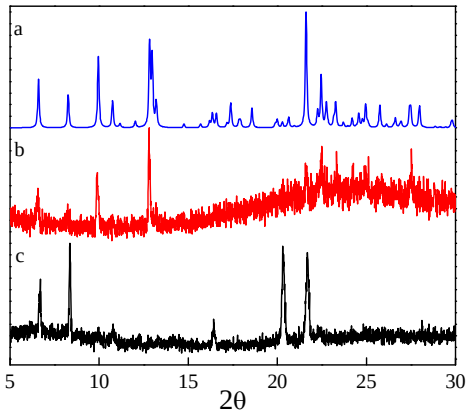

Figure 6.8 X-ray diffraction patterns of D3: **a**) calculated powder pattern of D3 in polymorph **1**; **b**) experimental powder pattern of D3 bulk crystals grown from solvent annealing in DCM on top of AAO template at room temperature; **c**) experimental powder pattern of D3 nanorods grown solvent annealing in DCM at room temperature using AAO template; less peaks were shown due to the preferred orientations of nanorods while they are aligned in the template.

6.2.3 Polymorphs of D4

D4 has multiple polymorphs at room temperature depends on the solvents used for recrytsallization as illustrated in Figure 6.9. At room temperature D4 usually grows as polycrystalline crystals instead of sing crystals, so none crystal structures of the room

temperature polymorphs were solved. At high temperature (68 ºC), D4 has only one polymorph; the structure is shown in Figure 6.10.

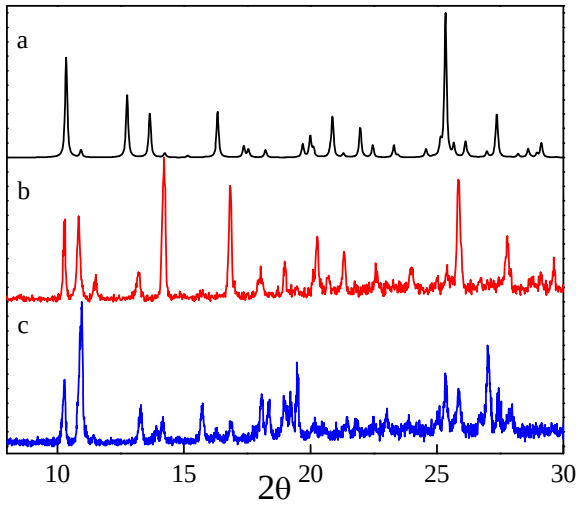

Figure 6. 9 X-ray diffraction patterns of D4: **a**) calculated powder pattern of D4 from the solved structure; **b**) experimental powder pattern of D4 bulk crystals grown from acetonitrile at room temperature; **c**) experimental powder pattern of D4 bulk crystals grown from THF at room temperature. Different patterns of **a**), **b**) and **c**) signify the existence of multiple polymorphs of D4 at room temperature.

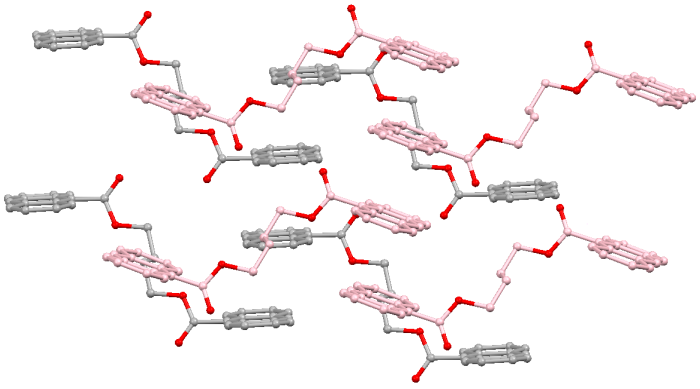

Figure 6. 10 Crystal structure of D4's polymorph from 68 ºC annealing.

The packing motif of this polymorph is herringbone pair. To differentiate different layers of D4 molecules, the first layer molecules are colored in pink, while the second layer molecules colored in gray. The distance between each two paired anthracenes is 3.72 Å, thus this polymorph of D4 is photo-polymerizable in solid-state.

6.2.4 Polymorphs of D6

D6 tends to be in the form of 'oil' rather than crystal. Although we managed to obtain the structure of one polymorph of D6, further research was not continued to explore if D6 has multiple polymorphs due to the difficulty to recrystallize D6. The structure of D6 polymorph is shown in Figure 6.11.

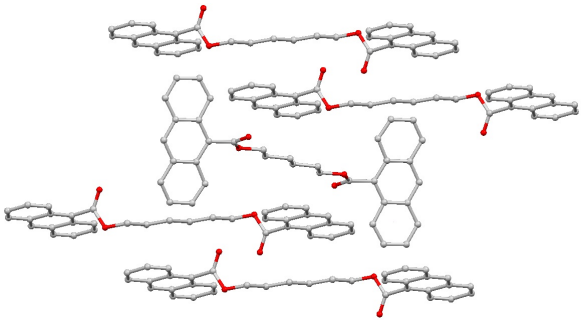

Figure 6.11 Crystal structure of D6: anthracenes are offset-alligned to each other, thus there are no reactive pairs.

Although the crystal structure of D6 shows that D6 is not photoreactive, we observed the opposite result. The single crystal of D6 (from the same batch of the single crystal which was used for structure solving) fractured under photo irradiation as shown in Figure 6.12. To eliminate the possibility that the fracture may come from the heating effect of the irradiation, we carried out this experiment in water. Further research will need to be carried out to explain this seemingly contradictory observation. Powder X-ray

diffraction measurement should be able to tell us if the photo-induced fracture of D6 comes from a different polymorph or the defect of the crystal which enables the solid-state photoreactivity.

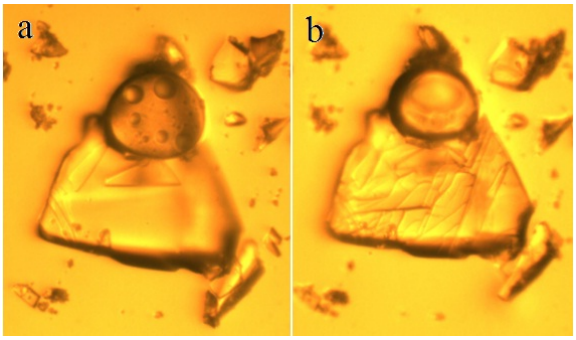

Figure 6.12 Optical microscopy images of D6 single crystal before and after 440 nm irradiation: the crystal fractured upon irradiation; the experiment was carried out in water.

6.2.5 Polymorphs of D12

D12 crystals are photo-polymerizable in solid-state; we managed to grow single crystal of D12, yet the structure couldn't be resolved due to too much disorder in the crystal. The two anthracenes on the two sides of the long alkyl chain fluctuate, and thus introduce disorder to the crystals.

6.3 Photo-polymerizable Nanorods of D3 and D4

Among all the solid-state photoreactive polymer precursors, D3 and D4 are with known crystal structures and controllable polymorph growth. Thus, we chose D3 and D4 for continual research of photo-polymerizable crystalline nanorods.

6.3.1 D3 Nanorods

D3 nanorods were grown from AAO template, and their SEM images are shown in Figure 6.13. However, at this point we are not able to control the crystalline orientation of D3 nanorods. Figure 6.14 shows the powder X-ray diffraction patterns of different batches of D3 nanorods standing in the AAO template. D3 nanorods in Figure 6.14b and 6.14c are grown from the same condition, yet they are with different orientations.

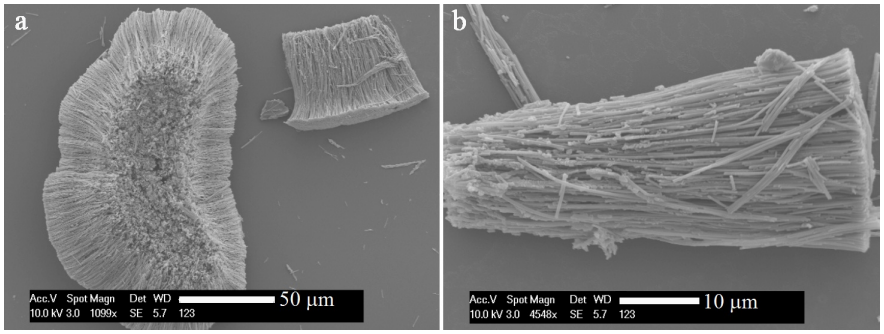

Figure 6. 13 SEM images D3 nanorods: **a)** the scale bar is 50 µm; **b)** the scale bar is 10 µm.

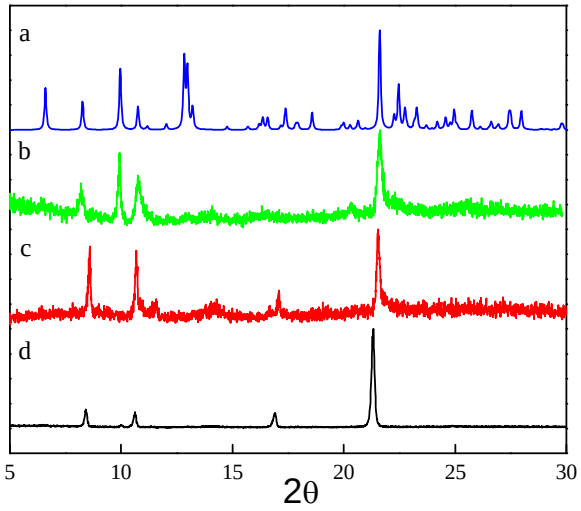

Figure 6. 14 Powder X-ray diffraction patterns of D3; a) calculated powder pattern of polymorph **1**; b) D3 nanorods standing in the AAO template, grown from THF at 68 ºC annealing; c) D3 nanorods standing in the AAO template, grown from THF at 68 ºC annealing on a different day, with less peaks than the D3 nanorods in b); d) D3 nanorods standing in the AAO template, grown from DCM at 68 ºC.

6.3.2 D4 Nanorods

Compared with the multiple orientations of D3 nanorods, D4 nanorods only show one orientation while they are standing in the AAO template, (110) or (002) as shown in Figure 6.15. The orientations of (110) and (002) are shown in Figure 6.16. For both (110) and (002), the polymerization directions of D4 molecules are perpendicular to the rod axis. Ideally, each molecular layer of the cross-section is a single polymer molecule after polymerization. At this point, we haven't developed method to grow (110) only or (002) only nanorods.

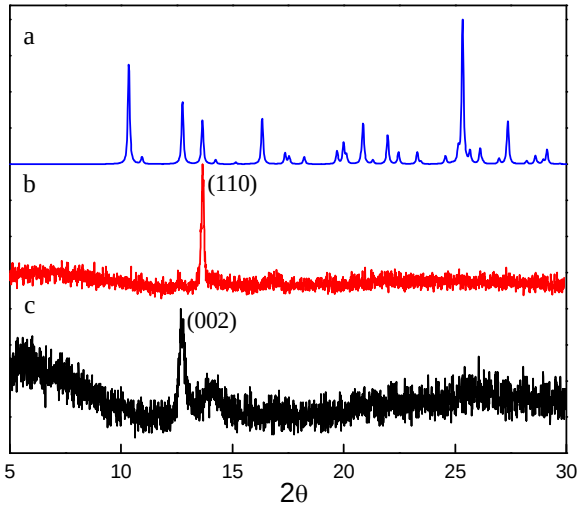

Figure 6. 15 Powder X-ray diffraction patterns of D4; a) Calculated powder pattern of the photoreactive polymorph of D4; b) D4 nanorods standing in the AAO template with the (110) orientation; c) D4 nanorods standing in the AAO template with the (002) orientation.

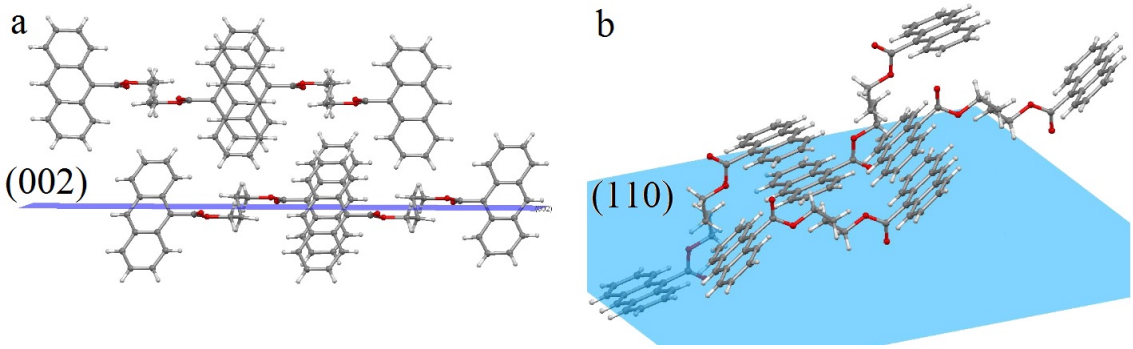

Figure 6. 16 Crystal orientations of D4 crystals.

We used the sodium dodecyl sulfate (SDS) pretreated AAO template to grow D4 nanorods, and all the D4 nanorods are thus coated with SDS individually to avoid congregation. Figure 6.17 shows the polyvinyl alcohol (PVA) film doped with the SDS-coated D4 nanorods. Further research of how the doped nanorods strengthen the property of the film after polymerization hasn't been carried out.

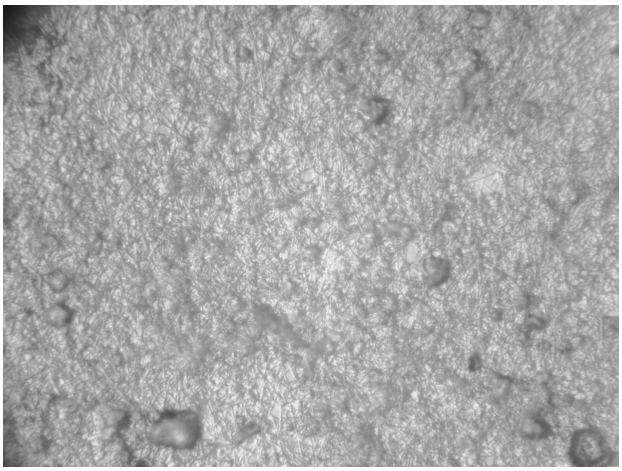

Figure 6. 17 Polyvinyl alcohol (PVA) films doped with sodium dodecyl sulfate (SDS)-coated D4 nanorods.

6.4 Conclusions

A serie of dianthracene esters analogue to the photopolymerizable D1 has been synthesized. Similar to D1, they all have multiple polymorphs in both room temperature and high temperature. Methods have been developed to control the photopolymerizable polymorphs of the bulk crystals, yet more effort would be needed to control the orientations of the nanorods. Pretreatment of the AAO template with the surfactant sodium dodecyl sulfate can help avoid the congregation of the polymer precursor nanorods, and thus prepare more evenly-doped polymer films. Further measurements would be needed to test the improvement of the film properties after the doping of these polymer nanorods.

Reference

1. Al-kay, R. O.; Dillon, R. J.; Kaiser, J. M.; Mueller, L. J.; Guirado, G.; Bardeen, C. J. Photopolymerization of Organic Molecular Crystal Nanorods, **2007**, 40, 9040

Chapter 7 Conclusions and Future Research Directions

This theis studies the photomechanically responsive molecular crystal nano- and micro-structures based on anthracene derivatives.

7.1 Conclusions

A family of 9-anthracene carboxylic acid esters with various lengthy or bulky substituents is synthesized. The variations in the molecular structures and crystal packing motifs cause some of these ester molecules lose their photoreactivity in solid-state. All the photoreactive molecules can be fabricated into nanorods. The nanorods of 9-anthracenecarboxylic acid (1-methyl-cyclohexyl) ester (9MCHAE) show the largest expansion in length (~25%). Although the molecule 9MCHAE has the largest photoresonse, it was not the molecule with the longest or the bulkiest substituents in this family of 13 esters. This indicates that there is no necessary relationship between the molecular structures and the crystal structures or between the molecular structures and the solid-state photoreactivities. We cannot predict the crystal structures or the solid-state photoreactivity only based on the molecular structures.

A detailed study of the photochemistry of 9-anthracenecarboxylic acid tert-butyl ester (9TBAE) unveils that a metastable crystalline intermediate photodimer (SSRD) is the determine factor for the micro-scale photoresponse of the nanorods. This metastable SSRD slowly converts into a low energy equilibrium photodimer (SGD) over the course of weeks. This metastable-SSRD-phenomenon is not only limited to compound 9TBAE; it’s a general characteristic of 9-anthracene carboxylic acid ester molecular crystals. Thus,

we can't predict the macro-scale photoresponse of the molecular crystal structures only based on the equilibrium reactant and product crystal structures.

Long wavelength tail irradiation method is applied to obtain the single crystals of a mixture of 20% dimer with 80% monomer. This partially reacted dimer (PRD) has the same structural conformation as the metastable SSRD. They both have the ester groups pointing inward of the anthracene pairs; and SGD has its ester groups pointing outward of the anthracene pairs, for comparison. However, the unit cell parameters of SSRD remain unknown due to the fact the unit parameters of PRD are largely affected by the 80% unreacted monomer. Thus, molecular crystals containing anthracene esters are not promising materials for the potential applications of photoactuation out of several reasons. (1) They are not reversible; (2) It is a big challenge to solve the crystal structure of the metastable intermediate SSRD, to have better understanding of how the molecular level photochemistry gives rise to the micro-scale photomechanical motions. (3) They don't give uniform photoresponse due to the variation of crystallinity and surface adhesion.

Compare with anthracene derivatives, molecular crystals of 9-anthracene carboxylic acid (9AC) are more promising material due to its reversibility at room temperature. In this dissertation, we present a new mode of reversible photomechanical motions in 9AC microstructures. Microribbons consisting of oriented 9AC molecules undergo reversible twisting motions upon uniform irradiation. All the features of these twisting microribbons such as size-dependant twist period and time-dependant untwisting motions are consistent with an interfacial strain model. The generation of interfacial strain between the unreacted monomer and the photoreacted dimer regions upon

irradiation, is the cause of the twisting motions of the microribbons. The time-dependant untwisting of the microribbons in dark is the result of the releases of the interfacial strain due to the dissociation of the photodimers into the monomers. These microribbons of 9AC can be promising components for photoactuation devices due to three of their advantages. (1) They are reversible. (2) The twisting motions are generated by uniform irradiation, while the photo-induced bending of nanorods relies on the selective irradiation. Uniform irradiation is cheaper and easier than selective irradiation. (3) The twisting motion is superior to the bending or expansion motions for the applications of photoactuation. The discovery of the reversible twisting microribbons also shines light on the strategies of property improvements of photoreactive materials: besides the modification of structures, the modification of the morphology might also be a good path to improve the photoresponse of molecular crystals.

To strengthen the reversibility of molecular crystals, a family of 9-anthracene carboxylic acid derivatives with different substituents are synthesized and studied in their crystal structures, photomechanical responses, and photophysical properties. We found that the substitution at the 10^{th} position often led to a complete loss of photoreactivity due to changes in either the crystal packing or steric repulsion. Among the five 10^{th} position substituted 9anthracenecarboxylic acids, only 10-fluoro-9anthracenecarboxylic acid, shows the reversible photomechanical responses, but with a much longer recovery time. We also tried to modify the carboxylic acid group, by adding a vinyl group between the carboxylic acid and the 9-carbon of the anthracene, resulted in crystals that show good photoreactivity and no fracture, but no reversibility. Attempts to self-consistently

rationalize observed trends in terms of excited state lifetimes or steric effects were only partially successful. This illustrates how competing effects complicate the search for an improved photomechanical material based on the 9AC framework. Thus, molecular crystals containing 9AC is still the best candidate for photoactuation.

7.1 Future Research Directions

In order to gain a predictive understanding of how molecular-level solid-state photochemistry gives rise to the micro-scale photo-induced motions, it's crucial to solve the crystal structure of SSRD for the future research. There are two possible approaches to solve SSRD: a) obtain a qualified single crystalline nanorod of SSRD, and solve it by synchrotron single crystal X-ray diffraction; b) Computational modeling, and using the powder X-ray diffraction pattern of SSRD as the standard to determine the accuracy of the calculated structure. Dr. Jingfeng Lai in prof. Muller's group has been working on the computational modeling of SSRD through Material Studio. His recent set of data shown in Figure 7.1 is very encouraging. Figure 7.1a is the calculated powder X-ray diffraction pattern from his calculated SSRD structure; and Figure 7.1b is the experimental powder X-ray diffraction pattern for SSRD crystalline powders. The signature peak of SSRD at 10.77 º is fitted accurately, same for other major peaks. In the future, if we can establish a standard procedure to solve SSRD of different molecules through Material Studio, and develop a corresponding model based on the crystal structures of monomers and calculated SSRD, then the prediction of macroscopic shape changes can be possible.

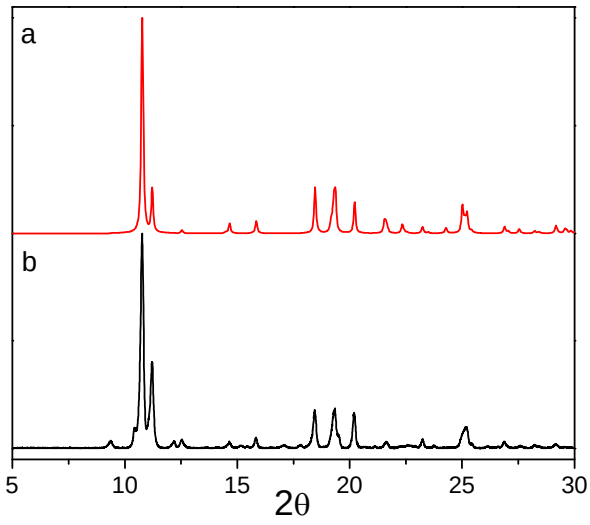

Figure 7. 1 Powder X-ray diffraction patterns of SSRD: a) calculated pattern from Dr. Jinfeng Lai's calculated SSRD; b) experimental pattern from SSRD crystalline powder.

We have several different proposals for the future research directions of the 9AC molecular crystals: (1) Apply this micro-ribbon preparation procedure to other photoreactive molecular crystals in which the molecules are packed in a stack that each molecule can possibly react with both neighbor molecules. Thus there would be unreacted monomer molecules 'left out' statistically to generate the interfacial strain within the crystalline ribbons. One candidate molecule is 3-Anthracen-9-yl-acrylic acid (9AAC), which has similar packing motif to the 9AC. Since the photochemistry of 9AAC is not reversible, we can use it to study how the solid-state photochemistry gives rise to the micro-scale twisting motions on the molecular level.

(2) Microribbons with uniform size would be more useful as photoactuators. A possible route for us to modify the floating drop method to grow ribbon with uniform size is to use templates. A preliminary design of the template is shown in Figure 7.2a. The

template is like an ice tray without the bottom; it can be made out of metal, which is stable in both water and organic solvents. While applying this template, it would stand in water; and the interface of water and organic solvent can serve as the flat surface for 9AC crystals to grow upon. An alternative design is to have four posts as shown in Figure 7.2b.

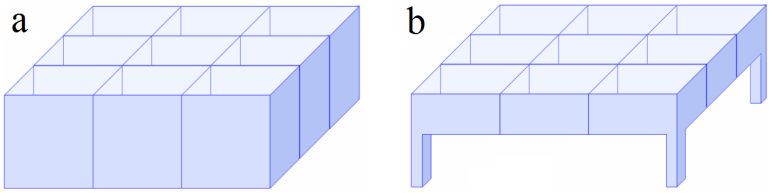

Figure 7. 2 Preliminary design of the template, the templates are empty at the bottom for both a) and b).

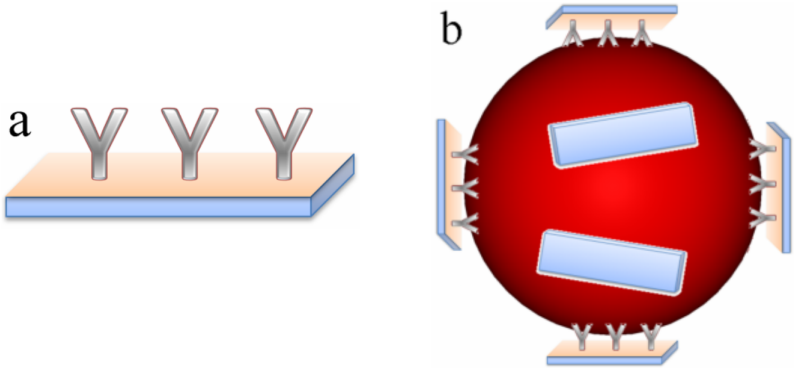

Figure 7. 3 a) Preliminary design of 9AC device: 9AC ribbon was covered with thin layer of gold, and the bio-functional groups were attached to the gold layer; **b**) A possible scheme for 9AC devices to be applied to biological system.

(3) Make devices with the twisting ribbons for biological applications. A preliminary design of the device is shown in Figure 7.3a. One side of the ribbon is coated with a thin layer of gold; the gold serves as a connecting media to have bio-functional groups attached to the ribbon. A possible scheme to apply this device in biological system is illustrated in Figure 7.3b. Through these bio-functional groups, the devices can

be installed to the target object. Using two-photon irradiation for better penetration and safety in bio-systems, the photo-induced twisting motions of the installed devices would deform the target. This process can be repeated until the target is completely damaged.

(4) Explore cocrystals of 9AC: two possible combinations are: (a) cocrystal of 9-anthracene carboxylic acid (9AC) and 10-fluoro-9-anthracene carboxylic acid; and (b) cocrystal of 9-anthracene carboxylic acid (9AC) and 3-Anthracen-9-yl-acrylic acid (9AAC). The cocrystals may render us new modes of photoresponse.

Appendix I AFM

A1.1 Procedures of Scanning

A1.1.1 Installation of Probes

There are two types of probes we used: contact mode probes and tapping/intermittent-contact mode probes. Contact mode probes are made from silicon nitride, which are harder and wear more slowly with use. Intermittent contact mode probes are made from silicon, which are softer and more flexible, suitable for tapping. For all the measurements in this dissertation, the intermittent contact mode probes NSC35 from Mikromasch were used to acquire data. The following steps demonstrate how to install a probe:

1st, tilt the AFM head back, and unplug the probe holder from the AFM head. Special caution should be paid while unplugging the red connectors as shown in Figure A1.1, make sure to apply the force to the red connector instead of the wires on the red connectors (These thin wires are easily torn out). Then unscrew the probe holder from the scanner through the hole as shown by the arrow in Figure A1.2

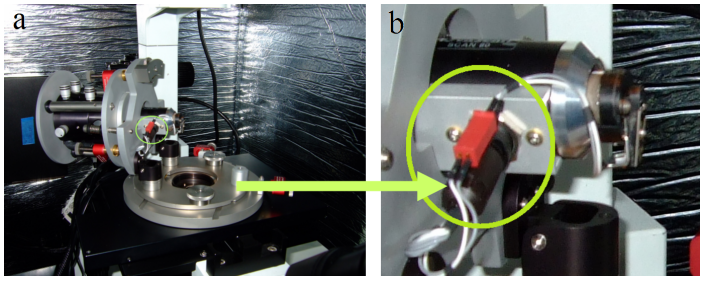

Figure A1. 1 Digital camera pictures **a**) Novascan ESPM 3D AFM head, tilted. **b**) Zoom-in image of AFM scanner, to show the red connectors between the probe holder and the scanner.

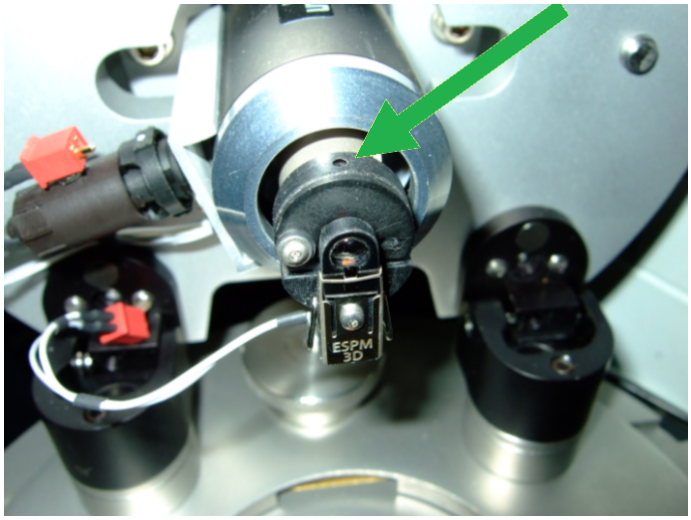

Figure A1. 2 Unscrew the probe holder from the scanner through the hole pointed by the arrow using 0.50 ball-end hex key. In this picture the red connecters were already disconnected from each other.

2nd, install the probe holder to the probe holder seat by tightening the screw which was loosened in 1st step ; Lift the front of the bail by pressing down where the letters 'ESPM 3D' are. Figure A1.3 shows the image of the probe holder. Compared with older versions of probe holders, this version of probe holder is designed to be lifted up by finger instead of loosening the screw next to the letters.

Figure A1. 3 Image of the probe holder with the probe underneath, the probe holder is still attached to the scanner; the probes can be taken out or put in simply by pressing down the letters 'ESPM 3D' while the probe holder installed to the platform which holds the probe holder for probe switching.

3rd, Place the new AFM probe underneath the front edge the bail and let go the back of the bail to hold the probe; make sure to examine the position of the probe from all angles that the probe is sitting flat on the angled sapphire window. Small adjustment of the position of the probe (e.g. more toward left or right or center of the sapphire window as shown in Figure A1.4) to get better signal is usually needed at the step of aligning the laser. It is usually the higher the better for the signals, at least 4000 a.u.

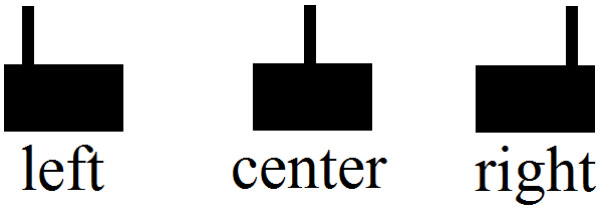

Figure A1. 4 Schematic showing the relative positions of the AFM probe

4th, Install the probe holder to the scanner by operating the opposite procedure of 1st step: tighten the screw and plug the red connectors. Now the probe is installed. The next step would be lowering the AFM head back to the stage with extra caution, making sure that the sample surface is not too close to the probe to damage it; lock the AFM head and then adjust for best signal level. The details are covered in the following.

A1.1.2 Partial Procedures of Scanning (with Trouble Shooting)

1st, turn on the power of AFM, the button is located at the back of the 'novascan ULNPowerSupply' box. Wait for an hour for the AFM to warm up, then turn on the Novascan program by clicking the icon 'Novascan 3D SPM Combo 4.65'. While turning on the novascan 3D SPM combo 4.65, it may give out the warning box which says

'unable to locate the DSP card in the computer's PCI bus' as shown in Figure A1.5. If the AFM is already warmed up for an hour, then restart the computer can solve this problem; otherwise wait for an hour until AFM is warmed up and try again.

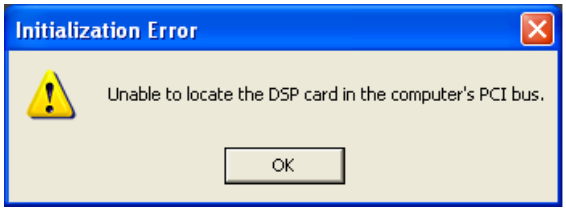

Figure A1. 5 Warning information concerning no DSP card while starting the scanning program; click OK, then restart the computer; AFM can't function without DSP card.

2nd, A window would pop up for scan head selection as shown in Figure A1.6; we usually use the 80 um open loop head.

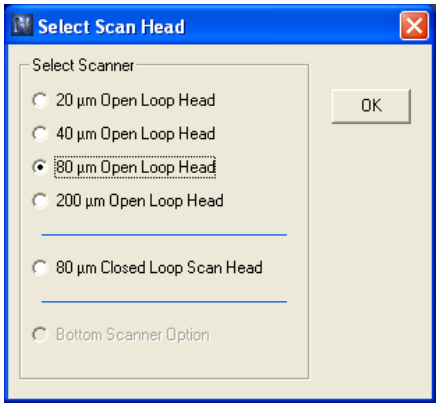

Figure A1. 6 Pop-up window right after initializing the program, choose the open loop head corresponding to the scan size. We usually use the 80 um open loop head.

3rd, turn on the laser by clicking the *laser* button. If the probe is already installed, and AFM head is locked, then move to next step. If the probe is not installed or installed but the AFM head is still tilted back, then stay in this step. (After installing the probe, never try to lower the AFM head back to the stage without the laser on.)

After turning on the laser, then turn on the laser spot in the alignment window by turning the alignment-window-mirror-knob as indicated by the arrow in Figure A1.7. The alignment-window-mirror-knob a knob to control a built-in mirror; if the mirror is on, the laser signal from the probe would be reflected to the alignment window as a sign to indicate the distance between the probe and the sample surface; if the mirror is off, the laser signal from the probe would be reflected to the detector to collect data. During the measurements, the mirror needs to be turned off, otherwise there would be no signal going to the detector and the program wouldn't proceed. However, the mirror needs to be turned on and make sure to pay close attention to this red laser spot while lowering the AFM head back to the stage. If the red spot stays still, this indicates the probe is not too close to the surface, and it's safe to continue lowering down the AFM head; if it moves slightly, or get fussy, that means the probe is touching the sample surface. Tilt the AFM head back right away. If there is no red spot in the alignment window, either the probe is already broken; or the laser is not focused on the probe, which can be adjusted by the Laser X Position knob and Laser Y Position knob as shown in Figure A1.8.

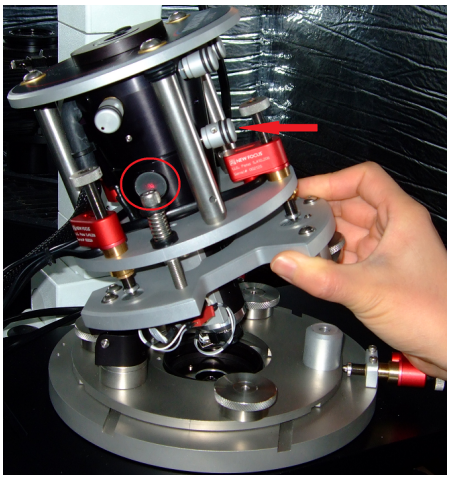

Figure A1. 7 Digital camera image of AFM head, with AFM tilt back and held by hand. The window with a red laser spot in the center is the alignment window, and the alignment-window-mirror-knob is pointed by the arrow in the image. While tilting the AFM head back or lowering it down to the surface, it is recommended to use both hands because the AFM head is just sitting on the microscope stage, there is no attachment. If use only hand to move the AFM head, it is easily moved horizontally.

There are two ways to make the scanner go further away from the sample surface; (1) Electronically, clicking *withdraw* button in the program, and type in a number to indicate distance, the larger the number, the larger the distance between the probe and the sample surface; Try to start with some number like 50. b) Manually, raise the stage of scanner by clock-wisely rotating the three knobs a, b, and c as shown in Figure A1.8. Make sure each time rotate a small angle and the same angle for all three knobs; otherwise the probe wouldn't be parallel to the surface and it can cause unnecessary troubles like scratching the surface, damage the sample or damage to the tip.

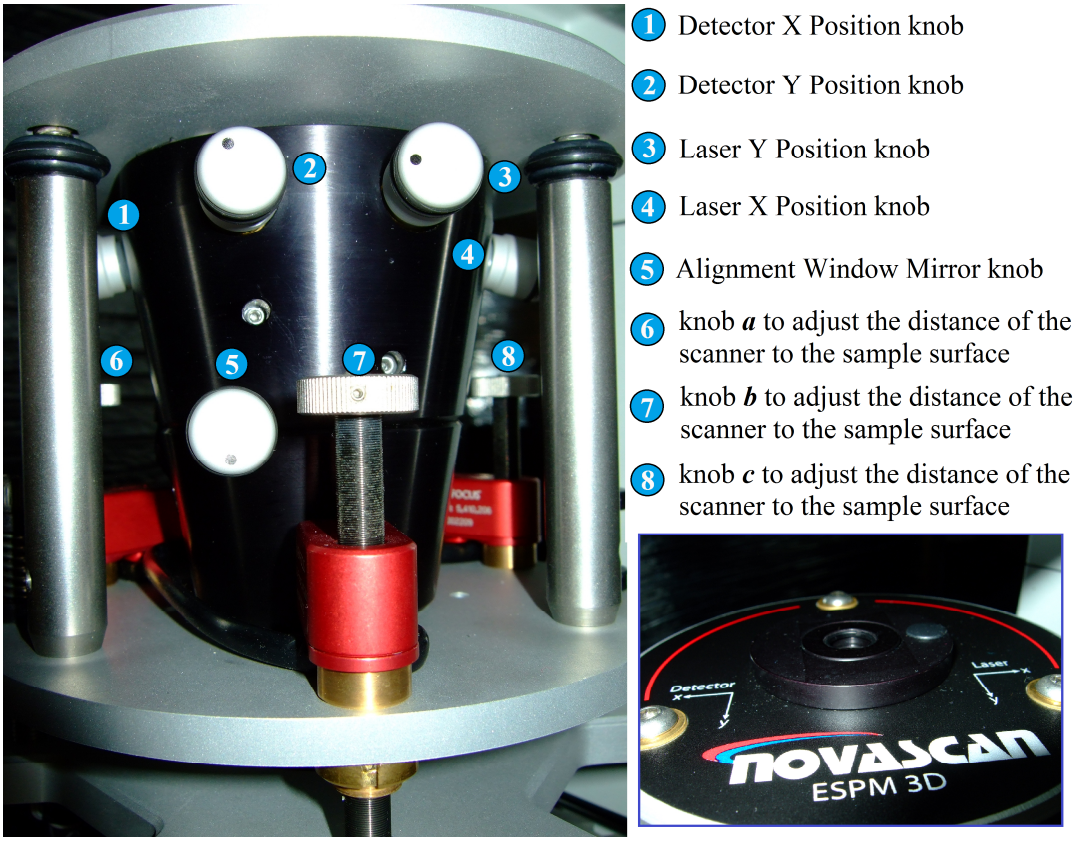

Figure A1. 8 Digital camera image of the topper part of the AFM scanning head. The inset at the right bottom shows the top of the AFM scanning head, which gives axis information for the knobs 1, 2, 3 and 4.

4th, lowering down the AFM head back to the stage with caution so as not to break the probe. Lock the head by clock-wise rotating the knob as shown in Figure A1.9.

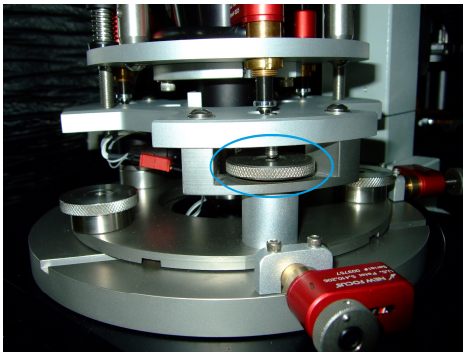

Figure A1. 9 AFM scan head has two parts, upper part and lower part. The knob used to unlock/lock these two parts are circled in the above digital camera image.

5th, align the laser optics. It's straightforward to align the laser optics, just follow the AFM manual. Be careful not to over rotate the Detector X Position knob and Detector Y Position knob (It is the same for Laser Y Position knob and Laser Y position knob; if you can only get good signal when the knob is at a point that it couldn't be rotated anymore, this may be a sign that AFM system needs to be realigned).

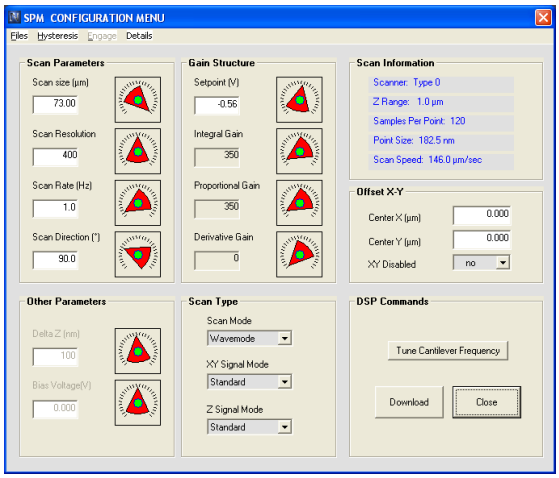

Figure A1. 10 SPM configuration window

6th, choose the scan parameters in the *Configuration* window as shown in Figure A1.10, which determine how an image is going to be obtained. The AFM manual covers the details about the most appropriate value for each parameter.

Contact Mode: choose *Z height* for *Scan Mode*; after choosing the right values of each parameter, it's ready to go for scanning.

Intermittent Contact Mode/Tap Mode: we usually use *Wavemode* as the *Scan Mode*; intermittent contact mode's set-ups are more complicated than that of the contact mode: after choosing the right values of each parameter, click *Download*, *Tune Cantilever Frequency*, and it will automatically close the *SPM Configuration* window (as

shown in Figure A1.10) and meanwhile open a new window, *Wave Configuration* window, to tune the cantilever frequency.

7th, if it's contact mode scan, move on to next step; if it's intermittent contact mode scan, tune the cantilever frequency according to the AFM manual.

8th, follow the AFM manual to engage the probe to the sample surface. Note that if the probe is far from the surface, it would take 'forever' for the probe to engage with the sample surface electronically. One thing you can do to shorten engagement time is to manually lower the probe by anti-clock wisely rotating the three knobs a, b, and c as shown in Figure A1.8. Make sure to rotate the same angle on all three knobs and each time take a small angle rotation; meanwhile turn on the alignment window to pay close attention to the laser spot until it moves or starts to get fussy. At this point, if you didn't rotate all three knobs equally, undo the ones you just rotated. Important: click the *Withdraw* button and withdraw for 50. To get better engagement, it is better to let the system run it electronically. After bring the probe close enough to the surface manually, then withdraw the probe from the surface a certain distance, thus the program can do the engagement electronically. It would take about 5 min.

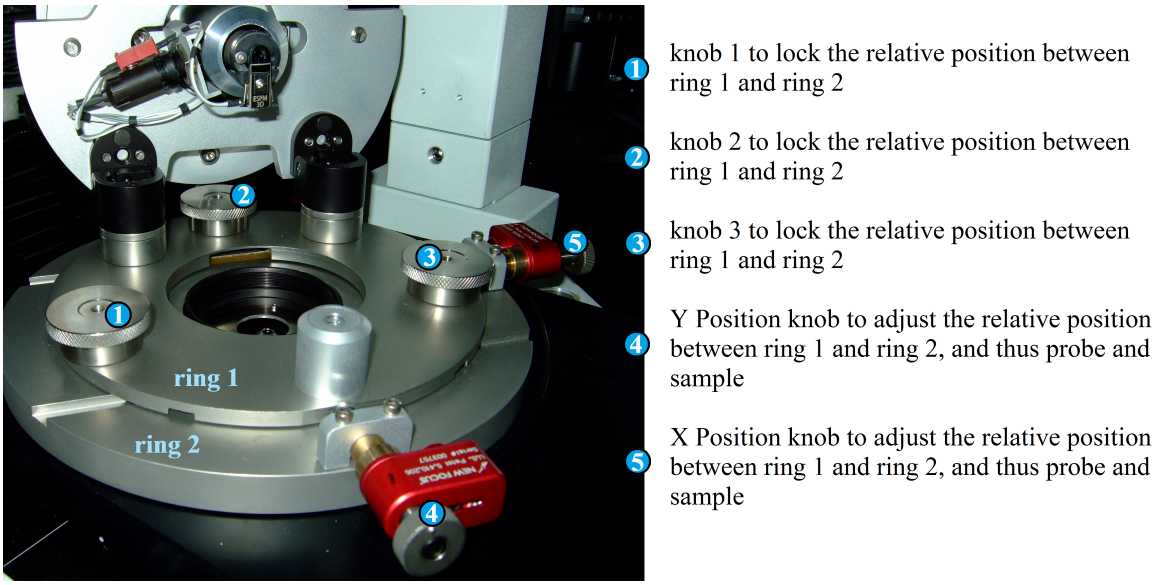

Figure A1. 11 Digital camera image of the lower part of the AFM scanning head

9th, Locate the probe to the interesting area of the sample: 1) focus the objective on the sample (the probe would also be at the focus since it's already engaged to the sample surface); 2) move the sample stage of the Olympic microscope to identify spots/areas need to be scanned; 3) move the probe to the interested area of the sample by firstly unlocking knob 1 and 2 as shown in Figure A1.11, then adjusting X position knob and Y position knob in between ring 1 and ring 2 to move the relative position of the probe and the sample.

We mentioned earlier in this section that the top part of the AFM head is locked to the lower part of the AFM head by the knob shown in Figure A1.9. For the lower part of the AFM head, there are two parts: ring 1 and ring 2 as shown in Figure A1.11. The top part of the AFM head is directly locked to ring 1, thus the probe (installed at the top part of the head) and the ring 1 are one body. The sample holder with the sample is installed at the center of ring 2, so the sample and the ring 2 are one body. Ring 1 and ring 2 are

locked to each other by knobs 1, 2 and 3. Thus, we move the relative position of the probe and the sample through moving the relative position of ring 1 and ring 2. Note: DO NOT unlock knob 1, 2, and 3 at the same time, otherwise ring 1 would bounce up from ring 2 (they are connected by springs). It can damage the scanner.

After moving the probe to the desired area of the sample, it's ready to scan. The AFM manual has detailed description about how to use the program to run the scan.

A1.2 Calibration

Calibration is a procedure which sets the ability of the instrument to accurately measure distances in X, Y and Z directions, using standards of known accuracy. The standards we use were purchased from Mikromasch: TGG01 grating is used to calibrate X axis and Y axis, with the pitch size 3.0 µm as shown in Figure A1.12; TGZ02 grating is used to calibrate Z axis, with the step height 84 nm as shown in Figure A1.13. Note that for the calibration of Z axis, the AFM will be calibrated most accurate in a certain range of the step height. For example, if we use the standard with 84 nm step height, the AFM would be most accurate with sample heights around 100 nm. If the sample heights are in the range of µm, then AFM needs to be recalibrated with a different standard of corresponding step height.

.

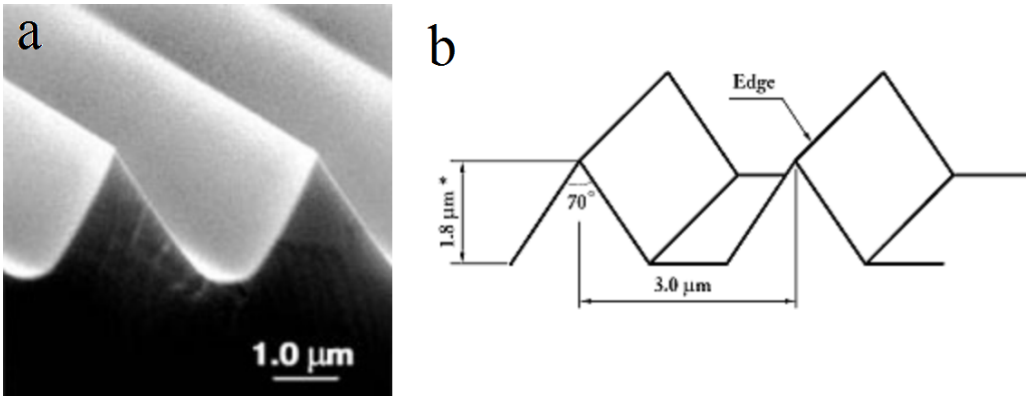

Figure A1. 12 a) SEM image of TGG01 grating, which is for X axis and Y axis calibration; **b**) schematic of TGG01 grating, the step height value is given for information only, not for vertical calibration purposes.

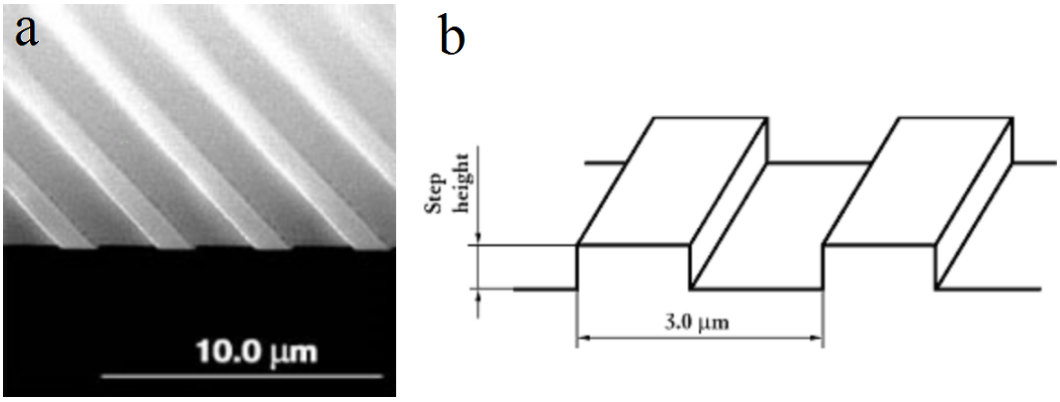

Figure A1. 13 a) SEM image of TGZ02 grating, which is for Z axis; **b**) schematic of TGG02 grating, the step height is 84nm, and the pitch value is given for information only, not for lateral calibration purposes.

A1.2.1 Standard Alignment

To get good images for calibration, the gratings need to be aligned (either parallel or perpendicular) to the scanning probe as shown in Figure A1.14a; it's tolerable if it's within ±2º degrees of tilt; otherwise, the tilt may affect the accuracy of the calibration. The schematic in Figure A1.14 is for demonstration of alignment only, the relative sizes of the gratings and the AFM probe are not necessarily correct.,

One little trick to help align the standard is to use the two knobs on the sample holder (as shown in Figure A1.3b) as a reference: if we draw a line to go through these two knobs, this line is either aligned with the X axis or the Y axis of the scanning direction depends on how we position the sample holder. Try to align the patterns of the standard with these two knobs by eyes, then scan; if the grating lines in the scanned image are not within ±2º degrees of tilt, withdraw the scan head, adjust the standard, and scan again, until it's well aligned. These trial scans can be stopped as soon as we can tell if it's well aligned or tilted.

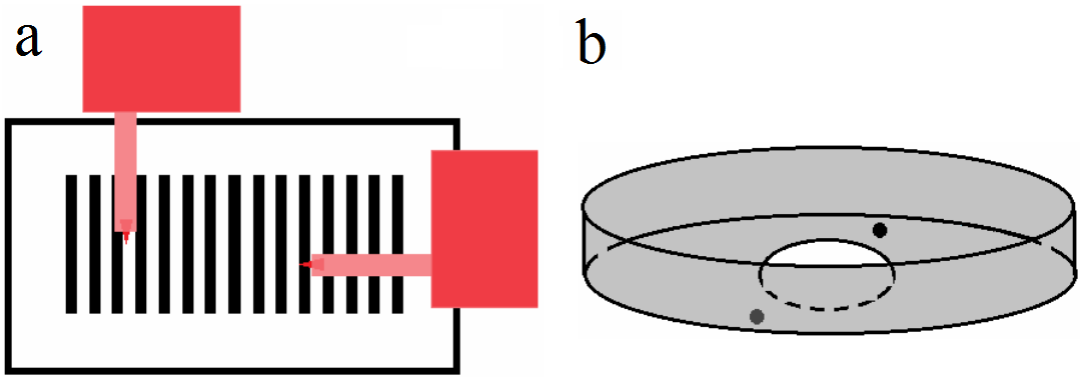

Figure A1. 14 a) Schematic of the parallel or perpendicular alignment of the gratings with the AFM probe; **b**) AFM sample holder, the two knobs can serve as reference to help alignment.

Figure A1.15 shows the scanned images of well-aligned standard. Figure A1.15a shows pitches aligned vertically with Y axis, and it's for X axis calibration; Figure A1.15b shows pitches aligned horizontally with X axis, and it's for Y axis calibration. Note that the minimum number of pitches shown in a scanned image qualified for calibration is five; since the pitch size of the standard we use is 3 µm, 5 pitches would be

15 µm. Thus, with 3 µm pitch size standard, 15 x 15 µm scan is the smallest scanning size. We will explain later about the minimum scanning size.

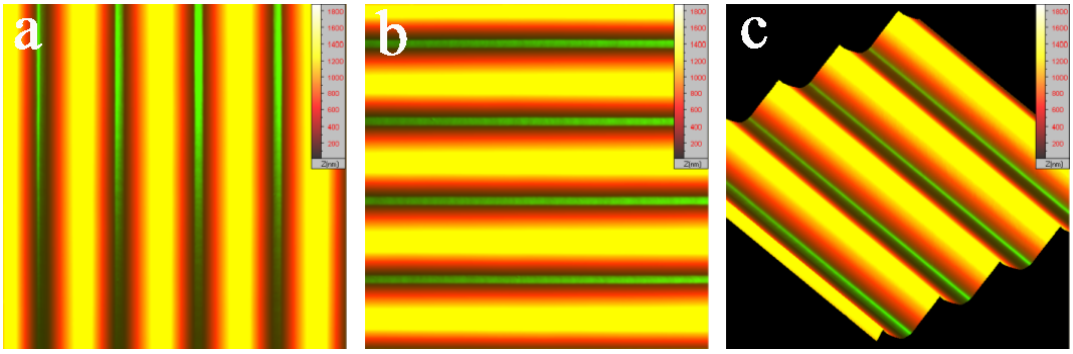

Figure A1. 15 AFM images **a**) the gratings aligned for X axis calibration; **b**) gratings aligned for Y axis calibration; **c**) 3D appearance for **a**) and **b**), these are 15x15 µm scans.

A1.2.2 Back Up the Spm.ini File

Note that it's always good to back up the original spm.ini file before calibration. Spm.ini is a file which contains the information of calibration factors for X, Y and Z axis; for example, the Z axis calibration factor (Ceramic Z Expansion) specifies the maximum Z motion of the probe when the maximum Z axis voltage is applied to the PZT. The spm.ini file contains different sections entitled with [head number], and the main change from the new calibration will be seen under the section of [head 11]. If a mistake happened in the process of calibration, we can always apply the original spm,ini file, and restart from there.

A1.2.3 Multi-Scan Calibration vs. Single-Scan Calibration

There are two methods available for calibrating the XY performance of the instrument. (I) Calibrate by single-scan, where the system uses the results of one scan to predict the scanner characteristics over the full lateral range of the PZT. (II) Calibrate by multi-scans, where the system performs several scans at different scan sizes to more accurately calibrate the movement of the PZT across the full lateral range of the instrument. We used multi-scan calibration after the fact that single-scan calibration was not enough to calibrate our system. A common problem for single-scan-calibrations is that the pitch size varies from the center to the edge of the scanned area. Figure A1.16 illustrates that the pitch size in the center appears larger than the pitch size in the edge.

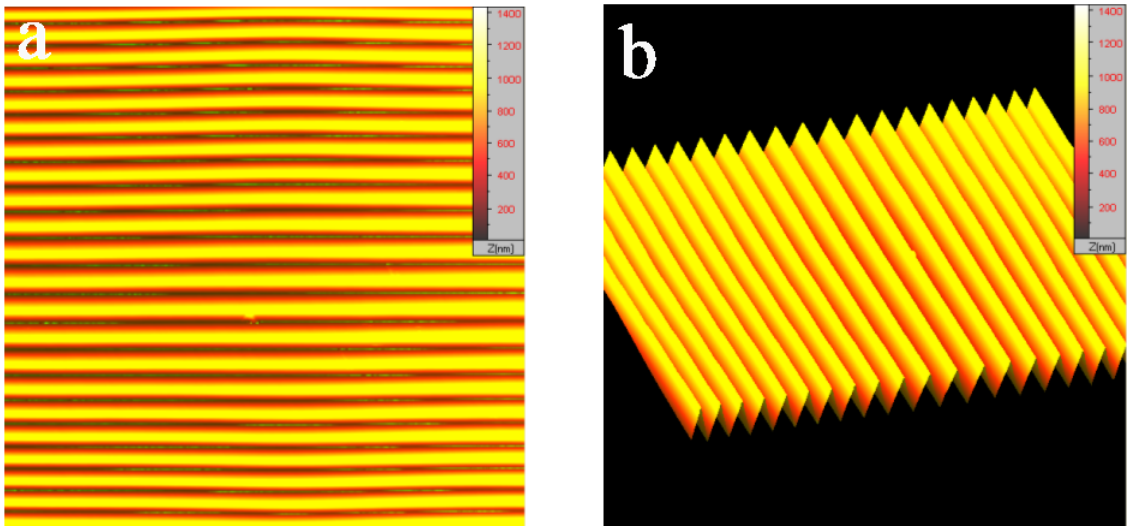

Figure A1. 16 AFM images **a)** In a 80x80 µm scan the pitch in the center of the image appears larger than the pitch in the edgy; **b)** 3D appearance of image **a).**

The solution to this problem is to run a multi-scan calibration, which starts with the smallest scan size, and then works all the way up to the largest scan size. In this way the software is only making small corrections each time to the spm.ini file and it gives more accurate results. One important thing is that to achieve the most accurate scanning

results for data collection, always calibrate close to the scanning size you will use to acquire data. For example, don't calibrate X axis and Y axis to 80 µm and then collect data using 40 µm scans (we only need to calibrate to 40 µm if we will acquire data by 40 µm scans); or calibrate Z axis at 100 nm and then collect data with sample heights of several micrometers.

A1.2.4 X-axis Calibration

Scan configuration parameters set-up:

Scan type needs to match the type of cantilever. Select *Z height* for a contact type cantilever and *Wavemode* for intermittent contact type cantilever.

Scan size Start with the smallest scan size, could be 15 µm or 20 µm, then increase 5 µm or 10 µm each time, until the size of the scan head; for example, if 80x80 µm scan head is chosen, start with 15 µm, then 20 µm, 30 µm, 40µm, 50 µm, 60 µm, 65 µm, 70 µm, 75 µm, and 80 µm. With the choice of scan head, choose the one most close to the scan size for the future data acquirements.

Scan rate 1 Hz is good. Exception: if the sample surfaces need to be scanned with very slow rate, for example, 0.2 Hz, then the best accuracy would be achieved by calibrating at the same slow rate.

Setpoint Follow the manual instructions, depending on the type of cantilever.

Scan Direction Always set to 0º. Note that we can use 0º or 90º or any direction while collecting data, but the scan direction can only be set to 0º.

Intergral, Proportional, and Derivative Gain Typical settings would be 350, 350, and 0, respectively. Values should be varied to suit the particular cantilever being used, however.

Scan Resolution 300 for 20 µm and 40 µm scan heads, 400 for 80 µm scan head, and 1000 for 180 µm scan head.

XY Disabled, Center X, Center Y Set to No, 0, 0, respectively.

XY Signal Mode, Z signal Mode These must be set to 'Standard'.

After scanning, the lines of the grating are aligned vertically with the Y axis as shown in Figure A1.15a; if necessary, use *Streak Removal* to remove defects in the image, such as dust particles and bridges between the lines. Then go to *Dimention*/*Calibration Menu*/*Set Grating Reference*, set 3 µm for the pitch size when using TGG01, or corresponding value match the grating being used. Next step, go to *Dimention*/*Calibration Menu*/*X axis: Grating***,** to initiate the calibration. After the software analyzes the current scan and gives potential calibration factors, check the predicted 'actual scan size', if it matches the expected scan size (pitch size x numbers of pitches), click 'yes' at the dialog box to update the calibration of the instrument.

A1.2.5 Y-axis Calibration

Rotate the grating 90º on the sample holder after the calibration for X axis and make sure to align the grating to the probe. The settings of scanning parameters for Y axis calibration are the same as the settings for X axis calibration; the procedure for Y

axis calibration is similar to the procedure for X axis calibration, one thing different is that after scanning, the image needs to be rotated 90º first by clicking *Dimention*/*Calibration Menu/Rotate image 90º*.

A1.2.5 Z-axis Calibration

Most settings of the scanning parameters for Z axis calibration are the same as the settings for X, Y axis calibration. One thing different is that Z-axis calibration has to be carried out under tapping mode (*Wavemode*) with intermittent-contact cantilever. After scanning, first flatten the image using *3-point* flattening filter; then open the *Dimension Analysis* window, select the *Horizontal Section* under *Profile* to create a horizontal cross-section of the scanned surface. Next step, go to *Calibration Menu*/*Z axis: Two Point*, to initiate Z-axis calibration. Place the red and green cursors at an adjacent crest and trough in the cross-section. Note that the vertical distance between these two points (based on the current Z calibration factor in the system) is shown in the lower-right corner of the window. Press OK to continue with the calibration, or Cancel to cancel the process. A dialog box will appear requesting the known vertical separation between the green and red markers. Enter the manufacture's step height value. Be sure to pay attention to the units of this number. Press OK to complete the Z axis calibration.

A1.3 Packing Instructions

In 2010, we sent our AFM system back to be realigned. Here are the packing instructions. Figure A1.17 shows items needed to realign AFM system: AFM head, stage box, tip holder, sample holder and scanner.

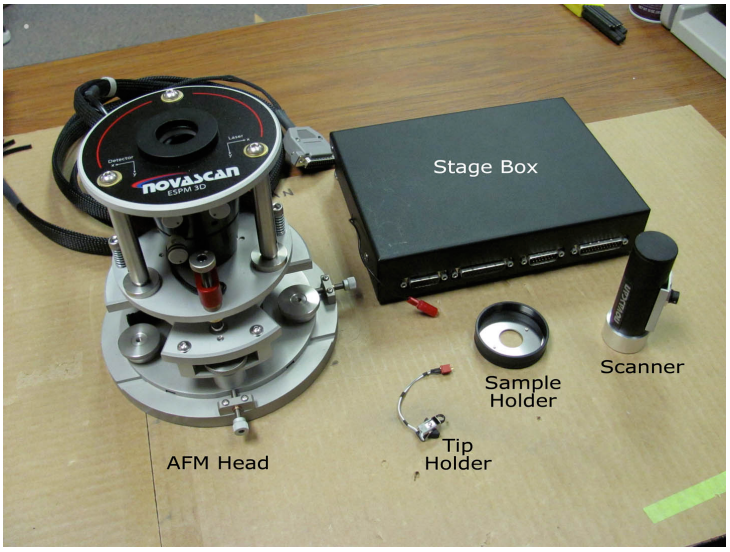

Figure A1. 17 Items needed to realign AFM system: AFM head, stage box, tip holder, sample holder assembly and scanner assembly.

Step 1) first label the stage box and connecting cables with masking tape for easier set up upon return, then disconnect all AFM cables from the stage box.

Steps 2) remove the sample holder from AFM head and set aside.

Steps 3) remove the scan tube and install the scanner shipping cover. Be sure to protect the scan tube from damage at all times. (The scanner shipping cover is located in a zip bag with label in the AFM packing boxes).

Step 4) Center the X/Y stage of ring 1 and ring 2 and install the shipping retainers under all X/Y translation lock down knobs, then tighten the lock down knobs as shown in Figure A1.18. (Shipping retainers are located in a zip bag with label in the AFM packing

boxes). Note that not unscrew the three lock-down knobs at the same time, always keep at least one knob tighten; otherwise ring 1 would be bounced up from ring 2.

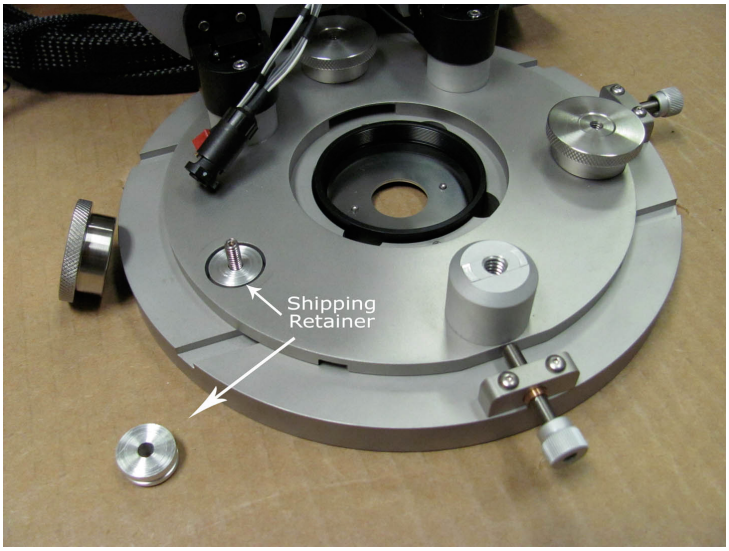

Figure A1. 18 Unscrew the lock-down-knobs which connect ring 1 and ring 2, install the shipping retainer as shown in the above Figure, and then screw the knobs back. It is recommended to do with the order of unscrew one lock-down knob, install the shipping retainer, screw knob back, and move on to next knob.

Step 5) Make sure all knobs and screws on the AFM head are tight and secure. Our scanner is removable, but for systems not having removable scanner assembly, make sure there are no loose parts that could impact the scan tube during shipping. Also make sure the stage assembly is raised up high enough so the scanner will not be impacted from the bottom by the box or packaging.

Step 6) Wrap the AFM head assembly in the anti-static bubble wrap. The head cables should be oriented to the top of the AFM head as shown in Figure A1.19.

Step 7) Place the AFM head in the inner packing box. Make sure translation screws are oriented to the corners of the box as shown in Figure A1.20.

Figure A1. 19 Wrap the AFM head with anti-static bubble wrap; with the cables oriented to the top of the AFM head.

Figure A1. 20 Place the wrapped AFM into the inner packing box with foam at the bottom, make sure to have translation screws are oriented to the corners of the box**.**

Step 8) Pack the gray foam around the AFM head as shown in Figure A1.21. Make sure the AFM head is secure in the box and can not move from side to side.

Figure A1. 21 Pack more foam around AFM head inside of inner packing box

Step 9) Coil the AFM cables and place them on top of AFM head. Orient the connectors so they don't damage the top of the AFM head as shown in Figure A1.22.

Figure A1. 22 Coil the AFM cables and place them on top of AFM head

Step 10) Seal the inner box and insert the corner foam protectors both at the bottom and at the top as shown in Figure A1.23.

Figure A1. 23 Add foam protectors between the inner packing box and outer packing box.

Step 11) Seal the outer box and ship by next day delivery.

Step 12) Pack the stage box, sample holder, tip holder and scanner assembly in a separate box and ship by next day delivery. Wrap all parts in sufficient foam or bubble wrap to prevent damage. Double boxing is always safer than single boxing.

A1.4 Scanner Installation

After realignment, AFM system needs to be reinstalled by following the opposite steps of AFM packing instruction. Here is some advice for installing AFM scanner. Make sure the power to the AFM controller is turned off when the scanner connector is unplugged.

Step 1) Unscrew and remove the scanner protection cover as shown in Figure A1.24. The scan tube will be especially vulnerable at this time. Use care not to touch or jar the exposed tube.

Figure A1. 24

Step 2) screw the scanner bezel ring onto the end of the scan tube as shown in Figure A1.25. Again, using care not to touch or jar the exposed scan tube.

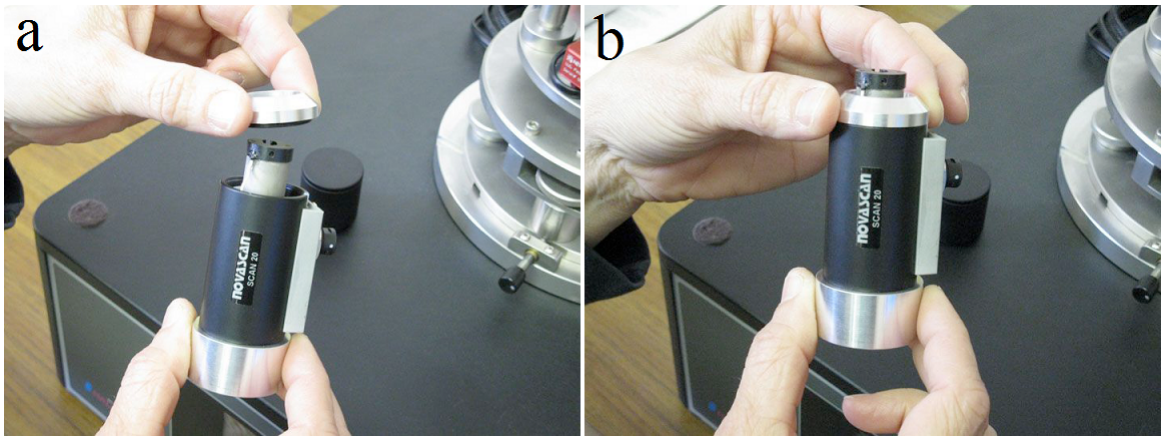

Figure A1. 25

Step 3) Insert the scan tube assembly into the scanner clamp in the AFM head, make sure to 'seat' the scanner fully into the position. Align the scanner so that the oblong opening in the scanner end is perpendicular to the stage base as shown in Figure A1.26. The scanner may also be rotated to obtain the best alignment once the tip holder and probe have been mounted.

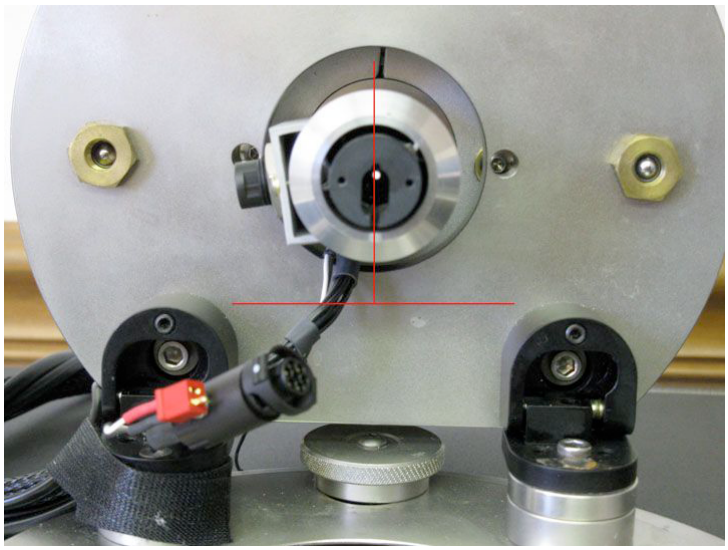

Figure A1. 26

Step 4) Tighten the side scanner clamp screw as shown in Figure A1.27.

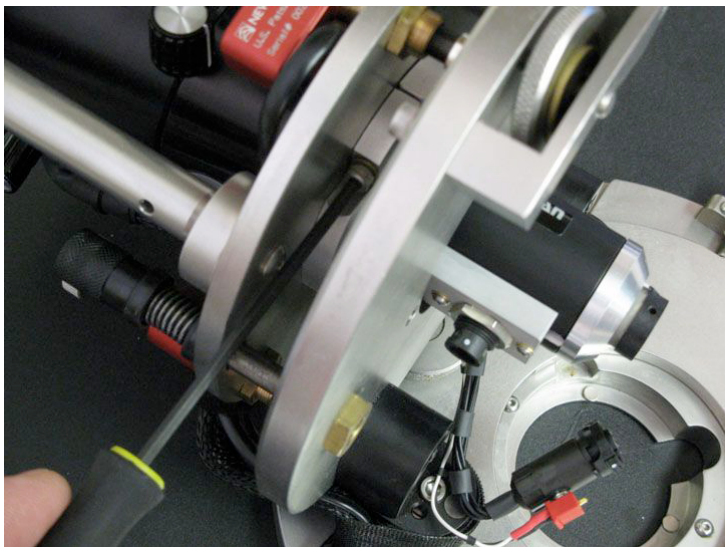

Figure A1. 27

Step 5) Tighten the right front scanner clamp screw as shown in Figure A1.28. Note that the left front scanner clamp screw should remain tightened at all times.

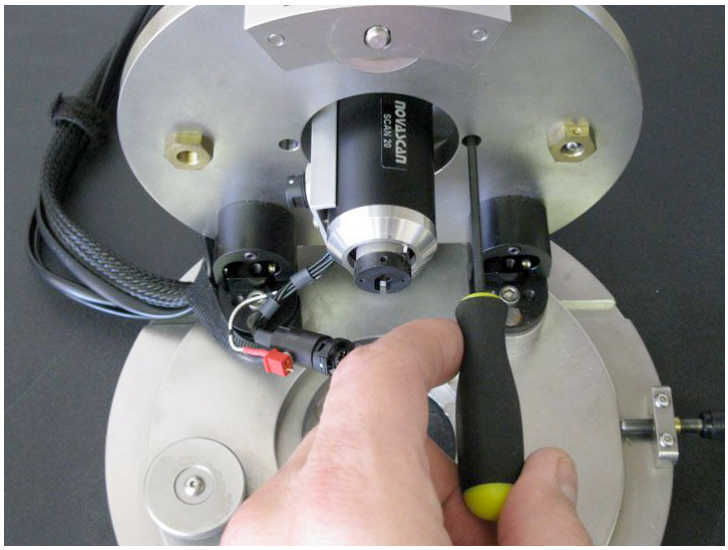

Figure A1. 28

Step 6) Line up the white dots on the scanner connector and push the pieces together as shown in Figure A1.29. Squeeze the top and bottom of the top and bottom of the connector and pull to release.

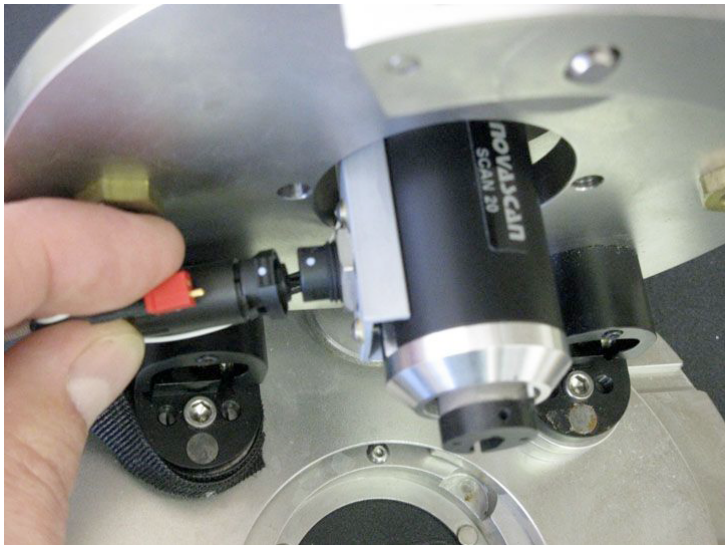

Figure A1. 29

The scanner is now installed.

A1.5 Parameters for AFM probes

Intermittent contact mode probe:

NSC35, Cantilevers	Resonant Frequency, kHz			Spring Constant, N/m			Length l±5,µm	Width w±3,µm	Thickness t±0.3,µm
	min	typ	max	min	typ	max			
A	165	210	240	3.5	7.5	12.5	110	35	2
B	240	315	405	6.5	14	27.5	90		
C	120	150	190	3.5	4.5	8.5	130		

Table A1. 1 Parameters for AFM probe NSC35

Appendix II Properties of anthracene ester derivatives

A2.1 Melting point of 1 to 13

Table A2. 1 Melting points of anthracene ester derivatives

Anthracene esters	Melting Point(°C)
1	110~111
2	112~113
3	74~76
4	44.5~46
5	42~43
6	56.5~57
7	92.5~93.5
8	158~159
9	126~127
10	105.5~106.5
11	125~126
12	124~125
13	211~212

A2.2 NMR Spectra of 1 to 13

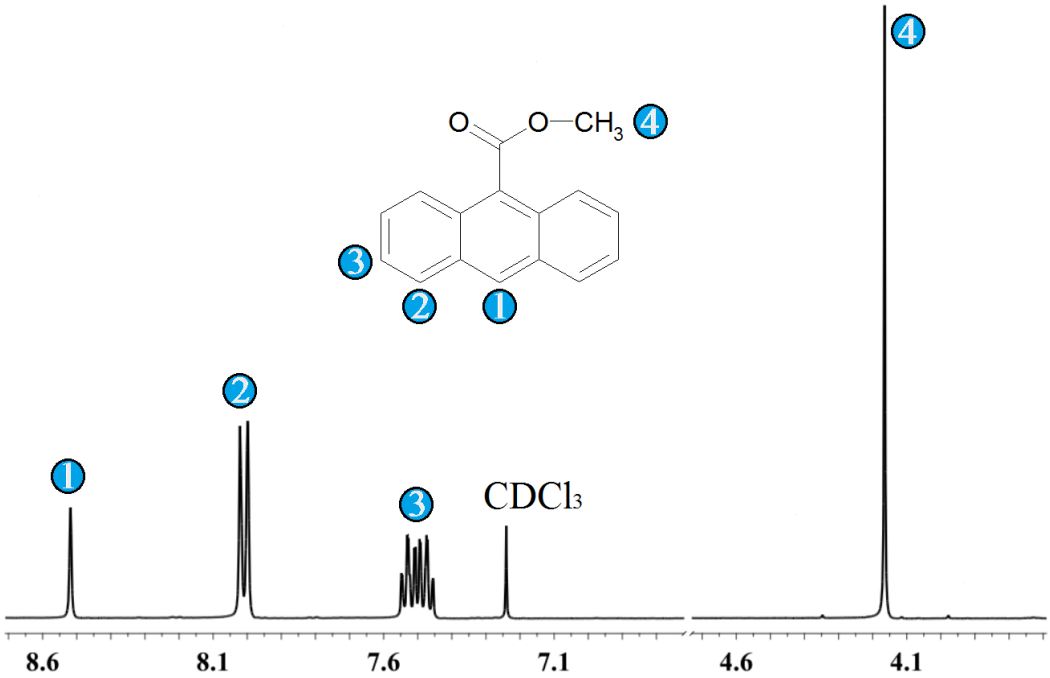

Figure A2. 1 ^{1}H-NMR (400Hz) of **1** in $CDCl_3$: δ 4.17 (s, 3H), 7.51 (m, 4H), 8.01 (d, 4H), 8.52 (s, 1H)

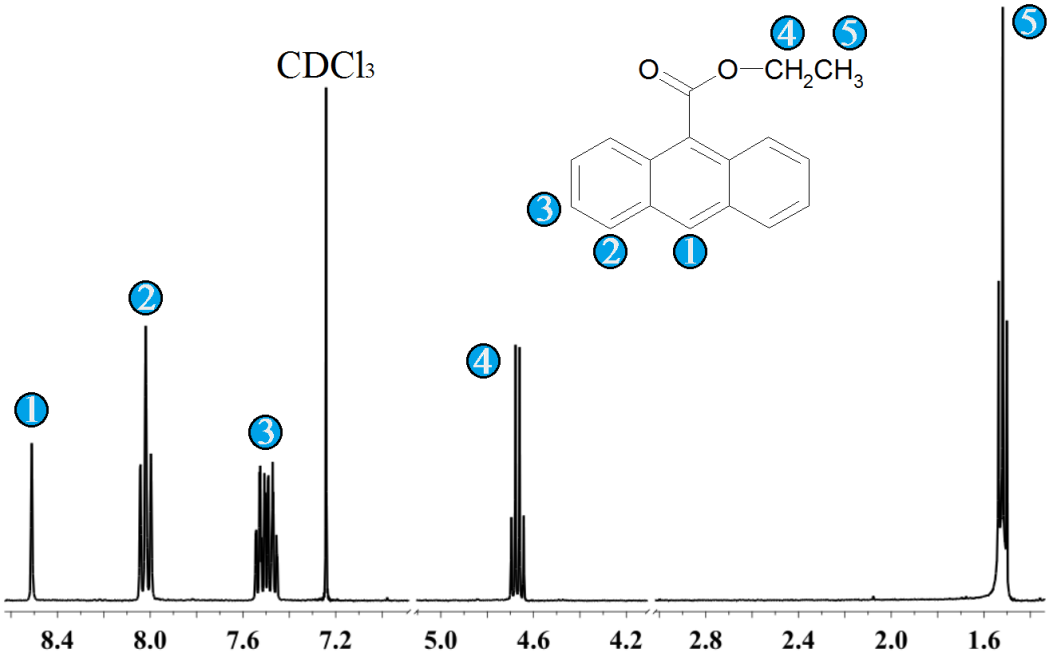

Figure A2. 2 ^{1}H-NMR (400Hz) of **2** in $CDCl_3$: δ 1.52 (t, 3H), 4.67 (m, 2H), 7.51 (m, 4H), 8.02 (m, 4H), 8.51 (s, 1H)

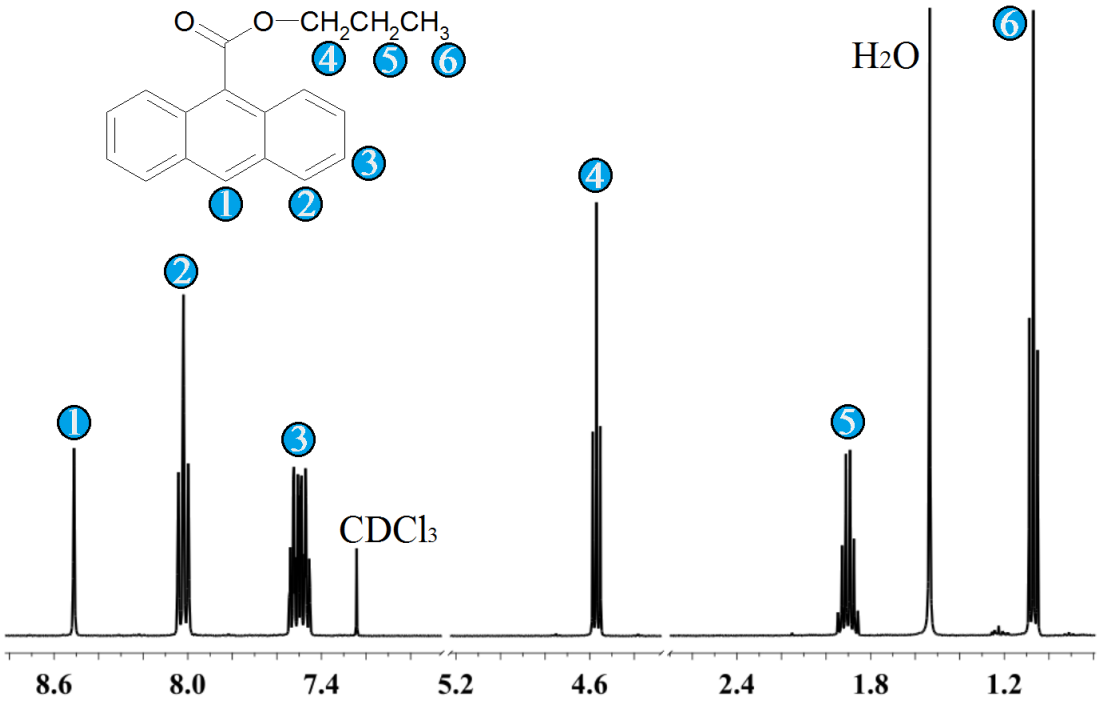

Figure A2. 3 ^{1}H-NMR (400Hz) of **3** in $CDCl_3$: δ 1.06 (m, 3H), δ 1.89 (m, 2H), 4.57 (m, 2H), 7.51 (m, 4H), 7.99 (m, 4H), 8.51 (s, 1H)

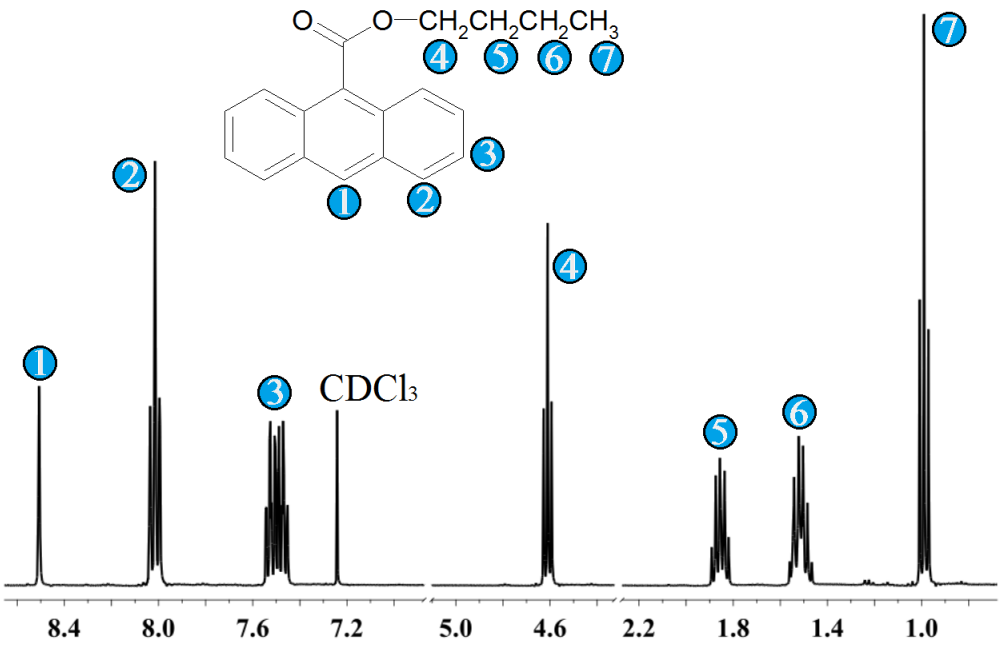

Figure A2. 4 ^{1}H-NMR (400Hz) of **4** in $CDCl_3$: δ 0.95 (m, 3H), 1.50 (m, 2H), 1.85 (m, 2H), 4.59 (m, 2H), 7.49 (m, 4H), 8.00 (m, 4H), 8.50 (s, 1H

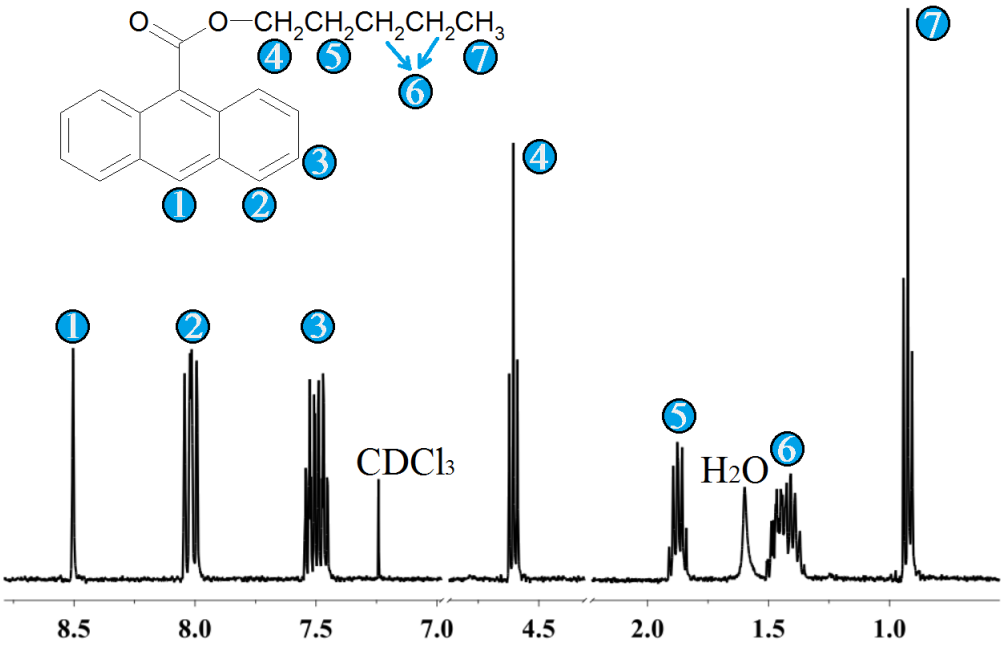

Figure A2. 5 ^{1}H-NMR (400Hz) of **5** in $CDCl_3$: δ 0.91 (m, 3H), 1.40 (m, 4H), 1.88 (m, 2H), 4.60 (m, 2H), 7.48 (m, 4H), 7.99 (m, 4H), 8.49 (s, 1H). Peak at 1.54 is from water.

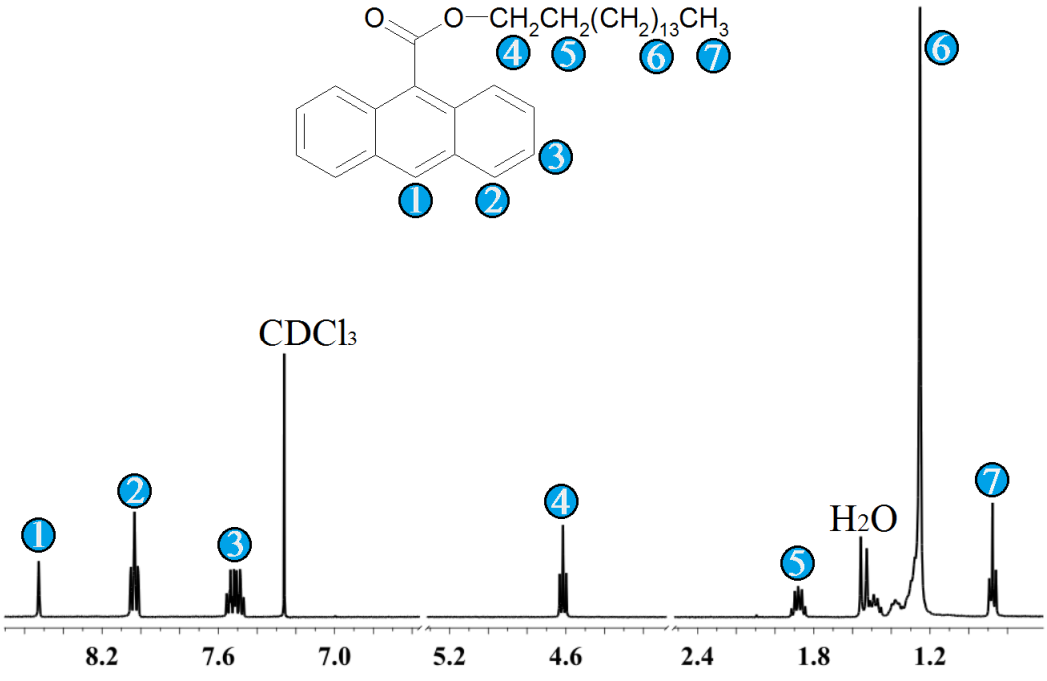

Figure A2. 6 ^{1}H-NMR (400Hz) of **6** in $CDCl_3$: δ 0.86 (m, 3H), 1.43 (m, 26H), 1.85 (m, 2H), 4.59 (m, 2H), 7.50 (m, 4H), 8.01 (m, 4H), 8.51 (s, 1H)

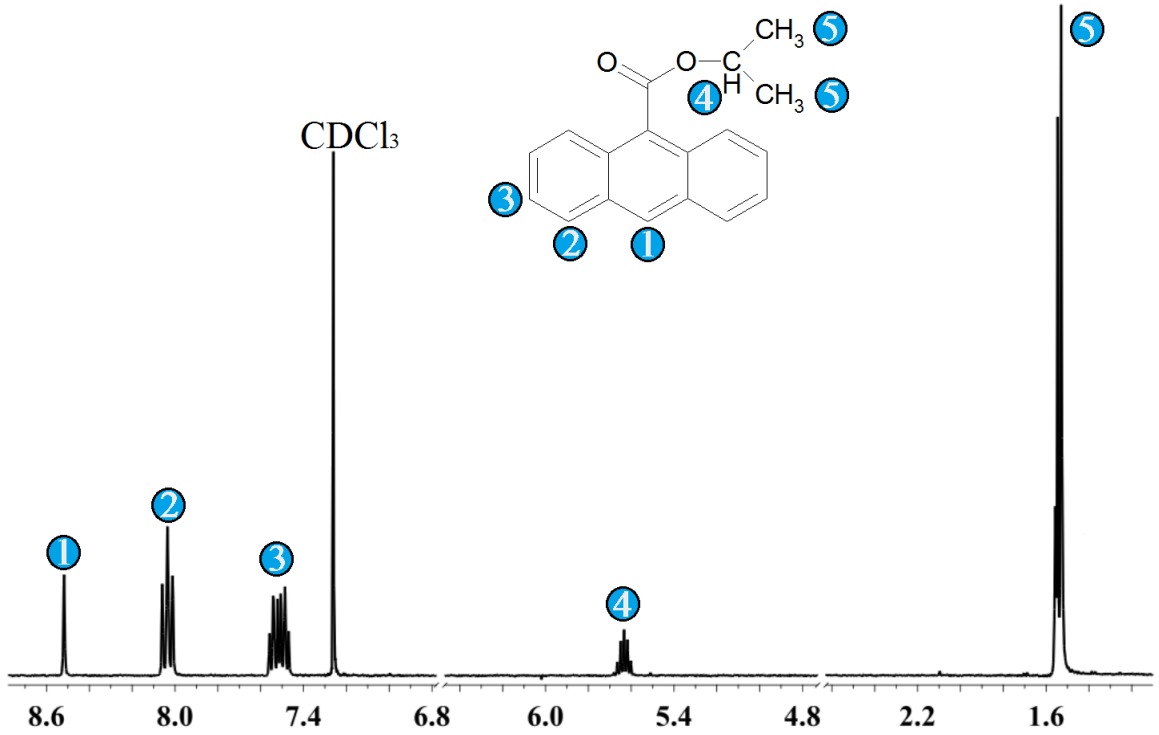

Figure A2. 7 ^{1}H-NMR (400Hz) of **7** in $CDCl_3$: δ 1.54 (d, 6H), 5.63 (m, 1H), 7.51 (m, 4H), 8.03 (m, 4H), 8.52 (s, 1H).

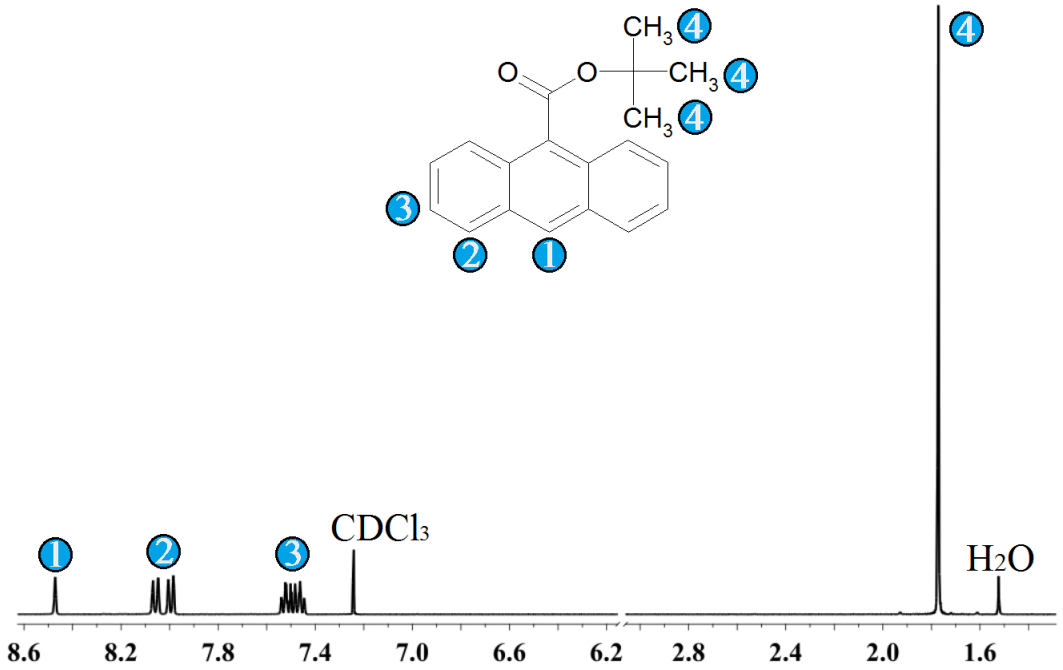

Figure A2. 8 ^{1}H-NMR (400Hz) of **8** in $CDCl_3$: δ 1.77 (s, 9H), 7.50 (m, 4H), 8.03 (m, 4H), 8.47 (s, 1H). Peak at 1.54 is from water.

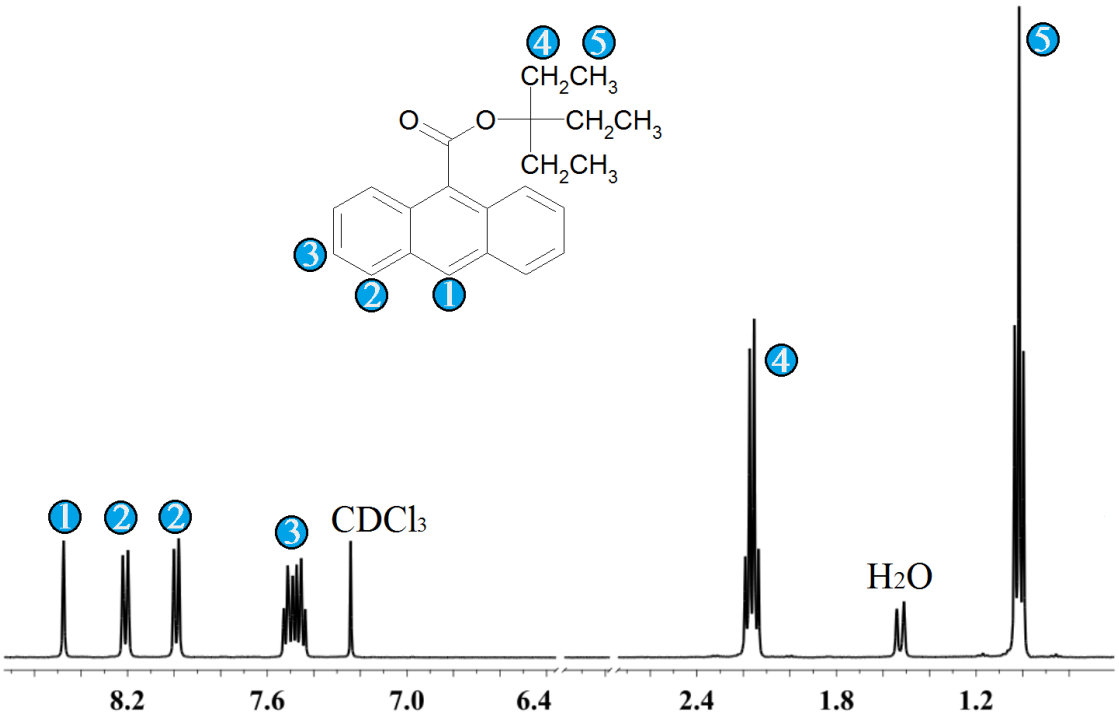

Figure A2. 9 ^{1}H-NMR (400Hz) of **9** in $CDCl_3$: δ 1.01 (t, 9H), 2.16 (q, 6H), 7.48 (m, 4H), 7.99 (d, 2H), 8.21 (d, 2H), 8.47 (s, 1H). Peaks at 1.54 are from water.

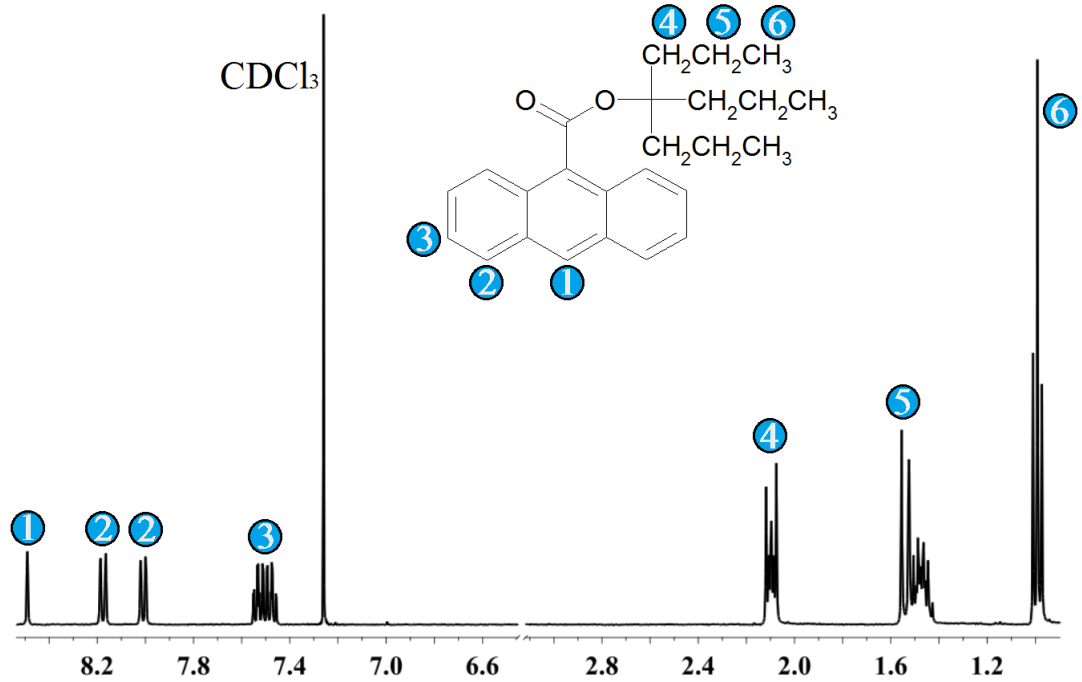

Figure A2. 10 ^{1}H-NMR (400Hz) of **10** in $CDCl_3$: δ 0.98 (t, 9H), 1.45 (m, 6H), 2.08 (m, 6H), 7.50 (m, 4H), 7.99 (d, 2H), 8.16 (d, 2H), 8.48 (s, 1H)

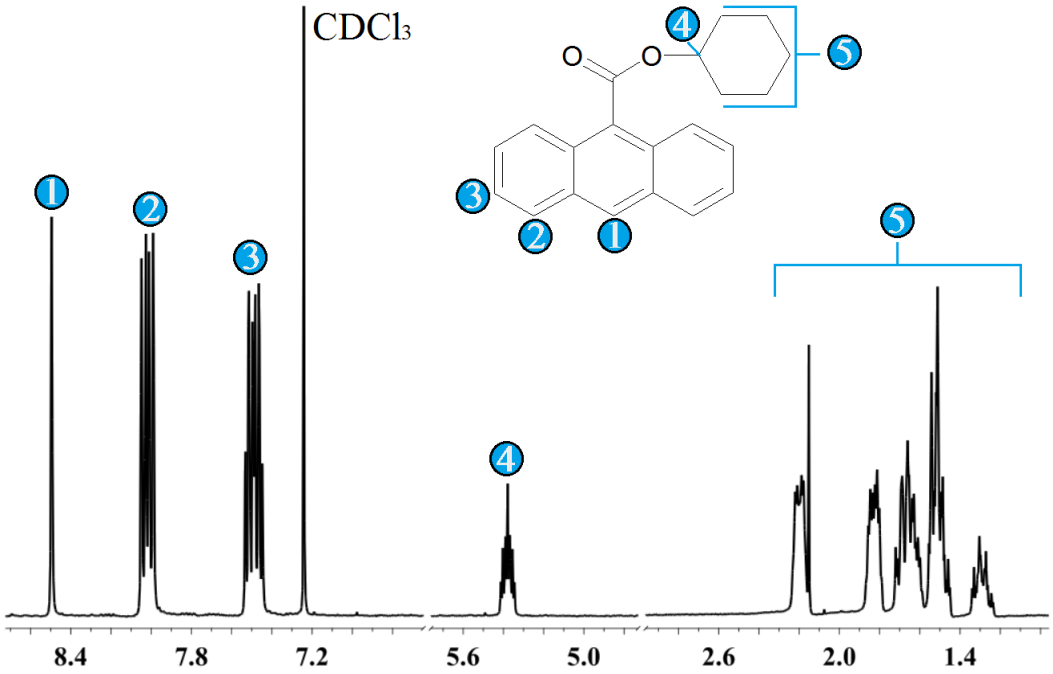

Figure A2. 11 ^{1}H-NMR (400Hz) of **11** in $CDCl_3$: δ 1.29 (m, 2H), 1.59 (m, 4H), 1.81 (m, 2H), 2.17 (m, 2H), 5.38 (m, 1H), 7.49 (m, 4H), 8.02 (m, 4H), 8.50 (s, 1H)

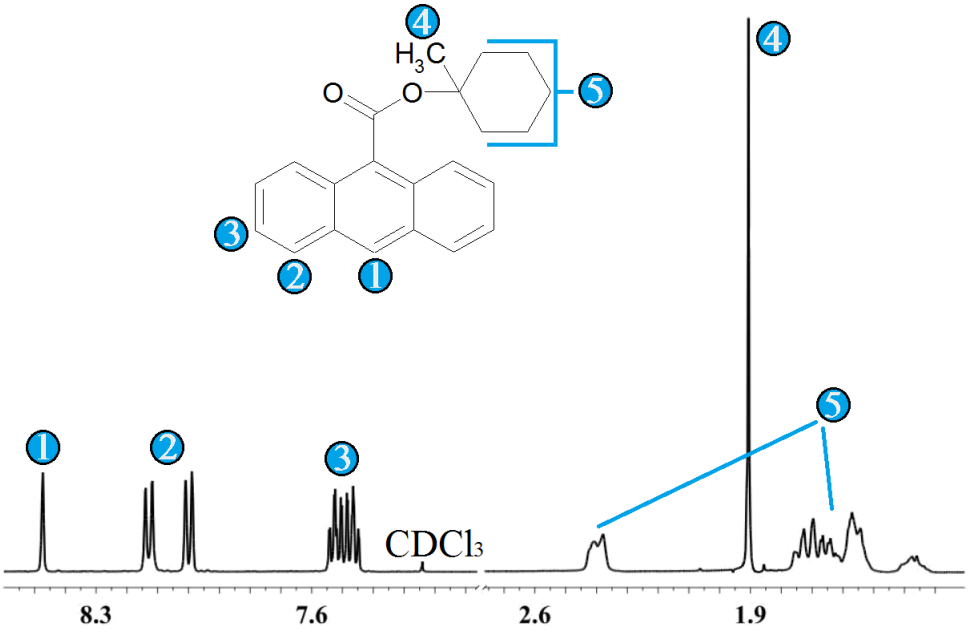

Figure A2. 12 ^{1}H-NMR (400Hz) of **12** in $CDCl_3$: δ 1.55 (m, 8H), 1.91 (s, 3H), 2.40 (m, 2H), 7.49 (m, 4H), 8.00 (d, 2H), 8.13 (d, 2H), 8.47 (s, 1H).

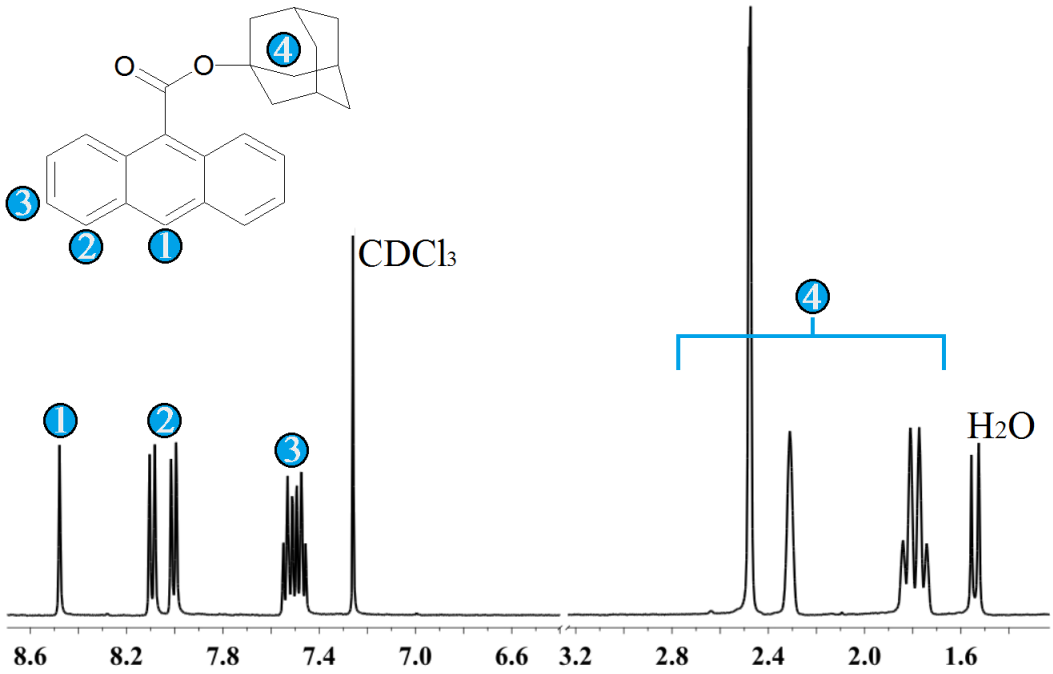

Figure A2. 13 ^{1}H-NMR (400Hz) of **13** in $CDCl_3$: δ 1.77 (m, 6H), 2.29 (s, 3H), 2.45 (s, 6H), 7.48 (m, 4H), 8.03 (d, 4H), 8.46 (s, 1H). Peaks at 1.54 are from water.

Table A2. 2 Crystal data and refinement for compounds 1-3

Compund	**1**	**2**	**3**
Empirical formula	$C_{16} H_{12} O_2$	$C_{17} H_{14} O_2$	$C_{18} H_{16} O_2$
Formula weight	236.26	250.28	264.31
Temperature	100(2) K	100(2) K	296(2) K
Wavelength	0.71073 Å	0.71073 Å	0.71073 Å
Crystal system	Monoclinic	Orthorhombic	Triclinic (#2)
Space group	P2(1)/n	Pna2(1)	P-1
Unit cell dimensions	a = 11.2274(4) Å α= 90°	a = 8.5056(7) Å α= 90°	a = 7.8529(4) Å α= 87.9208(8)°
	b = 7.6159(3) Å β= 104.9815(5)°	b = 10.1688(8) Å β= 90°	b = 8.5743(4) Å β= 80.4985(8)°
	c = 14.2498(5) Å γ = 90°	c = 14.4684(12) Å γ = 90°	c = 11.4604(6) Å γ = 67.0534(7)°
Volume	1177.04(7) $Å^3$	1251.40(18) $Å^3$	700.52(6) $Å^3$
Z	4	4	2
Density (calculated)	1.333 Mg/m^3	1.328 Mg/m^3	1.253 Mg/m^3
Absorption coefficient	0.087 mm^{-1}	0.086 mm^{-1}	0.081 mm^{-1}
F(000)	496	528	280
Crystal size	0.55 x 0.50 x 0.43 mm^3	0.60 x 0.22 x 0.21 mm^3	0.51 x 0.30 x 0.20 mm^3
θ range for data collection	2.07 to 29.13°	2.45 to 30.02°	1.80 to 29.57°
Index ranges	-15<=h<=15, -9<=k<=10, -19<=l<=19	-11<=h<=11, -14<=k<=14, -20<=l<=20	-10<=h<=10, -11<=k<=11, -15<=l<=15
Reflections collected	12258	17886	15701
Independent reflections	3170 [R(int) = 0.0162]	3654 [R(int) = 0.0249]	3918 [R(int) = 0.0146]
Completeness to θ = 29.13°	99.8 %	99.9 %	99.8 %
Absorption correction	Semi-empirical from equivalents	Semi-empirical from equivalents	Semi-empirical from equivalents
Max. and min. transmission	0.9636 and 0.9536	0.9823 and 0.9502	0.9839 and 0.9603
Refinement method	Full-matrix least-squares on F^2	Full-matrix least-squares on F^2	Full-matrix least-squares on F^2
Data / restraints / parameters	3170 / 0 / 164	3654 / 1 / 173	3918 / 175 / 238
Goodness-of-fit on F_2	1.070	1.063	1.059
Final R indices [I>2sigma(I)]	R1 = 0.0405, wR2 = 0.1173	R1 = 0.0335, wR2 = 0.0872	R1 = 0.0482, wR2 = 0.1469
R indices (all data)	R1 = 0.0438, wR2 = 0.1207	R1 = 0.0360, wR2 = 0.0895	R1 = 0.0672, wR2 = 0.1676
Largest diff. peak and hole	0.367 and -0.274 e.$Å^{-3}$	0.374 and -0.174 e.$Å^{-3}$	0.228 and -0.163 e.$Å^{-3}$

Table A2. 3 Crystal data and refinement for compounds 4-6

Compound	**4**	**5**	**6**
Empirical formula	$C_{19}H_{18}O_2$	$C_{20}H_{20}O_2$	$C_{31}H_{42}O_2$
Formula weight	278.33	292.36	446.65
Temperature	296(2) K	100(2) K	100(2) K
Wavelength	0.71073 Å	0.71073 Å	0.71073 Å
Crystal system	Monoclinic	Triclinic (#2)	Triclinic
Space group	P2(1)/c (#14)	P-1	P-1
Unit cell dimensions	a = 9.783(3) Å α= 90° b = 8.098(3) Å β= 97.331(5)° c = 19.488(6) Å γ = 90°	a = 8.6243(7) Å α= 113.3094(12)° b = 9.3234(8) Å β= 101.2927(12)° c = 10.7823(9) Å γ = 93.6011(13)°	a = 6.9024(4) Å α= 87.7209(10)° b = 9.0519(6) Å β= 82.2444(10)° c = 20.6141(13) γ = 82.4091(10)°
Volume	1531.3(9) $Å^3$	771.27(11) $Å^3$	1264.68(14) $Å^3$
Z	4	2	2
Density (calculated)	1.207 Mg/m^3	1.259 Mg/m^3	1.173 Mg/m^3
Absorption coefficient	0.077 mm^{-1}	0.080 mm^{-1}	0.071 mm^{-1}
F(000)	592	312	488
Crystal size	0.34 x 0.33 x 0.25 mm^3	0.23 x 0.22 x 0.12 mm^3	0.55 x 0.29 x 0.05 mm^3
θ range for data collection	2.10 to 25.68°	2.12 to 29.57°	1.99 to 28.70°
Index ranges	-11<=h<=11, -9<=k<=9, -23<=l<=23	-11<=h<=11, -12<=k<=12, -14<=l<=14	-9<=h<=9, -12<=k<=12, -27<=l<=27
Reflections collected	16430	16933	26928
Independent reflections	2898 [R(int) = 0.0223]	4295 [R(int) = 0.0279]	6537 [R(int) = 0.0265]
Completeness to θ = 29.13°	100.0 %	99.7 %	99.8 %
Absorption correction	Semi-empirical from equivalents	Semi-empirical from equivalents	Semi-empirical from equivalents
Max. and min. transmission	0.9814 and 0.9742	0.9907 and 0.9820	0.9962 and 0.9624
Refinement method	Full-matrix least-squares on F^2	Full-matrix least-squares on F^2	Full-matrix least-squares on F^2
Data / restraints / parameters	2898 / 178 / 247	4295 / 9 / 229	6537 / 0 / 299
Goodness-of-fit on F_2	1.016	1.010	1.089
Final R indices [I>2sigma(I)]	R1 = 0.0401, wR2 = 0.1095	R1 = 0.0432, wR2 = 0.1116	R1 = 0.0420, wR2 = 0.1182
R indices (all data)	R1 = 0.0588, wR2 = 0.1279	R1 = 0.0641, wR2 = 0.1276	R1 = 0.0565, wR2 = 0.1286
Largest diff. peak and hole	0.122 and -0.134 $e.Å^{-3}$	0.411 and -0.219 $e.Å^{-3}$	0.351 and -0.210 $e.Å^{-3}$

Table A2. 4 Crystal data and refinement for compounds 7-9

Compound	**7**	**8**	**9**
Empirical formula	$C_{18}H_{16}O_2$	$C_{19}H_{18}O_2$	$C_{22}H_{24}O_2$
Formula weight	264.31	278.33	320.41
Temperature	100(2) K	296(2) K	100(2) K
Wavelength	0.71073 Å	0.71073 Å	0.71073 Å
Crystal system	Monoclinic	Monoclinic	Monoclinic
Space group	I2/a	P2(1)/n (#14)	P2(1)/c
Unit cell dimensions	a = 16.5454(12) Å α= 90° b = 7.5826(5) Å β= 95.2065(11)° c = 22.0553(15) Å γ = 90°	a = 9.1313(7) Å α= 90° b = 17.5205(14) Å β= 99.9029(14)° c = 9.7613(8) Å γ = 90°	a = 7.6558(4) Å α= 90° b = 17.7701(9) Å β= 97.1985(7)° c = 12.6438(6) Å γ = 90°
Volume	2755.6(3) $Å^3$	1538.4(2) $Å^3$	1706.56(15) $Å^3$
Z	8	4	4
Density (calculated)	1.274 Mg/m^3	1.202 Mg/m^3	1.247 Mg/m^3
Absorption coefficient	0.082 mm^{-1}	0.077 mm^{-1}	0.078 mm^{-1}
F(000)	1120	592	688
Crystal size	0.32 x 0.23 x 0.03 mm^3	0.20 x 0.17 x 0.10 mm^3	0.53 x 0.50 x 0.43 mm^3
θ range for data collection	1.85 to 27.48°	2.32 to 24.71°	1.99 to 29.57°
Index ranges	-21<=h<=21, -9<=k<=9, -28<=l<=28	-10<=h<=10, -20<=k<=20, -11<=l<=11	-10<=h<=10, -24<=k<=24, -17<=l<=17
Reflections collected	23259	23942	31489
Independent reflections	3166 [R(int) = 0.0484]	2630 [R(int) = 0.0352]	4793 [R(int) = 0.0201]
Completeness to θ = 29.13°	99.9 %	100.0 %	100.0 %
Absorption correction	Semi-empirical from equivalents	Semi-empirical from equivalents	Semi-empirical from equivalents
Max. and min. transmission	0.9975 and 0.9745	0.9925 and 0.9845	0.9676 and 0.9598
Refinement method	Full-matrix least-squares on F^2	Full-matrix least-squares on F^2	Full-matrix least-squares on F^2
Data / restraints / parameters	3166 / 0 / 183	2630 / 36 / 224	4793 / 0 / 220
Goodness-of-fit on F_2	1.022	1.038	1.033
Final R indices [I>2sigma(I)]	R1 = 0.0496, wR2 = 0.1117	R1 = 0.0470, wR2 = 0.1144	R1 = 0.0376, wR2 = 0.1058
R indices (all data)	R1 = 0.0765, wR2 = 0.1286	R1 = 0.0688, wR2 = 0.1303	R1 = 0.0412, wR2 = 0.1093
Largest diff. peak and hole	0.272 and -0.311 $e.Å^{-3}$	0.361 and -0.274 $e.Å^{-3}$	0.456 and -0.235 $e.Å^{-3}$

Table A2. 5 Crystal data and refinement for compound 10-12

Compound	**10**	**11**	**12**
Empirical formula	$C_{25}H_{30}O_2$	$C_{21}H_{20}O_2$	$C_{22}H_{22}O_2$
Formula weight	362.49	304.37	318.40
Temperature	10	11	12
Wavelength	0.71073 Å	0.71073 Å	0.71073 Å
Crystal system	Monoclinic	Triclinic	Triclinic
Space group	P2(1)/n	P-1	P-1
Unit cell dimensions	a = 10.0442(4) Å α= 90° b = 13.8741(5) Å β= 94.1613(7)° c = 30.5325(12) Å γ = 90°	a = 11.2996(5) Å α= 88.7806(7)° b = 12.3091(6) Å β= 74.3156(7)° c = 12.3511(6) Å γ = 75.1626(7)°	a = 8.1422(7) Å α= 80.8542(13)° b = 9.8073(8) Å β= 87.0945(13)° c = 10.3190(9) Å γ = 86.9151(13)°
Volume	4243.6(3) $Å^3$	1596.65(13) $Å^3$	811.61(12) $Å^3$
Z	8	4	2
Density (calculated)	1.135 Mg/m^3	1.266 Mg/m^3	1.303 Mg/m^3
Absorption coefficient	0.070 mm^{-1}	0.080 mm^{-1}	0.082 mm^{-1}
F(000)	1568	648	340
Crystal size	0.45 x 0.42 x 0.26 mm^3	0.45 x 0.43 x 0.09 mm^3	0.41 x 0.39 x 0.17 mm^3
θ range for data collection	1.99 to 29.57°	1.71 to 29.13°	2.11 to 28.28°
Index ranges	-13<=h<=13, -19<=k<=19, -42<=l<=42	-15<=h<=15, -16<=k<=16, -16<=l<=16	-10<=h<=10, -13<=k<=13, -13<=l<=13
Reflections collected	46800	28959	16115
Independent reflections	11893 [R(int) = 0.0390]	8567 [R(int) = 0.0263]	4018 [R(int) = 0.0365]
Completeness to θ = 29.57°	100.0 %	99.7 %	99.6 %
Absorption correction	Semi-empirical from equivalents	Semi-empirical from equivalents	Semi-empirical from equivalents
Max. and min. transmission	0.9818 and 0.9695	0.9929 and 0.9650	0.9861 and 0.9675
Refinement method	Full-matrix least-squares on F^2	Full-matrix least-squares on F^2	Full-matrix least-squares on F^2
Data / restraints / parameters	11893 / 0 / 494	8567 / 0 / 415	4018 / 0 / 218
Goodness-of-fit on F^2	1.044	1.036	1.084
Final R indices [I>2sigma(I)]	R1 = 0.0464, wR2 = 0.1125	R1 = 0.0442, wR2 = 0.1090	R1 = 0.0425, wR2 = 0.1135
R indices (all data)	R1 = 0.0624, wR2 = 0.1214	R1 = 0.0576, wR2 = 0.1169	R1 = 0.0529, wR2 = 0.1244
Largest diff. peak and hole	0.352 and -0.254 $e.Å^{-3}$	0.394 and -0.263 $e.Å^{-3}$	0.284 and -0.355 $e.Å^{-3}$

Table A2. 6 Crystal data and refinement for compound 13

Compound	**13**
Empirical formula	$C_{25}H_{24}O_2$
Formula weight	356.44
Temperature	13
Wavelength	0.71073 Å
Crystal system	Monoclinic
Space group	P2(1)/n
Unit cell dimensions	a = 17.3689(7) Å α= 90°
	b = 6.3517(2) Å β= 113.1194(5)°
	c = 17.6297(7) Å γ = 90°
Volume	1788.74(12) $Å^3$
Z	4
Density (calculated)	1.324 Mg/m_3
Absorption coefficient	0.082 mm^{-1}
F(000)	760
Crystal size	0.55 x 0.43 x 0.26 mm_3
Theta range for data collection	2.11 to 29.13°.
Index ranges	-23<=h<=23, -8<=k<=8, -24<=l<=24
Reflections collected	24919
Independent reflections	4822 [R(int) = 0.0209]
Completeness to theta = 29.57°	99.9 %
Absorption correction	Semi-empirical from equivalents
Max. and min. transmission	0.9790 and 0.9562
Refinement method	Full-matrix least-squares on F_2
Data / restraints / parameters	4822 / 0 / 244
Goodness-of-fit on F_2	1.046
Final R indices [I>2sigma(I)]	R1 = 0.0394, wR2 = 0.1072
R indices (all data)	R1 = 0.0430, wR2 = 0.1109
Largest diff. peak and hole	0.423 and -0.262 $e.Å^{-3}$

Appendix III [1]HNMR of 9-anthracene carboxylic acids

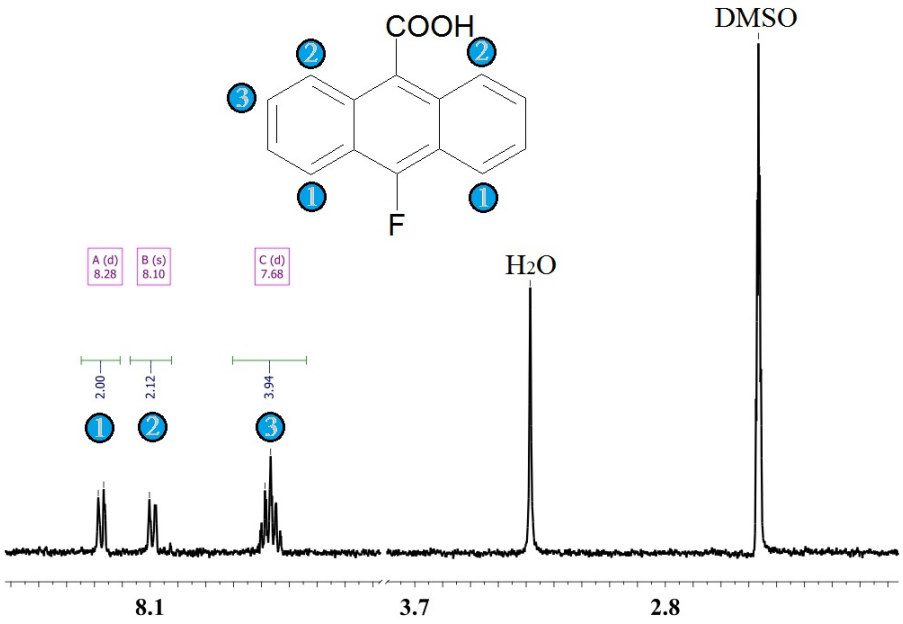

Figure A3. 1 [1]H-NMR of 10-fluoro-9-anthracene carboxylic acid **2**: (d-DMSO) δ (ppm), 7.6-7.7 (multiplet, 4H), 8.05-8.15 (doublet, 2H), 8.25-8.30 (doublet, 2H). The proton of carboxylic acid was not showing.

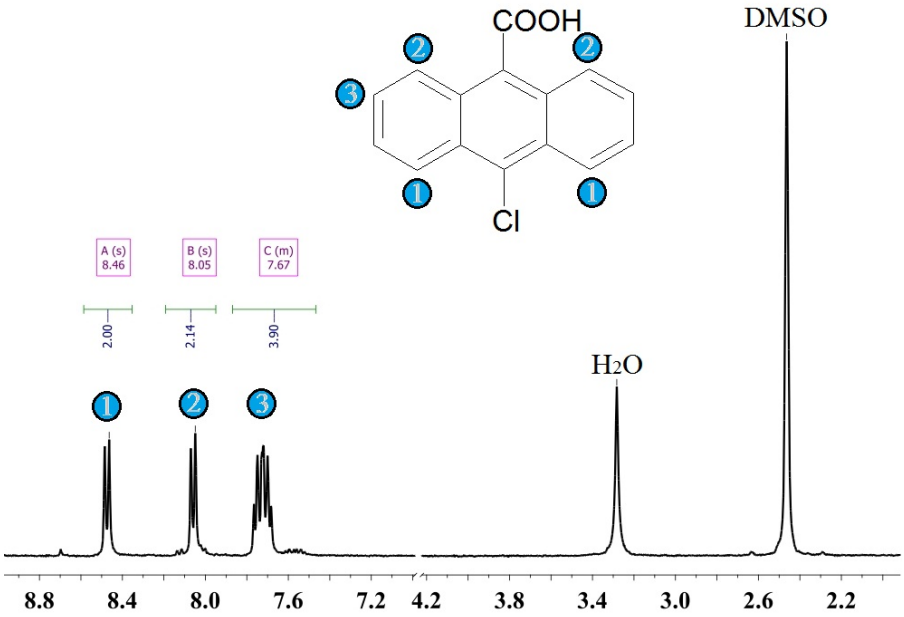

Figure A3. 2 [1]H-NMR of 10-chloro-9-anthracene carboxylic acid **3**: (d-DMSO) δ (ppm) 7.6-7.8 (multiplet, 4H), 8.0-8.1 (doublet, 2 H), 8.4-8.5 (doublet, 2H)

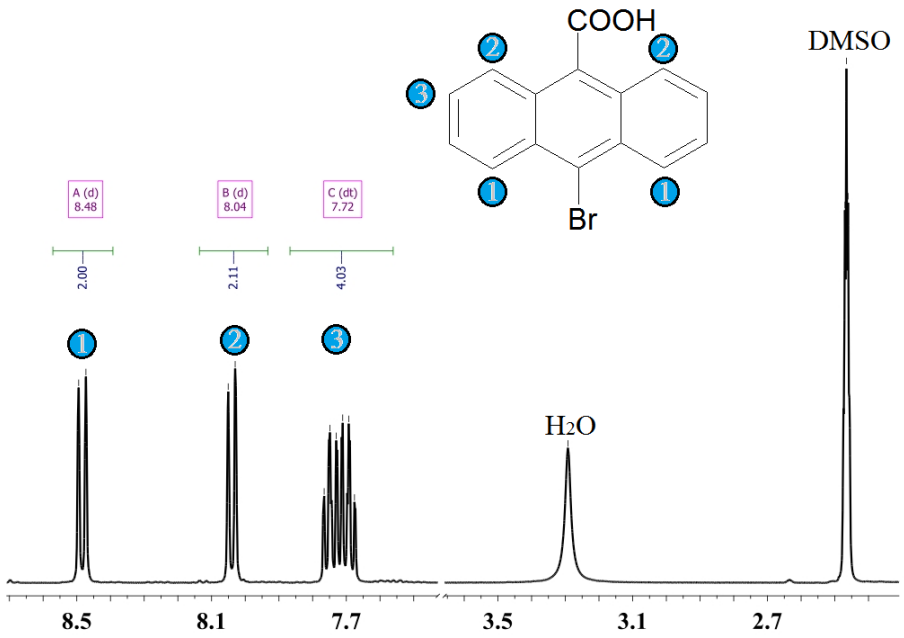

Figure A3. 3 ^{1}H-NMR of 10-bromo-9-anthracene carboxylic acid **4**: (d-DMSO) δ (ppm) 7.6-7.8 (mutiplet, 4H), 8.0-8.1 (doublet, 2H), 8.4-8.5 (doublet, 2H)

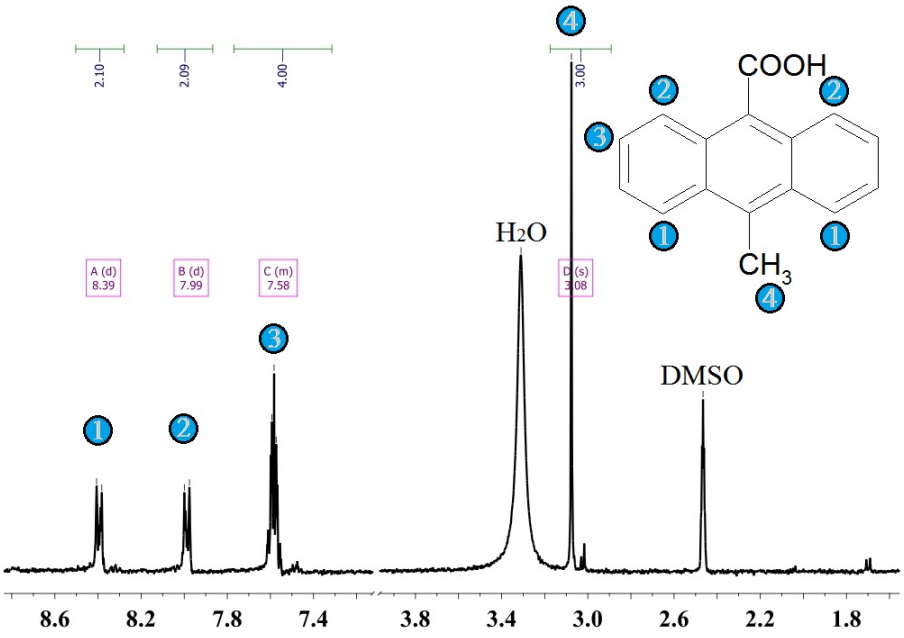

Figure A3. 4 ^{1}H-NMR of 10-methyl-9-anthracene carboxylic acid **5**: (d-DMSO) δ (ppm) 3.0-3.1 (singlet, 3H), 7.5-7.7 (multiplet, 4H), 7.95-8.05 (doublet, 2H), 8.35-8.45 (doublet, 2H)

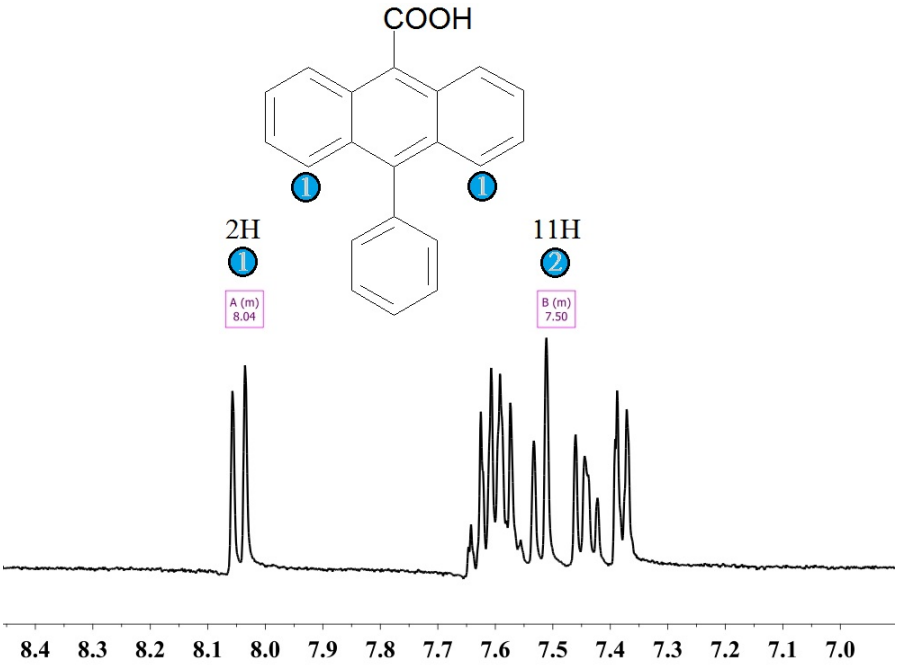

Figure A3. 5 [1]H-NMR of 10-phenyl-9-anthracene carboxylic acid **6**: (d-DMSO) δ (ppm) 7.35-7.65 (multiplet, 11H), 8.0-8.1 (multiplet, 2H, peri-H)

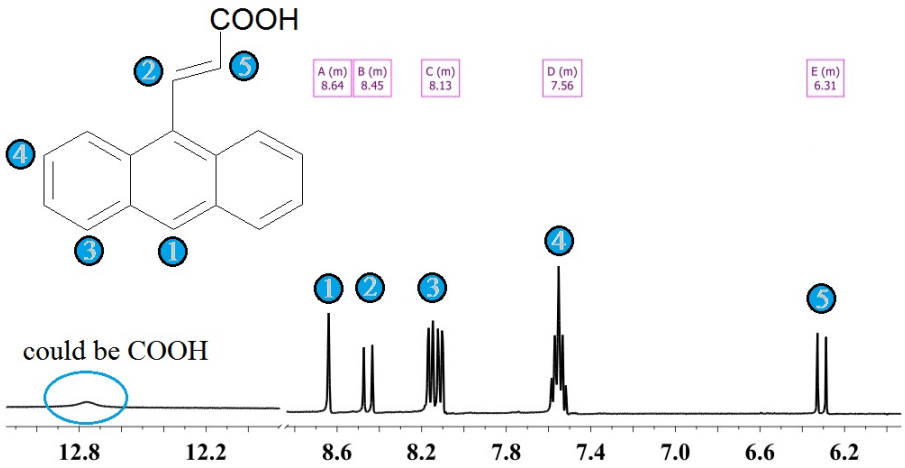

Figure A3. 6 [1]H-NMR of 3-Anthracen-9-yl-acrylic acid **7** :(d-DMSO) δ (ppm) 6.25-6.35 (doublet, 1H), 7.5-7.6 (mutiplet, 4H), 8.1-8.2 (multiplet, 4H), 8.4-8.5 (doublet, 1H), 8.6-8.7 (singlet, 1H)

Appendix IV Properties of bisanthracene esters

Table A4. 1 Crystal structure and packing information for D2 and two polymorphs of D3

ID	D2	D3 triclinic	D3 monoclinic
Empirical formula	C_{32} H_{22} O_4	C_{33} H_{24} O_4	C_{33} H_{24} O_4
Formula weight	470.5	484.52	484.52
Temperature	296(2) K	296(2) K	296(2) K
Wavelength	0.71073 Å	0.71073 Å	0.71073 Å
Crystal system	Triclinic	Triclinic	Monoclinic
Space group	P-1 (#2)	P-1 (#2)	P2(1)/c (#14)
Unit cell dimensions	a = 7.6118(4) Å α= 96.0618(9)° b = 9.0254(5) Å β= 109.6528(9)° c = 9.7039(5) Å γ = 110.8892(9)°	a = 8.7768(6) Å α= 95.0253(12)° b = 11.4287(8) Å β= 93.8645(12)° c = 13.5055(10) Å γ = 109.7005(11)°	a = 15.496(3) Å α= 90° b = 11.748(2) Å β= 95.456(3)° c = 14.238(3) Å γ = 90°
Volume	566.96(5) $Å^3$	1263.70(16) $Å^3$	2580.3(8) $Å^3$
Z	1	2	4
Density (calculated)	1.378 Mg/m^3	1.273 Mg/m^3	1.247 Mg/m^3
Absorption coefficient	0.090 mm^{-1}	0.083 mm^{-1}	0.081 mm^{-1}
F(000)	246	508	1016
Crystal size	0.26 x 0.11 x 0.06 mm^3	0.40 x 0.11 x 0.09 mm^3	0.41 x 0.31 x 0.05 mm^3
θ range for data collection	2.31 to 27.48°	1.52 to 23.25°	2.18 to 22.12°
Index ranges	-9<=h<=9, -11<=k<=11, -12<=l<=12	-9<=h<=9, -12<=k<=12, -14<=l<=14	-16<=h<=16, -12<=k<=12, -15<=l<=15
Reflections collected	10386	17329	20217
Independent reflections	2597 [R(int) = 0.0234]	3634 [R(int) = 0.0267]	3206 [R(int) = 0.0425]
Completeness to θ = 29.13°	99.9 %	100.0 %	99.6 %
Absorption correction	Semi-empirical from equivalents	Semi-empirical from equivalents	Semi-empirical from equivalents
Max. and min. transmission	0.9943 and 0.9770	0.9928 and 0.9677	0.9960 and 0.9678
Refinement method	Full-matrix least-squares on F_2	Full-matrix least-squares on F_2	Full-matrix least-squares on F_2
Data / restraints / parameters	2597 / 0 / 163	3634 / 0 / 334	3206 / 735 / 515
Goodness-of-fit on F_2	1.031	1.034	1.012
Final R indices [I>2sigma(I)]	R1 = 0.0534, wR2 = 0.1412	R1 = 0.0426, wR2 = 0.1076	R1 = 0.0414, wR2 = 0.1010
R indices (all data)	R1 = 0.0892, wR2 = 0.1680	R1 = 0.0700, wR2 = 0.1295	R1 = 0.0792, wR2 = 0.1296
Largest diff. peak and hole	0.375 and -0.187 $e.Å^{-3}$	0.160 and -0.131 $e.Å^{-3}$	0.184 and -0.127 $e.Å^{-3}$

Table A4. 2 Crystal structure and packing information for D4 and D6

ID	D4	D6
Empirical formula	C_{34} H_{26} O_4	C_{36} H_{30} O_4
Formula weight	498.55	526.6
Temperature	296(2) K	296(2) K
Wavelength	0.71073 Å	0.71073 Å
Crystal system	Monoclinic	Triclinic
Space group	P2(1)/c (#14)	P-1 (#2)
Unit cell dimensions	a = 8.2092(6) Å α = 90°	a = 8.5118(3) Å α= 81.0972(7)°
	b = 10.8450(8) Å β= 99.9743(11)°	b = 12.5529(5) Å β= 72.8014(7)°
	c = 14.0837(10) Å γ = 90°	c = 13.9437(6) Å γ= 86.6227(7)°
Volume	1234.90(16) $Å^3$	1405.95(10) $Å^3$
Z	2	2
Density (calculated)	1.341 Mg/m^3	1.244 Mg/m^3
Absorption coefficient	0.087 mm^{-1}	0.080 mm^{-1}
F(000)	524	556
Crystal size	0.44 x 0.28 x 0.18 mm^3	0.53 x 0.17 x 0.06 mm^3
Theta range for data collection	2.38 to 29.13°	1.54 to 25.03°
Index ranges	-11<=h<=11, -14<=k<=14, -19<=l<=19	-10<=h<=10, -14<=k<=14, -16<=l<=16
Reflections collected	17361	22704
Independent reflections	3323 [R(int) = 0.0287]	4960 [R(int) = 0.0240]
Completeness to theta = 29.13°	99.9 %	100.0 %
Absorption correction	Semi-empirical from equivalents	Semi-empirical from equivalents
Max. and min. transmission	0.9846 and 0.9626	0.9949 and 0.9585
Refinement method	Full-matrix least-squares on F^2	Full-matrix least-squares on F^2
Data / restraints / parameters	3323 / 0 / 172	4960 / 0 / 361
Goodness-of-fit on F_2	1.044	1.025
Final R indices [I>2sigma(I)]	R1 = 0.0442, wR2 = 0.1203	R1 = 0.0408, wR2 = 0.1027
R indices (all data)	R1 = 0.0656, wR2 = 0.1357	R1 = 0.0655, wR2 = 0.1188
Largest diff. peak and hole	0.332 and -0.174 $e.Å^{-3}$	0.170 and -0.164 $e.Å^{-3}$

Appendix V Data of the dimensions of 9AC microribbons

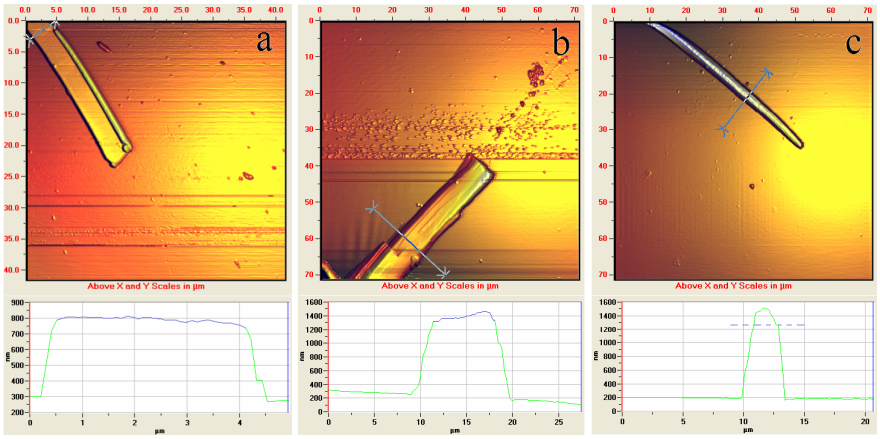

Figure A5. 1 Examples of AFM profile images of microribbons

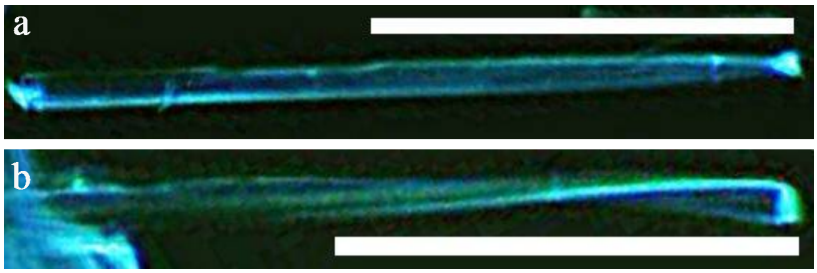

Figure A5. 2 Fluorescence microscopy images of twisted ribbons on a solid substrate where AFM profiles could be measured. As shown in the above images, many ribbons showed only a half-twist, which could still be used to obtain L_{twist}. The scale bars are 50 µm.

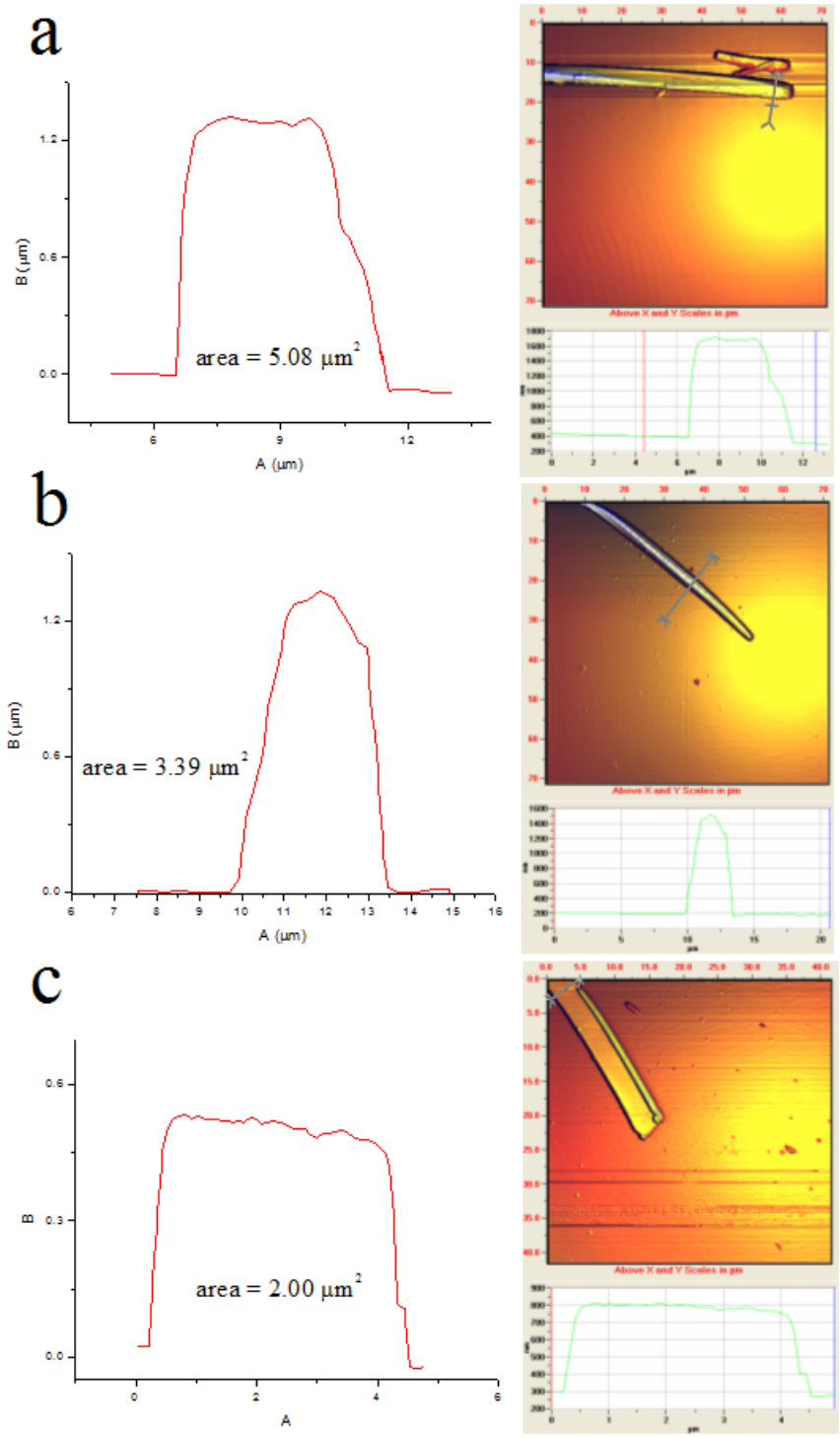

Figure A5. 3 The cross-section areas of the ribbons were obtained through numerical integration of the AFM profiles using Origin 8.0, as shown for three different ribbons.